

NATIONAL AERONAUTICS AND SPACE ADMINISTRATION

Technical Report 32-1526

Volume XII

The Deep Space Network

Progress Report

For September and October 1972

**CASE FILE
COPY**

**JET PROPULSION LABORATORY
CALIFORNIA INSTITUTE OF TECHNOLOGY
PASADENA, CALIFORNIA**

December 15, 1972

NATIONAL AERONAUTICS AND SPACE ADMINISTRATION

Technical Report 32-1526

Volume XII

The Deep Space Network

Progress Report

For September and October 1972

JET PROPULSION LABORATORY
CALIFORNIA INSTITUTE OF TECHNOLOGY
PASADENA, CALIFORNIA

December 15, 1972

**Prepared Under Contract No. NAS 7-100
National Aeronautics and Space Administration**

Preface

This report presents DSN progress in flight project support, TDA research and technology, network engineering, hardware and software implementation, and operations. Each issue presents material in some, but not all, of the following categories in the order indicated:

Description of the DSN

Mission Support

- Interplanetary Flight Projects
- Planetary Flight Projects
- Manned Space Flight Projects
- Advanced Flight Projects

Radio Science

Supporting Research and Technology

- Tracking and Ground-Based Navigation
- Communications, Spacecraft/Ground
- Station Control and Operations Technology
- Network Control and Data Processing

Network Engineering and Implementation

- Network Control System
- Ground Communications
- Deep Space Stations

Operations and Facilities

- Network Operations
- Network Control System Operations
- Ground Communications
- Deep Space Stations
- Facility Engineering

In each issue, the part entitled "Description of the DSN" describes the functions and facilities of the DSN and may report the current configuration of one of the five DSN systems (Tracking, Telemetry, Command, Monitor and Control, and Test and Training).

The work described in this report series is either performed or managed by the Tracking and Data Acquisition organization of JPL for NASA.

1187-100-100

Contents

DESCRIPTION OF THE DSN

DSN Functions and Facilities	1
N. A. Renzetti	

MISSION SUPPORT

Interplanetary Flight Projects

Helios Mission Support	5
P. S. Goodwin	
NASA Code 311-03-21-50	

Planetary Flight Projects

Mariner Venus/Mercury 1973 Mission Support	10
E. K. Davis	
NASA Code 311-03-21-60	
Viking Mission Support	14
D. J. Mudgway	
NASA Code 311-03-21-70	

SUPPORTING RESEARCH AND TECHNOLOGY

Tracking and Ground-Based Navigation

X-Band Radar Development	19
C. P. Wiggins	
NASA Code 310-10-64-01	
X-Band Uplink Microwave Components	22
H. R. Buchanan	
NASA Code 310-10-64-03	
RF Properties of the 64-m-Diameter Antenna Mesh Material as a Function of Frequency	26
T. Y. Otoshi	
NASA Code 310-20-66-02	
An Analysis of System Performance Under the Severe Weather Conditions at Goldstone, December 1971	32
M. S. Reid	
NASA Code 310-20-66-02	
Very Long Baseline Interferometry (VLBI) Possibilities for Lunar Study	35
M. A. Slade, P. F. MacDoran, and J. B. Thomas	
NASA Code 310-10-60-50	

Contents (contd)

Determination of the Helios Spacecraft Attitude by Polarization Measurement	40
----------------------------------------------------------------------------------------------	-----------

B. D. Mulhall

NASA Code 310-10-60-52

Phase-Stable, Low-Phase-Noise Filters for Reference Signals	44
------------------------------------------------------------------------------	-----------

G. F. Lutes

NASA Code 310-10-62-03

Complex Mixer Error Analysis	47
-----------------------------------------------	-----------

R. Winkelstein

NASA Code 310-10-62-04

Communications, Spacecraft/Ground

Excessive Shaft Friction Variation Corrected by Lubricant Change	51
-----------------------------------------------------------------------------------	-----------

H. McGinness

NASA Code 310-20-65-02

Frequency Generation and Control: Atomic Hydrogen Dissociator	56
--------------------------------------------------------------------------------	-----------

H. Erpenbach and D. Norris

NASA Code 310-10-62-01

Improved RF Calibration Techniques — A Practical Technique for Accurate Determination of Microwave Surface Resistivity	59
-----------------------------------------------------------------------------------------------------------------------------------------	-----------

R. Clauss and P. D. Potter

NASA Code 310-20-66-02

PARADES Structural Design System Capabilities	68
----------------------------------------------------------------	-----------

R. Levy and R. Melosh

NASA Code 310-20-65-01

Improved RF Calibration Techniques: Commercial Precision IF Attenuator Evaluation	74
----------------------------------------------------------------------------------------------------	-----------

C. Stelzried, B. Seidel, M. Franco, and D. Acheson

NASA Code 310-20-66-02

Improved RF Calibration Techniques: System Operating Noise Temperature Calibrations	83
------------------------------------------------------------------------------------------------------	-----------

M. S. Reid

NASA Code 310-20-66-02

Optimum Noncoherent Receiver at Low Signal-to-Noise Ratio for Unknown Doppler Shifted Signals	88
----------------------------------------------------------------------------------------------------------------	-----------

J. K. Holmes

NASA Code 310-20-67-03

Optimum Frame Sync Acquisition for Biorthogonally Coded Telemetry	92
------------------------------------------------------------------------------------	-----------

B. K. Levitt

NASA Code 310-20-92-02

Iterative Design of Antenna Structures	100
---------------------------------------------------------	------------

R. Levy

NASA Code 310-20-65-01

Contents (contd)

Station Control and Operations Technology

Two-Station Interferometer Analog Input Channel	112
------------------------------------------------------------------	------------

T. O. Anderson
NASA Code 310-30-68-06

DSN Research and Technology Support	124
------------------------------------------------------	------------

E. B. Jackson and R. B. Kolbly
NASA Code 310-30-69-02

An Inventory and Procurement Policy for the Deep Space Network	131
-------------------------------------------------------------------------------	------------

I. Eisenberger, F.-R. Maiocco, and G. Lorden
NASA Code 310-30-69-01

Network Control and Data Processing

A Demonstration of DSN Clock Synchronization by VLBI	149
-----------------------------------------------------------------------	------------

W. J. Hurd
NASA Code 310-40-72-02

On the Weight Enumerators of Quadratic Residue Codes	161
-----------------------------------------------------------------------	------------

J. Mykkeltveit, C. Lam, and R. McEliece
NASA Codes 502-33-92-03 and 310-40-70-02

Sequential Decoding With a Noisy Carrier Reference	167
---------------------------------------------------------------------	------------

J. W. Layland
NASA Code 310-40-72-02

An Execution Analyzer for the Sigma 5 Computer	176
-----------------------------------------------------------------	------------

C. C. Klimasauskas
NASA Code 310-40-72-01

Complex Mixer System	189
---------------------------------------	------------

L. C. Constenla
NASA Code 310-40-72-04

A Multicomputer Communications System	195
--------------------------------------------------------	------------

J. W. Layland and W. Lushbaugh
NASA Code 310-40-72-02

NETWORK ENGINEERING AND IMPLEMENTATION

Deep Space Stations

Dual Carrier	200
-------------------------------	------------

R. H. Smith
NASA Code 312-03-12-00

A Dual-Ignitron Crowbar	205
------------------------------------------	------------

E. J. Finnegan
NASA Code 311-03-14-21

Contents (contd)

Digital Frequency Shifter	209
--------------------------------------------	------------

R. N. MacClellan

NASA Code 312-03-31-46

Hydrostatic Bearing Runner Leveling at Overseas 64-m-Diameter Antenna	214
--------------------------------------------------------------------------------------------	------------

H. P. Phillips

NASA Code 311-03-42-45

OPERATIONS AND FACILITIES

Deep Space Stations

DSS Receiving System Saturation at High Signal Levels	220
------------------------------------------------------------------------	------------

H. C. Younger

NASA Code 311-03-14-52

Spectrum of an Asynchronously Biphase Modulated Square Wave	226
------------------------------------------------------------------------------	------------

J. R. Lesh

NASA Code 311-03-13-11

DSN Functions and Facilities

N. A. Renzetti
Mission Support Office

The objectives, functions, and organization of the Deep Space Network are summarized. The Deep Space Instrumentation Facility, the Ground Communications Facility, and the Network Control System are described.

The Deep Space Network (DSN), established by the National Aeronautics and Space Administration (NASA) Office of Tracking and Data Acquisition under the system management and technical direction of the Jet Propulsion Laboratory (JPL), is designed for two-way communications with unmanned spacecraft traveling approximately 16,000 km (10,000 mi) from Earth to planetary distances. It supports or has supported, the following NASA deep space exploration projects: Ranger, Surveyor, Mariner Venus 1962, Mariner Mars 1964, Mariner Venus 67, Mariner Mars 1969, Mariner Mars 1971, Mariner Venus-Mercury 1973 (JPL); Lunar Orbiter and Viking (Langley Research Center); Pioneer (Ames Research Center); Helios (West Germany); and Apollo (Manned Spacecraft Center), to supplement the Spaceflight Tracking and Data Network (STDN).

The Deep Space Network is one of two NASA networks. The other, STDN, is under the system management and technical direction of the Goddard Space Flight Center. Its function is to support manned and unmanned Earth-orbiting and lunar scientific and communications satellites. Although the DSN was concerned with unmanned lunar spacecraft in its early years, its primary objective now and into the future is to continue its support of planetary and interplanetary flight projects.

A development objective has been to keep the network capability at the state of the art of telecommunications and data handling and to support as many flight projects as possible with a minimum of mission-dependent hardware and software. The DSN provides direct support of each flight project through that project's tracking and

data system. This management element is responsible for the design and operation of the hardware and software in the DSN which are required for the conduct of flight operations.

Beginning in FY 1973 a modified DSN interface has been established with the flight projects. In lieu of the SFOF, a multimission Mission Control and Computing Center (MCCC) has been activated as a separate functional and management element within JPL. This function, as negotiated with each flight project, will provide all computing and mission operations support for missions controlled from JPL. DSN computing support will be provided separately by the DSN. Radio metric, telemetry, and command data interfaces with the DSN are a joint DSN, MCCC, and flight project responsibility. The organization and procedures necessary to carry out these new activities will be reported in this document in the near future.

The DSN function, in supporting a flight project by tracking the spacecraft, is characterized by five network systems:

- (1) DSN Tracking System. Generates radio metric data; i.e., angles, one- and two-way doppler and range, and transmits raw data to mission control.
- (2) DSN Telemetry System. Receives, decodes, records, and retransmits engineering and scientific data generated in the spacecraft to Mission Control.
- (3) DSN Command System. Accepts coded signals from mission control via the GCF and transmits them to the spacecraft in order to initiate spacecraft functions in flight.
- (4) DSN Monitor and Control System. Instruments, transmits, records, and displays those parameters of the DSN necessary to verify configuration and validate the network. Provides operational direction and configuration control of the network and primary interface with flight project Mission Control personnel.
- (5) DSN Test and Training System. Generates and controls simulated data to support development, test, training and fault isolation within the DSN. Participates in mission simulation with flight projects.

The facilities needed to carry out these functions have evolved in three technical areas: (1) the Deep Space Stations (DSSs) and the telecommunications interface

through the RF link with the spacecraft is known as the Deep Space Instrumentation Facility (DSIF); (2) the Earth-based point-to-point voice and data communications from the stations to Mission Control is known as the Ground Communications Facility (GCF); (3) the network monitor and control function is known as the Network Control System (NCS).

I. Deep Space Instrumentation Facility

A. Tracking and Data Acquisition Facilities

A world-wide set of Deep Space Stations with large antennas, low-noise phase-lock receiving systems, and high-power transmitters provide radio communications with spacecraft. The DSSs and the deep space communications complexes (DSCCs) they comprise are given in Table 1.

Radio contact with a spacecraft usually begins when the spacecraft is on the launch vehicle at Cape Kennedy, and it is maintained throughout the mission. The early part of the trajectory is covered by selected network stations of the Air Force Eastern Test Range (AFETR) and the STDN of the Goddard Space Flight Center.¹ Normally, two-way communications are established between the spacecraft and the DSN within 30 min after the spacecraft has been injected into lunar, planetary, or interplanetary flight. A compatibility test station at Cape Kennedy (discussed later) tests and monitors the spacecraft continuously during the launch checkout phase. The deep space phase begins with acquisition by 26-m DSSs. These and the remaining DSSs listed in Table 1 provide radio communications until the end of the mission.

To enable continuous radio contact with spacecraft, the DSSs are located approximately 120 deg apart in longitude; thus a spacecraft in deep space flight is always within the field-of-view of at least one DSS, and for several hours each day may be seen by two DSSs. Furthermore, since most spacecraft on deep space missions travel within 30 deg of the equatorial plane, the DSSs are located within latitudes of 45 deg north and south of the equator. All DSSs operate at S-band frequencies: 2110-2120 MHz for Earth-to-spacecraft transmission and 2290-2300 MHz for spacecraft-to-Earth transmission. An X-band capability is being readied for future missions beginning in 1973.

¹The 9-m (30-ft) diam antenna station established by the DSN on Ascension Island during 1965 to act in conjunction with the STDN orbital support 9-m (30-ft) diam antenna station was transferred to the STDN in July 1968.

To provide sufficient tracking capability to enable returns of useful data from around the planets and from the edge of the solar system, a 64-m (210-ft) diam antenna subnet will be required. Two additional 64-m (210-ft) diam antenna DSSs are under construction at Madrid and Canberra and will operate in conjunction with DSS 14 to provide this capability. These stations are scheduled to be operational by the middle of 1973.

B. Compatibility Test Facilities

In 1959, a mobile L-band compatibility test station was established at Cape Kennedy to verify flight-spacecraft/DSN compatibility prior to the launch of the Ranger and Mariner Venus 1962 spacecraft. Experience revealed the need for a permanent facility at Cape Kennedy for this function. An S-band compatibility test station with a 1.2-m (4-ft) diameter antenna became operational in 1965. In addition to supporting the preflight compatibility tests, this station monitors the spacecraft continuously during the launch phase until it passes over the local horizon.

Spacecraft telecommunications compatibility in the design and prototype development phases was formerly verified by tests at the Goldstone DSCC. To provide a more economical means for conducting such work and because of the increasing use of multiple-mission telemetry and command equipment by the DSN, a Compatibility Test Area (CTA) was established at JPL in 1968. In all essential characteristics, the configuration of this facility is identical to that of the 26-m (85-ft) and 64-m (210-ft) diameter antenna stations.

The JPL CTA is used during spacecraft system tests to establish the compatibility with the DSN of the proof test model and development models of spacecraft, and the Cape Kennedy compatibility test station is used for final flight spacecraft compatibility validation testing prior to launch.

II. Ground Communications Facility

The GCF provides voice, high-speed data, wideband data, and teletype communications between the Mission Operations Center and the DSSs. In providing these capabilities, the GCF uses the facilities of the worldwide NASA Communications Network (NASCOM)² for all long

²Managed and directed by the Goddard Space Flight Center.

distance circuits, except those between the Mission Operations Center and the Goldstone DSCC. Communications between the Goldstone DSCC and the Mission Operations Center are provided by a microwave link directly leased by the DSN from a common carrier.

Early missions were supported by voice and teletype circuits only, but increased data rates necessitated the use of high-speed and wideband circuits for DSSs. Data are transmitted to flight projects via the GCF using standard GCF/NASCOM formats. The DSN also supports remote mission operations centers using the GCF/NASCOM interface.

III. Network Control System

The DSN Network Control System is comprised of hardware, software, and operations personnel to provide centralized, real-time control of the DSN and to monitor and validate the network performance. These functions are provided during all phases of DSN support to flight projects. The Network Operations Control Area is located in JPL Building 230, adjacent to the local Mission Operations Center. The NCS, in accomplishing the monitor and control function does not alter, delay, or serially process any inbound or outbound data between the flight project and tracking stations. Hence NCS outages do not have a direct impact on flight project support. Voice communications are maintained for operations control and coordination between the DSN and flight projects, and for minimization of the response time in locating and correcting system failures.

The NCS function will ultimately be performed in data processing equipment separate from flight project data processing and specifically dedicated to the NCS function. During FY 1973, however, DSN operations control and monitor data will be processed in the JPL 360/75 and in the 1108. In FY 1974 the NCS data processing function will be partly phased over to an interim NCS processor, and finally, in FY 1975, the dedicated NCS data processing capability will be operational. The final Network Data Processing Area will be located remote from the Network Operations Control Area so as to provide a contingency operating location to minimize single point of failure effects on the network control function. A preliminary description of the NCS appears elsewhere in this document.

Table 1. Tracking and data acquisition stations of the DSN

DSCC	Location	DSS	DSS serial designation	Antenna		Year of initial operation
				Diameter, m (ft)	Type of mounting	
Goldstone	California	Pioneer	11	26(85)	Polar	1958
		Echo	12	26(85)	Polar	1962
		(Venus) ^a	13	26(85)	Az-El	1962
		Mars	14	64(210)	Az-El	1966
—	Australia	Woomera	41	26(85)	Polar	1960
Tidbinbilla	Australia	Weemala (formerly Tidbinbilla)	42	26(85)	Polar	1965
		Ballima (formerly Booroomba)	43	64(210)	Az-El	Under construction
—	South Africa	Johannesburg	51	26(85)	Polar	1961
Madrid	Spain	Robledo	61	26(85)	Polar	1965
		Cebreros	62	26(85)	Polar	1967
		Robledo	63	64(210)	Az-El	Under construction

^aA research-and-development facility used to demonstrate the feasibility of new equipment and methods to be integrated into the operational network. Besides the 26-m (85-ft) diam Az-El mounted antenna, DSS 13 has a 9-m (30-ft) diam Az-El mounted antenna that is used for interstation time correlation using lunar reflection techniques, for testing the design of new equipment, and for support of ground-based radio science.

Helios Mission Support

P. S. Goodwin
Mission Support Office

Project Helios is a joint deep space project of the Federal Republic of West Germany and the United States. Two solar orbiting spacecraft are planned, the first to be launched in mid-1974 and the second in late 1975. The spacecraft will have a perihelion of approximately 0.25 AU and an aphelion of 1.0 AU. These highly elliptical orbits will come closer to the sun than any known or presently planned deep space venture.

Prior volumes of this series describe the history and organization of this program, the spacecraft configuration and trajectory, its telecommunications system, and the results of the semi-annual Helios Joint Working Group Meetings, which are held alternately in the United States and the Federal Republic of West Germany. This article deals with DSN activities since the Sixth Helios Joint Working Group Meeting, which was held at JPL in April-May 1972.

I. Introduction

Volume X (Ref. 1) of this report described the Tracking and Data System (TDS) activities and highlights of the Sixth Helios Joint Working Group (HJWG) Meeting, whose proceedings are recorded in its formal minutes (Ref. 2). This article summarizes the DSN activities since that date, including the DSN preparations for the Seventh HJWG Meeting, which will be held in Porz-Wahn (near Bonn), West Germany, October 25-31, 1972.

II. DSN/Helios Trainee Program

It is most appropriate to open this article with a discussion of the DSN/Helios Trainee Program (Ref. 3,

p. 19) since it has now come to a formal conclusion. In the 3-year period from September 1969 to September 1972, fifteen West German engineers spent 1 year at their government's expense in residency at the Jet Propulsion Laboratory to further their knowledge of space flight technology in their own particular fields by being assigned duties on JPL programs that employed techniques and skills needed by the Helios Project.

Now that the Trainee Program has concluded, it is proper to reflect upon its value. First, not enough can be said about the excellent caliber—both technical and personal—of those who participated in the program. Each Trainee was a credit to his country, his organization, and certainly to the Helios Project Management that selected

him for this purpose. Secondly, the program can be considered highly successful, despite the fact that it was not always possible to achieve 100% correlation between the Trainees' future Helios responsibilities and on-going JPL activities. Fortunately, this correlation was very high in a majority of the cases, and more than satisfactory in the remaining instances. The success of the Program has already been demonstrated by the Trainees who have returned to Germany and have contributed heavily to the Helios Project efforts, in both a technical and managerial capacity. Third, the intangible asset of "team spirit" that prevails throughout the Helios Project is due, in part, to the Trainee Programs instituted by the Project at such NASA facilities as the Goddard Space Flight Center and the Jet Propulsion Laboratory.

III. DSN Configuration for Helios Support

The expanding NASA-TDS effort in support of Project Helios is the result of two independent but overlapping factors. The first is the logical redefinition of responsibilities between NASA's Offices of Space Sciences (OSS) and Tracking and Data Acquisition (OTDA) which has evolved over the past year's time. The second factor is that Helios is now only slightly over 1½ years from launch, which means that the various line organization teams are building in preparation for launch and mission operations. The combination of these two factors has resulted in a slightly modified NASA-TDS structure from that originally depicted in Ref. 3 (Fig. 1, p. 20).

A. DSN Configuration for Helios

The presently planned DSN configuration for Helios, shown in Fig. 1, depicts a data flow pattern that is markedly similar to that described in Ref. 3. The significant difference lies in the DSN-Mission Control and Computing Center (MCCC)¹ interface. Prior to the redefinition of the OSS/OTDA division of responsibility, the MCCC was part of the DSN and hence funded by OTDA. Under the new organizational structure, the MCCC is funded by OSS in order to provide single Headquarters Office control over both the mission-independent and the mission-dependent Mission Control Center hardware/software activities. This, therefore, places the DSN interface as depicted in the upper right-hand corner of Fig. 1.

B. Interim Network Control System

The new DSN interface with the Flight Project Ground Data System is further depicted in Fig. 2. The significant

change shown in this figure is that all spacecraft-oriented data flow directly to/from the Deep Space Stations and the Mission Control and Computing Center (which houses the Flight Project activities) or, in the case of a Remote Mission Operations Center, the MCCC acts as the collecting/processing/distributing point for all spacecraft-oriented data. However, the DSN is still responsible for the Network Control function. To accomplish this, the Network Control System (NCS) is placed "off-line" to the flow of spacecraft data, but has access to it to the extent needed to perform network functions. The implementation of a Network Control System represents a new DSN activity, which has a planned but staggered operational readiness schedule that will be completed very close to the Helios-A launch date. Therefore, to accommodate Helios pre-mission testing and training as well as avoid confusion during Helios-A launch, an interim NCS configuration will become operational about 6 months prior to the first Helios launch and will contain the functions depicted in Fig. 2.

IV. Significant Events Since the Sixth Helios Joint Working Group Meeting

A. NSP and Other Interface Documentation

1. *NASA Support Plan (NSP)*. A preliminary NSP, dated September 1, 1972, was issued in response to the Deep Space Phase requirements set forth in the preliminary Helios Support Instrumentation Requirements Document (SIRD), dated September 1, 1971. This issue of the NSP treats the interface and the support requirements between the Helios spacecraft and the DSN, together with the spacecraft data that the DSN will deliver/receive via the DSN/MCCC interface to the Helios Ground Data System. Per NASA-OSS/OTDA agreement, the response to the Helios SIRD requirements for ground data processing will be contained in a new document titled "MCCC Support Plan (MSP)," which will be prepared by that organization. Progress regarding the MSP will be reported separately.

2. *SIRD*. Pre-signature copies of the final Helios SIRD were received by the DSN in mid-September 1972. This document is presently undergoing review prior to starting preparations for the final NSP, which is due April 1, 1973.

3. *Helios spacecraft/DSN interface*. The Helios Spacecraft Telecommunications Subsystem/DSN Interface Definition Document (JPL Document 613-6) is authored jointly by the DSN Manager for Helios and the Helios

¹Formerly called Space Flight Operations Facility (SFOF).

Spacecraft Systems Manager, each contributing his portion of the interface definition. At the present time, the DSN portion of the manuscript has received formal approval, and the document is now undergoing German author review and approval. Publication is anticipated prior to the end of the year.

4. Helios telecommunications link design. By mutual Helios Project/DSN agreement, the Helios Telecommunications Link Design and Performance Analysis Document will be maintained and controlled by the Project Office, but shall be constrained by the DSN performance parameters contained in the Interface Definition Document (613-6) mentioned above. The Link Design Document was originally issued on June 30, 1971, but has subsequently been updated—the latest update being in September 1972. It is anticipated that further updates may become necessary as the actual performance of the Prototype and Flight Model Spacecraft Telecommunications Subsystems becomes known.

B. DSN Planetary Ranging System Design

In response to an urgent Sixth HJWG action item, the DSN Management has made a decision to implement, for the Helios era, a 64-m-diameter antenna station planetary ranging system design that will be capable of using either a "continuous spectrum" (Tau) or a "discrete spectrum" (Mu) ranging code. This decision will permit the Helios Project to employ whichever ranging code best fulfills the mission objectives at the specific times the spacecraft is being supported by a DSN 64-m station. A planetary ranging system capability is not being planned for the DSN 26-m stations; however, the latter will retain the Mark I-A lunar continuous spectrum ranging capability, which can provide unambiguous range data to a distance of 800,000 km.

C. Status of Compatibility Test Effort

As mentioned in Ref. 1 (p. 15), compatibility tests were performed on the Helios Engineering Model (EM) Spacecraft Radio Subsystem (JPL Documents 613-5 and 613-8) during April 1972. While these tests can be considered satisfactory, two significant factors should be noted: first, the receiver employed in the tests has subsequently been replaced by a new design and second, the tests did not incorporate the spacecraft data handling portion of the equipment.

With respect to the first factor, a meeting held in July 1972 in Bonn, West Germany, between the TDS Manager and the Helios Spacecraft Telecommunications Sub-

system Manager concluded that certain of the Engineering Model Telecommunications Subsystem compatibility tests should be repeated for technical reasons. However, the Engineering Model spacecraft schedule was such that it was prohibitive to consider returning the Spacecraft Radio System to Deep Space Station (DSS) 71/Compatibility Test Area (CTA) 21 for this purpose. Instead, it was decided to repeat the tests using the Project-supplied Helios Test Set (HTS) while the EM spacecraft was still at the prime contractor's plant at Ottobrun, West Germany. These repeated compatibility tests are presently scheduled for later this year. While it is recognized that the HTS is not an exact technical substitute for a Deep Space Station, the test results (613-8) obtained from the EM transponder tests at DSS 71 did correlate reasonably well with similar tests performed on the EM transponder using the HTS equipment in Germany prior to its shipment to DSS 71. The technical importance of repeating these tests, therefore, outweighed the disadvantage of not being able to repeat them at a Deep Space Station.

The other factor, namely that no tests have yet been conducted regarding the Data System compatibility, is still considered significant because the next scheduled opportunity is not until the arrival in the U.S. of the Prototype Model in early 1974. Unfortunately, in this case, work-around techniques are not quite so obvious. One consideration is the possible use of spacecraft test tapes obtained by the HTS for checkout against the Ground Data System. However, for both technical and practical reasons, such test tapes have their maximum usefulness during the 6-month time period preceding the arrival of the Prototype Model for compatibility tests. Therefore, other possible techniques are being explored that might be employed at an earlier date in order to gain confidence in the total spacecraft/Ground Data System design.

V. DSN Preparations for the Seventh Helios Joint Working Group Meeting

The DSN is represented in the Helios Joint Working Group structure via membership on the TDS Subgroup Panel (see Fig. 1, p. 20, of Ref. 3). The total TDS agenda for the Seventh HJWG is quite extensive because it involves the activities of the Near-Earth Phase Network, the Deep Space Network, and the German Network, plus all of the ground data handling equipment in both the U.S. and in Germany that is necessary for real-time operations, as well as the production of the final Experiment Data Records (EDR). Within this ex-

tensive agenda, the DSN is particularly interested and expects to participate heavily in discussions regarding

- (1) The mutual compatibility of the overall telecommunications design with respect to the DSN.
- (2) The resolution of specific open questions, such as the use of coded vs. uncoded spacecraft telemetry during launch, the problem of DSN blind acquisition of the spacecraft in the event of loss of downlink, etc.
- (3) The detailed definition of the mission-independent interface between the DSN and the German Network in support of Helios.

The foregoing, plus related topics, are expected to undergo extensive discussion during the Seventh HJWG proceedings. In fact, because of the overcrowded nature of the formal TDS agenda, it may become necessary to treat some of these topics in special splinter sessions scheduled outside the formal Working Group proceed-

ings. In the interest of making these technical sessions as productive as possible, the DSN has organized special pre-meeting study teams on the above key agenda topics to analyze in depth the possible technical alternatives so that the Working Group sessions will have the benefit of the maximum available knowledge prior to making a decision on the best course of action for Helios to pursue. In this manner, it is hoped that the Seventh HJWG will prove to be highly productive for all participants.

VI. Conclusions

This article has provided a synopsis of the significant DSN activities since the Sixth Helios Joint Working Group Meeting. It is anticipated that the next article will report upon the findings and conclusions reached during the Seventh HJWG meeting, scheduled for October 25-31, 1972, at the Deutsche Forschungs und Versuchsanstalt für Luft- und Raumfahrt (DFVLR) facility at Porz-Wahn (near Bonn), West Germany.

References

1. Goodwin, P. S., "Helios Mission Support" in *The Deep Space Network Progress Report*, Technical Report 32-1526, Vol. X, pp. 14-19, Jet Propulsion Laboratory, Pasadena, Calif., Aug. 15, 1972.
2. *Project Helios Minutes of the Sixth Helios Joint Working Group Meeting at Jet Propulsion Laboratory, Pasadena, California, April 26-May 3, 1972*, Goddard Space Flight Center, Greenbelt, Md.
3. Goodwin, P. S., "Helios Mission Support," in *The Deep Space Network Progress Report*, Technical Report 32-1526, Vol. II, pp. 18-27, Jet Propulsion Laboratory, Pasadena, Calif., Apr. 15, 1971.

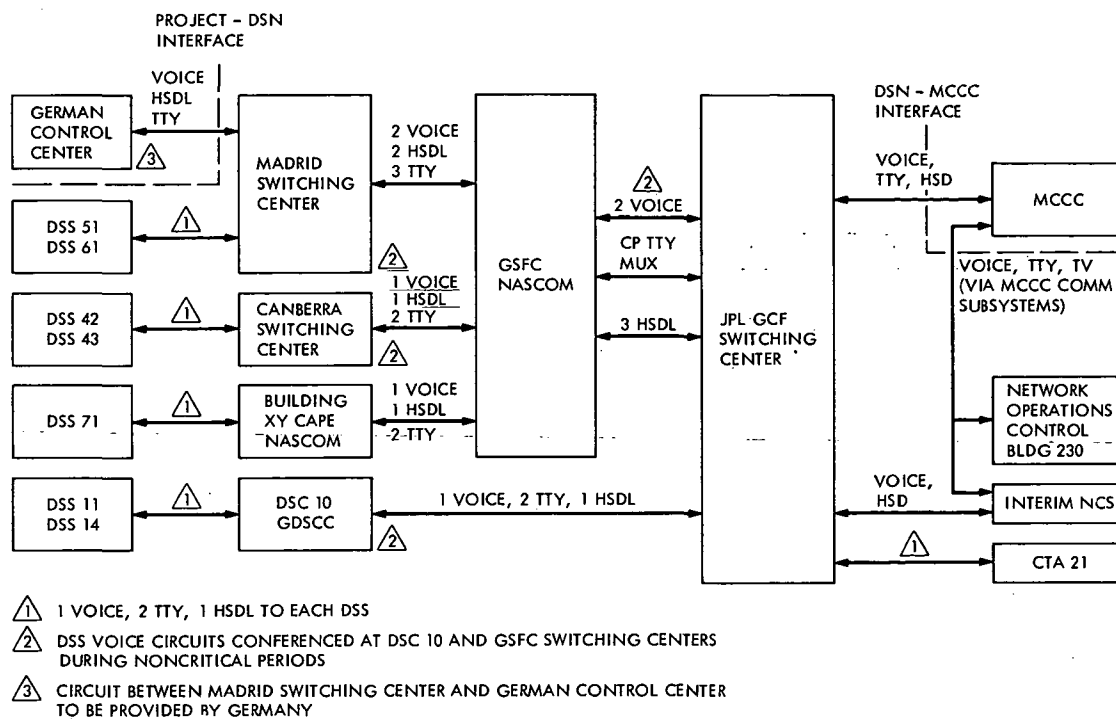


Fig. 1. Network configuration and ground communications plan for Helios

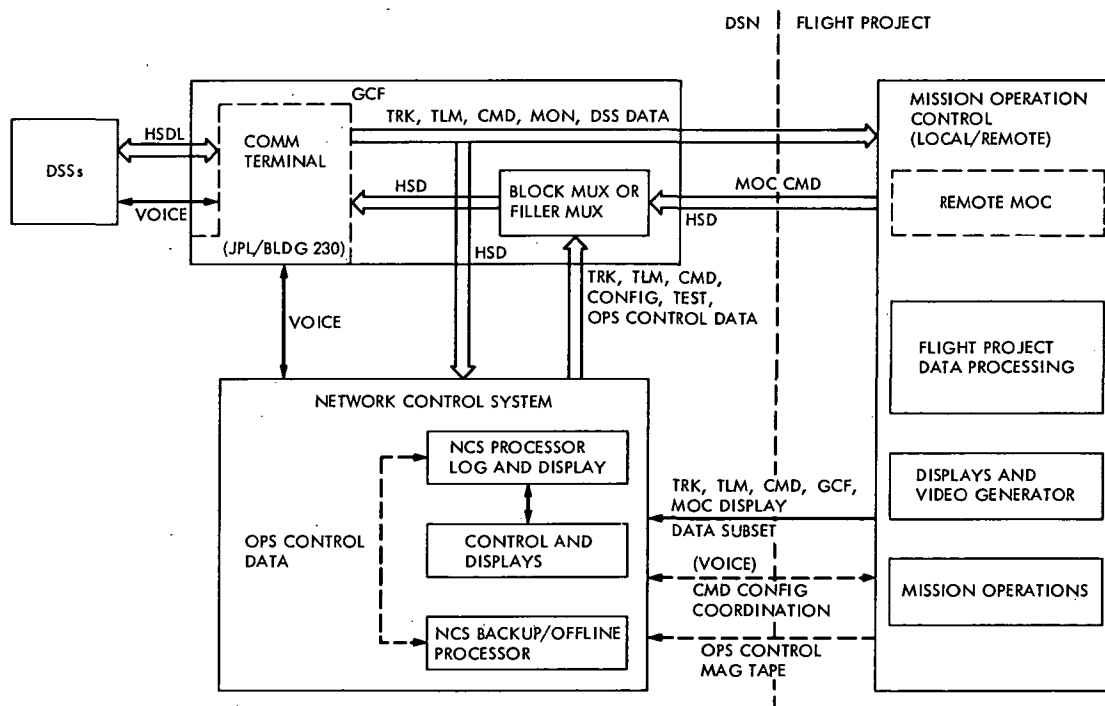


Fig. 2. Interim NCS/Facility/MOC interface

Mariner Venus/Mercury 1973 Mission Support

E. K. Davis
DSN Systems Office

Major planning and design activities and the associated reviews and documentation have been completed for Mariner Venus/Mercury 1973. This article summarizes achievements of the past year as the DSN fully enters the implementation and test phase.

I. Introduction

During the past year, the DSN Support Team for Mariner Venus/Mercury 1973 (MVM 73) has been involved primarily in planning and designing activities, including their review and documentation. These activities were completed in October 1972 as scheduled, and the DSN has fully entered the implementation phase. This article summarizes the key plans, design achievements, implementation/tests, and operations activities of the previous year. Additional information regarding DSN support for MVM 73 is contained in Refs. 1 through 5. Future articles will follow the progress of implementation and tests to DSN operational readiness.

II. Planning Activities

A. NASA Support Plan

The approved Support Instrumentation Requirements Document and the NASA Support Plan preparation guidelines were received from NASA Headquarters in July 1972. These documents provided the basis for final DSN capability and commitment planning. The NASA Support Plan preparation guidelines gave instructions for

supporting real-time 117.6-kbps data from DSS 14 to JPL and for expedited return of high-rate data from DSSs 43 and 63. These instructions provided for closure of the major open areas in DSN planning. Subsequently, the preliminary NASA Support Plan, which was produced in December 1971, was updated, coordinated with implementing organizations, and correlated with DSN budget plans. The NASA Support Plan was approved by JPL in September 1972 and forwarded for NASA Headquarters review and approval.

B. Project Management Plan

To clearly define the working interfaces and responsibilities for planning and control among Project elements, the DSN supported the Project's publication of the Mission Operations System-Tracking and Data System-Mission Control and Computing System Management Plan. Included are agreements regarding organizational interfaces, documentation, schedules, financial responsibilities, reviews, reporting, testing, configuration control, and operations support. These agreements, along with NASA Support Plan commitments, provide the basis for DSN detailed planning.

C. Project Master Test Plan

Extensive testing/training activities are required among the Project Systems [Mission Operations System-Tracking and Data System-Mission Control and Computing Center System-Spacecraft (MOS-TDS-MCCCS-S/C)] to achieve total readiness for mission operations support. To ensure coordinated planning, compatible schedules, and integrated objectives, the named Project Systems produced a preliminary Mariner Venus/Mercury 1973 Mission Operations Master Test Plan in September 1972. Open areas and recommendations from a formal review of the plan in September have been worked out. Approval and publication of the final plan is scheduled for November 1972. A new concept in this plan involves identification and testing of the Ground Data System (GDS), consisting of DSN, MOS, and MCCCS elements, under Space Flight Operations Section direction.

Included is DSN agreement to progress from Deep Space Station level testing to tests involving MCCCS and MOS technical elements to accomplish GDS end-to-end test and integration objectives concurrently with DSN subsystem/system tests. Basically, Deep Space Station (DSS) internal tests are to take place in April and May 1973, DSN tests and GDS integration in May and June 1973, and DSN operational verification tests/training in July 1973. Support for MOS test/training shall begin August 1, 1973, and continue to mid-October 1973.

D. DSN Support Plan

The DSN Support Plan for MVM 73 was published in October 1972. In addition to communicating commitments and agreements in the documents described above, the DSN Support Plan translates detailed requirements contained in the MOS Design Book level 3 specifications and communicates them in terms of DSN facility subsystems to an assembly level. Included are DSN internal requirements and guidelines regarding schedules, control, reviews, reports, test/training, documentation, and operational support. Required configurations specified in this plan are the result of the work of the DSN System Engineering Capability Planning Team and the DSN Support Team for MVM 73.

III. Design Activities

A. Functional Design

A joint MOS-DSN Functional Design Review was held in December 1971. A copy of the DSN material presented is contained in Ref. 4. Organizational changes made prior to the review which established the Office of Computing

and Information Systems (OCIS) resulted in uncertainties regarding interfaces and responsibilities for data processing, data records, and simulation support. Functional elements of each organization presented the design in an end-to-end manner without resolving these issues. These open areas were satisfactorily closed as the detailed design progressed.

The DSN DSS Telemetry and Command Data subsystem software functional design review was held in June 1972. DSN and Project representatives were included on the review board. The Project did not agree with the design for manual command entry/display in octal, since commands issued by the Project in pseudo-octal would require translation. This problem was resolved as discussed in the next section.

B. Detailed Design

A joint MOS-TDS-MCCCS detailed design review was held on July 11-12, 1972. A copy of the DSN material presented will be published in a future TDS Progress Report (No. 6). Included were DSS configurations for telemetry, tracking, command, and simulation which highlighted new hardware/software implementations and associated schedules. Detailed ground communication designs for wideband, high-speed, voice, and teletype circuits and associated implementation schedules were covered for DSN and Project support locations. A detailed design for supporting real-time 117.6-kbps data from DSS 14 to JPL was not presented, since approval was received only a few days prior to the review. However, this major open area was worked on and completed prior to the end of July.

The Telemetry and Command Data (TCD) software detailed design review was held by the Development Project Engineer in October as scheduled. The design included pseudo-octal entry/display of manual commands and accommodation of a critical command list as required, closing this MVM 73 open area. A design feature placing all projects on one TCD system tape caused concern because of the requirements for change and revalidation during flight operations. Continuing discussions are being held on this issue. In general, the TCD software design and development schedule is satisfactory for MVM 73.

C. Interface Design

The Project Systems have identified interfaces between systems which shall be controlled to maintain compatibility. These interfaces and general procedures regarding

their control are listed in Ref. 6. Appendices to this document containing detailed interface descriptions are scheduled to be completed in November 1972. DSN inputs to the appendices are being made based on DSN RF interface parameters contained in Ref. 7, on real-time data format descriptions contained in Ref. 8, and on hardware/electrical descriptions provided through the DSN Support Team for MVM 73.

IV. Implementation and Test Activities

With the completion of detailed design and interface definitions, DSN implementation has been initiated according to schedule. Major implementation activities include: S/X-band at DSS 14; subcarrier demodulator modifications to accommodate interplex modulation; simulation conversion assembly changes to provide interplex modulation, high data rates and tracking data for testing; monitor and control/digital instrumentation modifications to provide tracking data via high-speed lines; TCD software; and wideband ground communications. Implementation progress reports will be included in future issues of this series.

Wideband and high-speed circuits between Boeing-Kent and JPL are now being implemented and were to complete testing in October 1972 for a November 1, 1972, operational date. These circuits provide for communications between the Mission Test Computer (MTC) being used at Boeing for spacecraft system tests and the MTC at JPL, which is being implemented for telemetry processing during mission operations. However, the MTC at JPL will not be ready to receive data until December

1972. Therefore, to save lease costs, readiness of the support circuits has been moved to December 1, 1972.

During Flight 1 spacecraft component testing at the Telecom Development Laboratory (TDL), three 12-h tests were scheduled with CTA 21 to perform command and telemetry compatibility and system performance measurement tests. Because of schedule and hardware problems in the TDL, availability of spacecraft components for CTA 21 testing was reduced to one 12-h period. Command tests were satisfactory, but telemetry tests conducted gave less than satisfactory results. The unavailability of subcarrier demodulator modification kits and tuning procedures for interplex modulation apparently contributed to the results. Appropriate action has been taken to assure the availability of adequate time, procedures, and equipment to accomplish the compatibility testing in December 1972 during Flight 2 spacecraft component tests.

V. Operations Activities

DSS 14 continues to provide operational support to meet Venus/Mercury planetary ranging and radar requirements for ephemeris improvement and Mercury mapping.

VI. Areas Requiring Special Attention

DSN-Spacecraft RF compatibility testing has been flagged as an area of concern for the reasons stated in Section IV. This item was discussed during the Project's Ninth Quarterly Review on October 26, 1972, and specific action items were assigned.

References

1. *TDS Report for MVM'73*, TDS Progress Report No. 1, 615-13, Jet Propulsion Laboratory, Pasadena, Calif., Apr. 1, 1971 (JPL internal document).
2. *TDS Report for MVM'73*, TDS Progress Report No. 2, 615-14, Jet Propulsion Laboratory, Pasadena, Calif., July 1, 1971 (JPL internal document).
3. *TDS Report for MVM'73*, TDS Progress Report No. 3, 615-40, Jet Propulsion Laboratory, Pasadena, Calif., Jan. 15, 1972 (JPL internal document).
4. *TDS Report for MVM'73*, TDS Progress Report No. 4, 615-47, Jet Propulsion Laboratory, Pasadena, Calif., March 1, 1972 (JPL internal document).
5. *TDS Report for MVM'73*, TDS Progress Report No. 5, 615-61, Jet Propulsion Laboratory, Pasadena, Calif., Sept. 1, 1972 (JPL internal document).
6. *MVM'73 Spacecraft-Mission Operations System-Tracking and Data System-Mission Control and Computing System Interface Control Document*, 615-95, Jet Propulsion Laboratory, Pasadena, Calif., Sept. 20, 1972 (JPL internal document).
7. *DSN/Flight Project Interface Design Handbook*, 810-5, Jet Propulsion Laboratory, Pasadena, Calif. (JPL internal document).
8. *DSN System Requirements Detailed Interface Design*, 820-13, Jet Propulsion Laboratory, Pasadena, Calif. (JPL internal document).

Viking Mission Support

D. J. Mudgway
DSN Systems Office

DSN support for Viking continues to move forward into the implementation phase in accordance with new schedules developed to meet a new Viking requirement for advanced DSS readiness dates. Network configurations for the DSN Tracking System, DSN/Viking interfaces, and schedule revisions are discussed, and the continued investigation of the downlink interference effects caused by a dual carrier environment at DSS 13 is described.

I. Introduction

Over the past 2 months DSN support for Viking continued to move forward toward developing a definitive plan for implementation and operations. This activity was somewhat diverted by internal changes in the Tracking and Data Acquisition (TDA) Office organization, which required new definitions in working relationships between the DSN Managers, DSN Operations, DSN Systems Engineering, and the implementing divisions.

The outcome of this activity is depicted in Fig. 1, which shows the three clearly defined phases of DSN activity leading to commitment of DSN facilities to Project support. Existing schedules, interfaces, and documentation have had to be revised in the light of these new agreements.

II. Configuration

The DSN Tracking System configuration for Viking is shown in Fig. 2. Subsequent issues of this Technical Re-

port will describe the remaining systems; namely, Command, Test, and Training.

It should be noted that, to meet the navigation requirements of the second spacecraft prior to its Mars orbit insertion, it is necessary to provide planetary ranging capability at one 26-m-diameter antenna station (DSS 12). This requirement is necessitated by the fact that the entire 64-m subnetwork is entirely occupied in meeting the needs of the first Viking Orbiter/Lander, which will, by that time, be involved in Mars landed operations.

III. Interfaces

The RF interfaces between the DSN and Viking Orbiter and Viking Lander have been fully defined, and the documents are awaiting final review and signoff. The document describing the interface between the DSN and the Viking Mission Control and Computing Center remains in the development stage.

IV. Schedules

As mentioned above, a substantial revision of the Level 3 and Level 5 DSN schedules for Viking has been necessary following Viking demands for advanced readiness dates for all DSSs to May 1, 1975. Previous schedules were based on launch and cruise readiness only, with full readiness for planetary operations to follow several months after launch.

The necessary schedule revisions have been accomplished and are now being compared with the relevant budget line items to ensure that implementation plans are consistent with Viking needs.

The Management Information Control System (MICS) and computer-based Work Authorization Document

Schedule (WADSKED) are being used as tools in this process, which will lead to the development of a DSN Preparation Plan for Viking.

V. Problem Areas

The downlink interference problems caused by operation of dual carriers from a single antenna continue to be investigated at DSS 13. This developmental station has been completely reconfigured to provide a "test bed" which can be used for a detailed experimental study of these intermodulation product (IMP) effects. At this time, the reconfiguration is complete and is being checked out by verifying some of the earlier results obtained at DSS 14. Work is to continue toward a major review in late December 1972.

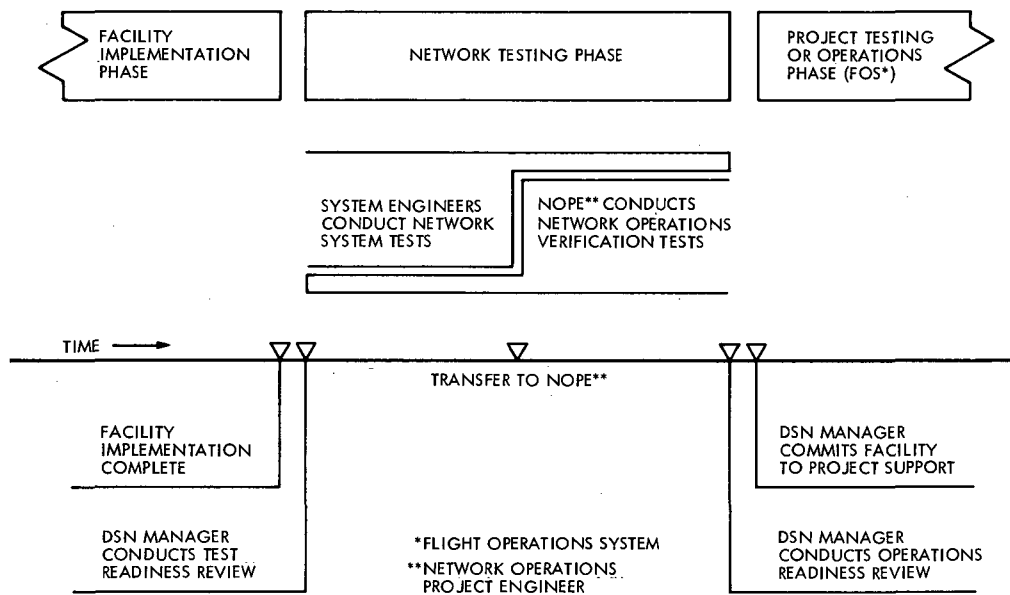
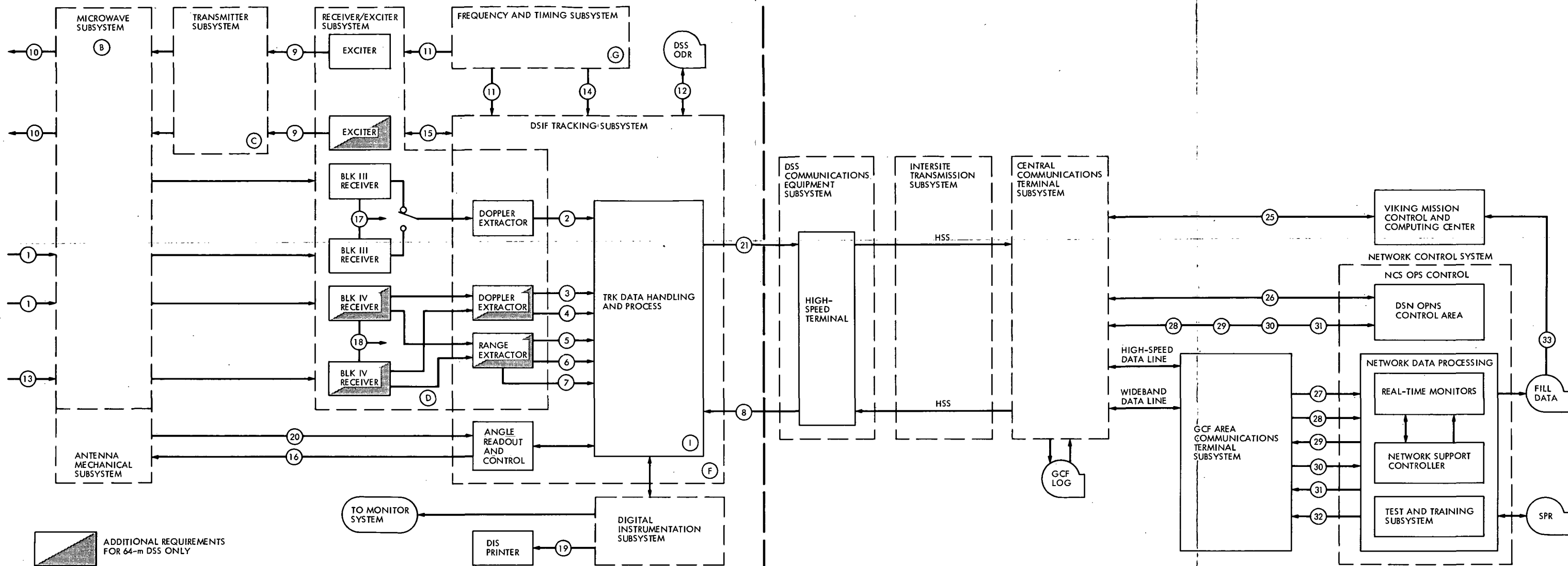


Fig. 1. Three phases of DSN activity



DATA FLOW PATHS

- ① TWO-WAY S-BAND DOWNLINKS FROM UP TO TWO ORBITERS OR ONE ORBITER AND ONE LANDER. TWO CARRIERS PER 64-m DSS; ONE CARRIER PER 26-m DSS
- ② S-BAND DOPPLER DATA FROM EITHER ONE OF TWO BLOCK III RECEIVERS
- ③ S-BAND DOPPLER DATA FROM ONE BLOCK IV RECEIVER
- ④ X-BAND DOPPLER DATA FROM THE OTHER BLOCK IV RECEIVER
- ⑤ S-BAND RANGING DATA FROM ONE BLOCK IV RECEIVER
- ⑥ X-BAND RANGING DATA FROM ONE BLOCK IV RECEIVER
- ⑦ S-BAND AND X-BAND DRVID DATA FROM ONE ORBITER OR ONE LANDER
- ⑧ HIGH-SPEED PREDICTS, ACQUISITION MESSAGES, STANDARDS AND LIMITS, AND ODR RECALL REQUESTS
- ⑨ TRANSMITTER DRIVE, MODULATED WITH RANGING SIGNALS WHEN REQUIRED. RANGE MODULATION OF ONLY ONE CARRIER AT A TIME
- ⑩ S-BAND UPLINKS TO TWO ORBITERS OR ONE ORBITER AND ONE LANDER. TWO CARRIERS PER 64-m DSS; ONE CARRIER PER 26-m DSS
- ⑪ REFERENCE FREQUENCY

- ⑫ DIGITAL ODR OF ALL SUBSYSTEM DATA OUTPUTS (DOPPLER, RANGE, ANGLES, FREQUENCY REFERENCES, STATION PARAMETERS, AND CALIBRATION DATA)
- ⑬ ONE-WAY COHERENT X-BAND DOWNLINK FROM EITHER ONE OF TWO ORBITERS
- ⑭ TIME
- ⑮ FREQUENCY REFERENCES AND SEQUENTIAL RANGING MODULATION
- ⑯ ANTENNA DRIVE SIGNALS
- ⑰ S-BAND AGC FROM EITHER OR BOTH BLOCK III RECEIVERS
- ⑱ S-BAND OR X-BAND AGC FROM EITHER OR BOTH BLOCK IV RECEIVERS
- ⑲ PAGE PRINT OF DSS PREDICTS FROM NCS OPERATIONS CONTROL
- ⑳ ANTENNA POINTING ANGLES
- ㉑ TRACKING DATA FROM DSIF TRACKING AND MONITOR AND CONTROL SUBSYSTEM (DTS) TO VMCCC VIA HSS
- ㉒ DSS PARTIAL STATUS AND DETECTED ALARMS TO DSN MONITOR SYSTEM

- ㉓ DSN TRACKING SYSTEM ALARMS TO DSN MONITOR SYSTEM
- ㉔ NOT USED
- ㉕ REAL-TIME TRACKING DATA AND GFC RECALL TO VMCCC VIA HSS FOR DATA PROCESSING
- ㉖ TRACKING REQUESTS TO AND DISPLAYS FROM NCS DATA PROCESSING FUNCTION
- ㉗ REAL-TIME DIGITAL TRACKING DATA FROM DSS TO RTM'S; REQUESTS FROM AND DISPLAYS TO DSN OPERATIONS AREA
- ㉘ REQUESTS FROM DSN OPERATIONS FOR TRACKING STANDARDS AND LIMITS
- ㉙ DISPLAYS OF TRACKING STANDARDS AND LIMITS DATA TO DSS/DSN OPERATIONS
- ㉚ REQUESTS FROM DSN OPERATIONS FOR RECALL OF TRACKING DATA
- ㉛ DISPLAYS TO DSN OPERATIONS/DSS OF RECALL TRACKING DATA/ NETWORK DATA PROCESSING
- ㉜ DSN SIMULATION DATA FOR TRACKING
- ㉝ FILE TRACKING DATA TO PROJECT ON TAPE

Fig. 2. DSN/VK75 Tracking System baseline functional requirements

Page Intentionally Left Blank

X-Band Radar Development

C. P. Wiggins

RF Systems Development Section

A high-power X-band radar is under development for use on the 64-m-diameter antenna at DSS 14. The 400-kW transmitter will operate at 8.495 GHz. Ground testing of portions of the transmitter will start early in 1973.

I. Introduction

A high-power X-band radar is under development for use on the 64-m-diameter antenna at DSS 14. This radar will provide the deep space communication and tracking technology necessary to support requirements for wider bandwidth at increased ranges. The increased antenna gain of 6.5 dB will decrease the observation time by a factor of 20, and the wider bandwidth will permit faster range codes for improved ranging.

II. Radar System

The X-band radar will be equipped with both a receiver and a transmitter (see Fig. 1). Initially, it will operate as a monostatic system, alternately transmitting and receiving the microwave signal for one round-trip time of flight.

The radar transmitter, receiver, microwave, and feed will be assembled into a new Cassegrain cone to be mounted in the upper or R&D position of the tricone at DSS 14. Excessive transmission losses will be avoided

by operating the transmitter in close proximity to the feed.

III. Radar Transmitter

The transmitter (see Fig. 2) will have the following characteristics:

Power output—400 kW CW.

Center frequency—8.495 GHz, fixed tuned.

Instantaneous bandwidth—50 MHz at -1 dB.

Two 250-kW klystron amplifiers of an existing design will be used, and a four-port hybrid will combine the two outputs into one waveguide. Remote phase monitoring and control will permit combining at maximum efficiency. The RF loads will allow operation of either or both power amplifiers without radiation from the antenna.

IV. High-Voltage Power

The transmitter will use the existing high-voltage power supply at DSS 14, which now provides power

for either the 400-kW DSN or the 450-kW R&D transmitters. The installed 400-Hz generating capacity at DSS 14 will produce only 1 MW of dc high voltage. The X-band klystrons are approximately 40% efficient; hence only 400 kW total RF power can be developed, although each klystron is capable of 250 kW at full voltage.

V. Cooling System

The DSS 14 cooling system will be modified to supply the new transmitter. The piping will be extended to module 3 of the tricone, and additional valves will be installed.

VI. Plans and Progress

The klystrons will be delivered early in 1973. Design of the transmitter is in process, and some of the components are being procured, including couplers, RF loads, waveguide parts, and coolant parts. A sufficient portion of the transmitter will be fabricated to allow ground testing the klystrons at DSS 13.

Techniques for controlling and monitoring the phasing of the two power amplifiers will be studied at low power using commercial waveguide components. Because of power handling and higher-order mode considerations, the high-power microwave components will use the special WR-125 waveguide size. (See article by H. R. Buchanan in this volume.)

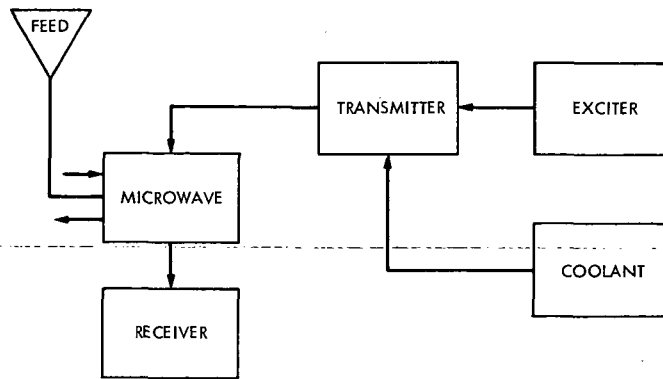


Fig. 1. X-band radar block diagram

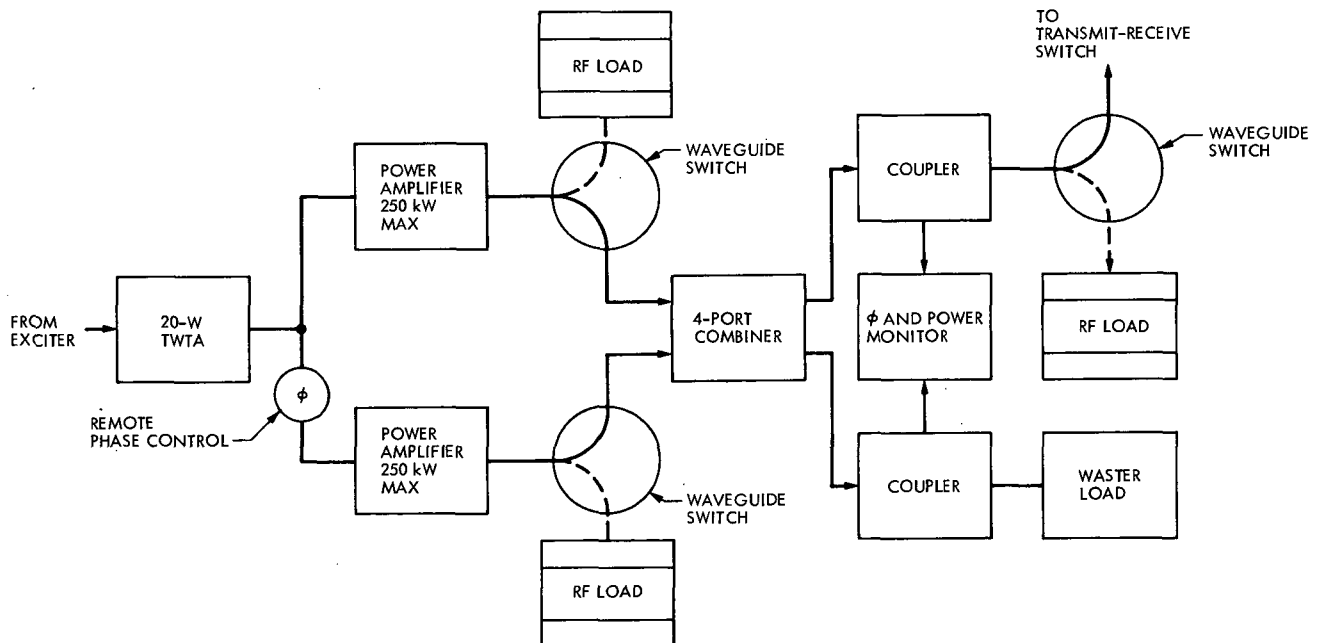


Fig. 2. 400-kW X-band radar transmitter

X-Band Uplink Microwave Components

H. R. Buchanan
RF Systems Development Section

Waveguide components for use in the 400-kW X-band radar system will be electrically stressed to a considerably greater extent than previously experienced in DSIF equipment. The electrical characteristics of several possible waveguide sizes have been investigated. A size has been selected which offers an adequate safety margin for the X-band radar and other possible X-band uplink applications.

I. Introduction

The design goal established for the uplink portion of the X-band radar equipment includes transmitting a nominal 400-kW signal at 8.495 GHz. Economic considerations have resulted in a design which utilizes two 250-kW klystron amplifiers whose outputs are combined into a single port. The X-band uplink program includes the development of microwave components such as a power combiner, waveguide switches, and a variety of waveguide transmission line assemblies which must operate satisfactorily at 400-kW levels.

II. Design Considerations

The theoretical power-handling capability of a waveguide system operating under ideal conditions is a function of the waveguide geometry and the operating frequency. The waveguide selected should have as large a cross-section as practical. However, it is of paramount importance to select a waveguide size which will support

only the fundamental mode throughout the anticipated range of operating frequencies. Figure 1 indicates the ratio of operating frequency to the fundamental cutoff frequency as a function of frequency for a number of commercial standard waveguide sizes. The frequency range of interest indicated in Fig. 1 covers the anticipated requirements for the DSIF (7.1 to 8.5 GHz).

The choice of WR-137 is unacceptable because of its proximity to the TE_{02} -mode region at the 8.495-GHz radar frequency. The WR-112 and WR-90 sizes are acceptable from mode considerations but have significantly reduced power-handling capability. A new waveguide size, shown in Fig. 1, designated as WR-125 approximates the power-handling and attenuation performance of WR-137 but is not subject to the higher-mode problems. The internal dimensions of the WR-125 waveguide are chosen to have an exact 2:1 ratio. This characteristic will permit a much simpler scaling of the waveguide hybrid developed for the 400-kW S-band diplexer for use in the X-band radar power combiner.

The choice of waveguide geometry and frequency determines the theoretical power-handling capability. However, several derating factors must be taken into account in an actual, field operating environment. Some significant factors are listed in Table 1 with maximum values anticipated in the X-band radar design. It is noted that the net derating factor is 0.28. A comparison of the power capability of the various waveguide sizes is given in Table 2. The theoretical power calculations are based on a maximum electric field of 30,000 V/cm under ideal conditions.

The selected waveguide size should also afford a low value of attenuation. This characteristic is of importance with high-power operation in maximizing the radiated power and minimizing the heat load on the waveguide cooling system. Low attenuation is also desirable throughout the receiving waveguide system in order to minimize the receiver effective system noise temperature. The attenuation of the various waveguide sizes is presented as a function of frequency in Fig. 2.

III. Conclusions

The data presented in the above tables and figures indicate that the WR-125 waveguide size is acceptable for use with the X-band radar system, and for other possible DSIF X-band applications. The next higher-mode cutoff frequency is well above the X-band radar frequency. The power capability is 50% higher and the attenuation is 27% lower than that for WR-112. The planned 400-kW level represents 16% of the theoretical maximum of the WR-125 waveguide.

A review of DSIF high-power experience indicates that the X-band clock synchronization transmitter has produced the largest electrical stress on a DSIF waveguide system to date. This transmitter operates at 7.15 GHz, with up to 150 kW into both WR-112 and WR-137 waveguide assemblies. In the WR-112 components, this operating power is 10% of the theoretical maximum. The safety margin for the X-band radar appears to be adequate using the WR-125 waveguide.

Table 1. Power derating factors

Parameter	Value	Derating factor
Electric field factor	Power combiner assumed to be worst component	0.70
Altitude	900 m above sea level	0.80
Maximum VSWR	1.10	0.90
Internal waveguide temperature	55°C	0.80
Dust particles, metal chips, moisture	—	0.70
Overall derating		0.28

Table 2. Waveguide power capability

Waveguide	Theoretical maximum power, MW		Derated maximum power, ^a MW	
	7.1 GHz	8.5 GHz	7.1 GHz	8.5 GHz
WR-90	0.53	0.88	0.15	0.25
WR-112	1.44	1.69	0.40	0.47
WR-125	2.25	2.50	0.63	0.70
WR-137	2.61	2.83	0.73	0.79
^a Derating 0.28.				

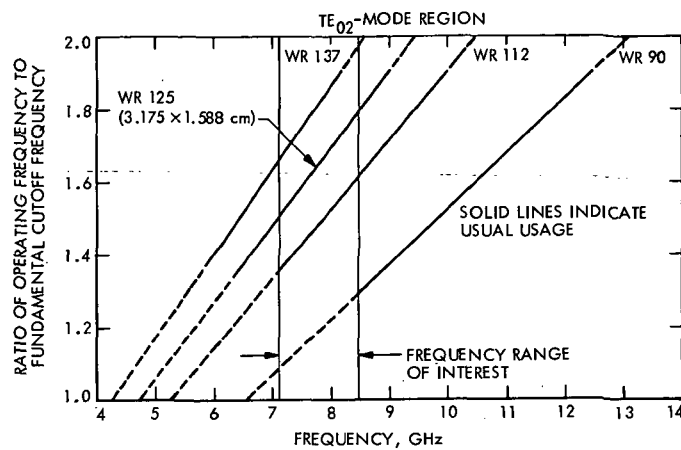


Fig. 1. Waveguide mode considerations

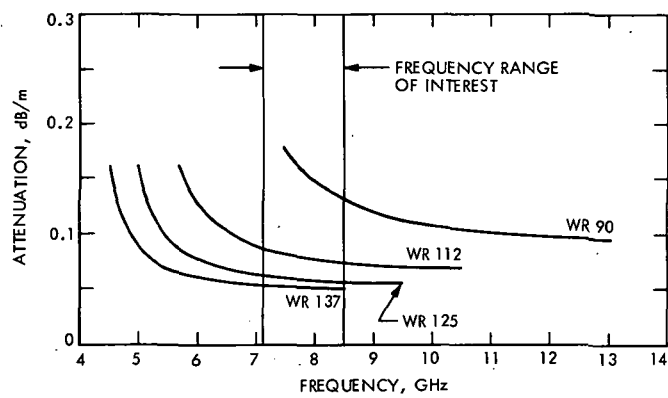


Fig. 2. Attenuation versus frequency

RF Properties of the 64-m-Diameter Antenna Mesh Material as a Function of Frequency

T. Y. Otoshi

Communications Elements Research Section

This article presents some accurate theoretical data on the RF properties of the perforated panels presently used as reflector surface material on the 64-m-diameter antenna. The properties are given for the frequency range of 1.0 to 30 GHz.

I. Introduction

In a recent report by this author (Ref. 1) approximate formulas were presented for calculating voltage reflection and transmission coefficients of a metallic plate perforated periodically with round holes. It was shown that the formulas were valid when the hole diameter and hole spacings were small compared to wavelength.

On the outer 47% radius of the 64-m-diameter antenna at DSS 14, perforated aluminum panels having 51% porosity and 4.763-mm ($\frac{3}{16}$ -in.) diameter holes are used as the reflective surface material. Experimental data (Refs. 2, 3) on this perforated plate material showed that the approximate formulas were accurate at S-band (2.295 GHz) and X-band (8.448 GHz) frequencies.

At K-band frequencies, the hole diameter becomes comparable in size to wavelength, and therefore the approximate formulas become inaccurate. One must therefore use more accurate formulas such as those derived by C. C. Chen (Refs. 4, 5). Chen formulated the boundary value problem for the perforated plate in terms of Floquet and orthonormal mode functions and then numerically solved the problem by use of the method of moments and a digital computer (Ref. 4). Because Chen

solves the perforated plate problem by rigorous analytical methods, his analyses apply to a large class of perforated plate problems and are not restricted to operating frequencies far below the cutoff frequency of the circular apertures.

This article presents numerical results of Chen's equations as applied to the perforated plate reflector surface material used on the 64-m-diameter antenna. The RF properties of the perforated plate are plotted for the frequency range of 1.0 to 30 GHz. Comparisons are made to the approximate formulas, which are given in the following section for convenient reference purposes.

II. Approximate Formulas

For a circular hole array having the geometry of Fig. 1 and an incident plane wave with the E-field polarized normal to the plane of incidence, the approximate expression for transmission loss is

$$(T_{dB})_1 = 10 \log_{10} \left[1 + \left(\frac{3ab\lambda_0}{2\pi d^3 \cos \theta_i} \right)^2 \right] + \frac{32t}{d} \sqrt{1 - \left(\frac{1.706d}{\lambda_0} \right)^2} \quad (1)$$

where $a, b, d \ll \lambda_0$. The parameters a and b are the spacings between holes as shown in Fig. 1, d is the hole diameter, λ_0 is the free space wavelength, t is the plate thickness; and θ_i is the incidence angle.

When the incident wave is a plane wave with the E-field polarized parallel to the plane of incidence, the approximate expression is

$$(T_{dB})_{//} = 10 \log_{10} \left[1 + \left(\frac{3ab\lambda_0 \cos \theta_i}{2\pi d^3} \right)^2 \right] + \frac{32t}{d} \sqrt{1 - \left(\frac{1.706d}{\lambda_0} \right)^2} \quad (2)$$

where $a, b, d \ll \lambda_0$. It should be pointed out that the square root factor in (1) and (2) has a significant effect when λ_0 becomes comparable to d , but this factor can be omitted when $\lambda_0 \gg d$.

Other RF properties of reflector surfaces that are of interest are reflectivity loss and reflection coefficient phase angles. Assuming that the resistive losses of the plate are negligible, then these properties are given approximately by

$$(R_{dB})_{\perp} \simeq -10 \log_{10} [1 - 10^{-(T_{dB})_{\perp}/10}] \quad (3)$$

$$(R_{dB})_{//} \simeq -10 \log_{10} [1 - 10^{-(T_{dB})_{//}/10}] \quad (4)$$

$$(\psi_r)_{\perp} \simeq 180 - \tan^{-1} \left[\frac{2\pi d^3 \cos \theta_i}{3ab\lambda_0} \right] \quad (5)$$

$$(\psi_r)_{//} \simeq 180 - \tan^{-1} \left[\frac{2\pi d^3}{3ab\lambda_0 \cos \theta_i} \right] \quad (6)$$

where $(\psi_r)_{\perp}$ and $(\psi_r)_{//}$ are expressed in degrees.

The approximate formulas for perpendicular and parallel polarizations become inaccurate for incidence angles greater than 60 deg and about 40 deg, respectively. It is assumed that since $a, b, d \ll \lambda_0$, the RF properties are es-

entially independent of the incidence plane orientation angle ϕ shown in Fig. 1.

III. Numerical Results and Conclusions

As defined by the geometry in Fig. 1, the physical properties of the perforated panels on the NASA/JPL 64-m-diameter antenna are: $d = 4.763$ mm (0.1875 in.), $a = 6.350$ mm (0.250 in.), $\alpha = 60$ deg, and $t = 2.286$ mm (0.090 in.). Since the perforated panels are located on the outer 47% radius of the antenna, the incidence angle θ_i will vary only between 17.4 and 30.6 deg (Ref. 6).

Figures 2-6 show frequency characteristics of theoretical transmission losses and reflection coefficient phase angles for a plane wave incident at $\theta_i = 0, 15$, and 30 deg and for perpendicular and parallel polarizations. The frequency plot for normal ($\theta_i = 0$ deg) incidence is included for informational purposes. At a given incidence angle, the RF properties have been plotted from 1.0 GHz to a K-band frequency at which the properties no longer appear to be isotropic (i.e., independent of the incidence plane orientation angle ϕ).

Theoretical data for the frequency plots are based on Chen's formulas (Refs. 4, 5) and on the approximate formulas by this author given by Eqs. (1), (2), (5), and (6). It can be seen that the approximate formulas are useful and accurate up to about 25 GHz ($d/\lambda_0 \simeq 0.4$) but deviate significantly from Chen's data as the frequency approaches 36.9 GHz (the TE_{11} mode cutoff frequency of the circular holes). Chen's transmission loss data, which were numerically obtained by use of the Univac 1108 computer, are believed to be accurate to about ± 0.5 dB in the region far below cutoff and ± 0.1 dB or less in the region close to cutoff.

Acknowledgement

The author wishes to acknowledge the cooperation and assistance of Dr. C. C. Chen of Hughes Aircraft Company, Fullerton, Calif., Dr. C. Yeh, JPL Consultant, and P. D. Potter of the JPL Communications Elements Research Section.

References

1. Otoshi, T.Y., "Precision Reflectivity Loss Measurements of Perforated Plate Mesh Materials by a Waveguide Method," *IEEE Trans. on Instrumentation and Measurements* (Special Issue), Nov. 1972 (to be published).
2. Otoshi, T. Y., "A Study of Microwave Leakage through Perforated Flat Plates," *IEEE Trans. on Microwave Theory Tech.*, Vol. MTT-20, pp. 235-236, March 1972.
3. Otoshi, T. Y., and Woo, K., "Further Studies of Microwave Transmission through Perforated Flat Plates," in *The Deep Space Network Progress Report for September and October 1971*, Technical Report 32-1526, Vol. VI, pp. 125-129, Jet Propulsion Laboratory, Pasadena, Calif., Dec. 15, 1971.
4. Chen, C. C., "Diffraction of Electromagnetic Waves by Conducting Screen Perforated Periodically with Circular Holes," *IEEE Trans. on Microwave Theory Tech.*, Vol. MTT-19, No. 5, pp. 475-481, May 1971.
5. Chen, C. C., "Transmission of Microwave through Perforated Flat Plates of Finite Thickness," FR 72-14-530, Hughes Aircraft Co., Fullerton, Calif., May 3, 1972.
6. Otoshi, T. Y., "Antenna Noise Temperature Contributions Due to Ohmic and Leakage Losses of the DSS-14 64-m Antenna Reflector Surface," in *The Deep Space Network Progress Report for July and August 1971*, Technical Report 32-1526, Vol. V, pp. 115-119, Jet Propulsion Laboratory, Pasadena, Calif., Oct. 15, 1971.

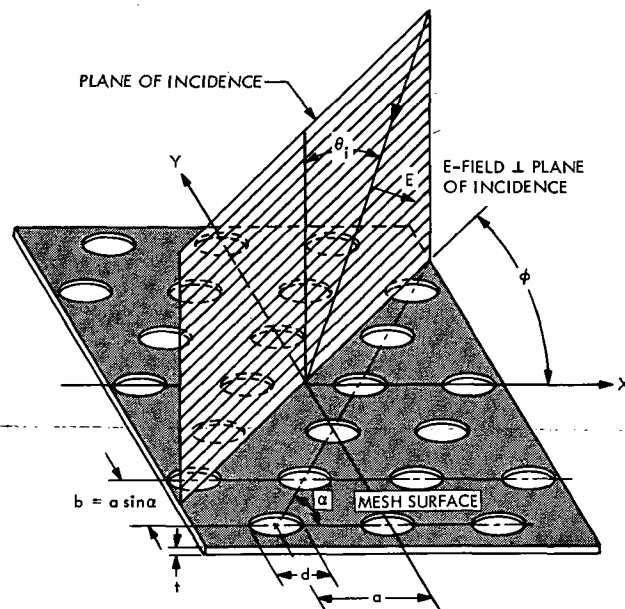


Fig. 1. Perforated plate geometry with an obliquely incident plane wave polarized with the E-field perpendicular to the plane of incidence

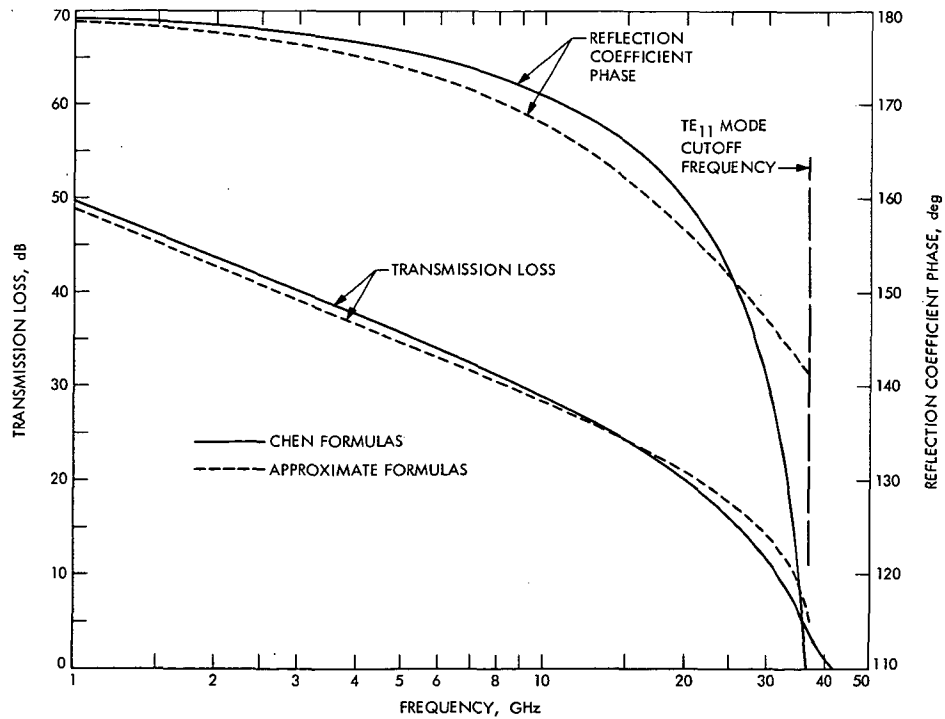


Fig. 2. 64-m-diameter antenna perforated plate transmission loss and reflection coefficient phase angle for either perpendicular or parallel polarization and 0-deg incidence angle

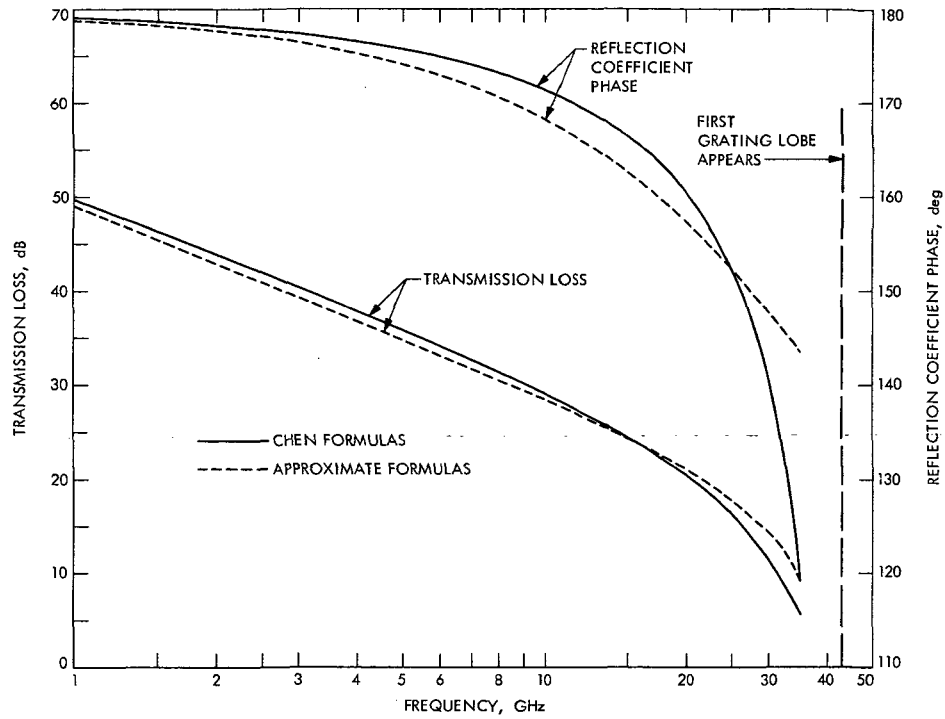


Fig. 3. 64-m-diameter antenna perforated plate transmission loss and reflection coefficient phase angle for perpendicular polarization and 15-deg incidence angle

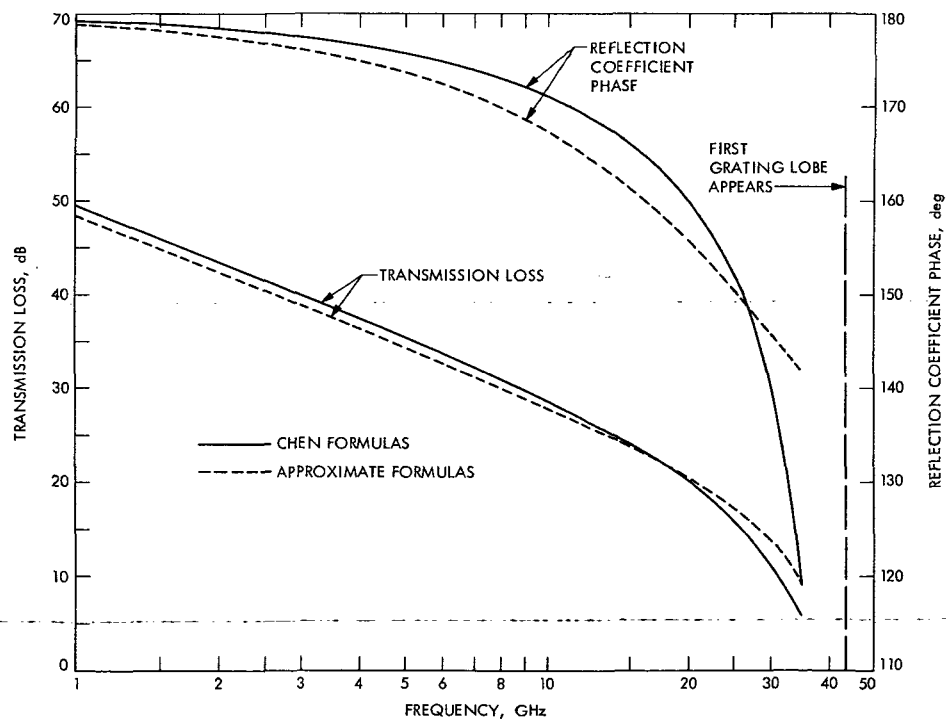


Fig. 4. 64-m-diameter antenna perforated plate transmission loss and reflection coefficient phase angle for parallel polarization and 15-deg incidence angle

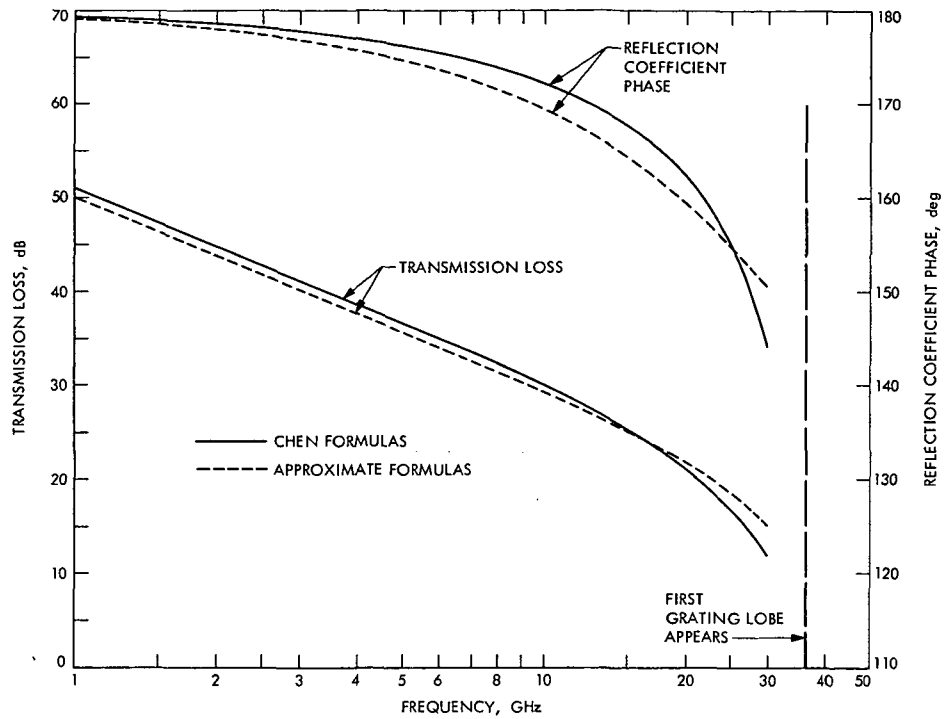


Fig. 5. 64-m-diameter antenna perforated plate transmission loss and reflection coefficient phase angle for perpendicular polarization and 30-deg incidence angle

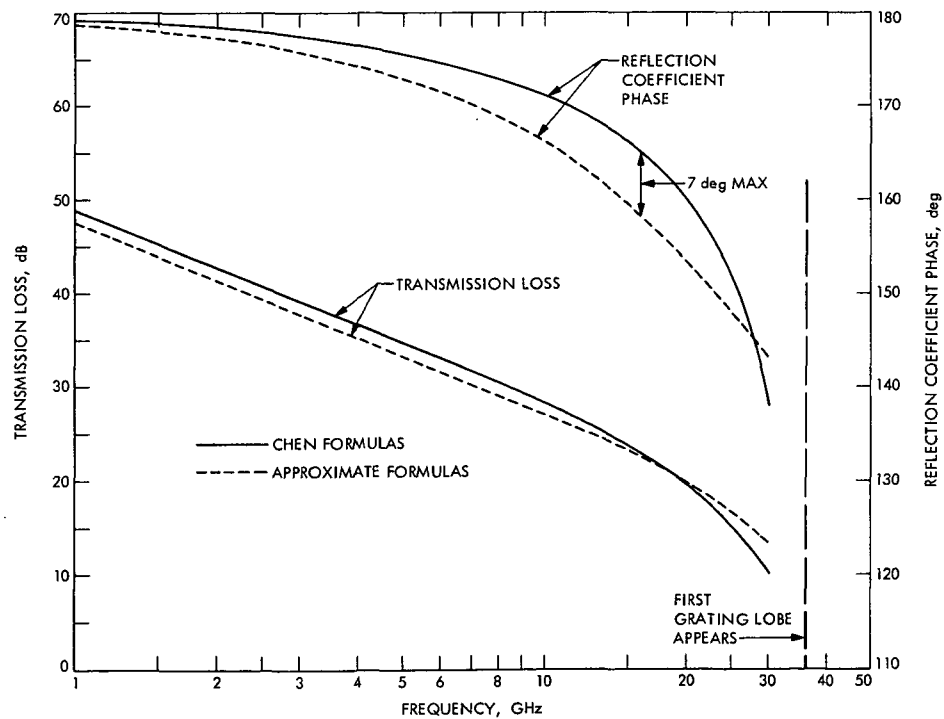


Fig. 6. 64-m-diameter antenna perforated plate transmission loss and reflection coefficient phase angle for parallel polarization and 30-deg incidence angle

An Analysis of System Performance Under the Severe Weather Conditions at Goldstone, December 1971

M. S. Reid

Communications Elements Research Section

Adverse weather conditions, unusual for the area in their severity, were experienced at Goldstone in December 1971. This article presents a summary of the analysis of the system performance under these conditions, and subsequent conclusions. The results of a brief study of cloud cover characteristics in the southwestern United States to a distance of several hundred miles from Goldstone, California, are also presented.

I. Introduction

Adverse weather conditions which were unusual for the area in their severity were experienced at Goldstone in December 1971. S-, X-, and K-band system sensitivity was degraded to a greater extent than has ever been recorded before at Goldstone. Some S-band tracking time was lost during this period. This article presents a summary of the analysis of the system performance and subsequent conclusions.

II. System Performance Analysis

Figure 1 shows S-, X-, and K-band system temperatures as a function of time for the period of December 27 through 30, 1971. Spacecraft tracking times are shown as well as S-band ground received signal loss computed from recorded automatic gain control (AGC) voltages. Weather conditions, antenna snow cover, and outside ambient air temperatures are also presented for this period. Snow started falling at approximately 1800 GMT, December 27, and again at approximately 2100 GMT,

December 28. The two snowfalls stopped at about 0400 GMT, December 28, and 0900 GMT, December 29, respectively. Intermittent light rain preceded the first snowfall on December 27. Ambient air temperatures at DSS 14 dropped from December 25 to 29, when a low of -8°C was recorded and the temperature was less than -5°C for $4\frac{1}{2}$ h.

The signal loss section of the figure shows that the received signal loss reached a peak of -5.5 and -7 dB in two of the three tracking periods covered.

In the lowest section of the figure, excess system temperatures are plotted for S-, X-, and K-bands. Excess system temperature is defined as that portion of the measured system temperature which is in excess of the system temperature to be expected in clear, dry weather at the given antenna elevation angle. S-band data are shown dotted, X-band solid, and K-band dashed. Data gaps, due to equipment malfunction or other problems, are shown by breaks in the lines. The S- and X-band data were reduced from analog records. The K-band

data were recorded in digital form. This recording system was limited in dynamic range, although it was more reliable than the analog system and capable of providing greater resolution. The limited dynamic range of the recording system is clearly shown in the figure when the system is saturated. S-band and X-band data were derived from total power radiometers. Gain stability and additional reliability were achieved at K-band by the use of a noise-adding radiometer (Ref. 1).

III. Conclusions

- As a result of the experience gained by operation of the station during these severe environmental conditions, it was concluded that the primary effect of dry snow is not the snowfall itself in the atmosphere but rather the accumulation of snow on the antenna surface. This can reduce antenna efficiency and increase the operating noise temperature. The effect of severe environmental conditions, however, can be minimized by proper procedures modified by mission requirements. In the case of the December 1971 snowfall, the snow was wet and the ambient temperature below zero for many hours, with the result that the wet snow froze on the antenna surface. This made the removal of the snow and ice very difficult. Of the several methods used, the only successful one was tracking the sun when the weather cleared, which melted off the accumulated snow and ice.

The accumulation of snow or ice on the antenna surface must be avoided in as large a measure as possible by judicious stowing and dumping decisions. Real-time discussion between the project or experimenter and the station manager is necessary so that such decisions can be made effectively. Station procedures for operating under severe environmental conditions have been modified in the light of this experience. Furthermore, it is recommended that an investigation be made to consider

the possibility of developing a reliable method to maintain the horn covers free of moisture and ice in all weather conditions. This is particularly important for the X- and K-band horns.

IV. Cloud Cover Characteristics Study

A brief study was commissioned from a contractor of cloud cover characteristics in the southwestern United States (Ref. 2). The purpose of the study was to obtain preliminary information, to a distance of several hundred miles from Goldstone, on the frequency of possible microwave attenuation and system degradation at various locations in the Southwest. Simultaneous observations of cloud cover were examined in pairs for six locations in California and Arizona. One member of each pair was a Goldstone reference in each case. The reference station was Edwards Air Force Base, which is one of the closest meteorological stations to Goldstone. The simultaneous occurrence of nearly-clear sky conditions at one of the locations was considered to be of primary interest. Data used in the study consisted of cloud cover observations taken four times per day at each location over an extended period of time.

The results of this preliminary study indicated that the probability of experiencing nearly-clear skies at one and/or the other of the paired stations increases when the second station is beyond George Air Force Base. On the other hand, an increase from approximately 100 miles to 200 miles from Goldstone does not significantly increase the probability. Furthermore, the characteristic storm tracks, which generally lie to the north of Goldstone, should also be taken into consideration. It may be concluded from the study that areas to the east and southeast represent the most favorable direction for improvement in overall cloud conditions.

References

1. Batelaan, P. D., Goldstein, R. M., Stelzried, C. T., "A Noise Adding Radiometer for use in the DSN," *The Deep Space Network*, Space Programs Summary 37-65, Vol. II, p. 66, Jet Propulsion Laboratory, Pasadena, Calif., 1970.
2. Smith, T. B., *Study of Cloud Cover Relationships*, Internal Document, Contract 953564, prepared for the Jet Propulsion Laboratory by Meteorology Research, Inc., Altadena, Calif., October 1972.

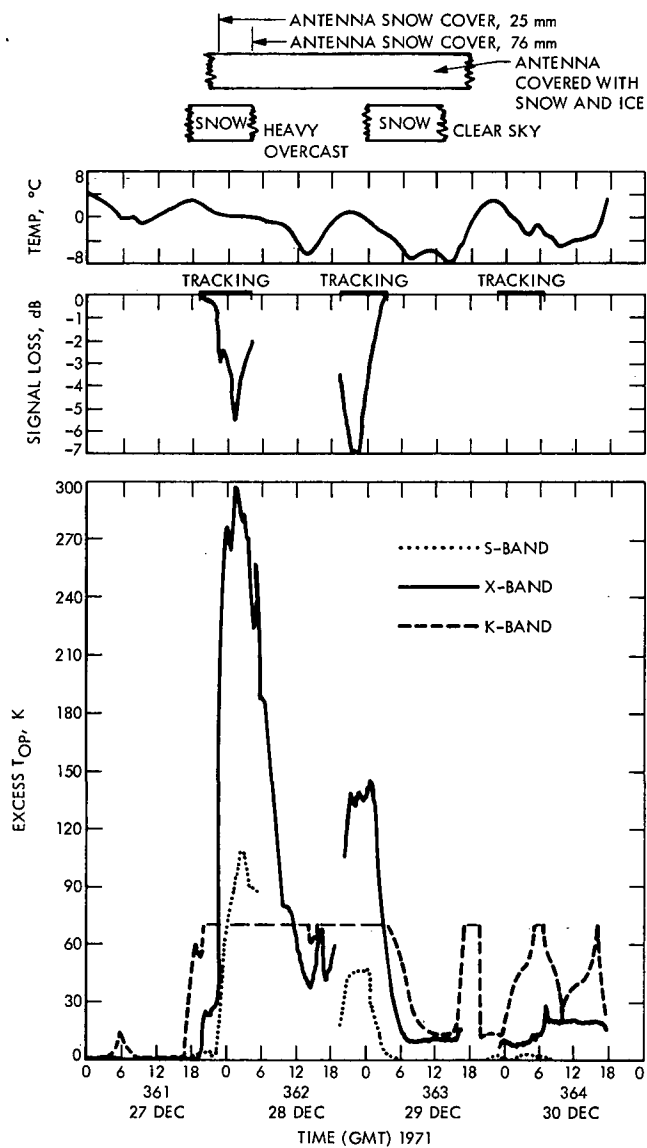


**Fig. 1. Microwave and meteorological data,
 December 27-30, 1971**

Very Long Baseline Interferometry (VLBI) Possibilities for Lunar Study

M. A. Slade, P. F. MacDoran, and J. B. Thomas
Tracking and Orbit Determination Section

The availability of several channels of transmissions from the lunar surface and lunar orbiting vehicles presents opportunities for demonstrating the utility of radio interferometric tracking. The expected accuracy of such very long baseline interferometry (VLBI) tracking is expected to be equivalent to 50 cm (transverse to the line of sight) at the moon's distance, affording significant opportunities for studies of lunar dynamics and selenodesy. In addition to direct applicability to lunar study, VLBI tracking of these several lunar-based signals provides an opportunity to evaluate simultaneous multiprobe tracking techniques which could significantly enhance the Viking 1975 and Pioneer Venus 1977 missions, where multiprobe tracking is imperative.

I. Introduction

As part of the development of new methods of spacecraft tracking and navigation for the Deep Space Network, the utility of very long baseline interferometry has been explored using S-band transmissions from the Apollo lunar surface experiment packages (ALSEP) and from the Mariner 9 orbiter. The experimental results from Mariner 9 will be outlined in a future article. This article

describes results obtained using the ALSEPs as the radio source and the very interesting opportunities in selenodesy and lunar dynamics afforded by this technique.

II. Applications

Briefly, these opportunities include the application of VLBI for measurement of the following:

- (1) Differential angular separation of the lunar-fixed ALSEP S-band radio signals equivalent to 50 cm or better, transverse to the line of sight, for selenodetic control.
- (2) Relative angular displacement of a lunar orbiting vehicle (e.g., Apollo 17 Command and Service Module equivalent to 50-cm displacement and 0.05 mm/s velocity with respect to the lunar-fixed ALSEPs.
- (3) Angular relationship of the moon relative to the inertial frame of extragalactic radio sources to an accuracy of 0.1 to 0.01 arc second.
- (4) Lunar physical librations equivalent to 0.1 arc second (selenocentric).

These experimental opportunities should be exploited as soon as possible because of the finite lifetime of the ALSEP S-band radio transmission.

III. Procedure

The fundamental observational procedure for these measurements is the use of explicit differencing of observations from different sources so as to allow cancellation of mutual error sources. The differencing mode of observations takes on several forms:

- (1) Interferometry differences between the various available ALSEPs themselves; (e.g., ALSEP 12, 14, 15, 16, and 17) in order to establish angular selenodetic control and the measurement of lunar libration.
- (2) Difference between the radio transmissions from the lunar orbiting phase of the Apollo 17 Command and Service Module (CSM) relative to the lunar fixed ALSEPs (12, 14, 15, 16, and 17) in order to constrain the CSM position for the metric photographic experiments.
- (3) The interferometer difference between the ALSEP signals and a nearby extragalactic radio source, so as to measure the center of mass motion of the moon relative to an inertial frame of angular reference.

Figure 1 illustrates the overall VLBI technique. The technique is inherently passive, requiring only that two independently operated stations receive the same time series of electrical signals. These radio signals may be from either a natural source (e.g., a quasar), or a man-made source, such as an ALSEP or a spacecraft. Since this technique operates by receiving S-band (13-cm) radio

signals, it is an all-weather method. The theoretical foundations of this technique are given in Refs. 1 and 2.

An interferometer composed of 26-m-diameter tracking antennas is well suited to simultaneous reception of all the ALSEPs since a 26-m-diameter antenna has a 3-dB beam width of 0.33 deg and the ALSEPs are very strong in the radio source sense (approximately 50,000 flux units, compared with 5 flux units for a strong quasar).

Several DSN baselines would be useful for lunar observations—specifically, Goldstone/Madrid, Goldstone/Australia, Australia/South Africa, and South Africa/Madrid. All these baselines will offer considerable flexibility for measurements of the moon, since the moon has a wide excursion in declination during the month; e.g., with the moon at positive declination, the Goldstone/Madrid, Madrid/Johannesburg, and Goldstone/Australia baselines will be most advantageous. However, with the moon at negative declination, the Madrid/South Africa, Goldstone/Australia, and Australia/South Africa baselines will be most advantageous. This occurs because the moon must obviously be mutually visible to the two stations composing the interferometer; thus, at negative declinations greater than 20 deg, there is no arc of mutual visibility on a Goldstone/Madrid baseline.

IV. Experience to Date

Actual interferometric reception of ALSEP signals has been acquired using the Goldstone 64-m-diameter and Madrid 26-m-diameter stations in September 1971. A JPL hydrogen maser frequency system was used in California, and a Smithsonian Astrophysical Observatory hydrogen maser was used in Spain for deriving the radio system local oscillator signals. A sample of the results obtained with the Goldstone/Madrid baseline is shown in Fig. 2. This figure is the result of differencing the observed, minus the computed (including a constant linear phase rate) interferometer phase.

Since the ALSEPs move very rapidly with respect to the fixed extragalactic radio sources typically used in VLBI, it was necessary to adapt existing lunar ephemeris programs to accomplish cross correlation signal detection. As seen in Fig. 2, a phase noise of 0.02 cycles RMS has been achieved over a 10-min time span. The difference between the 0.008 cycle individual point (12 s of integration) precision and the 0.02 cycle 10-min precision is probably due to systematic errors introduced by a combination of frequency system instability and the differential transmission media variations. These data were acquired by

using frequency synthesizers to generate the first local oscillator signals, and thus their instabilities were multiplied by a factor of 96. As shown in the Radio System Configuration Section, any further experiments would use fixed frequency multipliers, limiting this error source to less than 10^{-3} cycles.¹

V. Estimated Performance

Observing several ALSEPs simultaneously could afford a significant canceling of frequency system and transmission media variations over a time scale of several seconds and longer. In addition, platform parameter errors of station location uncertainties and the effects of polar motion and universal time are self-canceling. Thus, the relevant interferometer phase statistic is approximately 0.008 cycles. For the Goldstone/Madrid baseline (8,500 km), at these S-band wavelengths (13 cm), each cycle corresponds to an angular change of 0.003 arc second. Therefore, 0.008 cycles phase measurement precision affords a 24 micro-arc-second angular precision equivalent to 5 cm transverse displacement at the moon's distance.

However, systematic error sources prevent exploitation of this 5-cm angular equivalent measurement precision. Because all the ALSEPs' signals do not traverse precisely the same atmospheric paths to the receiving stations, the differencing does not entirely remove the atmospheric effects. The expected uncertainties remaining after calibration for the troposphere and the ionosphere combine to be equivalent to 50 cm of displacement at the moon's distance. Such calibrations are felt to be valid for elevation angles greater than 10 deg. There appears some hope for atmospheric parameter estimations from the data

¹Figure 3 illustrates the switching mode which would be used in the proposed experiments. The switching time would be reduced to 6 s instead of 240 s, allowing the phase to be accurately connected.

themselves, thereby allowing for some improvement in the differential angular measurement accuracy.

To summarize, the instrument measuring *precision* gives 5 cm, or better, but systematic Earth atmospheric effects degrade these measurements, so that only 50-cm accuracy will be realized initially.

VI. Radio System Configuration

Figure 4 illustrates a possible receiving station configuration for VLBI ALSEP experiments using the DSN. The dotted boxes denote experiment-particular modules. These modules are of relatively simple nature, being made up of mostly commercially available components. The 24-kHz bandwidth digital recording model shown is one which has been used extensively in VLBI Earth physics and DSN development experiments. The results shown in Fig. 2 were derived with this 24-kHz data-taking mode and a modified version of the data reduction software.

VII. Summary

The possibilities for lunar studies made available by the existence of the ALSEP S-band transmissions are essentially unique and should be undertaken as soon as possible because of the finite lifetime of the ALSEP signals themselves. This opportunity to develop multiprobe tracking techniques should also be of considerable interest to the Viking 1975 and Pioneer Venus 1977 missions. In the Viking mission, there will be two orbiters and two Mars landers to be tracked. During the Pioneer Venus mission, five vehicles will enter the Venusian atmosphere, requiring simultaneous tracking to determine relative probe positions. Such tracking may also provide the major measurement of the transverse winds.

References

1. Thomas, J. B., "An Analysis of Long Baseline Radio Interferometry," in *The Deep Space Network Progress Report*, Vol. VII, pp. 37-50, Jet Propulsion Laboratory, Pasadena, Calif., Feb. 15, 1972.
2. Thomas, J. B., "An Analysis of Long Baseline Radio Interferometry, Part II," in *The Deep Space Network Progress Report*, Vol. VIII, pp. 29-38, Jet Propulsion Laboratory, Pasadena, Calif., Apr. 15, 1972.

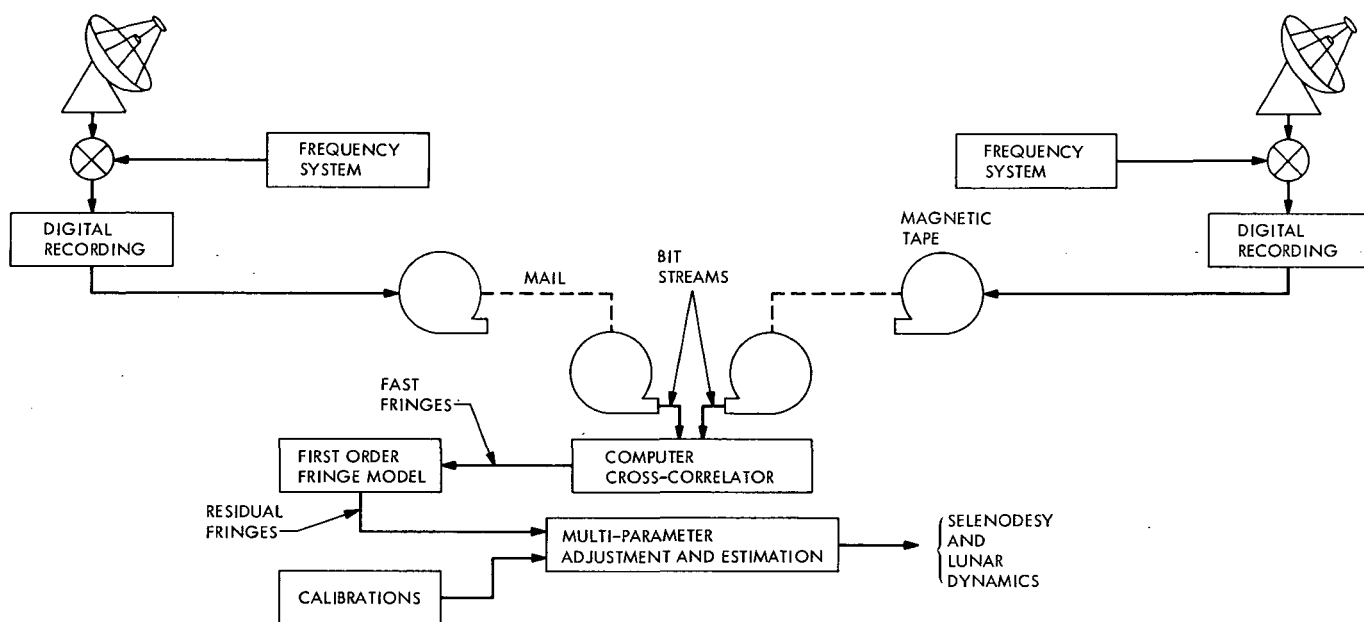


Fig. 1. The VLBI technique

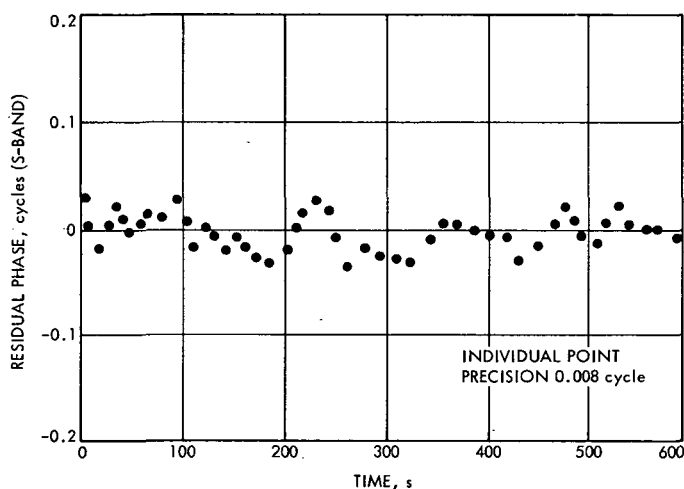


Fig. 2. Goldstone/Madrid VLBI observation of Apollo 15 ALSEP (Sept. 7, 1971)

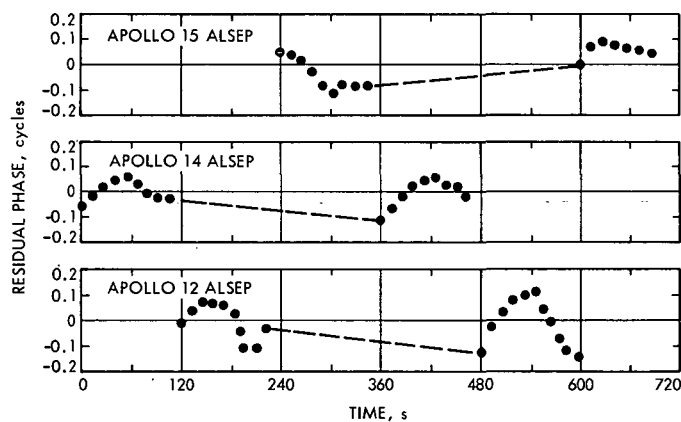


Fig. 3. An example of the switching-type mode to be used in proposed experiments (Goldstone/Madrid VLBI observations made on Sept. 7, 1971)

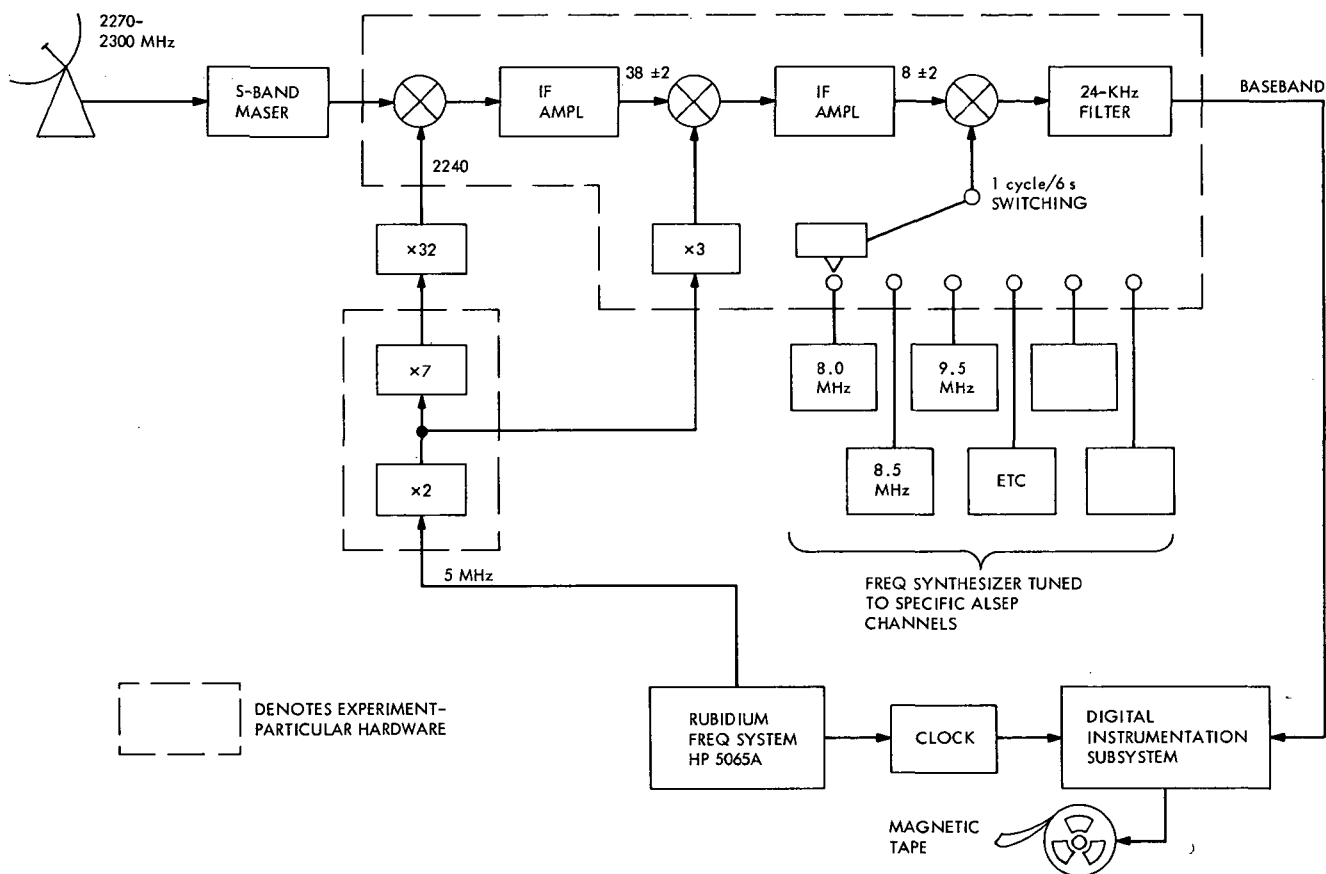


Fig. 4. Deep Space Station configuration for multichannel ALSEP radio science

Determination of the Helios Spacecraft Attitude by Polarization Measurement

B. D. Mulhall

Tracking and Orbit Determination Section

The possibility of determining the attitude or orientation of the Helios spacecraft by means of polarization measurements of the spacecraft radio signal is described. One principal error source is the Faraday rotation of the S-band radio signal by Earth's ionosphere. If this effect can be removed by independent measurements of the ionosphere, then the orientation of the spacecraft in two dimensions perpendicular to the spacecraft line-of-sight can be determined to better than 0.5 deg.

The Helios spacecraft is required to point certain instruments in the direction of the sun. A problem arises in that the spacecraft orientation in space cannot be determined if a Canopus sensor is not incorporated in the spacecraft system. An alternative to determining the orientation in two dimensions perpendicular to the line-of-sight of the spacecraft would be to measure the polarization angle of the linearly polarized S-band signal transmitted by the spacecraft. One major problem in this approach is the effect of Earth's ionosphere. As the signal passes through the ionosphere, the polarization angle is rotated by the Faraday effect. This rotation amounts to several degrees, depending on the density of electrons in the ionosphere and the elevation angle of the spacecraft.

To remove this error source, a possible solution is to make independent measurements of Earth's ionosphere (e.g., from ATS-1, a geostationary satellite, by Faraday rotation at VHF). These measurements can then be mapped to the line-of-sight of the Helios spacecraft by techniques described in Ref. 1.

Figures 1 and 2 present two typical comparisons. The upper graph shows the Pioneer data (designated ●) in terms of total electron content (TEC) and the mapped satellite data (designated □). The lower graph shows the difference between the Pioneer and the satellite (Pioneer data minus satellite data). From these two figures, one can see that, for higher elevation angles near meridian transit, the comparisons are quite good. However, at rise or at set, the two curves tend to diverge widely. This is most likely due to the breakdown of the assumption of a reference point at a constant altitude to facilitate computation of Earth's magnetic field vector along the ray-path. On some days, the Pioneer data were so noisy that no calculation was attempted. In the case of Pioneer 9, some of the noise could have been due to solar coronal effects. Disturbances in Earth's ionosphere could also introduce noise in either the Pioneer 6 or 9 data.

Figure 3 shows the difference in polarization angle between the Pioneer and the rotation predicted by mapping the satellite data to the Pioneer line-of-sight. The Pioneer

polarization angle measurement occasionally dropped below 90 deg, which may be due to equipment problems or, more likely, misorientation of the Pioneer spin axis. It cannot have been caused by Earth's ionosphere (though the solar corona can produce such an effect). Note that Pioneer 9 has a slight positive bias, while Pioneer 6 has a smaller negative bias. These biases could be due to misalignment of the two spacecraft rotation axes to the ecliptic plane. Since the measurements were taken at about the same time, and are both east and west of the tracking station, it is not likely that the biases are the result of errors in mapping.

The numbers used to produce Fig. 3 are tabulated in Table 1. The percentage error in the predicted polarization angle is generally less than 20%. If we agree to attribute the constant or the bias error to spacecraft orientation, then the error would be 0.3 deg or smaller (1 sigma).

The Pioneer orientation can vary slowly over one spacecraft revolution about the sun by about 1 to 1.5 deg.¹ The spacecraft should always return to its initial orientation at the end of the revolution. Consequently, over a

¹Private communication from A. J. Siegmeth, JPL.

period of a month, a small bias in orientation may be expected.

In conclusion, the orientation of a spacecraft can be determined to a few tenths of a degree by making S-band polarization measurements if the spacecraft maintained its attitude for weeks at a time, and if the polarization measurements can be accumulated and averaged over several days. This is assuming that the spacecraft is not near solar occultation, at which time the solar corona effects would overwhelm any attempt at using this technique.

Individual passes might be adequate. However, the possibility of ionospheric storms would indicate that data for several days should be accumulated so that the technique could be applied under quiet ionospheric conditions.

Acknowledgment

G. Levy of the Communications Elements Research Section suggested this application. The author also wishes to acknowledge the assistance of Dr. A. R. Cannon of Stanford University and Dr. H. T. Howard of the Center for Radar Astronomy, Stanford University.

Reference

1. Mulhall, B. D., *User's Guide to Ionospheric Comparison Program*, JPL Internal Document TM 391-380, Jet Propulsion Laboratory, Pasadena, Calif., Oct. 25, 1972.

Table 1. Pioneer line-of-sight data

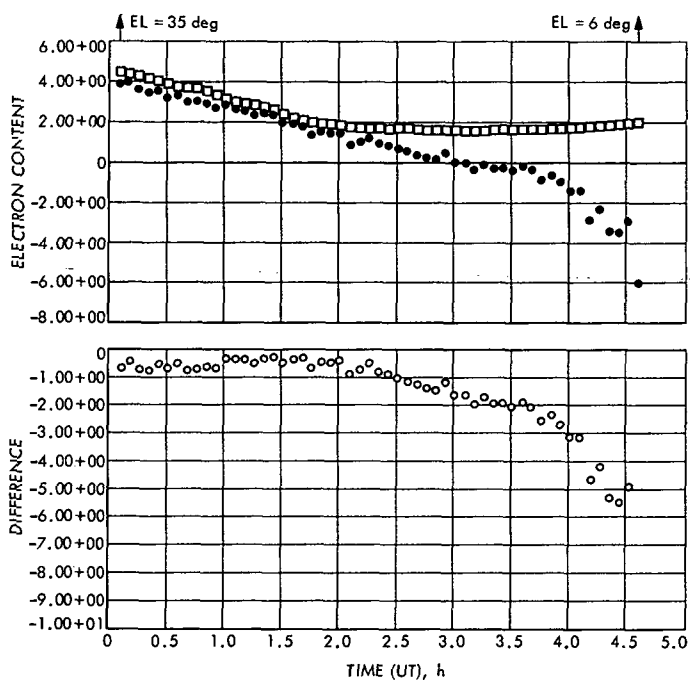
Date M D Y	UT, h	TEC ^a , 10 ¹⁷ m ⁻²	Error, 10 ¹⁷ m ⁻²	Polarization ^b , deg	Error, deg	Error, %	Pioneer elevation ^c , deg	Pioneer azimuth ^c , deg
Pioneer 6								
11 04 70	1.8	6.2	-0.28	3.3	-0.15	4.5	25.8	210
05	1.7	5.1	-0.58	2.5	-0.28	11.4	26.5	209
08	Not usable							
09	Not usable							
10	1.6	2.9	-0.65	0.8	-0.18	22.4	28.4	206
11	1.4	3.4	-1.4	1.2	-0.50	41.2	29.7	203
12	Not usable—large trends in differences							
14	1.4	3.8	-0.49	1.6	-0.21	12.9	30.2	203
16	Not usable							
18	Not usable—large trends in differences							
21	1.4	2.4	-0.26	0.4	-0.04	10.8	32.4	202
Average polarization error = -0.23 deg, standard deviation = 0.16 deg								
Pioneer 6								
12 10 70	1.5	2.2	-0.22	0.1	-0.01	12.3	38.8	202
11	Not usable							
12	1.8	1.2	-0.02	-0.07 ^d	-0.001	16.3	38.2	207
14	Not usable							
24	1.0	0.9	-0.40	-0.21 ^d	-0.094	44.5	46.2	194
Average polarization error = -0.035 deg, standard deviation = 0.052 deg								
Pioneer 9								
10 04 70	Not usable							
06	Not usable							
07	Not usable							
10	Not usable							
11	Not usable							
13	21.8	7.97	0.796	4.5	0.45	10.0	31.4	242
14	22.2	9.63	1.00	5.3	0.55	10.4	27.7	245
15	Not usable							
17	16.7	8.43	1.47	5.6	0.98	17.4	43.0	140
18	16.4	5.28	0.3	2.6	0.15	5.7	39.5	134
20	16.0	4.74	0.57	2.0	0.24	12.0	35.4	129
21	19.8	5.83	0.27	3.9	0.18	4.6	46.3	205
Average polarization error = 0.425 deg, standard deviation = 0.314 deg								

^aTotal electron content, 10¹⁷ electrons/m².

^bModulus 90 deg with respect to the ecliptic.

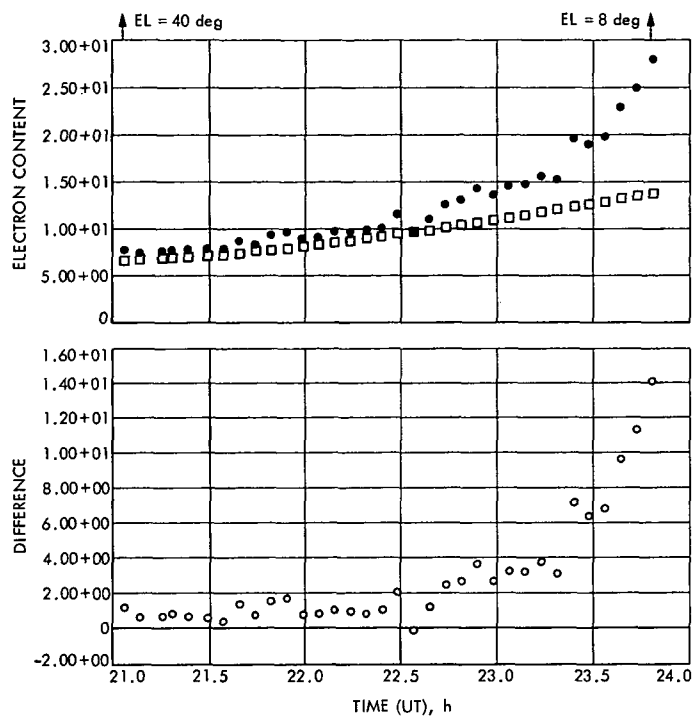
^cATS-1 viewed from Stanford University is at E1 = 37.2 deg, Az = 222.2 deg.

^dNegative polarization angles cannot be due to the ionosphere for the geometry of this experiment.



DATE 11/21/70 AVERAGE -2.569 STD. DEV. 1.598

Fig. 1. Pioneer 6 signal polarization



DATE 10/14/70 AVERAGE 1.897 STD. DEV. 3.362

Fig. 2. Pioneer 9 signal polarization

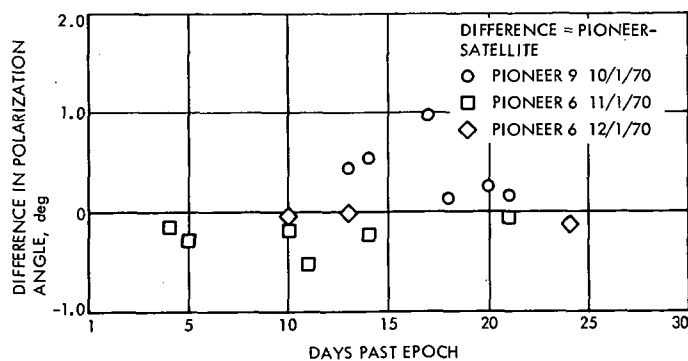


Fig. 3. Pioneer polarization angle differences

Phase-Stable, Low-Phase-Noise Filters for Reference Signals

G. F. Lutes

Communications Systems Research Section

Reference signals may be filtered by use of the phase-locking filter described which locks the phase of the output signal to the phase of the input signal. A very small phase drift may be achieved over a large temperature range without the use of temperature-controlled ovens, which are bulky and costly.

Filters were needed to clean up the outputs of the frequency dividers used in the hydrogen maser frequency standard. It was required that the filters have a low rate of phase drift with temperature as well as a small absolute phase shift.

Three methods of meeting the requirements were considered. The filter could have been stabilized by the use of temperature-compensating components, temperature-controlled ovens, or a scheme to phase-lock the output to the input.

Temperature compensation was impractical because of the stringent requirements; however, either of the two alternative methods would give satisfactory results. Although the best stability can be obtained with temperature-regulated ovens, they are undesirable because they are bulky and costly, and require a great deal of power.

Adequate stability was achieved in less space, with lower power consumption, and at less cost by use of the phase-locked filter described (Fig. 1). The input network of the filter is a lumped-circuit equivalent of a quadrature hybrid having two output signals of equal amplitude with a 90-deg phase difference and greater than 35 dB isolation between them. One signal goes through a voltage-tunable LC filter which is used as a voltage-controlled phase shifter having a range of $\sim \pm 60$ deg. The signal is then amplified, further filtered, and split into two equal, isolated, in-phase outputs, one of which goes to the distribution amplifier. The other output goes to a phase detector, where it is compared to the remaining output from the quadrature hybrid input network. The output of the phase detector is amplified with a low-noise, integrated circuit, operational amplifier and applied to the voltage-controlled phase shifter, which in turn cancels any phase variations between the input and output of the phase-locked filter.

A tuned amplifier was used in the loop, which gave the required filtering, better efficiency, and the required source impedance for best isolation in the power splitter. Phase drift due to the tank circuit changing with temperature was cancelled by the feedback loop.

The phase change caused by a 0 to 50°C change in temperature was measured to be ~ 0.5 deg, of which the major contribution was the drift in the phase detector.

The single-sideband phase noise of the complete filter is 140 dB below the carrier in a 1-Hz bandwidth 10 Hz from the carrier. This measurement was made using the method explained in Ref. 1.

Filters were breadboarded at 5, 10, and 20 MHz, with nearly identical phase drift and phase noise for the conditions described.

Reference

1. Meyer, R., and Sward, A., "Frequency Generation and Control: The Measurement of Phase Jitter," in *The Deep Space Network*, Space Programs Summary 37-64, Vol. II, pp. 55-58. Jet Propulsion Laboratory, Pasadena, Calif., Aug. 31, 1970.

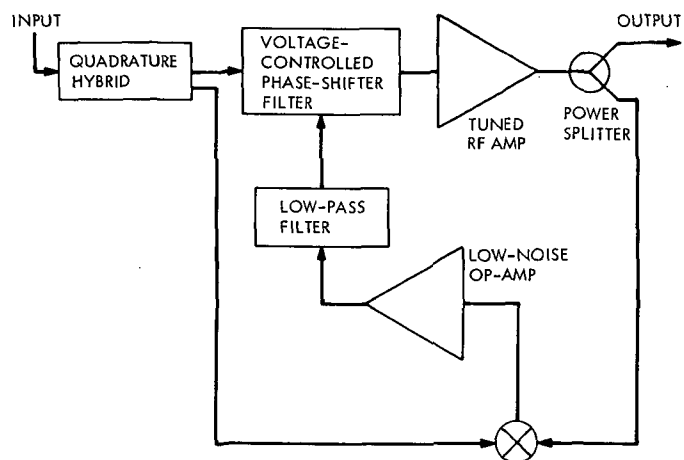


Fig. 1. Block diagram of typical filter

Complex Mixer Error Analysis

R. Winkelstein

Communications Systems Research Section

The complex mixer is composed of two channels. One channel contains the signal mixed with the sine of the reference frequency and the other contains the signal mixed with the cosine. Errors unique to this system are gain and phase shifts of one channel with respect to the other. When the power spectrum of the output of the mixer, considered as a complex quantity, is calculated, these errors produce an unwanted image response to each signal component in the true spectrum. This analysis was carried out to ensure that hardware specifications were sufficient to limit these image responses to tolerable levels. Calculations for various gain and phase errors show that image responses in the power spectrum for prototype hardware will be limited to less than 1% of the true signal components.

I. Introduction

The complex mixer is a receiver module which converts the intermediate-frequency (IF) signal from the receiver down to baseband frequency in two parallel channels. One channel mixes the IF signal with the sine of the reference frequency and the other mixes the IF signal with the cosine. The output of the first channel is considered to be the real component of the complex baseband signal and the output of the second channel the imaginary component. A computer samples the outputs of both channels and calculates the power spectrum of the baseband signal.

Differences in the gain and phase characteristics of physical hardware for each channel introduce certain errors in the calculated power spectrum. These errors take the form of image or ghost responses mirrored about the zero-frequency axis from the true signal components of the spectrum. In addition, the amplitudes of the true

signal components are also slightly in error. Since the power spectrum is usually normalized, consistent errors in amplitude are of little importance. However, the complex mixer system specifically distinguishes signals whose frequencies are below the mixing frequency from those above. Therefore, the introduction of image responses in the power spectrum is of major concern. The following analysis determines the relative magnitude of the ghost image as a function of the gain and phase errors in the complex mixer channels. It will be shown that specifications limiting the gain and phase errors in constructed complex mixer hardware are sufficient to limit the ghost image to less than 1% of the true signal component.

II. Spectral Calculations for an Ideal System

Prior to the error analysis, calculations of the power spectrum for an ideal system will be reviewed to serve as a basis for comparison. Such a system is shown in the simplified block diagram of Fig. 1. The unit power input

signal to both channels is displaced from the IF frequency ω_0 by an amount f and contains an arbitrary phase ϕ . In the upper channel, the input signal is multiplied by the sine of the IF frequency, and in the lower channel, it is multiplied by the cosine. Each channel has a low-pass filter, which blocks the sum terms while passing the difference terms of the multiplication operation. These filters are also used to attenuate signals whose frequencies are outside the sampling bandwidth and which otherwise might be aliased into the calculated spectrum.

Considering the output of the upper channel to be the real part of $f(t)$, $Rf(t)$, and the output of the lower channel to be the imaginary part of $f(t)$, $If(t)$, then

$$Rf(t) = -\frac{\sqrt{2}}{2} \sin(2\pi ft + \phi) \quad (1)$$

$$If(t) = \frac{\sqrt{2}}{2} \cos(2\pi ft + \phi) \quad (2)$$

where t is elapsed time. Combining Eqs. (1) and (2) gives

$$f(t) = \frac{\sqrt{2}}{2} \exp \left[i \left(2\pi ft + \phi + \frac{\pi}{2} \right) \right] \quad (3)$$

The analog-to-digital converters in both channels simultaneously sample the real and imaginary parts of $f(t)$ at a sampling period of Δ_t s to provide the sampled signal f_k :

$$f_k = f(k\Delta_t) \quad (4)$$

where k is the number of the particular sample of $f(t)$. The computer calculates the power spectrum P_n as

$$P_n = \frac{2}{N^2} |F_n|^2 = \frac{2}{N^2} F_n F_n^* \quad (5)$$

$$F_n = \sum_{k=0}^{N-1} f_k \exp \left(\frac{-i2\pi nK}{N} \right) \quad (6)$$

where n is the number of a particular spectrum point, N is the number of complex points in f_k used to compute the spectrum, and F_n^* is the complex conjugate of F_n .

From Eqs. (3), (4), (5), and (6), P_n is found to be

$$P_n = \frac{1}{N^2} \frac{\sin^2(N\pi f\Delta_t)}{\sin^2 \left[\pi \left(f\Delta_t - \frac{n}{N} \right) \right]} \quad (7)$$

It is seen from Eq. (7) that

$$P_n = P_{n+N} \quad (8)$$

and

$$P_n(f) = P_n \left(f + \frac{1}{\Delta_t} \right) \quad (9)$$

Moreover, if the frequency difference between adjacent points of the power spectrum P_n is denoted as Δ_f , then

$$\Delta_f \Delta_t = \frac{1}{N} \quad (10)$$

Use of the Fast Fourier Transform to calculate the power spectrum results in points being calculated for n in the range of zero through $N-1$. From Eq. (8), this range is equivalent to

$$-\frac{N}{2} \leq n \leq \frac{N}{2} - 1 \quad (11)$$

Frequencies outside this range are attenuated by the low-pass filters to prevent the aliasing indicated by Eq. (9).

III. Error Analysis

Unfortunately, the actual physical hardware in the complex mixer channels introduces small changes in gain and phase from the desired nominal values. Thus, Eqs. (1) and (2) become, respectively,

$$Rf(t) = -\frac{\sqrt{2}}{2} A \sin(2\pi ft + \phi + \epsilon_1) \quad (12)$$

$$If(t) = \frac{\sqrt{2}}{2} B \cos(2\pi ft + \phi + \epsilon_2) \quad (13)$$

where A and B are gains relative to unity, and ϵ is the phase error introduced in the indicated channel. Equation (4) becomes

$$f_k = \frac{\sqrt{2}}{4} \left\{ \exp \left[i \left(\phi + \frac{\pi}{2} \right) \right] [A \exp (i\epsilon_1) + B \exp (i\epsilon_2)] \exp (i2\pi f \Delta_t k) \right. \\ \left. + \exp \left[-i \left(\phi + \frac{\pi}{2} \right) \right] [A \exp (-i\epsilon_1) - B \exp (-i\epsilon_2)] \exp (-i2\pi f \Delta_t k) \right\} \quad (14)$$

From Eqs. (5), (6), and (14), the power spectrum is

$$P_n = \frac{\sin^2 (\pi N f \Delta_t)}{4N^2} \left[\frac{A^2 + B^2 + 2AB \cos (\epsilon_1 - \epsilon_2)}{\sin^2 [\pi(f\Delta_t - n/N)]} + \frac{A^2 + B^2 - 2AB \cos (\epsilon_1 - \epsilon_2)}{\sin^2 [\pi(f\Delta_t + n/N)]} \right. \\ \left. - 2 \frac{A^2 \cos [2(\phi + (N-1)\pi f \Delta_t + \epsilon_1)] - B^2 \cos [2(\phi + (N-1)\pi f \Delta_t + \epsilon_2)]}{\sin [\pi(f\Delta_t - n/N)] \sin [\pi(f\Delta_t + n/N)]} \right] \quad (15)$$

The first term in the brackets of Eq. (15) is the desired term, while the second and third terms are error terms. If many spectra are successively taken and averaged, then ϕ may be considered a uniform random variable between zero and 2π , resulting in the third term vanishing. Even for individual spectra, computer simulation of the complex mixer system shows that for 64-point spectra and larger, the worst-case increase in the image produced by the third term is less than 20%. For small ϵ , the cosine of $\epsilon_1 - \epsilon_2$ may be approximated by the first two terms of the cosine power series. Thus, the averaged power spectrum \bar{P}_n is

$$\bar{P}_n = \frac{\sin^2 (\pi N f \Delta_t)}{4N^2} \left[\frac{(A+B)^2 - AB\Delta_\epsilon^2}{\sin^2 [\pi(f\Delta_t - n/N)]} \right. \\ \left. + \frac{(A-B)^2 + AB\Delta_\epsilon^2}{\sin^2 [\pi(f\Delta_t + n/N)]} \right] \quad (16)$$

where Δ_ϵ is the difference in ϵ between the two channels. The denominator of the error term in Eq. (16) shows that the error is in the form of a ghost indication at an

n which is the negative of the n for the signal frequency f . The ratio P_r of the power in the error term to the power in the desired term is

$$P_r = \frac{(R-1)^2 + R\Delta_\epsilon^2}{(R+1)^2 - R\Delta_\epsilon^2} \quad (17)$$

where R is the ratio of A to B or the ratio of B to A . Figure 2 is a semi-log plot of Eq. (17) for Δ_ϵ in degrees.

IV. Conclusion

From Fig. 2, it is seen that complex mixer channels that are balanced in gain to within 10% and have less than 10 deg differential phase error will give rise to ghost image responses which are attenuated more than 20 dB. Since actual complex mixer hardware is adjusted for a gain balance within 5% and a phase error within 6 deg at all frequencies of interest, this analysis shows that the problem of ghost images in the computed power spectrum may be considered insignificant.

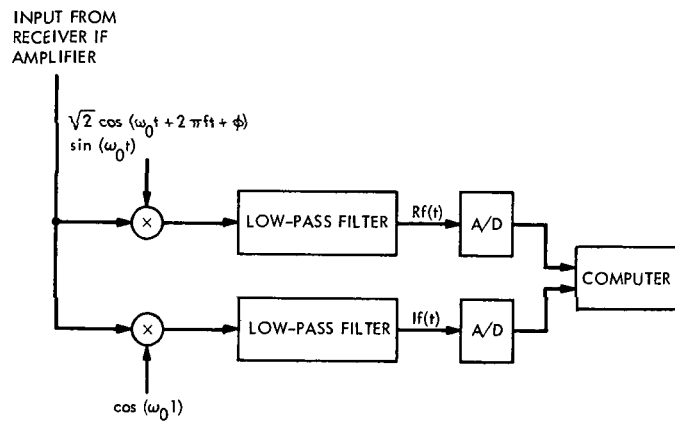


Fig. 1. Ideal complex mixer block diagram

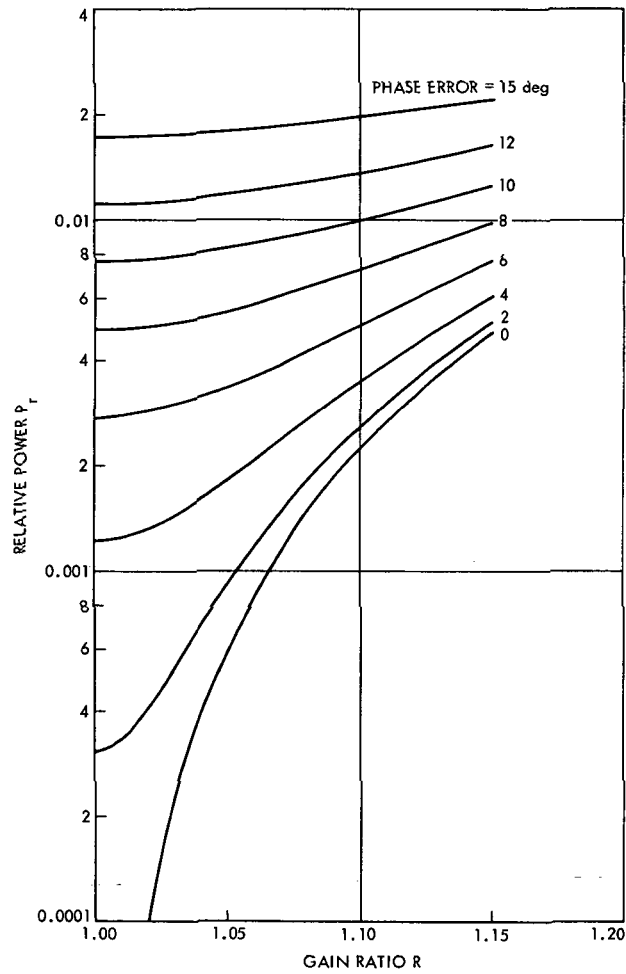


Fig. 2. Ghost image response

Excessive Shaft Friction Variation Corrected by Lubricant Change

H. McGinness
DSIF Engineering Section

During testing of the Master Equatorial for the 64-m-diameter antenna under construction in Australia, a drag torque variation ratio as large as 5 to 1 was observed on a shaft supported by two angular contact ball bearings. A change in the grease lubricant reduced the ratio to 1.1 to 1.0.

I. Introduction

During the testing of the assembled Master Equatorial for the 64-m-diameter antenna under construction in Australia, it was discovered that the polar axis drag torque was erratic. Figure 1 shows the position of the angular contact bearings and the forces acting on them. The axial load on the bearing can be varied by changing the thickness of a shim under the lower bearing retainer. The breakaway torque, that is, the torque required to produce a visible movement from a dead stop condition, varied from 9 to 51 m N. When the movement was just barely visible, the torque variation was considerably less but still much more than is desired.

The Master Equatorial was moved to an appropriate disassembly area and placed so that its polar axis was vertical, with the large bearing above the small bearing. Drag torque tests produced approximately the same results as those obtained with the polar axle at its normal operating attitude, i.e., inclined 35 deg from the horizontal. Next the bearing preload shim was removed, thus

reducing the thrust load on the upper bearing to 11000 N, the weight of the rotating fork assembly. The load on the lower bearing was zero. Many rotation tests were made at this configuration. The breakaway torques ranged from 7.9 to 39.5 m N, with values between 23 and 27 occurring frequently. During very slow movements, the torques ranged from 6.8 to 18.0 m N.

Immediately following a rapid turn of the axle, the slow-speed torque was likely to be near 7 m N, but as the barely visible motion continued, the drag torque increased. When the motion was stopped, following several seconds of slow rotation, the breakaway torque usually was between 23 and 40 m N, although occasionally an 8- to 11-m N breakaway was found. The polar axle was disassembled, and extraneous drag spots were searched for. None was found. The bearings were removed and taken, together with nominally identical spare bearings, to a bearing inspection laboratory¹ for further testing.

¹Bearing Inspection Inc., Santa Fe Springs, Calif.

II. Individual Bearing Tests

The small polar bearing was tested first. It is a standard size, angular contact ball bearing with a 150-mm bore, 225-mm outside diameter, and a width of 35 mm, and contains 22 balls of 22.20-mm diameter in a phenolic resin retainer. It was placed on a table with its axis vertical and loaded to 178 N axially. The breakaway drag torque varied from 0.045 to 0.113 m N. It definitely did not exhibit the characteristics of the installed Master Equatorial polar axle.

Next the large bearing (JPL part number 9435532) was tested. It is a special size, angular contact ball bearing with a 300-mm bore, 360-mm outside diameter, and a width of 33.20 mm, and contains 48 balls of 17.5-mm diameter in a phenolic resin retainer. It was placed with its axis vertical and loaded axially to 334 N. After slow turning by hand in the counterclockwise direction for several turns, an erratic drag torque developed which appeared to be the same as that experienced on the installed axle. The breakaway torque ranged from 0.28 to 1.86 m N. When a small motion was maintained, the torque variation was much smaller but still considerably more than desired.

In order to determine whether the problem was peculiar to this particular bearing, another nominally identical one was tested. Its breakaway torques ranged from 0.17 to 1.62 m N, essentially the same as those of the first one.

The large bearing was then spun as rapidly as possible by hand (estimated at two revolutions per second) for ten to twenty turns. Immediately afterwards, both the slowly moving and breakaway torques were reduced to approximately 0.23 m N, but after a few seconds they were back to much higher values. These tests were repeated several times with the same results. Both directions of rotation were tried.

It was surmised that in some way the lubrication was at fault. The grease in both the large and small bearings (grease No. 1)² had been selected with particular emphasis given to its ability to prevent fretting corrosion during shipment to the overseas site.

Two large bearings were cleaned of grease and tested dry under the 334-N axial load. Many slow turns were made in both directions searching for the large torque

variations, but none was found. Then spin-down tests were made. The bearing angular speed was measured and the time interval to reach zero speed recorded. The average decelerations were 0.304 rad/s² clockwise and 0.284 rad/s² counterclockwise for serial number 001 bearings. For serial number 003 bearings, the clockwise and counterclockwise average decelerations were 0.264 and 0.260 rad/s², respectively. The torques computed from these decelerations range from 0.059 to 0.050 m N, which was roughly the values obtained from a torque wrench while moving the bearing slowly.

Next a large polar bearing was lubricated with a very light oil (MIL-L-6085A), and many slow turns were made. The torque variation was very small.

A large polar bearing was filled with grease No. 2,³ which is the lubricant used in the Master Equatorial bearings at DSS 14, and loaded to 334 N axially. Grease No. 2 is a very stiff channeling grease, and many turns were required to obtain the most favorable performance. After a few hundred turns, drag breakaway torques of 0.56 to 0.68 m N were measured. A slow motion typically required 0.90 to 1.0 m N. No large torque variations were found.

The other large bearing (serial number 001) was filled with No. 3 grease⁴ and loaded to 334 N axially. This grease is also a channeling grease but channels much faster than No. 2. After only a few turns, the breakaway torques ranged from 0.11 to 0.17 m N, and the slow-moving torques were approximately the same. Many slow turns were made searching for the phenomenon of high torque variation, but it was never found.

III. Polar Axle Test

The large and small bearings, both refilled with grease No. 3, were re-installed in the Master Equatorial. With the polar axle vertical and no preload shim installed, the breakaway drag torques ranged from 2.6 to 2.8 m N, and the barely visible moving torques were the same.

The preload shim thickness was adjusted to increase the preload by an estimated 8900 N, that is, the large bearing thrust load was increased from 11,100 to 20,000 N and the small bearing thrust from 0 to 8900 N. The breakaway torques varied from 7.3 to 7.9 m N, and the moving

²Aeroshell 7.

³Andoc C.

⁴Anderol 757.

torques were the same. A hundred or more slow turns were made searching for large torque variations, but none was found.

IV. Conclusions

The comparative drag torque values for the large polar bearing are shown in Table 1. A dramatic reduction in torque variation ratio, namely from 5.60 to 1.07, was obtained by changing from grease No. 1 to grease No. 3.⁵

Three different types of angular contact ball bearings are used on the Master Equatorial. When lubricated with grease No. 1, two types performed acceptably, whereas the performance of the third was most unsatisfactory. It

⁵Both No. 1 and No. 3 contain a diester oil. The thickener in No. 3 is lithium soap, that in No. 1 is "Microgel."

is interesting to note that the large polar bearing is of a special size, whereas the small polar bearing and the declination axis bearings are of standard size. The large polar bearing is slightly smaller in cross section but almost twice as large in pitch diameter as the small polar bearing. Hence, its bearing retainer is much more flexible than that of the small polar bearing. It was noticed that these flexible retainers were slightly elliptical.

It is believed the erratic action of the large polar bearing, when filled with grease No. 1, can be explained as follows: During a sufficiently fast rotation, the major diameter of the elliptical retainer sweeps a circular grease boundary which stays put. Between the grease boundary and the minor diameter of the ellipse, a space exists. But at very slow speeds, the grease sloughs off into this space, and has to be continually plowed out of the way as rotation continues, thus causing a variation in drag torque.

Table 1. Torque value ranges

Conditions	Grease No. 1		Grease No. 2		Grease No. 3	
	Breakaway torque, m N	Slow-moving torque, m N	Breakaway torque, m N	Slow-moving torque, m N	Breakaway torque, m N	Slow-moving torque, m N
Large polar bearing configuration	51				7.90	7.90
	9				7.35	7.35
Installed in Master Equatorial, normal position	39	18			2.8	2.8
	8	7			2.6	2.6
Installed in Master Equatorial, polar axis vertical, reduced preload						
Test bench, 334-N thrust	1.86		0.68	1.0	0.17	0.17
	0.28		0.56	0.9	0.11	0.11

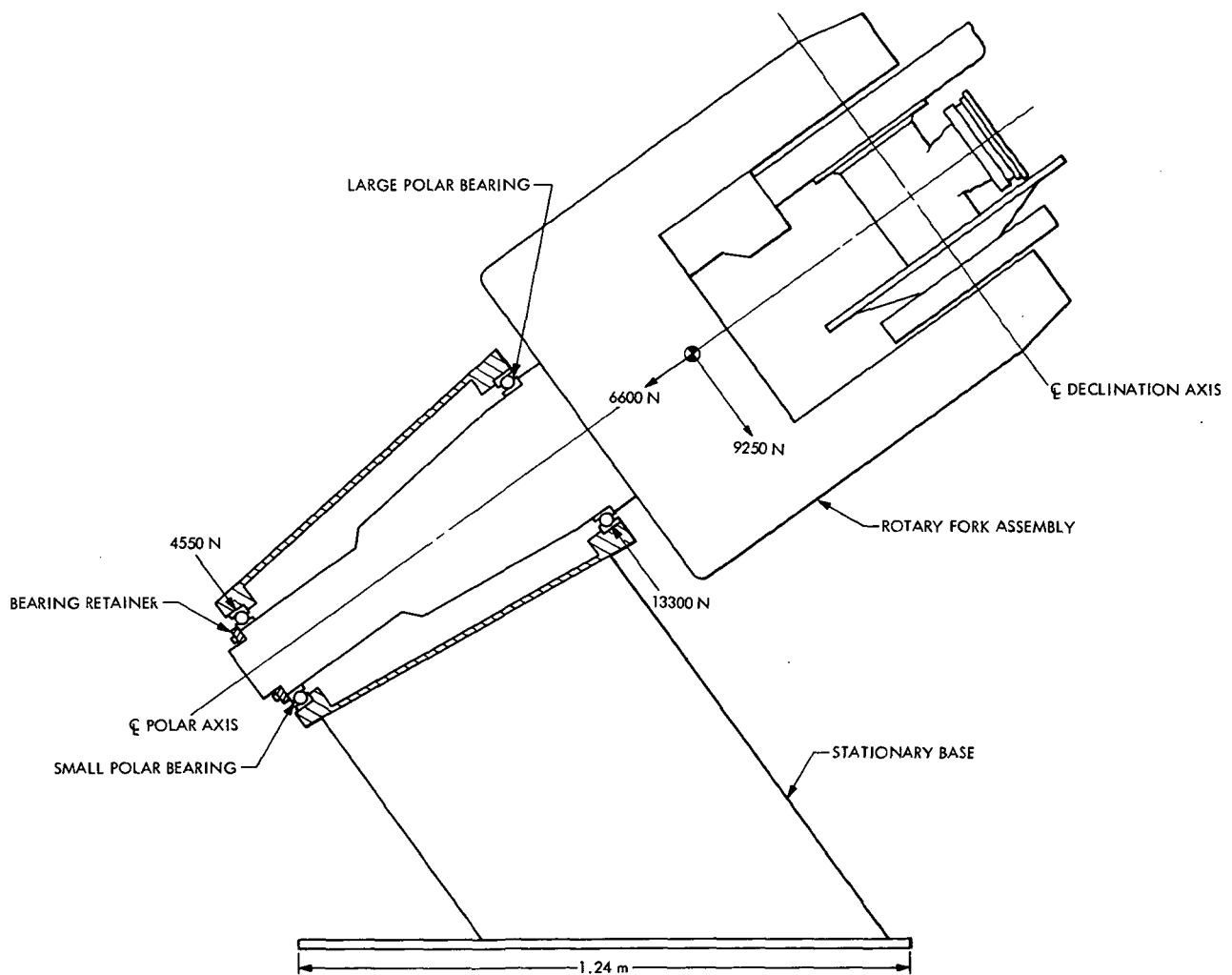


Fig. 1. Schematic of Master Equatorial showing polar axis bearings and loads (in Newtons)

Frequency Generation and Control: Atomic Hydrogen Dissociator

H. Erpenbach and D. Norris
Communications Elements Research Section

This article describes a long-life hydrogen gas discharge source for the JPL hydrogen maser. The lifetime of this source has been extended from approximately 6 months to 2 years or more by changing the geometry of the RF power coupling mechanism. Other improvements over the older type source are: (1) the gas discharge may be started without increasing hydrogen pressure, and (2) an acceptable impedance match to the RF power generator can be achieved over a broader range of operating hydrogen pressures.

I. Introduction

The hydrogen maser uses a collimated beam of hydrogen atoms. These are prepared in an RF discharge dissociator such as that shown in Fig. 1. The present JPL discharge bulb is fabricated of 7740 Pyrex glass tubing, 50 mm in diameter \times 64 mm in length, with a capillary tube 6.5 mm in diameter for the entrance of hydrogen. Opposite the capillary tube is a glass multitube collimator consisting of an array of 800 tubes, 50 μ m in diameter. Dissociated atoms traveling in the direction of the collimator axis are used in the maser oscillator process. The collimator provides a pressure drop from the discharge source bulb to the vacuum chamber to maintain the optimum discharge pressure of approximately 100 μ m.

II. Design Concept

An RF network is required to couple the output of a crystal controlled 125-MHz, 5-W source to the hydrogen gas discharge in the bulb. This network must present a

good impedance match to the power source over the normal range of operating gas pressures used in the masers.

Figure 2 shows the dissociator bulb inserted in the coupling network used previously at JPL. Here, a tuned 1:9 step-up transformer couples the RF energy to a pair of thin electrodes on opposite sides of the bulb. The resulting voltage on these electrodes was apparently high enough to cause the glass wall adjacent to each electrode to sputter glass internally and produced a thin, yellow film on the surface. It is thought that the buildup of this film allowed recombination of the atoms to molecular hydrogen, a process which depletes the supply of atoms. As the film became thicker, the maser output power gradually decreased and finally ceased. This chemical action resulted in an approximate dissociator life of 6 months before maser output power degradation became noticeable and replacement with a new dissociator was necessary. No attempt has been made to analyze the composition of this film.

A new RF coupling network was designed which has resulted in a dissociator lifetime in excess of 2 years. The criterion of this design was to lower the RF voltage gradient across the dissociator bulb by an order of magnitude over the previous design described above. This new RF coupling network with a dissociator bulb inserted is shown in Fig. 3. The circuit consists of a single-turn coil of copper strip around the bulb, which is matched with a series-parallel L-network to the 50- Ω VHF power source. A single turn of 2-mm copper wire was tried, but the resulting discharge was not as uniform as with the 25-mm strip.

III. Conclusion

The new RF coupling network has been operating for 2 years with no noticeable degradation. This new circuit configuration has also demonstrated two other operating improvements over the previous circuit: (1) It is no longer necessary to increase hydrogen gas flow when igniting the discharge, which is a very desirable feature since changes in gas flow can have a deleterious effect on maser frequency stability. (2) A good impedance match to the VHF power source is maintained over a wider range of operating gas pressures than previously achieved.

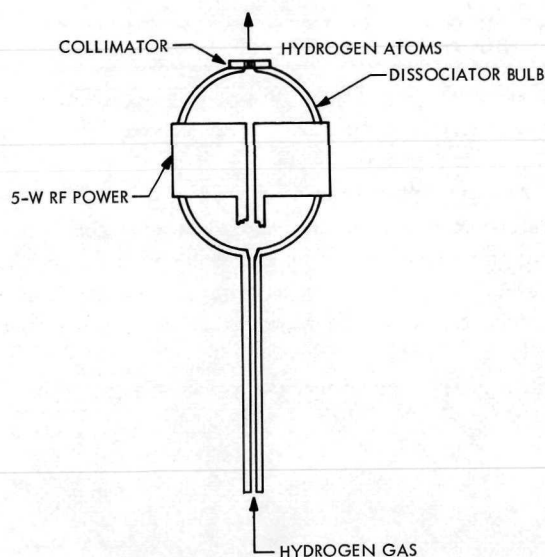


Fig. 1. Dissociator bulb schematic

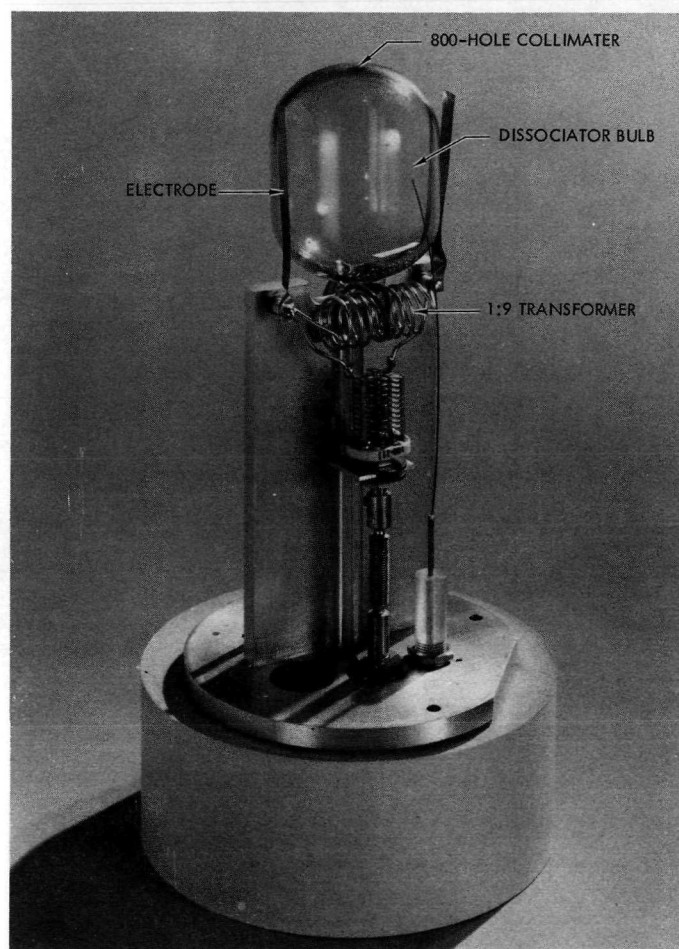


Fig. 2. Original RF coupling network

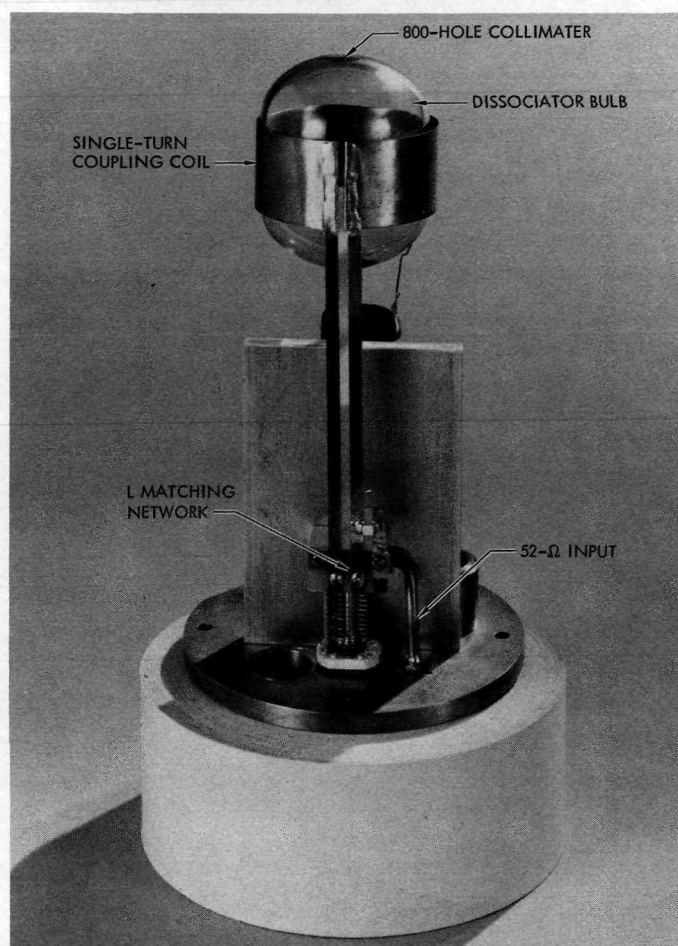
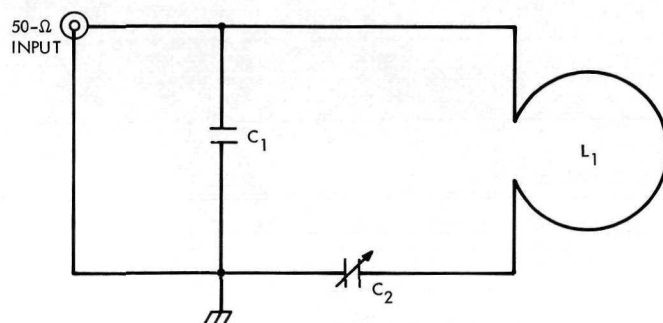


Fig. 3. New RF coupling network



C_1 68 PF, 500 WV dc
 C_2 2.7 TO 19.6 PF
 L_1 DISSOCIATOR COUPLING LOOP. SINGLE-TURN COPPER STRAP, 25 mm WIDE, 0.25 mm THICK, 50 mm DIAMETER, 0.14 μ H

Fig. 4. Schematic diagram of RF coupling network

Improved RF Calibration Techniques—A Practical Technique for Accurate Determination of Microwave Surface Resistivity

R. Clauss and P. D. Potter
Communications Elements Research Section

In this article, a surface loss measurement technique using a TE_{011} -mode circular waveguide cavity resonator is described. A novel feature of this technique is the use of a standard cavity, with a test sample (a flat plate) forming one of the end walls of the cavity. The unique properties of this cavity eliminate the need for intimate contact between the test surface and the rest of the cavity; a surface contact problem is thereby avoided.

Precision Q-measurement equipment is required for this technique. Formulas for the surface resistivity of the sample as a function of the measured cavity Q are derived. Preliminary test data are presented and compared with predicted values, where available. The method described in this article appears to have a wide range of applicability.

I. Introduction

An important consideration in the design, analysis, and calibration of low-noise and/or high-power antenna systems is the dissipative loss associated with the metallic surfaces. Such losses contribute to the receiver system noise temperature and, if nonlinearities exist, contribute noise from transmitter-induced microwave fields. In addition to noise effects, conductor losses cause heating during high-power transmission, which can cause deterioration or failure of microwave components. The calibration of the loss associated with various possible metallic surfaces is thus of importance.

In this reporting, a technique is described which, given the availability of suitable instrumentation, provides rapid and accurate data on the surface resistivity (and hence losses) of any surface of reasonable conductivity (a metal). The dependence of resistivity upon material, surface finish, and discontinuities in the surface can be rapidly evaluated. The required sample of material is a small plate of reasonable but not excessively good flatness. The technique basically involves the precise measurement of the bandpass characteristics of a resonant cavity, one wall of which is formed by the sample under test. A brief analysis of the cavity resonator characteristics is given in the following section.

II. Properties of the TE₀₁₁ Cavity Resonator

A cylindrical waveguide is defined as one in which the cross-sectional size and shape do not change with the longitudinal dimension. Waves propagate along such a waveguide with characteristics rigorously derivable from the scalar wave equation. If two transverse walls are placed across the waveguide, a propagating wave is reflected when it impinges on the two end walls, and a standing wave is created, thus forming a cavity resonator. The unloaded quality factor Q_0 of the resonator is proportional to the electromagnetic stored energy in the resonator divided by the power dissipated in the walls of the resonator. The functional dependence of Q_0 upon the cavity geometry and the surface resistivity R_s of the walls may be accurately calculated. The starting point of this calculation is the waveguide propagation characteristic.

An important and useful cylindrical waveguide is the one in which the walls are smooth, high-conductivity metal of circular cross-section. The fields in the guide must represent a solution of Maxwell's equations, subject to appropriate boundary conditions at the waveguide wall. Two such types of solutions exist: transverse electric (TE) and transverse magnetic (TM) waves. Within each category, a finite number of independent solutions exist (for propagating waves) which are known as modes. Each mode has a specific set of equations which express the field variations within the waveguide as a function of geometry.

One mode in circular waveguides of particular interest is the so-called "low-loss" mode, the TE₀₁ mode. The double subscript index indicates that there is no azimuthal variation of field (see Fig. 1) and one radial field variation. The fields in this waveguide are given by (Ref. 1)

$$H_z = BJ_0(k_c r) \exp \left[\mp j \left(\frac{2\pi}{\lambda_g} \right) z \right] \quad (1a)$$

$$E_z = 0 \quad (1b)$$

$$E_\phi = \pm jBZ_0 \left(\frac{f_0}{f_c} \right) J'_0(k_c r) \exp \left[\mp j \left(\frac{2\pi}{\lambda_g} \right) z \right] \quad (1c)$$

$$H_r = -jB \left(\frac{\lambda_0}{\lambda_g} \right) \left(\frac{f_0}{f_c} \right) J'_0(k_c r) \exp \left[\mp j \left(\frac{2\pi}{\lambda_g} \right) z \right] \quad (1d)$$

$$E_r = 0 \quad (1e)$$

$$H_\phi = 0 \quad (1f)$$

where

$$j = \sqrt{-1}$$

B = an arbitrary constant

$J_0(k_c r)$ = zero-order cylindrical Bessel function of the first kind

$$J'_0(k_c r) = \frac{d}{d(k_c r)} [J_0(k_c r)]$$

f_0 = operational frequency

f_c = cutoff frequency

λ_0 = operational wavelength

$$\lambda_g = \text{guide wavelength} = \sqrt{1 - \left(\frac{\lambda_0}{\lambda_c} \right)^2}$$

$k_c a$ = first root (not including $x = 0$) of $J'_0(x) = 0$
= 1.84118

a = waveguide radius

z_0 = characteristic impedance of the medium
(such as air)

If parallel plates are introduced across the waveguide at a separation of one half guide wavelength ($l = \lambda_g/2$), a TE₀₁₁ mode cavity resonator is formed. The internal fields are given by the superposition of $+z$ and $-z$ traveling waves:

$$H_z = -2jBJ_0(k_c r) \sin \left(\frac{\pi}{l} z \right) \quad (2a)$$

$$H_r = -2jB \left(\frac{\lambda_0}{\lambda_g} \right) \left(\frac{f_0}{f_c} \right) J'_0(k_c r) \cos \left(\frac{\pi}{l} z \right) \quad (2b)$$

$$E_\phi = +2BZ_0 \left(\frac{f_0}{f_c} \right) J'_0(k_c r) \sin \left(\frac{\pi}{l} z \right) \quad (2c)$$

The total stored energy in the cavity, U_T , is given by the sum of the time-average electric and magnetic stored energies. Since, at resonance (i.e., $l = \lambda_g/2$), the time-average magnetic and electric stored energies are equal,

$$U_T = \frac{1}{2} \epsilon \iiint_V |E_\phi|^2 dv \quad (3)$$

$$U_T = 2\pi B^2 z_0^2 \left(\frac{f_0}{f_c} \right)^2 \epsilon \left(\frac{1}{k_c} \right)^2 U_1 \quad (4)$$

where

$$I_1 = \frac{(k_c a)^2}{2} J_0^2(k_c a) \quad (5)$$

and ϵ = permittivity of medium (such as air)

The total currents $\mathbf{J}(r, \phi, z)$ flowing in the cavity walls are given (for any reasonable conductor) by the surface currents which would exist in a cavity with walls of infinite conductivity. These currents are given by the boundary condition

$$\mathbf{J}_s = \mathbf{n} \times \mathbf{H} \quad (6)$$

where \mathbf{n} = outward normal (relative to the surface).

By substitution of (2a) and (2b), it is found that

$$\mathbf{J}_{s_{\text{cyl}}} = -2jBJ_0(k_c a) \sin\left(\frac{\pi}{l} z\right) \mathbf{a}_\phi \quad (7)$$

and

$$\mathbf{J}_{s_{\text{end}}} = -2jB\left(\frac{\lambda_o}{\lambda_g}\right)\left(\frac{f_o}{f_c}\right) J_0'(k_c r) \mathbf{a}_\phi \quad (8)$$

where

$$J_0'(k_c a) = 0$$

Examination of (7) and (8) reveals the unique and desirable properties of the TE_{011} mode cavity. The current is entirely circumferential and, moreover, is zero at the intersections of the cylindrical and end walls. These two properties make the contact of the test sample end wall and cylindrical wall uncritical and insensitive to problems such as contact resistance, lack of flatness, etc. This valuable property of the cavity is well known (Ref. 2).

The time-average power loss W_L in one of the cavity walls is given by

$$W_{L_{\text{wall}}} = \frac{R_{s_{\text{wall}}}}{2} \iint_s |J_s|^2 ds \quad (9)$$

where $R_{s_{\text{wall}}}$ = surface resistivity of the wall in ohms.

Performing the integrations, it is found that

$$W_{L_{\text{cyl}}} = \frac{R_{s_{\text{cyl}}} 4\pi B^2 a l I_1}{(k_c a)^2} \quad (10)$$

$$W_{L_{\text{end}}} = R_{s_{\text{end}}} 4\pi B^2 \left(\frac{\lambda_o}{\lambda_g}\right)^2 \left(\frac{f_o}{f_c}\right)^2 \frac{1}{(k_c)^2} I_1 \quad (11)$$

The total loss W_L is then given by

$$W_L = \frac{4\pi B^2 I_1 a^2}{(k_c a)^2} \left[R_{s_{\text{cyl}}} \left(\frac{l}{a}\right) + \left(\frac{\lambda_c}{\lambda_g}\right)^2 (R_{s_{\text{end } 1}} + R_{s_{\text{end } 2}}) \right] \quad (12)$$

The unloaded cavity Q_0 is given by,

$$Q_0 = \frac{\omega_0 U_T}{W_L} \quad (13)$$

where

$$\omega_0 = 2\pi f_o$$

and from (4), (12), and (13),

$$Q_0 = \frac{\left(\frac{\pi}{2}\right) z_0 \left(\frac{\lambda_c}{\lambda_o}\right)^2 \left(\frac{\lambda_g}{\lambda_o}\right)}{\left[R_{s_{\text{cyl}}} \left(\frac{l}{a}\right) + \left(\frac{\lambda_c}{\lambda_g}\right)^2 (R_{s_{\text{end } 1}} + R_{s_{\text{end } 2}}) \right]} \quad (14)$$

All of the parameters on the right side of Eq. (14) are known except for the surface resistivities; thus, having measured Q_0 , it is possible to solve for the surface resistivities.

III. Experimental Method

Accurate Q measurements for cavity resonators with high unloaded Q s require the use of precision measurement equipment. A Hewlett Packard 8320 stabilized microwave system was available for tests described in this article. A photograph of this system and additional equipment used to measure and record signal frequency, amplitude, and phase is shown in Fig. 2. This system¹ was immediately available for the tests described here. A block diagram of the test setup is shown in Fig. 3. The measurement system is amplitude- and frequency-stabilized. The dynamic range is sufficient to accurately

¹Designed and assembled by P. Hubbard and R. Berwin for the Communications Elements Research Section.

measure test cavities with up to 50-dB transmission loss. The loaded Q of a cavity is determined from recordings of the amplitude and phase of a test signal as it is swept through the cavity resonant frequency. The unloaded Q is calculated from the measured values which determine loaded Q (Q_l) and the transmission loss.

$$Q_0 = Q_l \left[\frac{L^{1/2}}{L^{1/2} - 1} \right] \quad (15)$$

where L = transmission loss ratio.

An aluminum cavity used to measure surface resistivity with this technique is shown in Fig. 4. The test plate forming one end of the cavity is not shown. The depth and rotation of the coupling loops can be adjusted for a cavity transmission loss that results in sufficient signal level for accurate measurement. The choke joint consists of a 1-mm wide groove which is 7 mm deep. The inner surface of the choke joint is machined back 0.25 mm and does not contact the surface of the test plate, which is clamped against the outer ring of the choke joint. The choke joint eliminates wrong mode resonances and reduces surface contact problems to an undetectable level. The cavity diameter is 5.7 cm, and the depth is 2.73 cm. The cavity dimensions were selected so that a standard aluminum tubing size (material which was on hand) could be used to form a cavity with high surface currents on the cavity ends at a resonant frequency near 8415 MHz.

Figure 5 shows the frequency response of the aluminum cavity with a solid copper test plate.

IV. Experimental Results and Conclusions

For the particular cavity described in the preceding section,

$$Q_0 = \frac{1576.344 \Omega}{[0.9577 R_{s_{cy1}} + 0.7329 (R_{s_{end1}} + R_{s_{end2}})]} \quad (16)$$

Four test samples were measured with the aluminum cavity described above: (1) aluminum alloy, (2) copper, (3) stainless steel, and (4) perforated aluminum plate. The thickness of the last was such that transmission through the plate was negligible. The test data obtained are shown in Table 1. The agreement between measured and predicted values is felt to be good, considering the preliminary nature of the experiment.²

The technique is readily applicable to the measurement of the effect of surface finish and perforated plate geometry. Because the cavity Q_0 is high, very high current densities are obtainable with a relatively modest power input. This fact suggests the possibility of using the technique to investigate noise problems caused by surface irregularities (such as joints) in high-power systems.

²Subsequent tests with an OFHC copper version of this cavity and test plates of OFHC copper and 2024 aluminum alloy resulted in measured R_s values of 0.02669 Ω for OFHC copper and 0.04459 Ω for 2024 aluminum alloy.

References

1. Ramo, S., and Whinnery, J. R., *Fields and Waves in Modern Radio*, Second Edition, John Wiley and Sons, New York, 1953, p. 375.
2. Ramo, S., and Whinnery, J. R., *Fields and Waves in Modern Radio*, Second Edition, John Wiley and Sons, New York, 1953, p. 430.

Table 1. TE_{011} mode cavity test data, aluminum cavity

Sample No.	Sample type	Q_0	R_s, Ω	R_s predicted ^a , Ω
1	Aluminum alloy	15,000	0.04336	0.04347 (2024 aluminum alloy)
2	Copper (unknown purity)	16,600	0.02954	0.02519 (OFHC type copper)
3	Stainless steel	2,820	0.6626	—
4	Perforated aluminum plate	10,000	0.11505	—

^aSupplied by D. A. Bathker, Communications Elements Research Section.

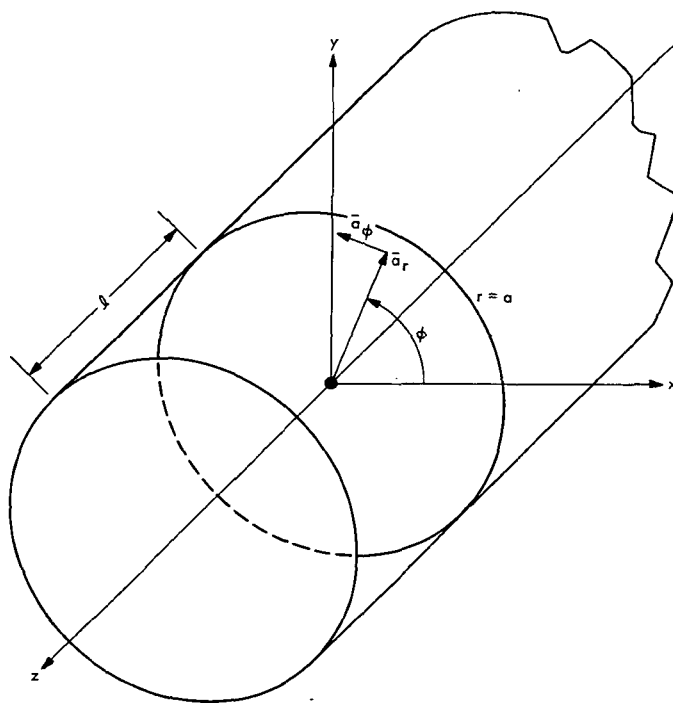


Fig. 1. Circular waveguide geometry

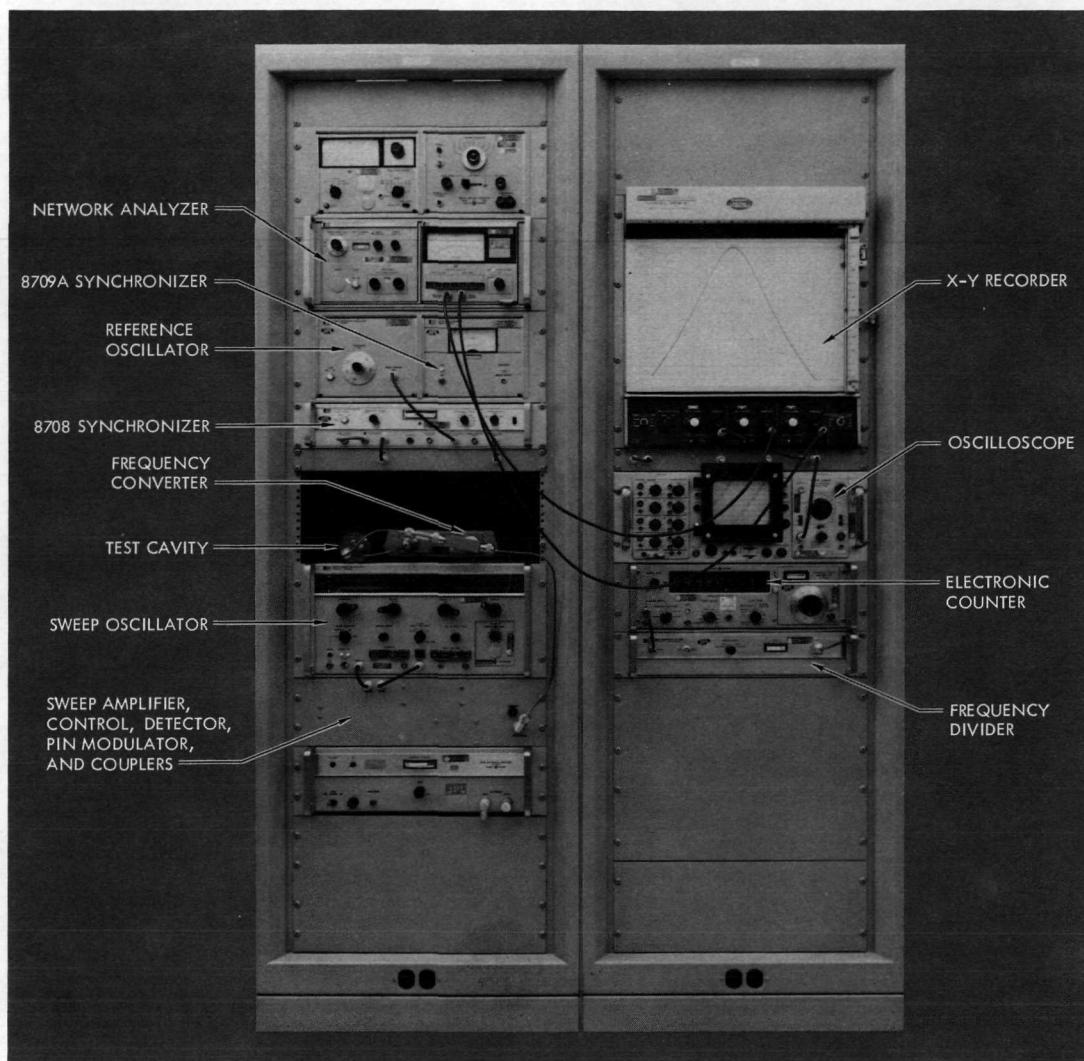


Fig. 2. Microwave equipment used for Q measurement

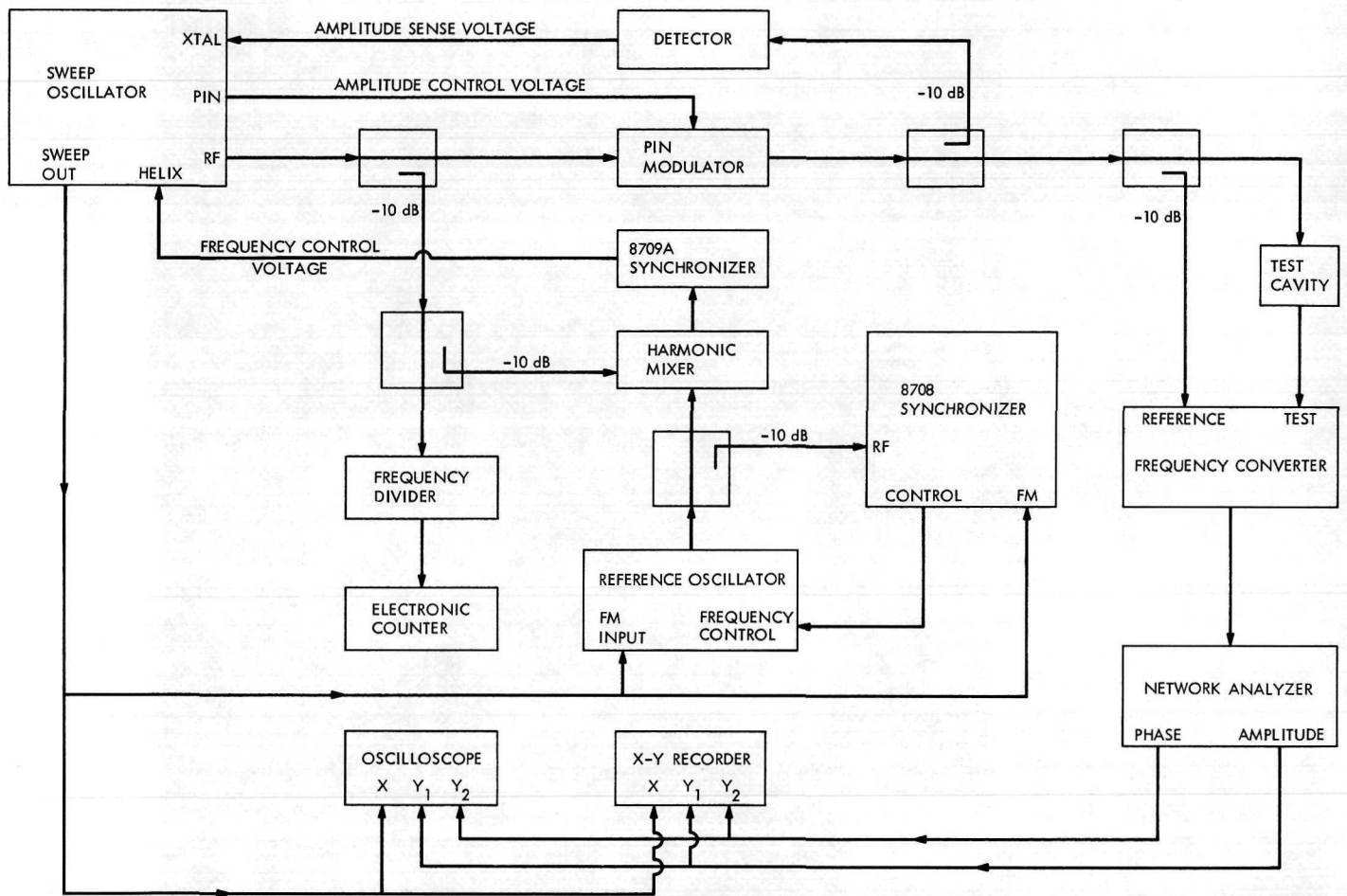


Fig. 3. Q measurement test setup block diagram

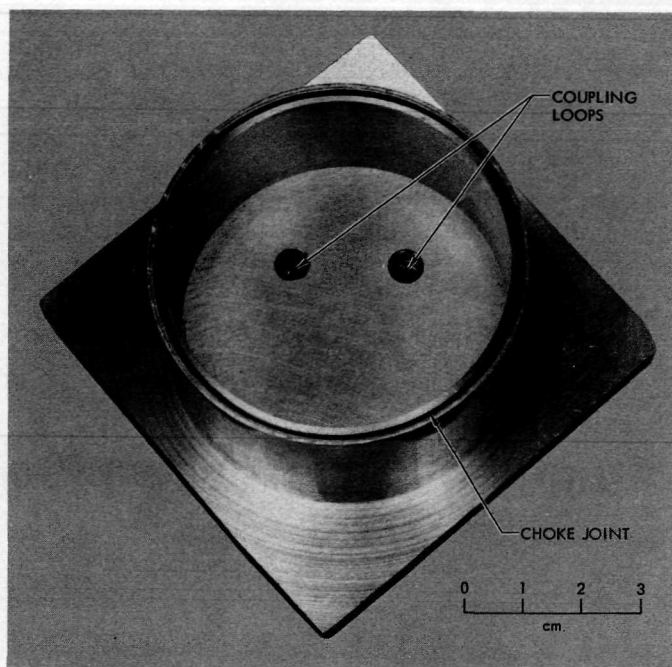


Fig. 4. Aluminum TE_{011} mode cavity resonator

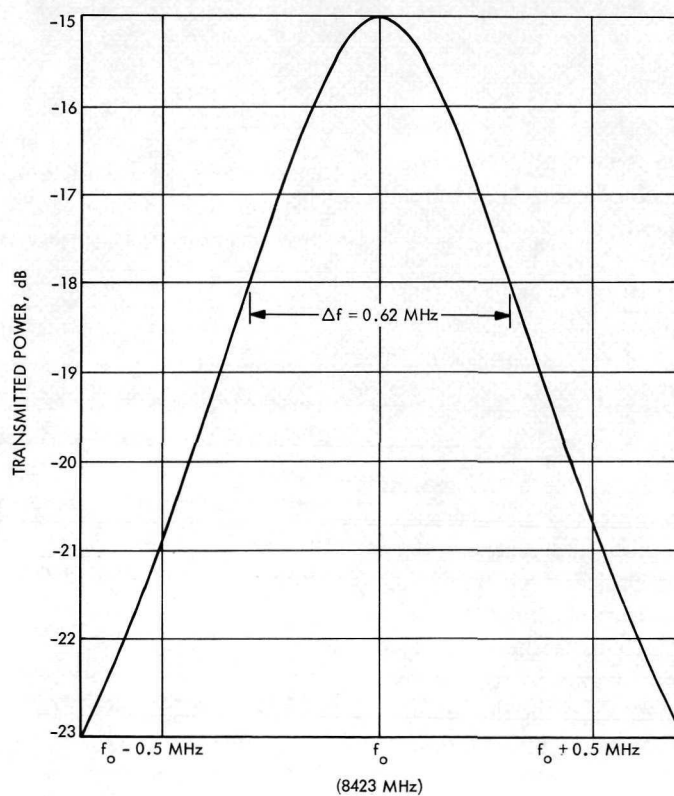


Fig. 5. Frequency response of test cavity resonator

PARADES Structural Design System Capabilities

R. Levy
DSIF Engineering Section

R. Melosh
Virginia Polytechnic Institute and State University

Design approaches, program capabilities, problem formulation, and user options are outlined for the PARADES program. PARADES is a new computer program for the analysis and design of parabolic antenna-reflector structures.

I. Introduction

PARADES is a special-purpose structural design computer program that is being developed for JPL by the Philco-Ford Western Development Laboratories, Palo Alto, California. The name is an acronym for Parabolic Reflector Analysis and Design Subsystem. The primary function of this program is to perform structural analysis of an initial reflector design, assess a selected measure of performance efficiency, and then improve the efficiency by redesign.

Since the task of PARADES is to improve the design of a structure with respect to some pre-established measure of efficiency by means of automated mathematical procedures, the program can be classified as operating within the field of Optimum Structural Design. This field began its contemporary development within the last decade and is a logical extension of rapidly expanding technology and computer implementation for the evaluation of structures by means of analysis of independently established designs.

Although structural optimization is currently an emergent field of technology, there is a host of widely differing

mathematical approaches that have been developed. These range in sophistication from extremely simple trial-and-error solution searches to the much more complex methods of mathematical programming. A brief review of some of the more prevalent methods is given in Ref. 1.

As yet there is no clear definition of which method is preferential for any specific application. In the present context, "preferential" is a qualitative concept since it implies a subjective evaluation of the design efficiency attained as well as the effort expended for the attainment. Furthermore, since applications are so diverse, it may never be possible to establish a universally suitable method for all applications.

Consequently, the PARADES program has adopted the practical philosophy of implementing a solution method that has been demonstrated as effective for the antenna design problem. This bypasses the alternatives of developing a new method, or extending an existing method unproven for the problem at hand. Therefore, the attendant risks of little effectiveness or even uselessness are avoided.

Another practical attitude adopted within PARADES is the recognition that design optimization, in the global sense, is a tenuous concept that is often either not achievable or, if achievable, not worth the ultimate extra effort. Although the word "optimization" has been accepted to characterize a broad technological field, a more realistic interpretation with respect to structure design would invoke the word "improvement." Accordingly, PARADES addresses itself to the task of attaining effective design improvement without specifically attempting to find an abstract mathematical optimum.

Although the solution approach adopted by PARADES has been previously established by Von Hoerner with his concept of "homologous design" (Ref. 2), many features of implementation, program scope, and user options that are incorporated are advanced and innovative. It is anticipated that these features will make PARADES an effective program that will be used for analysis only, and when it is not also required to employ its design capability.

II. Design Approach

The design task entails reassigning values of design variables to generate an admissible design of improved efficiency. The design variables are defined to be the cross-sectional properties of the structural members of a parabolic reflector. An admissible design precludes overstress, buckling failure, and excessive deflections with respect to limits and loadings established by the program user. The measure of efficiency is the rms of half the difference in pathlength of the RF energy beam in traveling from a deformed reflector surface to the focal point, compared with the pathlength from a surface that is a perfect paraboloid. The reflector surface of interest is equivalent to an infinite set of points for which pathlength differences exist; in practice, the surface is replaced by a finite set of "target" points, which are taken to be a representative sample of the entire set.

The deformations that are considered within PARADES for efficiency evaluation are the repeatable elastic surface deformations that result from the gravity loading of the weight of the structure plus other nonstructural supported components. Although this loading has constant magnitude, the direction of the gravity vector with respect to the antenna surface can change as the antenna elevation angle changes from the zenith to the horizon operational pointing positions. Consequently, there is an infinite set of gravity loadings for efficiency evaluation—

one for each attitude in the continuous spectrum of elevation attitudes.

However, by using formulations developed from the rigging angle concept (Ref. 3), it has been shown (Ref. 4) that loading at one particular elevation attitude is sufficient to characterize the efficiency of a particular design over the entire elevation range. This concept implies that the gravity loading at the so-called "rigging angle" attitude is compensated by adjustment of surface panels and the loading at other attitudes is effectively the net loading in moving away from the rigging attitude. Therefore, one of the innovations of PARADES, which permits the substitution of a single design loading condition, is to compute the optimal rigging angle associated with a particular structural design. Adjustment of the surface for the optimum rigging angle can be a major step toward efficiency improvement even if no other structural design changes are developed.

Homologous design, the primary design approach of PARADES, was defined by Von Hoerner (Ref. 2), as a design that would force the surface to respond elastically under loading by deforming from one perfect paraboloid into an alternative perfect paraboloid that could possibly have a different focal length, plus up to three independent rigid-body translations and two independent rigid-body rotations. In ideal situations, and also within minor approximation in many practical situations, the focal length change and the rigid-body motions of the alternative perfect paraboloid would have no effect on gain loss from surface distortion. If any of these "homology shifting parameters" were unacceptable from an RF standpoint, they could be suppressed during the mathematics of defining the alternative paraboloid. Then again, there would be no gain loss, provided that an homologous design could still be achieved.

Homology is theoretically achievable as long as there are as many design variables (member sizes) for selection as there are target points. This follows because one equation can be written for each point in the surface target set of points to express the deflection of the point from the alternative paraboloid. Therefore, the homology design procedure is to solve these equations for the values of the design variables that make the deflections zero. Since these equations are nonlinear, they are solved in approximation by means of influence vectors developed to find the gradient changes in deflection for changes in the design variables. Consequently, as is characteristic of all practical problems in the field of structural optimization, linear approximations used in the solution of

essentially nonlinear equations require that the design process must be iterative.

The iterative process entails repeated application of two operations until some measure of convergence or limit placed upon the allowable amount of computation is reached. These operations are:

- (1) Analysis of the starting design, or of the design that has currently been developed. This operation is mathematically "exact."
- (2) Redesign, which consists of selection of new member sizes. This operation is approximate because of the nonlinear relations between the design variables and the deflection response.

In many practical cases, perfectly homologous designs will not be achievable for one or more of the following reasons:

- (1) There are not enough design variables.
- (2) There are not enough free homology shift parameters.
- (3) Selections of the design variables are restricted, e.g., by side constraints such as overstress or excessive deflection for some other loading condition, by a minimum size restriction, by a requirement that certain members be assigned to groups with common sizes, by a limited candidate list of discrete sizes from which member sizes must be selected.

In these cases, PARADES will automatically solve the target point deflection equations in the least-squares sense. This will result in a minimum rms solution for the resulting design. Like the homologous design mode, this is also an iterative process.

In addition to the reflector design solution modes of homology and minimum rms, PARADES has a third mode of fully stressed design. This option was introduced because of its general usefulness for many non-reflector-type structural designs either as a final design or as a feasible starting point for another design procedure. It is well known that fully stressed design is not really an optimization approach because no efficiency measure is recognized. Also, fully stressed design is sometimes not achievable. Nevertheless, in some cases, it can produce the optimum weight vs. stress designs, or designs close to the optimum. It is also capable of rapid execution and convergence within few iteration cycles.

Mathematics and details of implementation of these design approaches are given at considerably greater length in Ref. 5. It should be noted that in either of the reflector design modes, PARADES constrains the structure weight to be invariant and takes the minimization of the rms performance measure as the objective. In the fully stressed design mode, PARADES seeks the smallest individual member sizes that will satisfy the stress constraints. This will tend to produce a relatively small, but not necessarily the smallest, total weight for an admissible structure.

III. Program Features and User Input

As the program incorporates analysis with the innovation of design capability, input data requirements are more extensive than for familiar programs devised to perform analysis alone. Nevertheless, because this is a special-purpose program directed primarily to antenna-reflector structures, user input requirements are simplified and operational efficiency is enhanced by taking advantage of the highly repetitive nature of this class of structures. Consequently, the amount of data to be prepared for input and the execution time for one cycle of design and analysis are each likely to be approximately the same or less than for standard programs that perform analysis only. Complete details and examples of input data preparation are given in Ref. 6.

As in customary analysis programs, the structure is defined by nodal grid intersection points, member connectivity, and property data, while the problem is defined by loading data and grid constraint lists. However, a distinctive feature of PARADES allows a substantial condensation of these data through its capability for modular input. This requires the user to define only one representative sector of the structure with respect to grids, connectivity, and loading. The program internally generates all sectors of the complete structure as defined by the user and assembles the correct number of replicate and mirror-image copies of the representative sector. The program also accepts special user input to define features of the structure that are not typical of the representative sector.

Formulating and solving of the load-deflection equations is done on a sector basis. Identical computations that are performed for one sector are not repeated for other sectors. As a further simplification, when structural symmetry, in conjunction with loading symmetry or antisymmetry, makes it possible to restrict the investi-

gations to one-half or one-quarter of the full structure, boundary conditions can be generated automatically for the part structure.

The structural connectivity as defined by the user consists of line elements. Elements can be offset from the terminal grid points, and slip and hinge joints can be specified. Direct stress, shear, torsion, and bending of these elements are considered in the analysis. Design is based upon the cross-sectional area and the one-to-one relationship of weight and area.

New members for an improved design can be selected on either an "idealized" or "realizable" basis. The idealized basis allows the program to compute the member size (area) from a continuous spectrum of sizes. The realizable basis restricts the choice of members to a discrete candidate list supplied by the user. The candidate list can contain any of eight classes of cross-section types. For each type, the user supplies the dimensions of the cross-section required to define the specific geometry, and the program computes all the necessary elastic and inertia properties for analysis and design. Figure 1 shows the cross-section classes available and the defining dimensions that are to be specified. The selection of particular members can be assigned to groups, with all of the members in each group being required to have a common size. From a practical standpoint, grouping often permits worthwhile economies in procurement, tooling, and fabrication that can overcome associated penalties in the design efficiency.

Reflector design for gravity rms is based upon two specific loadings applied parallel to the antenna aperture plane. The total loading, consisting of the weight of the structure and specified invariant external weights, is assembled by the program. Design admissibility is verified for any additionally specified loadings. Stress checks for design admissibility are based upon principal stresses computed at the end of the member with the highest strain energy density. The critical buckling stress is determined from the length and cross-section and included with direct stress in an interaction formula to account for beam-column effects.

Grid coordinates can be input either in rectangular or cylindrical form. The displacement output coordinate system is specified independently of the input form. For the antenna problem, the internal solution is performed in parabolic coordinates. This permits the reduction of the three customary displacements at each target node to the single component of distortion normal to the

parabola. The target set for rms analysis is defined by a weighting factor assigned to the grid point.

The extent of structure that can be analyzed depends mainly on the numbers of degrees of freedom in any sector. If this is less than about 180, total storage for code and data can fit in one 65K bank of the 1108 computer. Large antenna structures could be treated by extending core if the representative sector size could not be made small enough. Adding a second bank of core allows about 380 degrees of freedom in each sector. An option of the program can be used to restrict the number of elastic degrees of freedom at each node to three, rather than six. This is usually appropriate for a reflector structure, so that there can be about 60 nodes per sector for a standard-size core execution, and about 125 nodes if two core banks are assigned. Formulas are given in Ref. 6 to determine the exact core size needed for each problem. The program makes and outputs its own core size computation and will not proceed if storage is inadequate.

In the design mode, homology and minimum rms designs are available for reflector structures. Fully stressed design is available for any general structure, including reflectors. The user can specify the maximum number of redesign cycles. The program can terminate before this number is reached, depending upon an internal parameter that tests the current rate of design convergence. The program will punch decks defining the design achieved for use either in restart or for some other analysis application.

For minimum rms design, the user can specify the objective of minimum peak rms over the entire elevation range, which is accomplished within the program by choosing the rigging angle to make the rms at zenith equal to the rigging angle at the horizon. Alternatively, the user can specify the minimum weighted average rms over the horizon/zenith elevation range, with a weighting function equal to the cosine of the elevation angle and rigging angles computed accordingly by the program. The cosine weighting function provides the minimum expected rms for observations uniformly distributed in the hemisphere between horizon and zenith.

PARADES can execute in an analysis-only mode if desired. The advantages here for reflectors, compared to other standard analysis programs, are the modular input, the included rms computation as opposed to a post-processor program requirement, the comprehensive stress and buckling effect computations that are not

ordinarily available in other programs, and the structure cost estimate furnished by PARADES. This cost estimate is developed from user parameters specifying cost per unit length and volume of general structural material, and specific length and volume costs for particular cross-sections in each of the cross-section classes. In the analysis-only mode, user input can be condensed by deleting information associated with the design capability.

IV. Summary and Program Status

A summary of some of the distinctive features of program execution, data preparation, and optional usage is presented below.

- (1) Modular input with automatic generation of identical or mirror-image modules of structure and loading.
- (2) Automatic boundary-condition generation for half or quarter antenna structure investigation.
- (3) Stress and buckling interaction determination.
- (4) Line element properties determined from cross-section dimensions.

- (5) Rectangular or cylindrical coordinates for input or output.
- (6) Member offsets, hinges, slip joints.
- (7) Rms computations included with deflection analysis.
- (8) Design options for homology, minimum rms, or fully stressed design.
- (9) Automatic determination of rigging angle for minimum rms design for minimum peak or minimum average rms over elevation range.
- (10) Idealized or realizable design options.
- (11) Cost estimate furnished for best design.
- (12) Punched deck output for best design.
- (13) Analysis only, without design, mode of execution.
- (14) Grouping of members for common sizes.

A copy of the program has been delivered to JPL by Philco-Ford and has been compiled on our Univac 1108 computer. To date, the analysis capability of the program has been tested on a sample problem, and extensive testing of the design capability is currently in progress.

References

1. Levy, R., "Optimum Structural Design Study," in *The Deep Space Network, Space Programs Summary 37-59*, Vol. II, Jet Propulsion Laboratory, Pasadena, Calif., Sept. 1969.
2. Von Hoerner, S. "Homologous Deformations of Tilttable Telescopes," *Journal of Structural Division, ASCE*, No. ST-5, Oct. 1967.
3. Levy, R., "A Method for Selecting Antenna Rigging Angles to Improve Performance," in *The Deep Space Network, Space Programs Summary 37-65*, Vol. II, Jet Propulsion Laboratory, Pasadena, Calif., Sept. 1970.
4. Levy, R., "Antenna Rigging Angle Optimization Within Structural Member Design Size Optimization," in *The Deep Space Network Progress Report*, Technical Report 32-1526, Vol. I, Jet Propulsion Laboratory, Pasadena, Calif., Feb. 15, 1971.
5. Melosh, R., *Parabolic Reflector Analysis and Design Subsystem*, Technical Document, Vol. I, Philco-Ford Corp., Palo Alto, Calif., to be published, 1972.
6. Melosh, R., *Parabolic Reflector Analysis and Design Subsystem*, Users Report, Vol. II, Philco-Ford Corp., Palo Alto, Calif., to be published, 1972.

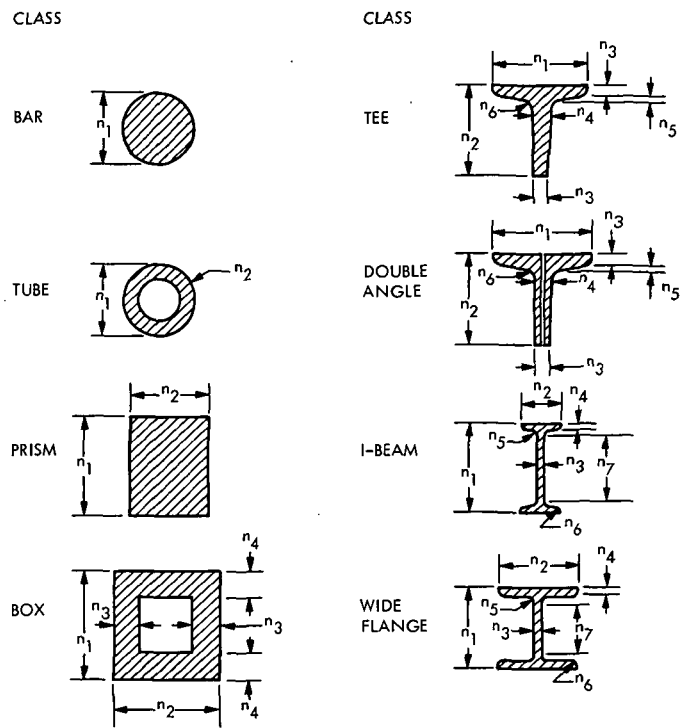


Fig. 1. PARADES line element cross-section classes

Improved RF Calibration Techniques: Commercial Precision IF Attenuator Evaluation

C. Stelzried, B. Seidel, M. Franco, and D. Acheson
Communications Elements Research Section

The IF attenuator normally used for system noise temperature calibrations is the largest single contributor to measurement inaccuracy. Various IF attenuators have been evaluated and calibrated using a National Bureau of Standards IF precision standard. Measurement techniques are indicated and results given. It is noted that there is a wide spread in the accuracy among various manufacturers and also in the same model type from a particular manufacturer. Excessive use appears to be an important factor in accuracy degradation.

I. Introduction

An analysis of low-noise receiving system operating noise temperature calibrations using the Y-factor technique has shown that the single largest source of calibration error is presently due to the IF attenuator (Ref. 1). Various commercial IF attenuators have been evaluated to determine actual performance and to select the unit with the greatest repeatability and accuracy. In addition, units with sufficient repeatability can actually be calibrated with a laboratory standard to a greater accuracy than normally available.

II. System Description and Performance

Figure 1 shows a block diagram of the laboratory calibration system. The laboratory standard attenuator (Fig. 2) was purchased from the National Bureau of Standards and has an accuracy of 0.005/10 dB and a repeatability

of approximately 0.0005 dB at 50 MHz. It was necessary to take particular care with the calibration system to obtain maximum stability. Coaxial hard line and shielding were used throughout so as to minimize loss of accuracy due to leakage. Particular care was taken to clean and tighten the coaxial connectors. Shielding was verified by the use of a high-level radiating probe. The strip-chart recorder was helpful in providing a null set point and recording system stability. Figure 3 shows a recording of typical system stability.

III. Measurement Technique

Although the basic measurement is quite straightforward, extreme care must be taken to ensure that leakage and drift do not corrupt the results. The problem of backlash is minimized in the test attenuator by always approaching the setting carefully from the same direction. The standard attenuator has an optical readout.

The actual measurements are made by first observing a null point on the strip-chart recorder and then changing the attenuator under test by the indicated amount from the reference setting. The standard attenuator is then changed by the amount necessary to bring the power at the detector back to its initial null point as indicated on the strip-chart recorder. The calibrated attenuation difference (dB) in the test attenuator is then equal to the attenuation difference (dB) in the standard attenuator. The error in the test attenuator is defined as the magnitude of the attenuation difference (dB) in the standard attenuator minus the magnitude of the attenuation difference (dB) in the test attenuator:

$$\text{error} = |\Delta_{\text{std}}| - |\Delta_{\text{test}}|$$

After each measured attenuator difference (dB), both attenuators are returned to their original reference null points so as to minimize the effects of drift in the signal source and the detector. Measurement and attenuator repeatability are verified by repeated runs.

IV. Results

Many attenuators from a number of manufacturers were tested. The results of these tests are plotted in

Figs. 4-6 showing the average of a number of measurement sets and the peak-to-peak deviations at each attenuator setting. Figure 4 indicates the performance for a unit that had long field use and relative poor performance (> 0.02 dB pk/pk). Figure 5 indicates the performance of another unit manufactured with considerably better performance than the units presently in use. Figure 6 shows the results of calibrations of typical attenuators with various amounts of service. A three-digit RF Techniques number (RFT XXX) is used to identify the unit tested. This is done because of the large difference in accuracy and repeatability even among units of the same make and model.

V. Conclusions

Waveguide-beyond-cutoff piston IF attenuators are useful devices when one requires a continuously variable means of changing the level of a signal. However, if one must know the change to a high degree of accuracy, then one must carefully select a unit that will meet that required repeatability and precision. There is a wide spread in performance of these attenuators among various manufacturers and also in the same model from a particular manufacturer. Excessive use is probably an important factor in performance degradation.

Reference

1. C. T. Stelzried, "Operating Noise-Temperature Calibrations of Low-Noise Receiving Systems," *Microwave Journal*, Vol. 14, No. 6, June 1971, p. 41.

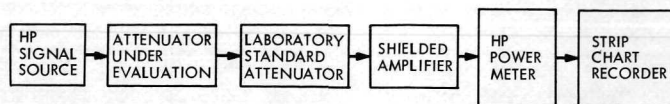


Fig. 1. Block diagram of IF attenuator calibration system

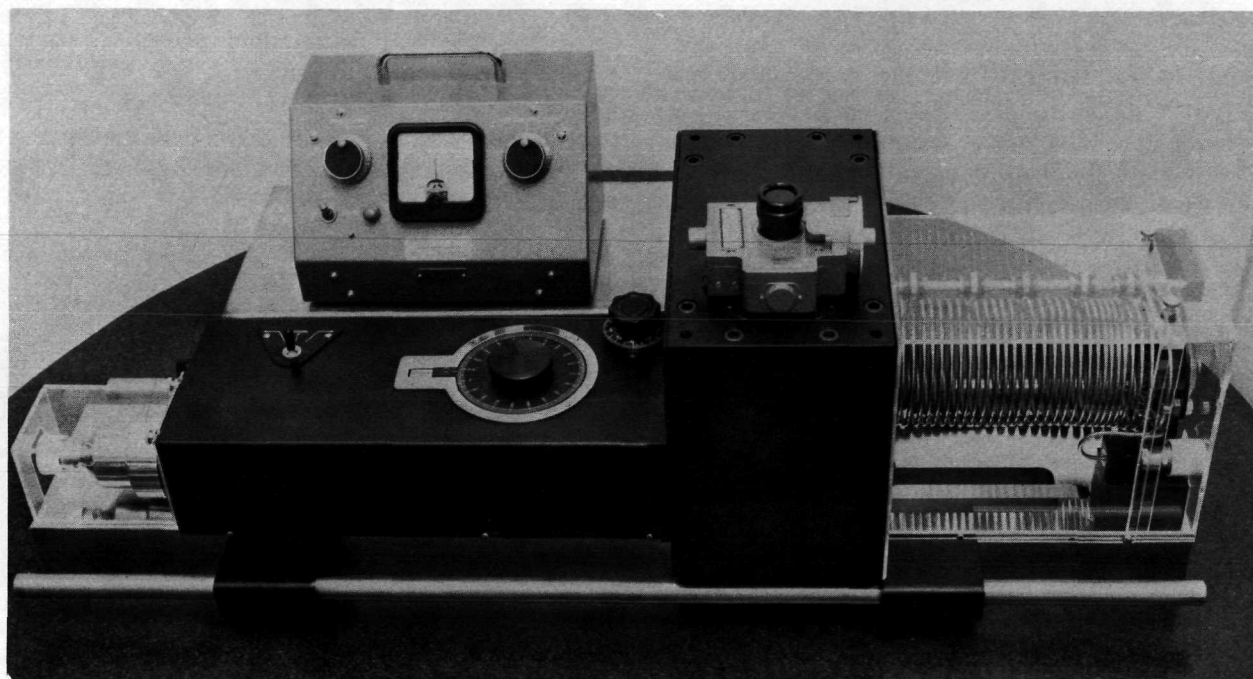


Fig. 2. Photograph of laboratory IF standard attenuator

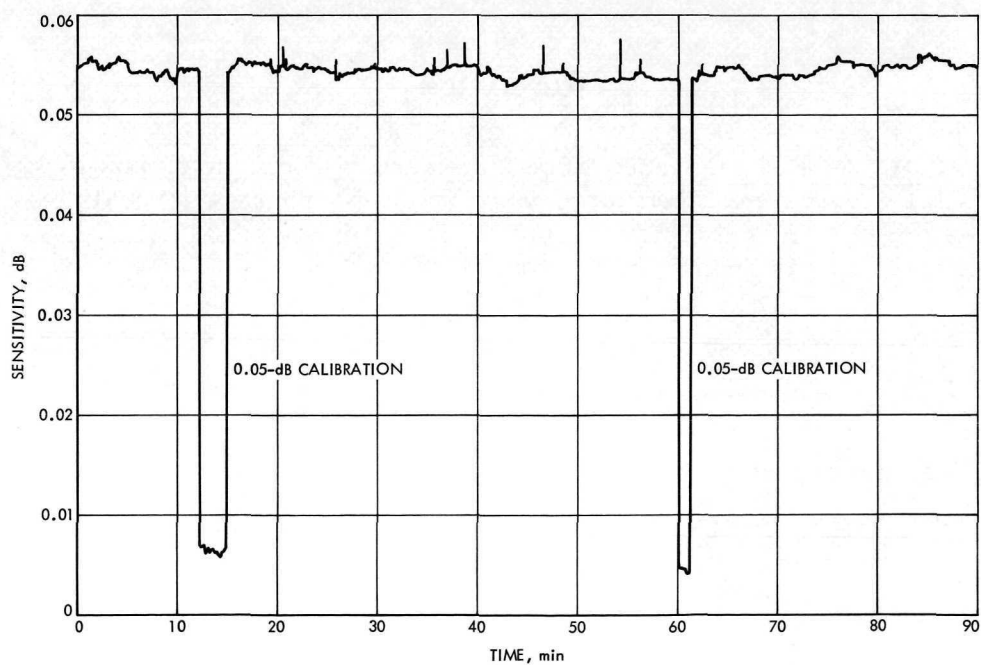


Fig. 3. Typical recording of IF attenuator calibration system stability

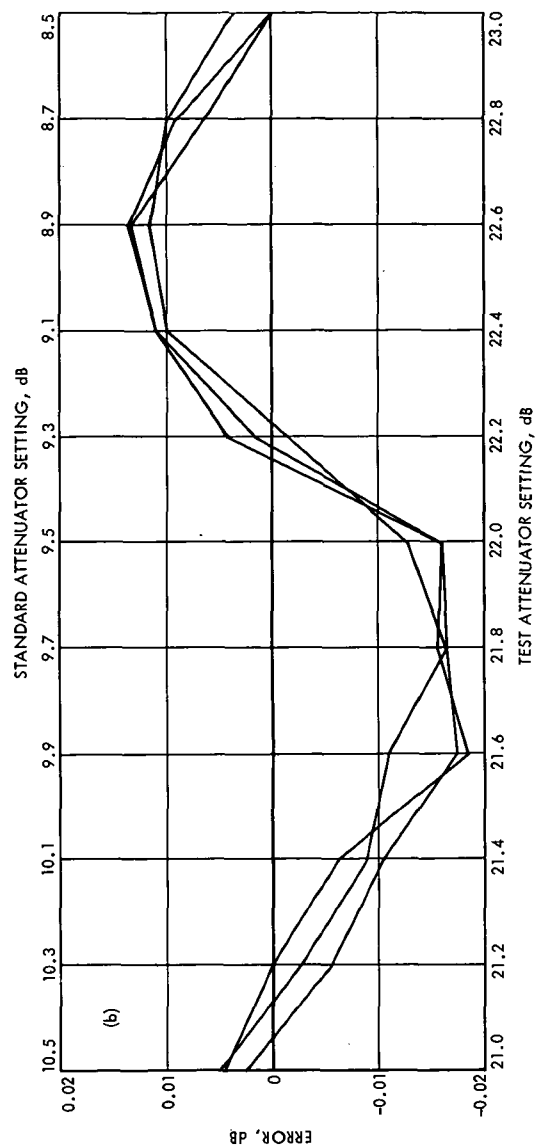
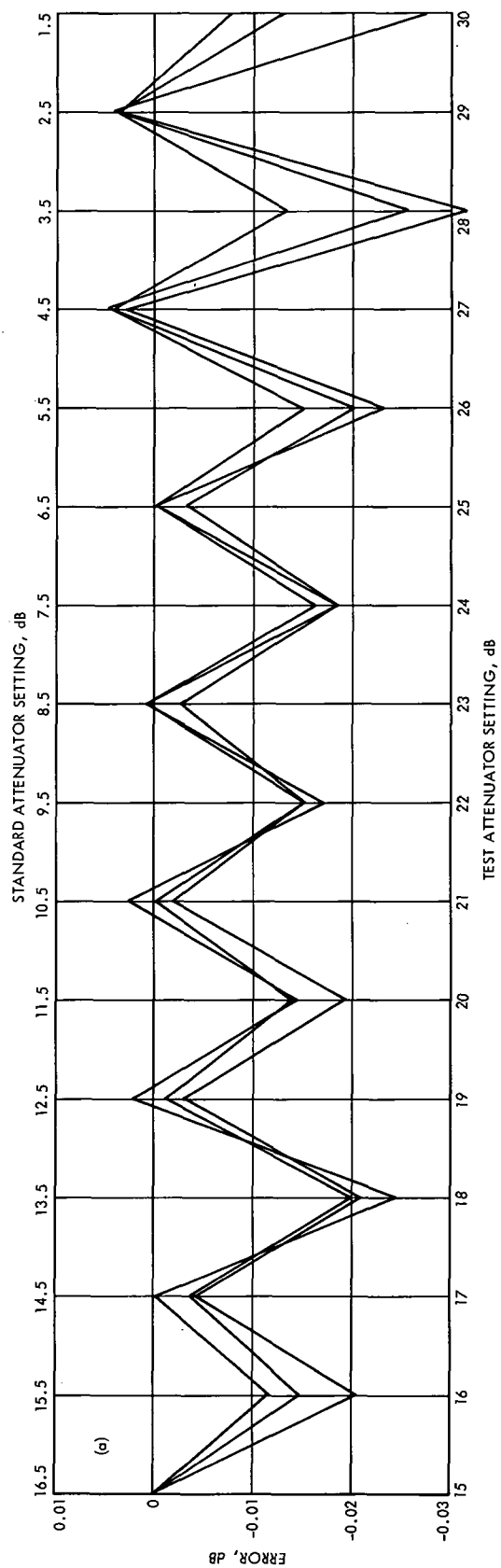


Fig. 4. Results of calibration of a heavily used attenuator:
(a) RFT 483, 15-dB range, 1-dB steps, (b) RFT 483, 2-dB range,
0.02-dB steps

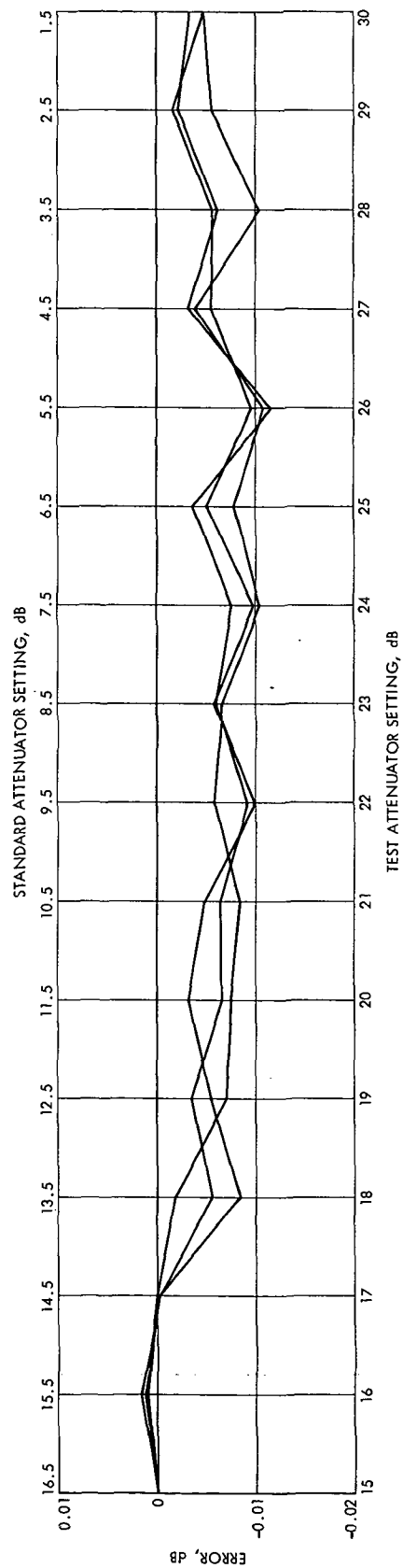


Fig. 5. Results of calibration of an atypical new attenuator (RFT 502, 15-dB range, 1-dB steps)

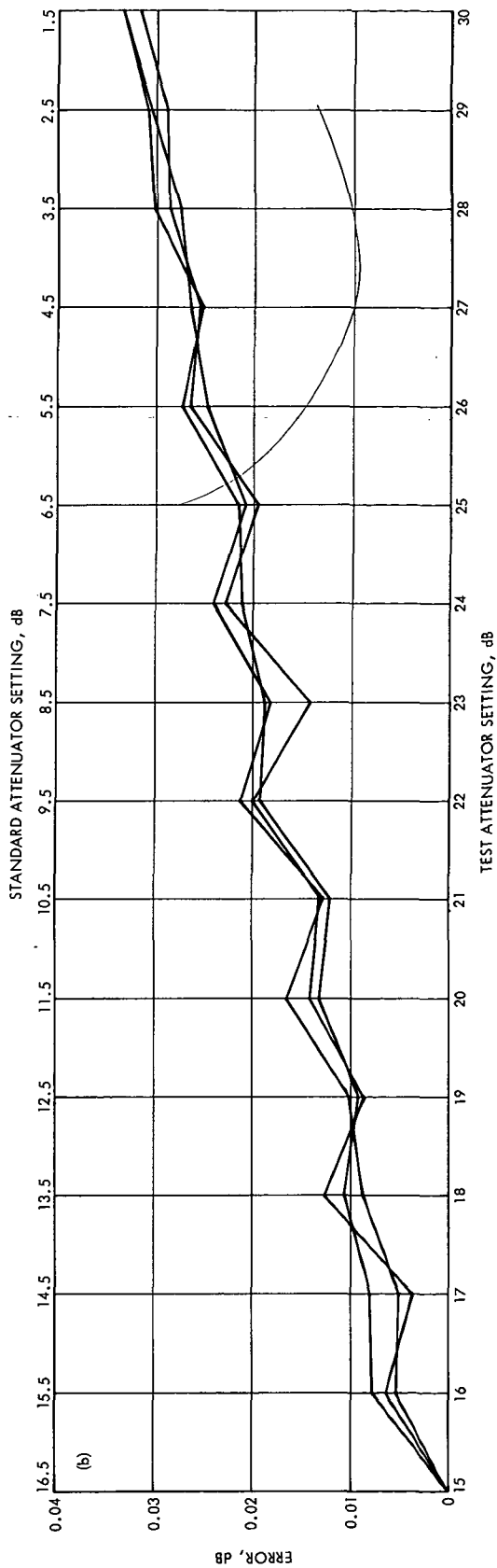
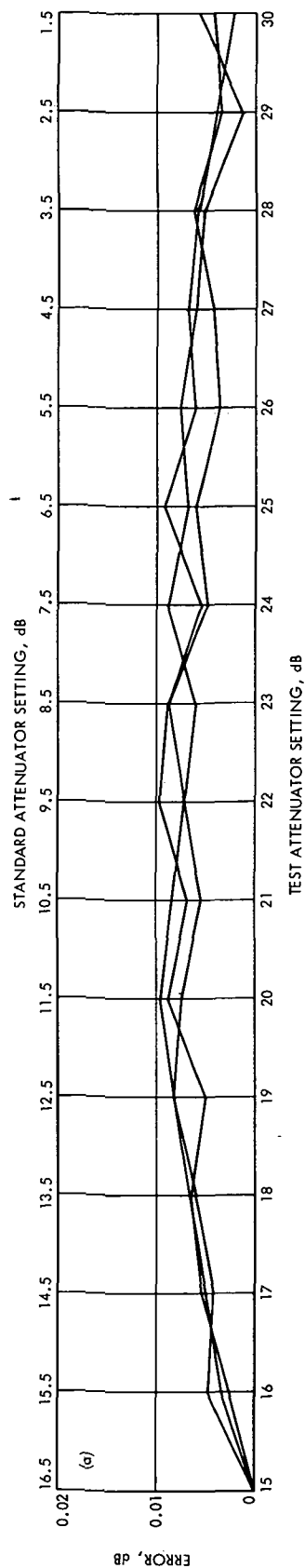


Fig. 6. Results of calibrations of a number of typical attenuators (data at 50 MHz): (a) RFT 485, 15-dB range, 1-dB steps, (b) RFT 487, 15-dB range, 1-dB steps, (c) RFT 496, 15-dB range, 1-dB steps, (d) RFT 497, 15-dB range, 1-dB steps, (e) RFT 498, 15-dB range, 1-dB steps, (f) RFT 490, 15-dB range, 0.5-dB steps, (g) RFT 490, 15-dB range, 1-dB steps, (h) RFT 499, 15-dB range, 1-dB steps

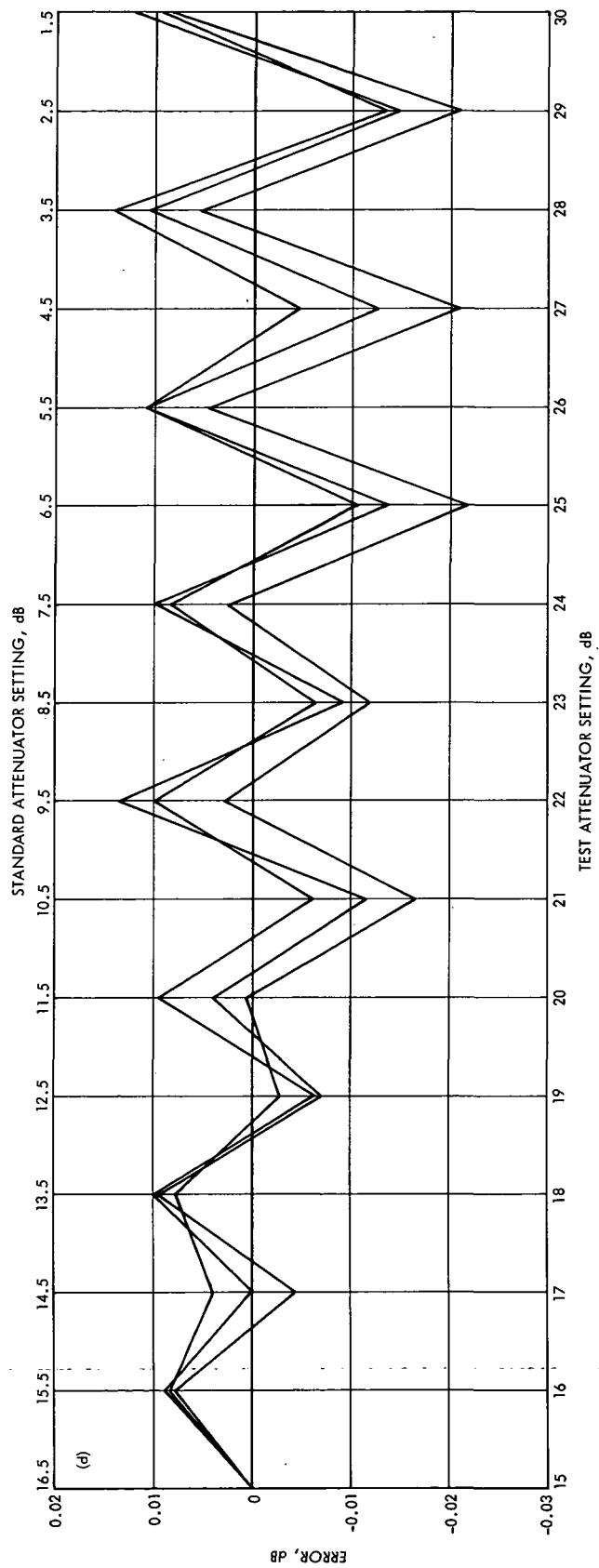
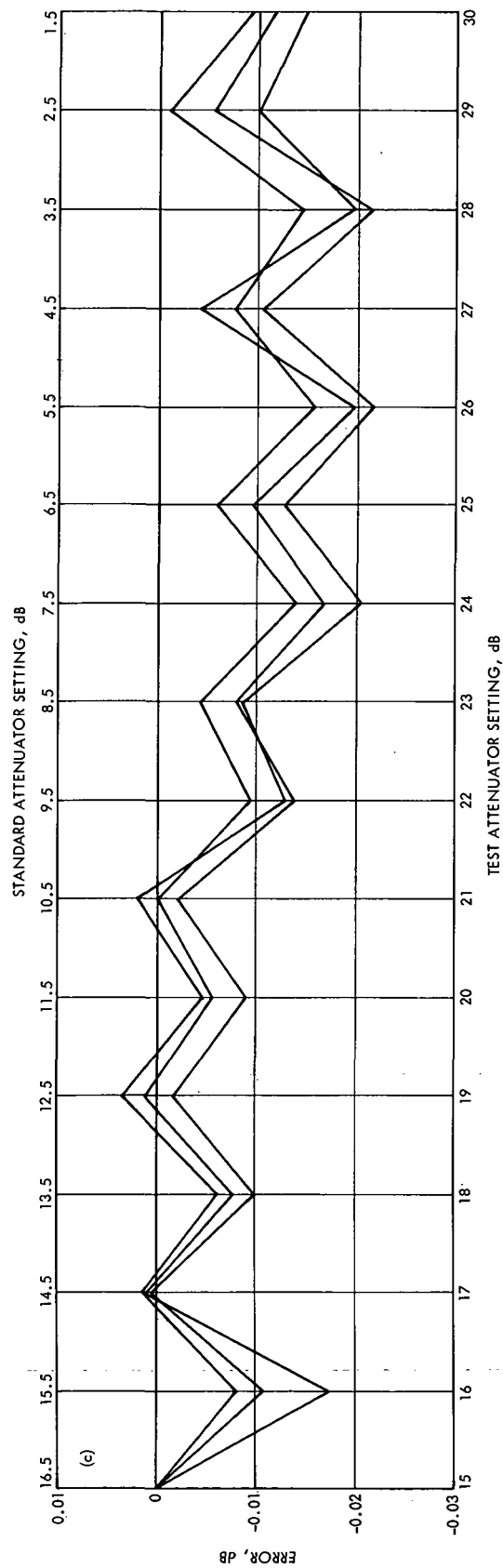


Fig. 6. (contd)

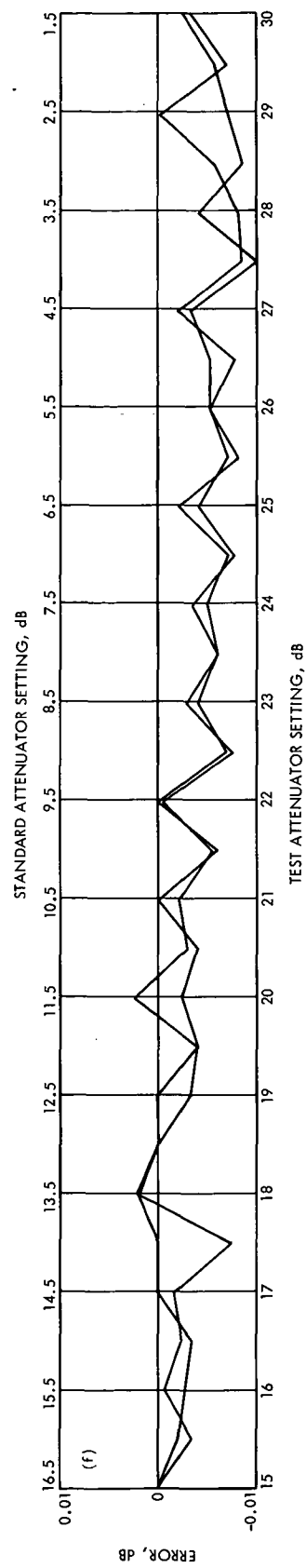
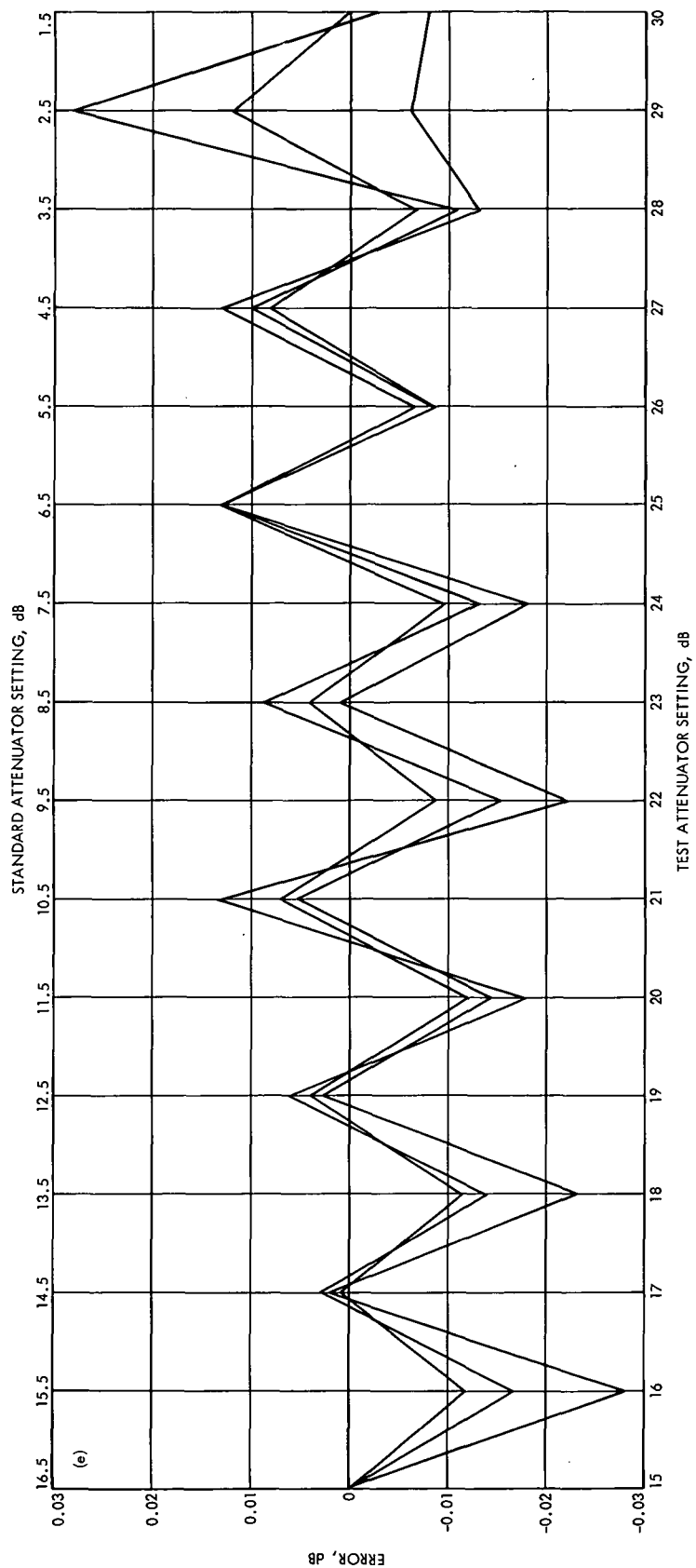


Fig. 6. (contd)

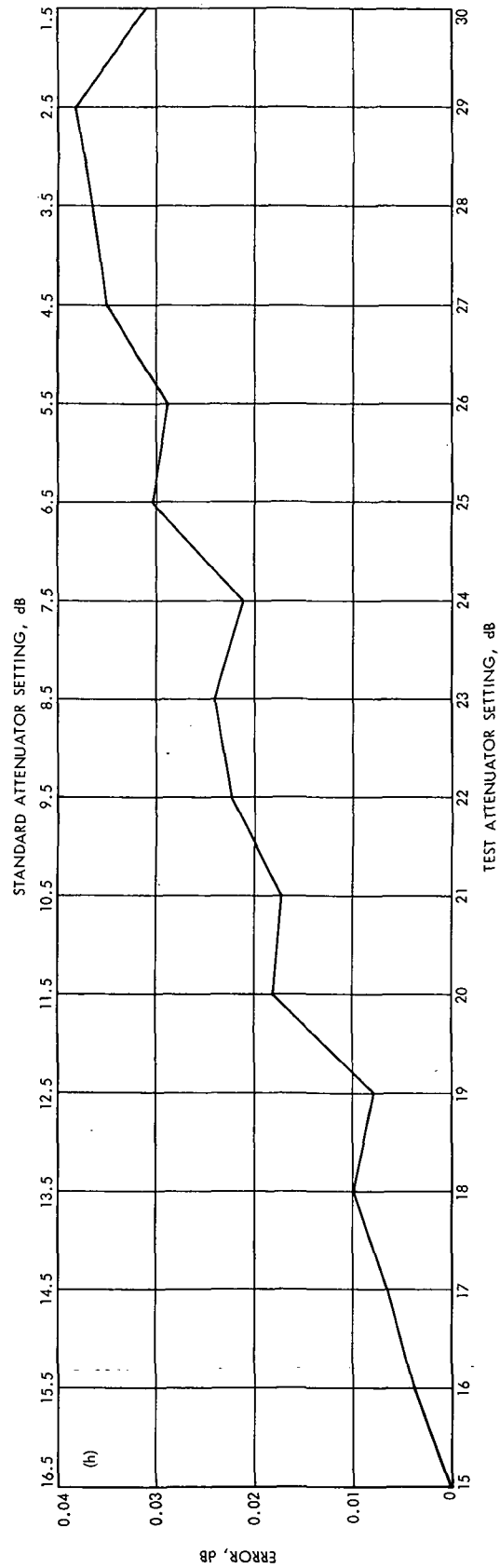
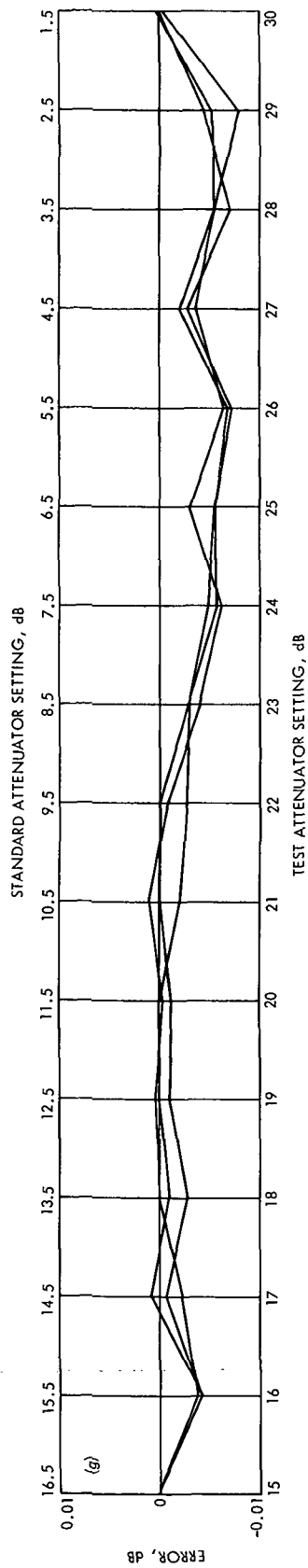


Fig. 6. (contd)

Improved RF Calibration Techniques: System Operating Noise Temperature Calibrations

M. S. Reid

Communications Elements Research Section

The system operating noise temperature performance and other calibration data of the low-noise research cones at the Goldstone Deep Space Communications Complex are reported for June 1, 1972, through September 30, 1972. The performance of the following cones is presented for this reporting period: the S-band radar operational cone at DSS 13, the S-band megawatt transmit cone at DSS 14, and the polarization diversity S-band cone at DSS 14. In addition to the above S-band calibration data, elevation profile measurements were made at fixed azimuth at 8415 MHz on the multifrequency X- and K-band cone.

The system operating noise temperature performance of the low-noise research cones at the Goldstone Deep Space Communications Complex is reported for the period of June 1, 1972, through Sept. 30, 1972. The operating noise temperature calibrations were performed with the ambient termination technique¹ (Ref. 1). System temperature calibrations were made on the following cones:

- (1) S-band radar operational (SRO) cone (and the gain standard horn) at DSS 13.
- (2) S-band megawatt transmit (SMT) cone at DSS 14.

The averaged operating noise temperature calibrations for the SRO cone (and the gain standard horn) at DSS 13,

¹Most of the measurements were taken by DSS 13 (Venus) and DSS 14 (Mars) personnel.

along with other calibration data, are summarized in Table 1. The maser in operation in the SRO cone throughout this reporting period was serial number 96S5. Measurements made with this maser connected to the gain standard horn at 2278.5 MHz are also shown in Table 1.

Averaged operating noise temperature calibrations and other calibration data are presented in Table 2 for the SMT cone at DSS 14, both in the low-noise path mode with the maser in the SMT cone (serial number 96S4) and duplexed with the maser in the Mod. 3 section (serial number 80S1). All SMT cone data were taken at 2295 MHz, with the subreflector correctly aligned.

The calibration data were reduced with JPL computer program 5841000, CTS20B. Measurement errors of each data point average are recorded under the appropriate

number in the tables. The indicated errors are the standard deviation of the individual measurements and of the means, respectively. They do not include instrumentation systematic errors. The averages were computed using only data with:

- (1) Antenna at zenith.
- (2) Clear weather.
- (3) No RF spur in the receiver passband.
- (4) Standard deviation of computed operating noise temperature due to measurement dispersion less than 0.15 K.

Figure 1 is a plot of system operating noise temperature of the SRO cone at DSS 13 as a function of time in day numbers. The frequency was 2278.5 MHz and the maser was No. 96S5. Figure 2 is a similar plot at 2388 MHz. Figures 3 and 4 show SMT cone operating noise temperatures as a function of time in day numbers, for the low-noise path (maser 96S4) and diplexed (maser 80S1), respectively. The frequency in Figs. 3 and 4 was 2295 MHz. In all these figures, data that satisfy the four conditions stated above are plotted as solid circles, while data that fail one or more conditions are plotted as open circles.

System operating noise temperatures of the polarization diversity S-band (PDS) cone are presented in Fig. 5 as a function of time. The frequency was 2295 MHz for all data. Both low-noise path and diplexed data are shown and the period covered is Jan. 1, 1972, through Sept. 30, 1972. In this figure, the averaged precision measurements reduced by computer program CTS20B have been augmented by single Y-factor numbers. Although these latter data were taken using the ambient termination method,

most of them were not reduced by computer program CTS20B, and therefore a greater time period is presented. These data were taken with the antenna at zenith, the subreflector correctly positioned in each case, but with no regard for weather conditions.

In addition to the above S-band system temperature calibrations, all of which were performed with the antenna at zenith, elevation profile measurements were made at X-band with various subreflector configurations. These data are presented in Figs. 6 and 7. In Fig. 6, system temperature is plotted as a function of elevation angle for 8415 MHz. The solid curve was obtained when the subreflector was correctly aligned on the appropriate main horn. When the subreflector was positioned on the PDS cone, the X-band radiometer yielded the dotted curve. Figure 7 is a similar plot of system temperature as a function of antenna elevation angle with the subreflector positioned on the SMT cone. In this figure, the correctly aligned subreflector data have been repeated for reference. The solid curve changes only an insignificant amount when the subreflector is switched between the X- and K-band main horns. The azimuth was fixed at 180 deg for all curves in Figs. 6 and 7, and the weather was clear and dry.

All elevation profile data were obtained with the Noise Adding Radiometer (NAR) developed at JPL (Ref. 2). System temperatures at X-band were first obtained at zenith using the ambient termination technique. Several Y-factors were computed, and an average operating noise temperature computed. This value was checked by using a microwave absorber placed over the X-band main horn. The radiometer noise diode temperature was then adjusted to calibrate the NAR.

References

1. Stelzried, C. T., "Operating Noise-Temperature Calibrations of Low-Noise Receiving System," *Microwave J.*, Vol. 14, No. 6, pp. 41-48, June 1971.
2. Batelaan, P. D., Goldstein, R. M., and Stelzried, C. T., "A Noise-Adding Radiometer for Use in the DSN," in *The Deep Space Network*, Space Programs Summary 37-65, Vol. II, pp. 66-69, Jet Propulsion Laboratory, Pasadena, Calif., Sept. 30, 1970.

Table 1. System operating noise temperature calibrations of the SRO cone (maser 96S5) and the gain standard horn (maser 96S5) on the 26-m-diameter antenna at DSS 13

Parameter	At 2278.5 MHz		At 2295 MHz	At 2388 MHz
	Gain standard horn	SRO cone		
Maser gain, dB	43.4 $\pm 0.95/0.43$ 5 measurements	43.5 $\pm 1.65/0.21$ 61 measurements	43.4 $\pm 0.78/0.56$ 2 measurements	32.0 $\pm 2.6/0.54$ 23 measurements
Follow-up receiver contribution, K	0.09 $\pm 0.01/0.003$ 5 measurements	0.27 $\pm 0.21/0.03$ 61 measurements	0.13 $\pm 0.05/0.03$ 2 measurements	0.53 $\pm 0.05/0.01$ 23 measurements
System operating noise temperature, K	30.2 $\pm 0.68/0.30$ 5 measurements	16.4 $\pm 0.50/0.07$ 61 measurements	16.2 $\pm 0.38/0.27$ 2 measurements	17.1 $\pm 0.33/0.07$ 23 measurements

Table 2. System operating noise temperature calibrations of the SMT cone at 2295 MHz on the 64-m-diameter antenna at DSS 14

Configuration	Low-noise path	Diplexed
Maser serial number	96S4	80S1
Maser gain, dB	48.1 $\pm 0.52/0.12$ 18 measurements	38.1 $\pm 2.3/0.57$ 16 measurements
Follow-up receiver contribution, K	0.18 $\pm 0.05/0.01$ 18 measurements	0.06 $\pm 0.01/0.002$ 16 measurements
System operating noise temperature, K	15.6 $\pm 0.18/0.04$ 18 measurements	26.9 $\pm 0.28/0.07$ 16 measurements

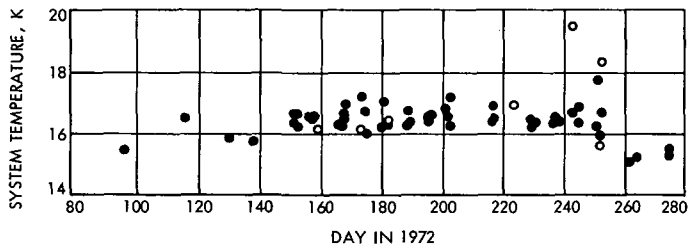


Fig. 1. System operating noise temperature calibrations of the SRO cone at 2278.5 MHz, plotted as a function of time in day numbers

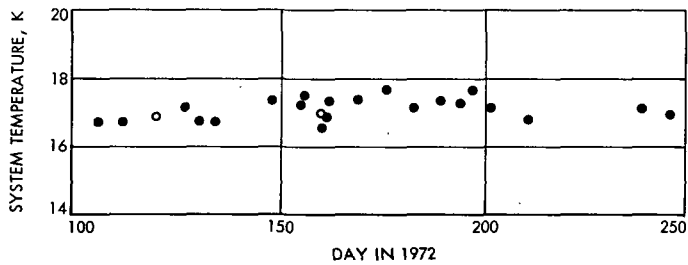


Fig. 2. System operating noise temperature calibrations of the SRO cone at 2388 MHz, plotted as a function on time in day numbers

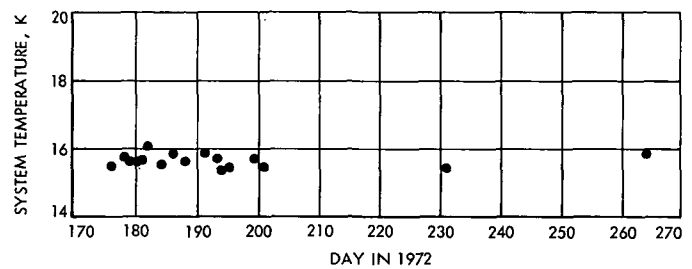


Fig. 3. System operating noise temperature calibrations of the SMT cone, low-noise path at 2295 MHz, plotted as a function of time in day numbers

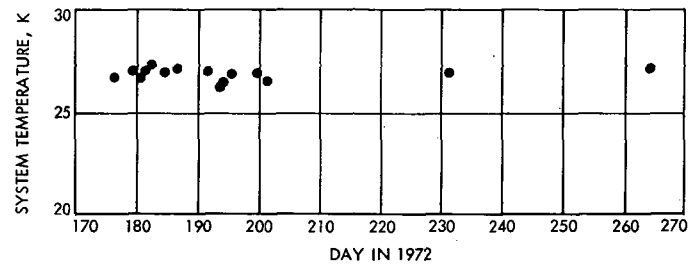


Fig. 4. System operating noise temperature calibrations of the SMT cone, diplexed at 2295 MHz, plotted as a function of time in day numbers

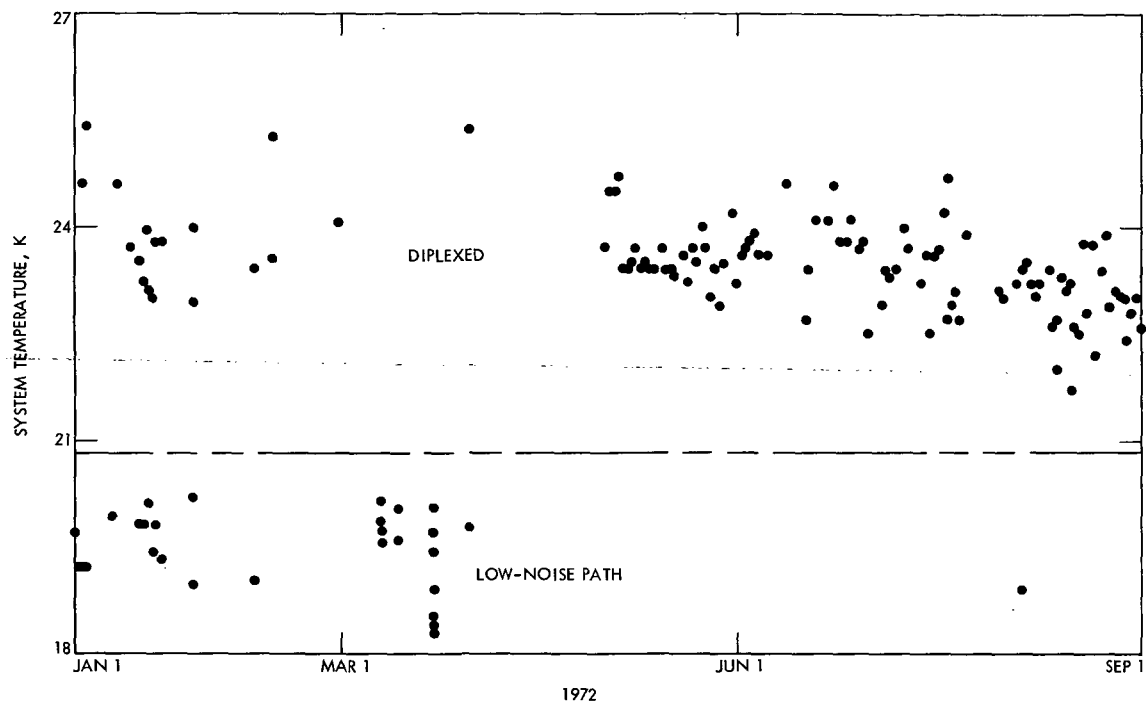


Fig. 5. System operating noise temperature calibrations of the PDS cone at 2295 MHz, both low-noise path and diplexed, plotted as a function of time in day numbers

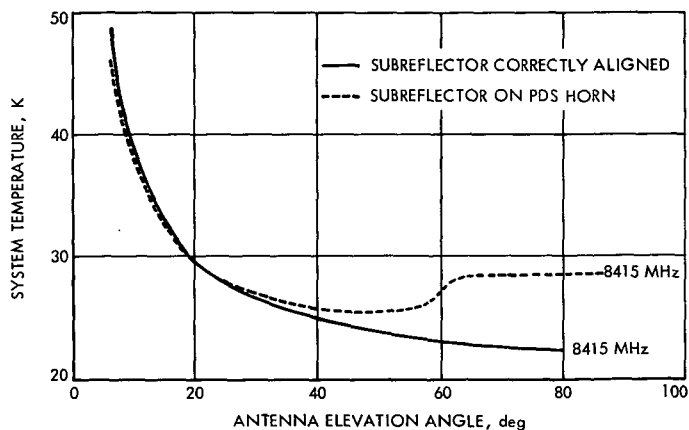


Fig. 6. System temperature elevation profiles at 8415 MHz with the subreflector correctly aligned and on the PDS horn

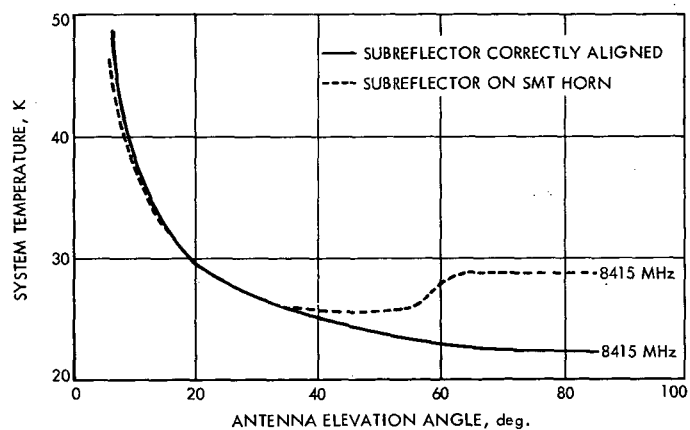


Fig. 7. System temperature elevation profiles at 8415 MHz with the subreflector correctly aligned and on the SMT horn

Optimum Noncoherent Receiver at Low Signal-to-Noise Ratio for Unknown Doppler Shifted Signals

J. K. Holmes

Communications Systems Research Section

An optimum low signal-to-noise ratio receiver is derived for the case when the received signal has unknown phase and an unknown doppler shift. This receiver appears to be new and is quite similar in form to the wideband frequency-shift-keyed receiver.

I. Introduction

The purpose of this article is to derive the optimum low-signal-to-noise ratio (SNR) noncoherent receiver when an unknown doppler shift is present on the received signal. This work was part of a low-data-rate receiver system study, with a possible application to Pioneer Venus.

The receiver derived here appears to be new and is quite similar to the existing noncoherent receiver (wideband frequency-shift-keyed (FSK) receiver) that has been used previously in radar systems as well as space telemetry applications where doppler is present. The wideband FSK receiver has two bandpass filters centered at the two possible transmitted tones and is wide enough in bandwidth to cover all possible doppler shifts. Following the

filters, a square-law detector (or a linear envelope detector) is used, which is, in turn, fed into an integrate-and-dump circuit. The system is shown in Fig. 1 in a realization useful for comparing with the receiver developed in this article.

II. Signal Model

We now consider the signal model used to develop the optimum receiver. Motivated by the interest in low-data-rate systems, we consider an assumed received signal of the form

$$y(t) = A \sin [\omega_0 t + \Omega_j t + \omega t + \phi] + n(t) \\ 0 \leq t < T, \quad j = 1, 2 \quad (1)$$

where A is the received signal amplitude, ω_0 is the center frequency, Ω_j is the known frequency offset corresponding to signal j , ω is the unknown doppler offset frequency, ϕ is the unknown phase of the received signal, and $n(t)$ is white Gaussian noise with two-sided spectral density $N_0/2$. We assume that the time of occurrence of the received signal is known exactly.

In order to proceed with the receiver derivation, some assumption about the unknown doppler frequency and phase must be made. We assume here that ω is a random variable having a density function given by

$$p(\omega) = \frac{1}{2\omega_u} \quad -\omega_u \leq \omega < \omega_u \quad (2)$$

where ω_u is the maximum assumed value of the doppler shift. In addition we assume that ϕ is a uniform random

variable on the interval $[-\pi, \pi]$. The optimum detection system is determined from the *a posteriori* probability that signal j was sent, given that $y(t)$ has been received, i.e., $P[j|y(t)]$. This can be obtained by computing $P(j|y(t), \phi, \omega)$ and averaging over ϕ and ω .

It has been shown by Viterbi (Ref. 1) and elsewhere that

$$P[j|y(t), \phi, \omega] = c \exp \left[\frac{2A}{N_0} \int_0^T y(t) \sin[\omega_0 t + \phi + \omega t + \Omega_j t] dt \right] \quad (3)$$

where c is a constant independent of j . Now with the assumption that the phase ϕ is uniform in $[-\pi, \pi]$ we have the result that

$$P[j|y(t)] = c \int_{-\omega_u}^{\omega_u} \int_{-\pi}^{\pi} \frac{1}{2\pi} \exp \left[\frac{2A}{N_0} \int_0^T y(t) \sin[\omega_0 t + \omega t + \Omega_j t + \phi] dt \right] d\phi p(\omega) d\omega \quad (4)$$

After making some algebraic manipulations and integrating on ϕ , we have

$$P[j|y(t)] = c \int_{-\omega_u}^{\omega_u} I_0 \left[\frac{2A}{N_0} \sqrt{\int_0^T \int_0^T y(t) y(s) \cos[\omega_0(t-s) + \Omega_j(t-s) + \omega(t-s)] dt ds} \right] p(\omega) d\omega \quad (5)$$

This result has been previously obtained using complex notation, by Ferguson (Ref. 2); however, he did not pursue this result to obtain the structure of the receiver other than to assert that at low signal-to-noise ratios it was quadratic. Equation (5) appears impossible to evaluate in closed form; however, with the assumption that we are concerned only with low signal-to-noise ratios, Eq. (5) with the use of Eq. (2) can be written as

$$P[j|y(t)] \cong c \left\{ 1 + \left(\frac{A}{N_0} \right)^2 \frac{1}{2\omega_u} \int_0^T \int_0^T y(t) y(s) \int_{-\omega_u}^{\omega_u} \cos[\omega_0(t-s) + \Omega_j(t-s) + \omega(t-s)] d\omega dt ds \right\} \quad (6)$$

Performing the integration on ω yields

$$P[j|y(t)] = c + \left(\frac{A}{N_0} \right)^2 c \int_0^T \int_0^T y(t) y(s) \cos[\omega_0(t-s) + \Omega_j(t-s)] \frac{\sin \omega_u(t-s)}{\omega_u(t-s)} dt ds \quad (7)$$

This result has been obtained by Raemer (Ref. 3), but the system to obtain the result was not given. A system that will perform the operation prescribed by Eq. (7) is given in Fig. 2.

In Fig. 2, $h_1(\tau)$ and $h_2(\tau)$ are the impulse responses and are given by

$$\left. \begin{aligned} h_1(\tau) &= \cos[\omega_0 \tau + \Omega_1 \tau] \frac{\sin \omega_u \tau}{\omega_u \tau}, & \text{for all } \tau \\ h_2(\tau) &= \cos[\omega_0 \tau + \Omega_2 \tau] \frac{\sin \omega_u \tau}{\omega_u \tau}, & \text{for all } \tau \end{aligned} \right\} \quad (8)$$

Since $h_1(\tau) \neq 0$ for all negative τ , we see that the receiver is not realizable. The transfer functions $H_1(f)$ and $H_2(f)$ associated with $h_1(\tau)$ and $h_2(\tau)$ are ideal bandpass filters. The structure of the ideal system is similar to the wide-band FSK receiver except that only one filter per tone is used instead of two. The filtered signal branch can be viewed as an estimator of the incoming signal frequency

so as to provide a phase- and frequency-coherent demodulation reference.

This optimum receiver requires ideal bandpass filters which introduce no delay in the signal. "Real" filters would introduce some delay but this delay could be equalized with a resulting increase in circuit complexity. Without delay compensation, the performance would be degraded.

We now show that if $\omega_u = 0$ the resulting receiver is the usual noncoherent receiver. Letting $\omega_u = 0$ in Eq. (7) and neglecting the constants, one has

$$D_j = \iint_0^T y(t) y(s) \cos [\omega_0(t-s) + \Omega_j(t-s)] dt ds \quad (9)$$

Expanding the cosine, we have

$$D_j = \left(\int_0^T y(t) \cos(\omega_0 t + \Omega_j t) dt \right)^2 + \left(\int_0^T y(t) \sin(\omega_0 t + \Omega_j t) dt \right)^2 \quad (10)$$

which is the optimum decision statistic for all signal-to-noise ratios for the noncoherent receiver with zero doppler offset.

The ordinary noncoherent receiver can be constructed using a system similar to Fig. 2. From Eq. (9) we see that the system of Fig. 1 can be used if $h_1(\tau)$ and $h_2(\tau)$ are defined as (noting that the system will be unrealizable)

$$\left. \begin{aligned} h_1(\tau) &= \cos(\omega_0 + \Omega_1)\tau, & \text{for all } \tau \\ h_2(\tau) &= \cos(\omega_0 + \Omega_2)\tau, & \text{for all } \tau \end{aligned} \right\} \quad (11)$$

The spectrum associated with each impulse response of Eq. (11) is a pair of delta functions occurring at $\pm(\omega_0 + \Omega_1)$ and $\pm(\omega_0 + \Omega_2)$ respectively. In other words, only the component of energy exactly at $\omega_0 + \Omega_1$ and $\omega_0 + \Omega_2$ is passed to provide the reference.

Equation (6) can be rewritten to show that the optimum low signal-to-noise ratio system requires the computation of S_i ; $i = 1, 2$, where S_i is given by

$$S_i = \int_{-\omega_u}^{\omega_u} \left\{ \left(\int_0^T y(t) \cos[(\omega_0 + \Omega_i + \omega)t] dt \right)^2 + \left(\int_0^T y(t) \sin[(\omega_0 + \Omega_i + \omega)t] dt \right)^2 \right\} \frac{1}{2\omega_u} d\omega$$

that is, the optimum low-SNR receiver with unknown doppler shift that can be viewed as a system to form spectral coefficients weighted with a uniform weighting.

References

1. Viterbi, A. J., *Principles of Coherent Communication*, McGraw-Hill, 1966.
2. Ferguson, M. J., "Communication at Low Data Rates—Oscillator Models and Corresponding Optimal Receivers," *IEEE Trans. Commun. Technol.*, Aug. 1968.
3. Raemer, H. R., *Statistical Communication Theory and Applications*, Section 7.1.4, Prentice-Hall, 1969.

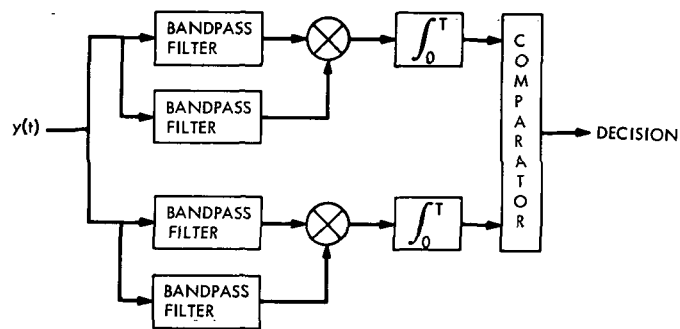


Fig. 1. Existing wideband FSK receiver

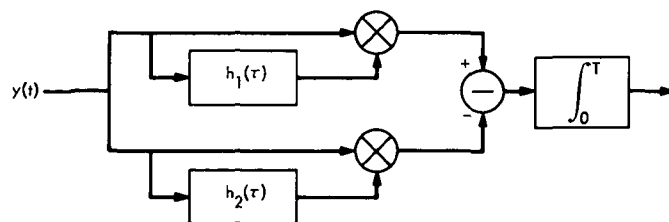


Fig. 2. Optimum low-SNR doppler-ambiguous receiver

Optimum Frame Sync Acquisition for Biorthogonally Coded Telemetry

B. K. Levitt

Communications Systems Research Section

An optimum frame sync algorithm for biorthogonally coded telemetry is described. This algorithm takes the coding into account and therefore performs significantly better than algorithms derived for uncoded telemetry, for only a slight increase in implementation complexity.

I. Introduction

As part of the overall task of guaranteeing a given level of telemetry link performance to NASA planetary projects, the problem of acquiring frame synchronization for biorthogonally coded data was investigated. The results of this study can also be applied to the Network Control System (NCS), where master telemetry frames must be stripped to obtain key spacecraft engineering measurements for retransmission to the DSIF stations, and to the Mission Control and Computing Center (MCCC).

In past planetary missions, frame synchronization has been achieved by detecting the periodic peaks of the cross correlation between the known binary frame sync sequence and the decoded bit stream. Because this cross correlation is based on the binary Hamming distance metric, the probability of false sync acquisition is minimized by selecting binary frame sync sequences with highly peaked autocorrelation functions, such as Barker and pseudonoise (PN) sequences.

This approach to the problem of frame sync acquisition is optimum for uncoded telemetry, where successive bit errors in the received bit stream are statistically independent. However, it is not optimum for coded telemetry because it does not take account of the existence of multiple bit error patterns in the decoded data as a result of statistically independent word errors. Despite this incongruency, frame sync acquisition algorithms based on the Hamming distance metric have continued to be used on Mariner missions with telemetry modes employing a (32,6) biorthogonal code.

To alleviate this situation, a frame sync procedure based on a word distance metric is proposed. It is argued heuristically below that this approach is optimum for biorthogonally coded data with regard to minimizing the probability of false sync acquisition. For this design criterion, the superiority of the word distance metric over the Hamming distance metric is demonstrated analytically. Although the frame sync problem is discussed below

in the specific context of the Mariner (32,6) biorthogonal code, the results can readily be extended to include any biorthogonal or orthogonal code.

II. Discussion

The problem of acquiring frame synchronization for binary phase-shift-keyed (PSK) telemetry modes employing a (32,6) biorthogonal code is examined below. The scope of the discussion is limited to the special case in which each frame contains N complete 6-bit words, including a frame sync prefix of K complete words. (The general case wherein the frame sync sequence and the frame itself do not contain integral numbers of words results in a more complicated optimum frame sync acquisition algorithm.) It is implicitly assumed below that word synchronization is correctly established prior to the application of the frame sync acquisition algorithm, so that only $\frac{1}{2}$ of the decoded data bits need be considered as possible starting locations for the received frame sync sequences.

Suppose frame synchronization is to be acquired by processing an arbitrary, contiguous span of N decoded words in order to locate the received sync sequence contained therein. If the frame sync decision is actually to be based on n such spans, the problem reduces to the above for a frame length of nN words and a sync sequence composed of nK noncontiguous words. The frame sync sequence will be denoted by the binary $6K$ -tuple $\mathbf{s} = (s_0, s_1, \dots, s_{K-1})$, where each s_i is a word. The span of N decoded words used to determine frame synchronization will be represented by the binary sequence $\mathbf{r} = (r_0, r_1, \dots, r_{N-1})$, where each r_i is a decoded word.

Define the m th K -word decoded segment

$$\mathbf{p}_m = (\mathbf{r}_m, \mathbf{r}_{m+1}, \dots, \mathbf{r}_{m+K-1})$$

where the subscripts are modulo N , and $0 \leq m \leq N - 1$. The objective is to determine which of the N segments \mathbf{p}_m is the most likely received frame sync sequence. In order to compare each \mathbf{p}_m with the frame sync sequence \mathbf{s} , the binary error sequence

$$\mathbf{e}_m = (\mathbf{e}_{0,m}, \mathbf{e}_{1,m}, \dots, \mathbf{e}_{K-1,m})$$

is formed, wherein the i th error word $\mathbf{e}_{i,m}$ is the bit-by-bit modulo 2 sum of s_i and \mathbf{r}_{m+i} . An appropriate frame sync metric to operate on each error sequence \mathbf{e}_m must now be devised. To this end, the probability distribution of \mathbf{e}_m^*

will now be examined, where \mathbf{p}_m^* is the actual received frame sync sequence.

When a binary PSK signal is demodulated using a carrier reference derived from the modulated signal, there is a binary phase ambiguity in the detector output: that is, the output of the block decoder can be data or inverted data ($\overline{\text{data}}$) with equal probability. Therefore, in the absence of any errors in \mathbf{p}_m^* due to noise, \mathbf{e}_m^* will contain all 0's or all 1's with probability $1/2$. This phase ambiguity is resolved when frame sync is established, according to whether \mathbf{p}_m^* resembles \mathbf{s} or $\overline{\mathbf{s}}$. For the (32,6) biorthogonal code, conditioned on data or $\overline{\text{data}}$ at the decoder output, the $\mathbf{e}_{i,m}^*$'s are statistically independent random binary 6-tuples with probability distributions

$$\Pr [\mathbf{e}_{i,m}^* | \text{data}] = \begin{cases} 1 - \epsilon_w; & \mathbf{e}_{i,m}^* = \mathbf{0} \\ \epsilon'; & \mathbf{e}_{i,m}^* = \mathbf{1} \\ \frac{1}{62}(\epsilon_w - \epsilon'); & \mathbf{e}_{i,m}^* \neq \mathbf{0}, \mathbf{1} \end{cases} \quad (1)$$

$$\Pr [\mathbf{e}_{i,m}^* | \overline{\text{data}}] = \begin{cases} 1 - \epsilon_w; & \mathbf{e}_{i,m}^* = \mathbf{1} \\ \epsilon'; & \mathbf{e}_{i,m}^* = \mathbf{0} \\ \frac{1}{62}(\epsilon_w - \epsilon'); & \mathbf{e}_{i,m}^* \neq \mathbf{0}, \mathbf{1} \end{cases} \quad (2)$$

where $\mathbf{0}$ is the 6-tuple containing all 0's, and $\mathbf{1}$ is similarly defined. In Eqs. (1) and (2), ϵ_w is the probability that a transmitted 6-bit word is incorrectly decoded, and, in particular, ϵ' is the probability that it is decoded to its complement, conditioned on the detection of data. Typically, ϵ' is sufficiently small that it can be neglected; for example, when $\epsilon_w \sim 0.5$, $\epsilon'/\epsilon_w \sim 10^{-5}$, and ϵ'/ϵ_w decreases monotonically as ϵ_w decreases. The assumption that ϵ' is in fact negligible is made in the work that follows.

Because ϵ_w is generally small, it is evident from Eq. (1) that, when the detector output is data, the probability that $\mathbf{e}_{i,m}^*$ is $\mathbf{0}$ is much greater than the probability that $\mathbf{e}_{i,m}^*$ is a particular mixed pattern of 0's and 1's. A similar statement can be made for the case where the detector output is $\overline{\text{data}}$.

Therefore, conditioned on the detection of data, most of the error words in \mathbf{e}_m^* can be expected to be 0's, with a small number of mixed error patterns; for the case of $\overline{\text{data}}$, most of the error words will be 1's, with some mixed patterns. Under the earlier assumption that ϵ' is negligible, \mathbf{e}_m^* cannot contain both 0's and 1's.

As shown in Eqs. (1) and (2), e_{i,m^*} has an equal probability of being any of the 62 mixed patterns of 0's and 1's. As a particular example,

$$\Pr [e_{i,m^*} = 000100] = \Pr [e_{i,m^*} = 011111] \cong \frac{\varepsilon_w}{62} \quad (3)$$

whether the detector output is data or $\overline{\text{data}}$. Conditioned on the detection of data, a frame sync acquisition algorithm based on the Hamming distance metric will be more likely to select p_{m^*} as the received frame sync sequence if a particular sync word error e_{i,m^*} is 000100 than if it is 011111. However, this is clearly not optimal since these two sync word error patterns are equally likely.

Because sync *word* errors are statistically independent, conditioned on data or $\overline{\text{data}}$ at the decoder output, whereas sync *bit* errors are not, the optimum frame sync acquisition algorithm should be based on a *word* distance metric. Furthermore, from the arguments above, it is evident that this metric should flag those word errors $e_{i,m}$ within a given error sequence e_m which are mixed patterns of 0's and 1's, treating all mixed word error patterns equally. Finally, under the assumption that ε' is negligible, the word distance metric should eliminate from consideration those indices m for which e_m contains both 0's and 1's. To this end, define the word distance 'metric' $C(e_m)$ to have the value $K + 1$ if e_m contains both 0's and 1's, and to be the number of mixed word error patterns in e_m otherwise. (Actually $C(e_m)$ is not a true metric because it does not satisfy the triangle inequality; however, it will still be referred to as a metric in a looser sense below.) Based on this metric, the following frame sync acquisition algorithm can be applied to the decoded sequence r :

- (1) For each index m in the range $0 \leq m \leq N - 1$, form the error sequence e_m .
- (2) Decide that $p_{\hat{m}}$ is the received sync sequence if \hat{m} is the index m that minimizes $C(e_m)$.
- (3) Decide that the decoder output is data if e_m contains 0's; otherwise, decide that the decoder output is $\overline{\text{data}}$.

Using a more rigorous mathematical derivation, it has been verified that this frame sync acquisition algorithm is optimum in the sense that it minimizes the probability of false synchronization, based on the observable r , for a given sync sequence s . And with respect to this algorithm, there is no longer any advantage to selecting a frame sync sequence with good autocorrelation properties relative to the binary Hamming distance metric. Allowing for the possibility of data or $\overline{\text{data}}$ at the decoder output, one can argue that the optimum s is any sequence in which the K 6-bit sync words s_i have mutually orthogonal 32-symbol code words.

III. Analysis

It has been argued above that for biorthogonally coded telemetry, a frame sync acquisition algorithm based on a word distance metric achieves the lowest probability of false synchronization. The next question of interest is how much better this optimum algorithm performs than other frame sync acquisition algorithms. As a partial measure of the superiority of the word distance metric algorithm, a union bound argument will now be used to compare its performance with that of a frame sync acquisition algorithm based on the Hamming distance metric. For convenience, these two algorithms will frequently be identified below by the terms "word metric algorithm" and "bit metric algorithm."

First consider the performance of the word metric algorithm using previously defined notation. Suppose p_{m^*} is the actual received frame sync sequence: then the word distance metric $C(e_{m^*})$ has the probability distribution

$$\Pr [C(e_{m^*}) = \gamma] = \binom{K}{\gamma} \varepsilon_w^\gamma (1 - \varepsilon_w)^{K-\gamma}; \quad 0 \leq \gamma \leq K \quad (4)$$

where ε_w is the word error rate. For those received segments p_m which do not overlap p_{m^*} , the word errors within the error sequence e_m each have an equal probability of being any of the 64 binary 6-tuples: the corresponding metric $C(e_m)$ has the probability distribution

$$\Pr [C(e_m) = \mu] = \begin{cases} 2 \binom{K}{\mu} \left(\frac{62}{64}\right)^\mu \left(\frac{1}{64}\right)^{K-\mu}; & 0 \leq \mu \leq K - 1 \\ \left(\frac{62}{64}\right)^K; & \mu = K \\ p_e; & \mu = K + 1 \end{cases} \quad (5)$$

The factor 2 in the first part of Eq. (5) is due to the possibility of data or $\overline{\text{data}}$ at the decoder output. The probability p_e that $C(e_m)$ will be $K + 1$, so that the index m will be eliminated from consideration, can be shown to equal $1 + (62/64)^K - 2(63/64)^K$; however, it does not enter directly into the calculations below. The frame sync acquisition algorithm computes $C(e_m)$ over the range $0 \leq m \leq N - 1$ seeking the index m for which $C(e_m)$ is minimized. The probability P_{FW} of false synchronization is simply the probability that one or more of the $C(e_m)$'s, for $m \neq m^*$, is less than $C(e_{m^*})$. Using the familiar union bounding technique,

$$P_{FW} = \Pr \left[\bigcup_{\substack{m=0 \\ m \neq m^*}}^{N-1} C(e_m) < C(e_{m^*}) \right] \leq \sum_{\substack{m=0 \\ m \neq m^*}}^{N-1} \Pr [C(e_m) < C(e_{m^*})] \quad (6)$$

For the $N - 2K + 1$ nonoverlapping indices m defined above, $C(e_m)$ and $C(e_{m^*})$ are statistically independent random variables; then Eqs. (4) and (5) can be used to show that

$$P_w \equiv \Pr [C(e_m) < C(e_{m^*})] = 2 \sum_{\gamma=1}^K \binom{K}{\gamma} \epsilon_w^\gamma (1 - \epsilon_w)^{K-\gamma} \sum_{\mu=0}^{\gamma-1} \binom{K}{\mu} \left(\frac{62}{64}\right)^\mu \left(\frac{1}{64}\right)^{K-\mu} \quad (7)$$

For the $2K - 2$ overlapping indices m (excluding m^*), the probability that $C(e_m)$ is less than $C(e_{m^*})$ depends on the choice of the frame sync sequence s . If the sync words contained within s have mutually orthogonal code words, as recommended earlier, a particular ρ_m that overlaps ρ_{m^*} should be less likely to resemble s on a word distance basis than a totally random, nonoverlapping ρ_m . Then

$$\Pr [C(e_m) < C(e_{m^*})] \leq P_w \quad (8)$$

for the overlapping indices. Combining Eqs. (6-8) yields the result

$$P_{FW} \leq (N - 1) P_w \quad (9)$$

The upper bound in Eq. (9) is tight when P_w is small, which occurs when ϵ_w is small.

Next, consider the performance of the bit metric algorithm. The Hamming weight of the binary $6K$ -tuple e_m , denoted by $H(e_m)$, is defined as the number of 1's in e_m . Then the Hamming distance between s and a given ρ_m is given by $H(e_m)$. If the decoder output were known *a priori* to be data, the bit metric algorithm would choose m to minimize $H(e_m)$. Because there is an equal probability of having data or $\overline{\text{data}}$, a large value of $H(e_m)$ should be regarded as favorably as a small value of $H(e_m)$. Therefore, the frame sync acquisition algorithm should choose m to maximize the normalized bit distance $B(e_m)$, defined according to

$$B(e_m) \equiv |3K - H(e_m)| \quad (10)$$

It is easier to calculate the distribution of $B(e_m)$ indirectly, by first finding the distribution of $H(e_m)$, and then using the formula

$$\Pr [B(e_m) = \mu] = \begin{cases} \Pr [H(e_m) = 3K]; & \mu = 0 \\ \Pr [H(e_m) = 3K - \mu] \\ + \Pr [H(e_m) = 3K + \mu]; & 1 \leq \mu \leq 3K \end{cases} \quad (11)$$

Regarding the data/ $\overline{\text{data}}$ ambiguity, it is evident that

$$\Pr [H(e_m) = \gamma | \overline{\text{data}}] = \Pr [H(e_m) = 6K - \gamma | \text{data}] \quad (12)$$

From Eqs. (11) and (12), one can show that the distribution of $B(e_m)$ conditioned on the presence of data is identical to that conditioned on $\overline{\text{data}}$, so that

$$\Pr [B(e_m) = \mu] = \Pr [B(e_m) = \mu | \text{data}] \quad (13)$$

That is, the distribution of $H(e_m)$ for the case of data is sufficient to determine the distribution of $B(e_m)$ averaged over the occurrence of data and $\overline{\text{data}}$.

It is generally assumed that the transmitted data (excluding the sync words) can be regarded as a stream of statistically independent, equally likely 1's and 0's. Consequently, the ρ_m 's which do not overlap ρ_{m^*} consist of a sequence of K independent, equally likely bits; therefore, for these indices,

$$\Pr [H(e_m) = \eta | \text{data}] = \binom{6K}{\eta} \left(\frac{1}{64}\right)^\eta; \quad 0 \leq \eta \leq 6K \quad (14)$$

Applying Eqs. (11) and (13), it is clear that for these indices,

$$\Pr [B(\mathbf{e}_m) = \mu] = \begin{cases} \binom{6K}{3K} \left(\frac{1}{64}\right)^K; & \mu = 0 \\ 2 \binom{6K}{3K - \mu} \left(\frac{1}{64}\right)^K; & 1 \leq \mu \leq 3K \end{cases} \quad (15)$$

The distribution of $H(\mathbf{e}_m^*)$ is more difficult to derive; it is computed in the Appendix to have the form

$$\begin{aligned} \Pr [H(\mathbf{e}_m^*) = \eta \mid \text{data}] \\ = \sum_{\gamma=0}^K \binom{K}{\gamma} A_{\eta,\gamma} \left(\frac{\epsilon_w}{62}\right)^\gamma (1 - \epsilon_w)^{K-\gamma}; \quad 0 \leq \eta \leq 5K \end{aligned} \quad (16)$$

where the factor $A_{\eta,\gamma}/(62)^\gamma$ is the probability of having a total of η bit errors within a sequence of γ incorrectly de-

coded 6-bit words. Under the assumption that ϵ' is negligible in Eq. (1), $A_{\eta,\gamma}$ is nonzero only in the range $\gamma \leq \eta \leq 5\gamma$, and this explains the range in Eq. (16). It is shown in the appendix that $A_{\eta,\gamma}$ satisfies the following recursive formula:

$$A_{\eta,0} = \begin{cases} 1; & \eta = 0 \\ 0; & \text{elsewhere} \end{cases} \quad A_{\eta,1} = \begin{cases} \binom{6}{\eta}; & 1 \leq \eta \leq 5 \\ 0; & \text{elsewhere} \end{cases}$$

for $\gamma \geq 2$,

$$A_{\eta,\gamma} = \begin{cases} \sum_{\mu=\max(\eta-5, \gamma-1)}^{\min(\eta-1, 5\gamma-5)} A_{\mu,\gamma-1} A_{\eta-\mu,1}; & \gamma \leq \eta \leq 5\gamma \\ 0; & \text{elsewhere} \end{cases} \quad (17)$$

Combining Eqs. (11), (13), and (16), the distribution of $B(\mathbf{e}_m^*)$ is found to have the form

$$\Pr [B(\mathbf{e}_m^*) = \xi] = \begin{cases} \sum_{\gamma=1}^K \binom{K}{\gamma} A_{3K,\gamma} \left(\frac{\epsilon_w}{62}\right)^\gamma (1 - \epsilon_w)^{K-\gamma}; & \xi = 0 \\ \sum_{\gamma=0}^K \binom{K}{\gamma} (A_{3K-\xi,\gamma} + A_{3K+\xi,\gamma}) \left(\frac{\epsilon_w}{62}\right)^\gamma (1 - \epsilon_w)^{K-\gamma} & 1 \leq \xi \leq 3K \end{cases} \quad (18)$$

The probability P_{FB} of false sync acquisition for the bit metric algorithm can now be upperbounded using Eqs. (15) and (18). Making the same assumptions concerning the overlapping and nonoverlapping indices m as in the case of the word metric algorithm, with the proviso that the sync word is a Barker or PN sequence now, it can be shown that

$$P_{FB} \leq (N-1) P_B \quad (19)$$

where P_B is the probability that $B(\mathbf{e}_m)$ exceeds $B(\mathbf{e}_m^*)$ for a nonoverlapping index m :

$$P_B = \Pr [B(\mathbf{e}_m) > B(\mathbf{e}_m^*)]$$

$$\begin{aligned} &= \frac{2}{(64)^K} \sum_{\gamma=1}^K \binom{K}{\gamma} \left(\frac{\epsilon_w}{62}\right)^\gamma (1 - \epsilon_w)^{K-\gamma} \left[A_{3K,\gamma} \sum_{\eta=0}^{3K-1} \binom{6K}{\eta} \right. \\ &\quad \left. + \sum_{\alpha=1}^{3K-1} A_{\alpha,\gamma} \sum_{\eta=0}^{\alpha-1} \binom{6K}{\eta} + \sum_{\beta=3K+1}^{6K-1} A_{\beta,\gamma} \sum_{\eta=0}^{6K-1-\beta} \binom{6K}{\eta} \right] \end{aligned} \quad (20)$$

Assuming the bounds in Eqs. (9) and (19) are tight, the superiority of the word metric algorithm over the bit metric algorithm is demonstrated by showing that $P_B/P_W > 1$ for any given K and ϵ_w . For example, Eqs. (7), (17), and (20) can be used to show that for $K = 1$,

$$\begin{aligned} P_W &= \frac{1}{32} \epsilon_w \\ P_B &= \frac{331}{(31)(32)} \epsilon_w \\ \Downarrow \\ \therefore \frac{P_B}{P_W} &= \frac{331}{31} = 10.68, \text{ for all } \epsilon_w \end{aligned} \quad (21)$$

and for $K = 2$,

$$\begin{aligned} P_W &= \frac{4}{(64)^2} \epsilon_w + \frac{246}{(64)^2} \epsilon_w^2 \\ P_B &= \frac{44,120}{(62)(64)^2} \epsilon_w + \frac{3,281,316}{(62)^2 (64)^2} \epsilon_w^2 \\ \Downarrow \\ \therefore \frac{P_B}{P_W} &= \frac{2,735,440 + 3,281,316 \epsilon_w}{15,376 + 945,624 \epsilon_w} \\ &= \begin{cases} 27.87; & \epsilon_w = 0.1 \\ 111.48; & \epsilon_w = 0.01 \\ 177.90; & \epsilon_w \rightarrow 0 \end{cases} \end{aligned} \quad (22)$$

For small ϵ_w , the following approximations are useful:

$$P_W \cong \frac{2K}{(64)^K} \epsilon_w \quad (23)$$

$$P_B \cong \begin{cases} \frac{331}{(31)(32)} \epsilon_w; & K = 1 \\ \frac{2K}{(62)(64)^K} (324K^4 + 432K^3 + 459K^2 + 246K + 62) \epsilon_w; & K \geq 2 \end{cases} \quad (24)$$

$$\Downarrow \\ \lim_{\epsilon_w \rightarrow 0} \frac{P_B}{P_W} = \begin{cases} \frac{331}{31}; & K = 1 \\ \frac{324K^4 + 432K^3 + 459K^2 + 246K + 62}{62}; & K \geq 2 \end{cases} \quad (25)$$

The limit of P_B/P_W as ϵ_w approaches zero is tabulated below for $1 \leq K \leq 5$. The results indicate that the word metric algorithm greatly outperforms the bit metric algorithm for small word error rates.

K	$\lim_{\epsilon_w \rightarrow 0} \frac{P_B}{P_W}$
1	1.068×10^1
2	1.779×10^2
3	6.910×10^2
4	1.919×10^3
5	4.343×10^3

IV. Conclusion

The problem of acquiring frame synchronization for biorthogonally coded telemetry was investigated. To minimize the probability of false synchronization, the optimum frame sync acquisition algorithm, which must operate on the decoded data, uses a word distance metric rather than the Hamming distance metric to locate the received frame sync sequence.

The optimum word metric algorithm was developed heuristically for the particular case in which each frame contains N complete words, including a frame sync prefix of K words. With respect to this algorithm, the optimum frame sync sequence is one in which the K sync words have mutually orthogonal code words.

The Mariner and Viking projects use telemetry modes employing a (32,6) biorthogonal code. For this specific case, the performance of the optimum word metric algorithm was compared analytically with the optimum frame sync acquisition algorithm based on the Hamming distance metric. It was demonstrated that the word metric algorithm is superior, particularly for large K and small word error rates.

For biorthogonally coded telemetry modes with non-integer values of N and K , as in the 1973 Mariner Venus Mercury mission, the optimum frame sync acquisition algorithm is generally more complicated than the word

metric algorithm considered in this report. Consequently, implementation considerations may dictate the use of a suboptimum algorithm based on the Hamming distance metric in this case.

It is recommended that future flight projects use integer values of N and K on biorthogonally coded telemetry modes so that optimum frame sync procedures can be easily employed. Furthermore, it should be stressed that improved performance is obtained when frame sync decisions are based jointly on several frames of decoded data, the number of frames being limited by the available storage capacity.

Appendix

Bit Error Distribution for (32,6) Biorthogonally Coded Telemetry

Suppose a sequence of K 6-bit words $s = (s_1, s_2, \dots, s_K)$ is transmitted over a communication link employing a (32,6) biorthogonal code. Because of additive channel noise, the resulting decoded sequence of K 6-bit words $r = (r_1, r_2, \dots, r_K)$ does not in general equal the transmitted sequence s . A binary error sequence

$$e = (e_1, e_2, \dots, e_K)$$

can be formed, where e_i is the modulo 2 sum of s_i and r_i : 1's in the error sequence e correspond to bit errors in the decoded sequence r .

It is assumed that the error words e_i are statistically independent random sequences with probability distributions

$$\Pr[e_i] = \begin{cases} 1 - \varepsilon_w; & e_i = 0 \\ \varepsilon_w/62; & e_i \neq 0, 1 \\ 0; & e_i = 1 \end{cases} \quad (A-1)$$

where ε_w is the word error rate for the communication link, 0 is the 6-tuple containing all 0's, and 1 is similarly defined. Note that Eq. (A-1) rules out the possibility that r_i can be the complement of s_i , corresponding to 6 bit errors in a given word. Also, if a word error is made, the decoded word is equally likely to be any binary 6-tuple containing from 1 to 5 bit errors, excluding the transmitted word and its complement.

Suppose γ of the words in r are incorrectly decoded: the probability of this event is

$$\binom{K}{\gamma} \varepsilon_w^\gamma (1 - \varepsilon_w)^{K-\gamma}; \quad 0 \leq \gamma \leq K$$

The $K - \gamma$ correctly decoded words contain no bit errors: all of the bit errors in r lie in the subset of K incorrectly decoded words. Let H denote the Hamming weight of e , which is equivalent to the number of bit errors in r . Define $A_{\eta, \gamma}/(62)^\gamma$ to be the probability of having a total of η bit errors in a group of γ incorrectly decoded words: then the probability distribution of H has the form

$$P_r[H = \eta] = \sum_{\gamma=0}^K \binom{K}{\gamma} A_{\eta, \gamma} \left(\frac{\varepsilon_w}{62} \right)^\gamma (1 - \varepsilon_w)^{K-\gamma}; \quad 0 \leq \eta \leq 5K \quad (A-2)$$

Since each word error contains from 1 to 5 bit errors according to Eq. (A-1), $A_{\eta, \gamma}$ is nonzero only in the range $\gamma \leq \eta \leq 5\gamma$: this explains the range in Eq. (A-2). The $A_{\eta, \gamma}$'s must now be determined to complete the expression for $\Pr[H = \eta]$.

If no word errors are made, there are no bit errors; therefore

$$A_{\eta, 0} = \begin{cases} 1; & \eta = 0 \\ 0; & \eta \neq 0 \end{cases} \quad (A-3)$$

The error word e_i for an incorrectly decoded word r_i is equally likely to be any binary 6-tuple with the exception of 0 and 1. Therefore, the probability of having η bit errors in a given incorrectly decoded word is simply the number of binary 6-tuples of Hamming weight η , divided by 62. Consequently

$$A_{\eta, 1} = \begin{cases} \binom{6}{\eta}; & 1 \leq \eta \leq 5 \\ 0; & \text{elsewhere} \end{cases} \quad (A-4)$$

For $\gamma \leq 2$, the probability of η bit errors within γ incorrectly decoded words is equal to the probability of μ bit errors in $\gamma - 1$ incorrect words, multiplied by the probability of $\eta - \mu$ bit errors within a single incorrect word, summed over the appropriate range of μ :

$$A_{\eta, \gamma} = \begin{cases} \sum_{\mu=\max(\eta-5, \gamma-1)}^{\min(\eta-1, 5\gamma-5)} A_{\mu, \gamma-1} A_{\eta-\mu, 1}; & \gamma \leq \eta \leq 5\gamma \\ 0; & \text{elsewhere} \end{cases} \quad (A-5)$$

The range of μ in Eq. (A-5) follows from the ranges over which $A_{\mu, \gamma-1}$ and $A_{\eta-\mu, 1}$ are nonzero. Thus $A_{\eta, \gamma}$ can be found recursively for $\gamma \geq 2$.

Iterative Design of Antenna Structures

R. Levy
DSIF Engineering Section

A new procedure is described for the design of antenna reflector structures for improved performance when subjected to the operational gravity loading. The design objective is to reduce the difference in pathlength of the RF energy beam that is reflected from the deformed surface with respect to the pathlength of the beam from a perfect paraboloidal surface. A virtual work formulation is used to state this objective in terms of the bar areas that compose the structure, which become the design variables. A special application of the Lagrange multiplier technique defines preferential redistributions of the design variables to improve performance. Improvements are developed subject to a primary constraint on total structure weight and additional practical side constraints. Design examples show efficient and effective applications of the described procedure.

I. Introduction

This article describes the mathematical procedure, implementation, and results of a computer program for parabolic antenna structure design to improve performance for gravity loading.

Performance of an initial, or preliminary, design can be improved by controlling the surface distortions caused by environmental loading. This loading is either random, such as results from wind and temperature, or deterministic from the effect of gravity. The gravity load results from the weight and the change in direction of the weight

vector relative to the structure with changes in antenna elevation attitude. Within these two classifications, only the gravity loading is both omnipresent and predictable, and it also tends to be the most significant with respect to performance. Therefore, design of the structure to control gravity loading distortions is a logical and feasible approach towards performance enhancement.

II. Related Background Research

In the last decade there has been substantial effort and literature describing diverse approaches in the field of

structural design. This work typically is classified within the technology of structural optimization. Much of this background research, however, has only indirect bearing on reflector structure design or upon the procedures to be described here.

Structural optimization has most frequently considered design for minimum structural weight (Ref. 1), subject to various primary behavioral constraints (such as stress, buckling, displacement) and side constraints (such as fabrication requirements). Here we will consider the reflector structure problem as a design for improved performance, rather than minimum weight. The structure weight will be the primary constraint and the behavioral constraints will be side constraints.

A special requirement, which is not usually considered for static loading, is that the loading should not be treated as invariant. This is necessary because the weight of the structural components, which is significant, is redistributed during design. Furthermore, instead of examining a limited number of design loading cases, reflector design is concerned with an infinite set of loadings in which the orientation of the gravity loading vector changes over a continuous range of antenna elevation attitudes.

An important background idea relating to reflector design is Von Hoerner's concept of homologous design (Ref. 2). In this, the design is established to make the deformations under loading conform to a parabolic surface. A homologous design, however, is not always achievable. In our approach, although we recognize and employ related concepts, no directed attempt is made toward achieving the perfectly homologous design.

Von Hoerner also supplies one of the relatively few procedures for static design which include variability of loading. This effect has also been considered in Ref. 3 with design for a minimum-weight objective in the presence of deflection constraints. Variability of loading is inherent in the relatively virgin field of design for dynamic constraints, and prevalent approaches are surveyed in Ref. 4.

Other design optimization techniques that are the most closely related to the procedures that will be used here are described in Refs. 5, 6, and 7. These procedures adopt optimality criteria for stress as a constraint and incorporate virtual work formulations to express displacements as other constraints. In particular, Gellatly and Berke (Ref. 6) show that the Lagrange multiplier technique is effective in developing design improvements for practical structures with realistic numbers of variables and degrees of

freedom. Kicher (Ref. 8) provides a comprehensive description of the application of the Lagrange multiplier within structural design.

III. Present Approach

The approach is to develop a mathematical definition of the design objective by means of a virtual work formulation. The objective function is then used with a special application of the Lagrange multiplier technique to develop an improved design. Since the design technique employed entails approximations, it is necessary to proceed iteratively towards the final design. The cyclic steps repeated during the iterations are analysis of the current design (mathematically "exact") and development of a preferential design (mathematically "inexact") from the analysis. Most of the prevalent structural design approaches are also iterative in this same way.

Mathematical derivation of the objective is founded upon the recently developed "rigging angle" concept (Refs. 9 and 10). This concept implies that the gravity loading at the so-called "rigging angle" attitude is compensated by adjustment of surface panels and the loading at other attitudes is effectively the net loading in moving away from the rigging attitude.

IV. Problem Formulation

A convenient measure of performance for design is the root mean square of half the difference in pathlength of the RF energy beam in traveling from a deformed reflector surface to the focal point compared with the pathlength from a surface that is a perfect paraboloid. The reflector surface of interest is equivalent to an infinite set of points for which pathlength differences exist; in practice the surface is replaced by a finite set of "target" points which are taken to be a representative sample of the entire set.

Accordingly, minimization or reduction of the mathematical expression for this half pathlength difference for gravity loading is taken to be the design objective function. The design variables are the cross-sectional areas of the individual bar members that compose the typical space-truss type of reflector structure. The primary constraint is a prespecified invariant total structure weight. Side constraints of minimum member sizes can be specified to preclude overstress and buckling. Additional constraints can be imposed to restrict the numbers of different member sizes. This last constraint is for fabrication economy and simplification. It is enforced by assigning par-

ticular members to groups that are required to have common sizes.

The foregoing definitions of objective function, design variables, and constraints categorize this as a problem of optimum design. Effectively, the problem is to redistribute a fixed amount of structural material to obtain an admissible design with improved performance. Here, the word "improved" is a realistic replacement for the word "optimum." The replacement is made because the (global) optimum is often undefinable, unachievable by direct procedures, or does not justify the undue effort that could be spent in the achievement.

This problem statement is essentially the same as for the Parabolic Antenna Reflector Design System (PARADES) program (Ref. 11). Here, however, we will describe a parallel in-house JPL effort that uses a different mathematical attack and a computer program that, although decidedly effective, is considerably less complex and, consequently, operates within a narrower scope.

V. Mathematics of Design Procedure

The improved design is developed by employing the virtual work principle to express an objective function stated in terms of the design variables and then using the Lagrange multiplier method to find new values of the design variables that improve the objective. Before doing this, it is helpful to describe the associated reflector surface geometry.

A. Reflector Geometry

The coordinate system used is shown in Fig. 1. The figure shows an antenna at a particular elevation attitude angle α . An X-Y-Z Cartesian coordinate system with origin at the paraboloidal vertex is defined. The Z-axis is the focal axis and the Y-Z plane is usually a plane of symmetry. The gravity loading is shown resolved into components parallel to the Y and Z axes.

The pathlength geometry relationship is shown diagrammatically in Fig. 2. Solid line V-G-C represents the original surface and the broken line represents the deflected surface. Target point G on the original surface is shown as deflected to point D. An incident ray parallel to the focal axis is shown crossing the aperture plane at A and is reflected at D to the focal point. With respect to the original surface, an alternative ray is shown to cross the aperture plane at B and then to be reflected at C to the focal point along the path C-D. Consequently, from the figure, it can be seen that the pathlength difference for

these two rays is the sum of the distances from E to C and from C to D. The component of the deflection normal to the surface is indicated by the dimension dn .

B. Virtual Work Principle

For practical purposes, and within minor approximation, the reflector structure can be considered as a framework of m one-dimensional bars, each of which is completely characterized by its area A , length L , elastic modulus E , and its density. For simplicity, and consistent with practical applications, assume that the modulus and density are the same for all bars. Let the structure be subjected to a real external loading vector $\{P\}$ and let $\{S\}$ be the associated vector of internal forces (stress resultants). In addition, define a dummy single load D of unit magnitude applied in a specified direction at one particular node of the structure and let $\{U\}$ be the associated internal force vector. Then, from the principle of virtual work,

$$1 \cdot \delta = \sum_{i=1}^m [(S_i L_i)/(A_i E)] \cdot U_i \quad (1)$$

where δ is the displacement of the structure at this node in the direction of D caused by the real load. In Eq. (1), the term on the left is the virtual external work of the unit load moving through the real displacement δ . The summation on the right is the internal virtual work expressed as the product of the real extension of each bar and the internal force caused by D . For a linearly elastic structure, Eq. (1) can be extended by superposition to represent the sums of the squares of the half pathlength difference of a set of surface target points from a perfect paraboloid. To do this, note that the half pathlength difference of a typical target point can be expressed as (Ref. 12)

$$\rho = \gamma_z \cdot dn \quad (2)$$

where γ_z is the direction cosine of the surface normal with respect to the reflector focal axis and dn is the component of distortion normal to the surface. Then, in Eq. (1), apply the unit load normal to the surface, and the summation on the right will give δ on the left equal to dn . Furthermore, replace the unit dummy load by a load normal to the surface of magnitude

$$D = \gamma_z^2 \cdot dn \quad (3)$$

Then it follows that Eq. (1) will give the square of the half pathlength difference at this target point as follows:

$$\rho^2 = \gamma_z^2 \cdot dn^2 = \sum_{i=1}^m (S_i U_i L_i)/(A_i E) \quad (4)$$

where each U_i is the internal force of the single dummy load $\gamma_i^2 dn$. Finally, apply a dummy loading vector $\{D\}$ that contains one load for each of n surface target points, each load applied normal to the local surface, with magnitude computed according to Eq. (3). Then by superposition it follows that the sums of squares of half pathlength deviations SS are given by

$$SS = \{\rho\}^t \{\rho\} = \sum_{i=1}^m (S_i U_i L_i) / (A_i E) \quad (5)$$

in which each U_i is the internal force for loading vector $\{D\}$. Finally, the rms half pathlength difference for the real loading is

$$\text{rms} = (SS/n)^{1/2} \quad (6)$$

Consequently, a reduction of the objective function (Eq. 5) results in reduction of the rms half pathlength differences (Eq. 6).

C. Objective Function

We will give a brief summary of pathlength difference and rigging angle relationships derived in Refs. 9 and 10. It was shown there for a linearly elastic structure that the displacements of the target set of points for two particular loading conditions provide sufficient information for the computation of the sums of squares of the half pathlength differences at any elevation attitude of the antenna. With reference to Fig. 1, the two required loading vectors, derived from the weight of all of the structural members plus supported non-structural components, are:

$\{P_y\}$ = loading vector for weight loading applied parallel to the reflector Y-axis.

$\{P_z\}$ = loading vector for weight loading applied parallel to the reflector Z-axis.

and let $\{u_y\}, \{u_z\}$ be the associated displacement vectors for the set of target points. Note that the structural nodes associated with the displacement vectors are a subset of the nodes associated with the loadings.

Furthermore, assume that at a particular elevation angle γ , the surface is adjusted to compensate the gravity loading deflections. This angle is called the "rigging angle" and defines the elevation attitude at which the surface is ideally a perfect paraboloid. At any other elevation angle α , the net displacement is therefore:

$$\{u\} = \eta \{u_y\} + \xi \{u_z\} \quad (7)$$

where, as can be seen from Fig. 2,

$$\left. \begin{aligned} \eta &= \cos \gamma - \cos \alpha \\ \xi &= \sin \gamma - \sin \alpha \end{aligned} \right\} \quad (8)$$

In practice, it is appropriate to consider the pathlength differences with respect to an alternative paraboloid that best fits the data. The alternate paraboloid is defined by a maximum of six "homology" fitting parameters as follows:

H_x = vertex shift parallel to the X axis

H_y = vertex shift parallel to the Y axis

H_z = vertex shift parallel to the Z axis

θ_x = rotation about the X axis

θ_y = rotation about the Y axis

K = focal change parameter = (original focal length / new focal length) - 1

For structures and loading symmetric about the Y-Z plane, the parameters H_x and θ_y are zero. The focal change parameter K is justified if the antenna has a dynamically adjustable focal point.

The following additional terms are defined:

$\{\rho_y\}, \{\rho_z\}$ = half pathlength differences vectors from the best fitting paraboloid for the corresponding loadings.

SS_y = sums of squares of half pathlength differences for Y-loading = $\{\rho_y\}^t \{\rho_y\}$

SS_z = sums of squares of half pathlength differences for Z-loading = $\{\rho_z\}^t \{\rho_z\}$

S_{yz} = $\{\rho_y\}^t \{\rho_z\}$

The sum of the squares of the half pathlength differences SS_α from the best-fitting paraboloid at elevation angle α can be expressed as

$$\{p\}^t \{p\} = \eta^2 SS_y + \xi^2 SS_z + 2\eta\xi \{p_y\}^t \{p_z\} \quad (9)$$

or

$$SS_\alpha = \eta^2 SS_y + \xi^2 SS_z + 2\eta\xi S_{yz} \quad (10)$$

The rms half pathlength difference is

$$(\text{rms})_\alpha = (SS_\alpha/n)^{1/2} \quad (11)$$

where n is the number of points in the target set. In practice it is customary to incorporate weighting factors

in Eqs. (9) and (10) to represent the relative importance (such as the local tributary aperture area) of each of the points in the target set. For simplicity of presentation, it is assumed here that all points are of equal weight.

Here, during the design procedure, we will choose the rigging angle to make the pathlength differences at the horizon and zenith attitudes equal. Although there are other choices that are logical, this will result in the smallest peak rms difference over the entire elevation attitude range. Then a simple computation gives the rigging angle directly as follows:

$$\gamma = \phi - \varepsilon \quad (12)$$

where

$$\varepsilon = \tan^{-1} \left(\frac{B}{A} \right)$$

$$\phi = \cos^{-1} \left(\frac{C}{[A^2 + B^2]^{1/2}} \right) \quad (13)$$

and the terms A , B , C in Eq. (13) are

$$\left. \begin{aligned} A &= 2SS_y - 2S_{yz} \\ B &= 2SS_z - 2S_{yz} \\ C &= SS_y - SS_z \end{aligned} \right\} \quad (14)$$

Then, because the computation of rigging angle will produce equal rms values at horizon and zenith, either of these two attitudes presents a suitable design loading case for reducing the extreme rms variation over the entire elevation range. It also has been found that the rigging angle is reasonably insensitive to change with respect to alternative designs with moderate differences, which is helpful during iterative design because the rigging angle computed for a previous design is taken as the rigging angle for development of the following design.

Then, from the foregoing, the infinite spectrum of loading cases that result from the continuous range of elevation attitudes from horizon to zenith is effectively replaced by a single design loading case. Therefore for design the real loading could be formed as

$$\{P\} = \eta \{P_y\} + \zeta \{P_z\} \quad (15)$$

However, it is preferable to apply $\{P_y\}$ and $\{P_z\}$ separately to determine the associated displacement and half pathlength vectors. Following this, a typical load D_k of

the dummy loading vector $\{D\}$ is computed to have the magnitude

$$D_k = \gamma_z \cdot (\eta \rho_y + \zeta \rho_z) \quad (16)$$

Equation (16) is evaluated at the k th target point and the load is applied normal to the surface at the point. Equation (16) follows from Eqs. (2) and (3) and the assumed linearity of displacements with respect to loading.

To use either the horizon or zenith attitudes as the design loading condition, α is set equal to 0 deg or 90 deg, respectively, in Eq. (8), and Eq. (7) is used in the computation of $\{S\}$ for Eq. (5). The displacements for the loading $\{D\}$ (Eq. 16) are used in the computation of $\{U\}$ for Eq. (5).

D. Design Algorithm

For design, we consider that the m bars of the structure are treated as a set of g bar groups, in which the i th group contains C_i bars of common area A_i . Consequently, the design variables become the group areas rather than the individual bar areas. There is no loss of generality in this, since a group can consist of $C_i = 1$ bar. The group length L_i is defined as the total length of bars in the group, or

$$L_i = \sum_{j=1}^{C_i} L_j \quad (17)$$

Also define a force term F_i for the i th group as

$$F_i = 1/L_i \sum_{j=1}^{C_i} S_j U_j L_j \quad (18)$$

Therefore, the virtual work W_i of the internal bar forces for the i th group is

$$W_i = (L_i F_i) / (A_i E) \quad (19)$$

For a structure comprising bars of the same material the constraint on total structure weight can be replaced by a volume constraint. Let V_p be the assigned volume of the bars; then the volume constraint is

$$\sum_{i=1}^g L_i A_i - V_p = 0 \quad (20)$$

Then, considering only the constraint of Eq. (20), we form the function G , which consists of the objective function augmented by the constraint equation times the Lagrange

multiplier λ . The objective function is formed by summing Eq. (19) over all the bar groups, thus

$$G = 1/E \sum_{i=1}^g (L_i F_i)/A_i + \lambda \left(\sum_{i=1}^g L_i A_i - V_p \right) \quad (21)$$

Taking the partial derivative of G with respect to A_i and setting this equal to zero results in g equations that will ideally lead to the optimal values of the design variables. The equations are of the following type:

$$0 = -(L_i F_i)/(A_i^2 E) + \lambda L_i \quad (22)$$

Solving Eq. (22) for each A_i , we obtain the new value

$$A_i = [F_i/(\lambda E)]^{1/2} \quad i = 1, 2, 3, \dots, g \quad (23)$$

Using Eqs. (23) in Eq. (20), λ can be found from

$$(\lambda E)^{1/2} = 1/V_p \cdot \sum L_i \cdot F_i^{1/2} \quad (24)$$

E. Restrictions and Modifications for Design Algorithm

Subject to restrictions that will be discussed subsequently, Eq. (23), in conjunction with Eq. (24), can be used to determine new values of the design variables A_i that will minimize the objective function for a constant weight of structural members. Nevertheless, the restrictions on the use of these equations are significant and require special modifications in the application.

The restrictions are:

- (1) In differentiating Eq. (21), it was assumed that F_i is not a function of A_i . This is strictly true only in the case of statically determinant structures. The typical antenna structure contains a substantial number of redundant bars, so that the foregoing derivations are only approximately true.
- (2) A side constraint could be violated by choosing A_i according to Eq. (23). Side constraints that are applicable are specific minimum areas to preclude stress or buckling failure. Another type of side constraint can be imposed to prevent unduly large changes with respect to the bar sizes of the preceding design. This will be called a "step-size ratio" limit and will be explained in conjunction with restriction 1.
- (3) The i th group can be specified as a group for which no size changes are permitted.

- (4) The F_i term for a particular group could be negative. Therefore, Eq. (23) becomes meaningless for real variables.

The first restriction entails an approximation in developing a new design. This approximation, plus the effects of bar grouping and variation of load distribution, are the only parts of the procedure that appear to be mathematically "inexact." The consequences are the requirement for an iterative design procedure in which the design approximations are corrected iteratively from cycle to cycle. Nevertheless, the magnitude of the approximations and corrections needed can be controlled to some extent by defining a limiting change in the design variables permitted from cycle to cycle. This step size ratio change R is employed to define the following restriction:

$$\text{abs}(\underline{A}_i - A_i)/A_i \leq R \quad (25)$$

where \underline{A}_i is determined from Eq. (23) and A_i is the design variable at the beginning of the cycle.

If the inequality is violated, the new design variable \underline{A}_i is established temporarily as follows:

$$\underline{A}_i = A_i (1 + R \text{sgn}(\underline{A}_i - A_i)) \quad (26)$$

The modification applied in conjunction with the second restriction is to test each \underline{A}_i computed from Eq. (23) or \underline{A}_i computed from Eq. (26) against the specified minimum area and to select the most critical from the test. The modification for the third restriction is to exclude the group from redesign.

The fourth restriction is accounted for by a major change in the design algorithm. The groups are identified according to whether or not F_i is positive or negative. When positive, the group is treated as described above. When negative, objective and constraint are interchanged in the Lagrangé multiplier formulation. Now the constraint becomes the internal virtual work for the positive groups and the objective is to minimize the volume of the negative groups. The constraint is taken to balance the positive virtual work as

$$SS_p - 1/E \cdot \sum (L_i \cdot F_i)/A_i = 0 \quad (27)$$

In Eq. (27), the summation is taken over only the groups with negative F_i , and SS_p is the predicted objective function resulting from new sizes of the bars with positive F_i . It can be shown from Eqs. (23) and (24) that

$$SS_p = \lambda \cdot V_p \quad (28)$$

Then by reformulating the Lagrange multiplier algorithm, we find for the bars with negative F_i

$$A_j = (-F_j)^{1/2} \cdot \sum_i [(-F_i)^{1/2} \cdot L_i] / (SS_p \cdot E) \quad (29)$$

Ideally, Eq. (29) would provide a zero objective function and structure of smaller volume than specified. However, in practical applications, the first two restriction categories preclude the ideal situation.

It can be seen that all of the restrictions and modifications, except for the fourth, cause violations of the constant volume constraint. This is overcome in the execution of the design algorithms by a procedure that maintains the volume for each design and also develops the design closely in accordance with the foregoing theory.

Before applying the Lagrange multiplier algorithm to the design groups, their F terms and volumes are identified as "positive," "negative," or "excluded." Then, within each cycle, the first operation is to apply Eq. (23) to the positive groups. This can result in some of the groups being bounded from either above or below. Lower bounds are recognized, but upper bounds from this operation are ignored.

The positive volume is then adjusted by removing the volume of lower-bounded groups and adjusting the augmented objective function (Eq. 21) accordingly. The algorithm is re-applied, and as the result some groups will no longer be at their upper bounds and some new groups may become lower-bounded. Again, lower bounds are recognized, upper bounds ignored, and the procedure is repeated until no new lower bounds appear.

After this, Eq. (29) is applied exactly once to the negative groups. Since the result of this application will permit new volume to be assigned to the positive groups, the augmented objective function is reconstructed and Eq. (23) is applied one more time.

If any unbalanced volume remains after this, it is distributed by proportion to positive and negative groups in a manner that will not violate any of the constraint boundaries. Although this results in repeated applications of the design algorithms during each design cycle, the arithmetic is performed on one-dimensional vectors of size equal only to the numbers of design variables. Accordingly, execution of the design algorithms proceeds rapidly and expends only a relatively small proportion of the computation time for each cycle.

VI. Example Applications

A. Computer Program

A computer program has been developed to implement these procedures. In its current form, it is a prototype of a larger-capacity program that is intended to have design capability for antenna structures in the 64-m-diameter class or larger. At present, problem size is restricted to the in-core capacity of the Univac 1108, Exec 8 Computer. Nevertheless, as will be seen, reasonably sized demonstration problems can be processed.

The program logic is designed especially for the problem at hand and takes advantage of favorable related features wherever possible. This, in conjunction with the present in-core computational feature, results in rapid execution of numerous design iteration cycles. For example, the execution time to design the sample structures that will be described later has been compared with the execution time to perform a verification static load-deflection analysis of the same structures with both the NASTRAN and SAMIS structural analysis programs. The design program has been found to generate complete designs, executing about ten iteration cycles within the same or less time required by either of these two programs. The additional time required following both analysis programs for a post-processor to perform the rms pathlength difference computations is not included in this comparison.

The primary size restriction of the design program is the size of the structural stiffness/decomposition. This is stored as a rectangular matrix with the number of rows equal to the number of elastic degrees of freedom and the number of columns equal to the matrix bandwidth. A problem size of 260 degrees of freedom with a bandwidth of 75 can be designed using one 65K core bank. The program is devised to recognize externally developed nodal sequencing definitions to control the bandwidth. The bandwidth definition is used only for storage arrangement and not for the stiffness matrix decomposition algorithm. A conventional LDU algorithm is modified to avoid the computations associated with the empty terms within the band during matrix decomposition.

The program user establishes the step size ratio R and the maximum number of associated iterations permissible. If the design objective converges to within a 1% change before this number of iterations is reached, this sequence of iterations is terminated. The best design from this sequence is identified as the starting point for new sequences of iterations with reduced step sizes. At pro-

gram termination, properties of the best design attained are punched on cards for a restart or for execution on another program.

Much of the data input is in NASTRAN format and an existing NASTRAN data deck will require only a limited amount of additional preparation for the design program. However, the only type of element connections and properties recognized are the NASTRAN CBAR, PBAR, and CONROD definitions.

B. Sample Problems

1. Baseline structure. The hypothetical antenna structure shown in Fig. 3 was used as a basis for computer program development and evaluation. This is called the "baseline structure" and represents a highly simplified model of a practical reflector. It contains most of the essential features of typical reflector frameworks, but the surface and structure have been subdivided into a relatively coarse grid to expedite the computations.

There are six identical ribs spaced at 60-deg increments, which are interconnected by the customary hoop and diagonal members. Three supports are shown at nodes 201, 203, and 205. The plane of the supports is taken to be capable of rotation about the X-axis to vary the elevation attitude.

The Y-Z plane is a plane of symmetry. There are a total of 19 nodes, with three translational degrees of freedom permitted for each node. Therefore, excluding supports, there are 48 degrees of freedom in the model. Surface target nodes are 101, 301-306, 401-406, which provide 13 points for rms computation. There are six framing members of identical topology and similar structural function in each of ten different design groups (five rib-member, three hoop-member, two diagonal-member), resulting in a total of 60 members.

The design program started from an initial structure in which the design variables for all groups were the same. All groups throughout the procedure were constrained to minimum area equal to one quarter of the starting area. The external nonstructural weight is equal to about twice the weight of the structural members and is applied to simulate loading of nonstructural surface panels.

2. Validation structure. This is a second structure established for program evaluation and is patterned closely as a coarse-grid approximation to the analytical model of an existing 26-m-diameter antenna. The validation model

contains about half as many radial ribs and circumferential hoop rings as the prototype. It also comprises members that simulate quadripod and counterweight structures and includes associated subreflector and ballast loads. The members of these components, since they are highly idealized, are placed in groups that are excluded from the design process. The typical inner "square girder" reflector support systems are also simulated.

Member sizes for the starting design were established to have cross section area distributions in similar proportion to the prototype. Minimum sizes were established to be approximately equal to one quarter of the initial. Because of symmetry with respect to the Y-Z plane, only one-half of the structure is considered. This half-section contains seven radial ribs and four rings, two legs of a quadripod, and the relevant portions of a counterweight and square girder. The structure is supported at the square girder by simulated elevation axis and ball-screw jack attachments.

The analytical model contains 83 nodes, 47 surface target points for rms computation, and 282 bars that are assigned to 56 design groups. Four groups are excluded so that 52 design variables are considered. There are 249 elastic degrees of freedom in the model, of which 26 are constrained, either by virtue of support or symmetry. The external nonstructural weight, which is predominated by the counterweight ballast simulation, is about three times that of the structural members. No sketch is included here to further describe the model.

VII. Results and Conclusions

Figure 4 shows the results of design iterations for the baseline structure. One sequence of 11 iterations with $R = 0.25$ is shown. The best rms value is obtained at cycle number 9, and the rms value here is about 55% of the initial. The horizon attitude loading was the design case, with rigging angle established to equate the zenith rms to the horizon rms. It can be seen here that the iterations proceed smoothly towards the best design.

The design for this problem was also run with larger values of R for initial sequences of five cycles followed by second sequences for which R was reduced. The results were considerably more erratic, but the effectiveness of the final designs thus obtained were about the same. In evaluating the design improvement shown, it should be noted that the objective is actually the sum of squares and not the rms values that are plotted. Therefore the final rms ratio of 55% is equivalent to a ratio of 30% on the mathematical design objective.

The iterative results obtained for the validation structure are shown on Fig. 5. Three iteration sequences are indicated in which up to four new designs per sequence were specified with $R = 0.60$, 0.24 , and 0.12 . The horizontal scales for the cycle numbers are in the approximate proportions of the related step size ratios.

As for the baseline structure, the horizon attitude was the design loading configuration. The rms value at the end of the fourth design of the first sequence was 46% of the starting value. The best design for the second sequence was found at its third cycle, equal to 36% of the initial. The third sequence achieved 32% of the initial rms value at the end of the third iteration and terminated here because of the convergence criterion (equivalent to $\frac{1}{2}\%$ change on rms). The 1108 computer execution time for all of the 11 design iterations plus the starting design analyses to initiate each sequence was less than 2 min. Each iteration was executed in about 8 s, and much of this time was consumed in preparing a substantial amount of response data and information for output.

It can be seen, especially in Fig. 5, that relatively large step size ratios tend to produce erratic convergence; the convergence becomes smoother as the ratio decreases. Establishing effective ratios appears to be the key toward most efficient program usage. However, the results of many other sample design tests for these structures with different ratios and sequence specifications indicate that there is no consistently best way to approach all problems. This became evident for the baseline structure when the design grouping constraints were relaxed to permit up to 60 design variables. As expected, this relaxation produced further improvements of the objective. However, the most significant finding was that in some cases large ratios permitted large undesirable jumps in the convergence and, in other cases, the design appeared to alternate between two distinguishable configurations. Notwithstanding the undisciplined behavior, some of these problem formulations were as effective as some of the better-behaved tests with

smaller ratios. When very small ratios were specified they led to extremely smooth convergence rates that were not always particularly effective because of the slow rate of descent.

Here we attribute this anomalous behavior to the iteration algorithm, as discussed previously with respect to the restrictions and corresponding modifications for design application. The consequences of this mathematically unsatisfactory convergence lie in the number of iteration cycles required to achieve an effective design. However, in a practical sense, the difficulty is overcome by the rapid rate at which the iterations are executed.

The effect of variation of the structural weight distribution does not seem to impose serious difficulties in obtaining the solution. This was established for the baseline structure by setting the bar density equal to zero to retain only the invariant nonstructural weight during the design. No substantial difference or improvement was observed in the convergence behavior.

It currently appears that the best way to approach a new design problem with no *a priori* knowledge of the convergence behavior is to establish a primary sequence with a large step size ratio and then reduce this successively. This provides the opportunity to find a point near a worthwhile minimum and to explore the region near this point more carefully in a subsequent sequence.

Present experience indicates that the reflector design problem (and possibly many other problems) is characterized by many local minima. It does not seem practical to explore all of these in an attempt to find the global optimum. A realistic appraisal of practical difficulties in structure design appears in Ref. 13. Nevertheless the program described here has been demonstrated to be an effective approach toward achieving a substantially improved design.

References

1. Schmit, L. A., "Problem Formulation, Methods and Solutions in the Optimum Design of Structures," *An Introduction to Structural Optimization*, Study No. 1, pp. 19-46, Solid Mechanics Division, University of Waterloo, Waterloo, Ontario, Canada, 1968.
2. Von Hoerner, S., "Homologous Deformations of Tilttable Telescopes," *J. Struct. Div.*, ASCE, No. ST-5, Oct. 1967, pp. 461-485.
3. Chern, J. M., "Optimal Structural Design for Given Deflection in Presence of Body Forces," *Int. J. Solids Struct.*, 1971, Vol. 7, pp. 373-382, Pergamon Press.
4. Pierson, B. L., "A Survey of Optimal Structural Design Under Dynamic Constraints," *Int. J. Num. Meth. England*, Vol. 4, 1972, pp. 491-497.
5. Dupuis, G., "An Iterative Approach to Structural Optimization," *Int. J. Num. Meth. England*, Vol. 4, 1972, pp. 331-336.
6. Gellatly, R. A., Berke, L., and Gibson, G., "The Use of Optimality Criteria in Automated Structural Design," *Third Conference on Matrix Methods in Structural Mechanics*, Wright Patterson Air Force Base, Ohio, Oct. 19-21, 1971.
7. Venkaya, V. B., "Design of Optimum Structures," *Conference on Computer Oriented Analysis of Shell Structures*, Palo Alto, California, Aug. 10-14, 1970.
8. Kicher, T. P., "Optimum Design-Minimum Weight Versus Fully Stressed," *J. Struct. Div.*, ASCE, Vol. 92, No. ST6, Dec. 1966, pp. 265-279.
9. Levy, R., "A Method for Selecting Antenna Rigging Angles to Improve Performance," in *The Deep Space Network*, Space Programs Summary 37-65, Vol. II, pp. 72-76, Jet Propulsion Laboratory, Pasadena, Calif., Sept. 1970.
10. Levy, R., "Antenna Rigging Angle Optimization Within Structural Member Size Design Optimization," in *The Deep Space Network Progress Report*, Technical Report 32-1526, Vol. I, pp. 81-87, Jet Propulsion Laboratory, Pasadena, Calif., Feb. 15, 1971.
11. Levy, R., and Melosh, R., "PARADES Structural Design System Capabilities," in this volume of *The Deep Space Network Progress Report*.
12. Utku, S., and Barondess, S. M., *Computation of Weighted Root-Mean-Square of Path Length Changes Caused by the Deformations and Imperfections of Rotational Paraboloidal Antennas*, Technical Memorandum 33-118, Jet Propulsion Laboratory, Pasadena, California, Mar. 1963.
13. Cornell, C. A., "Examples of Optimization In Structural Design," *An Introduction to Structural Optimization*, Study No. 1, pp. 143-164, Solid Mechanics Division, University of Waterloo, Waterloo, Ontario, Canada, 1968.

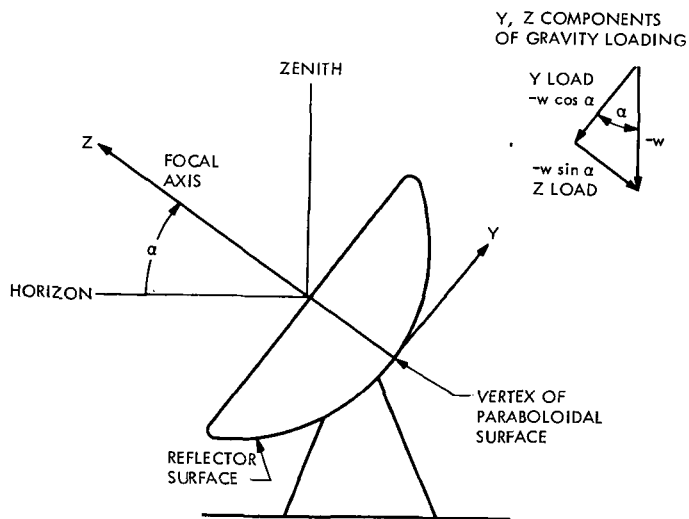


Fig. 1. Coordinate system for reflector

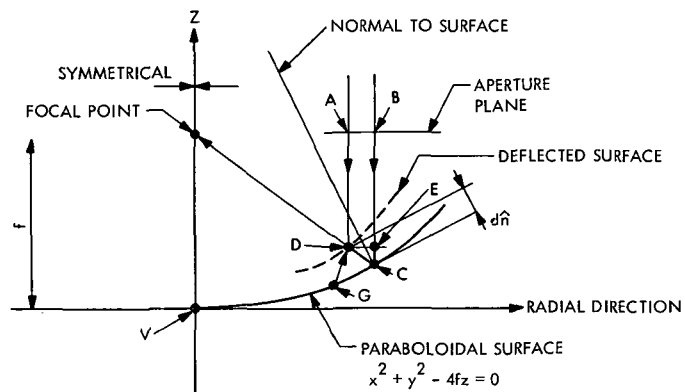


Fig. 2. Deflection geometry

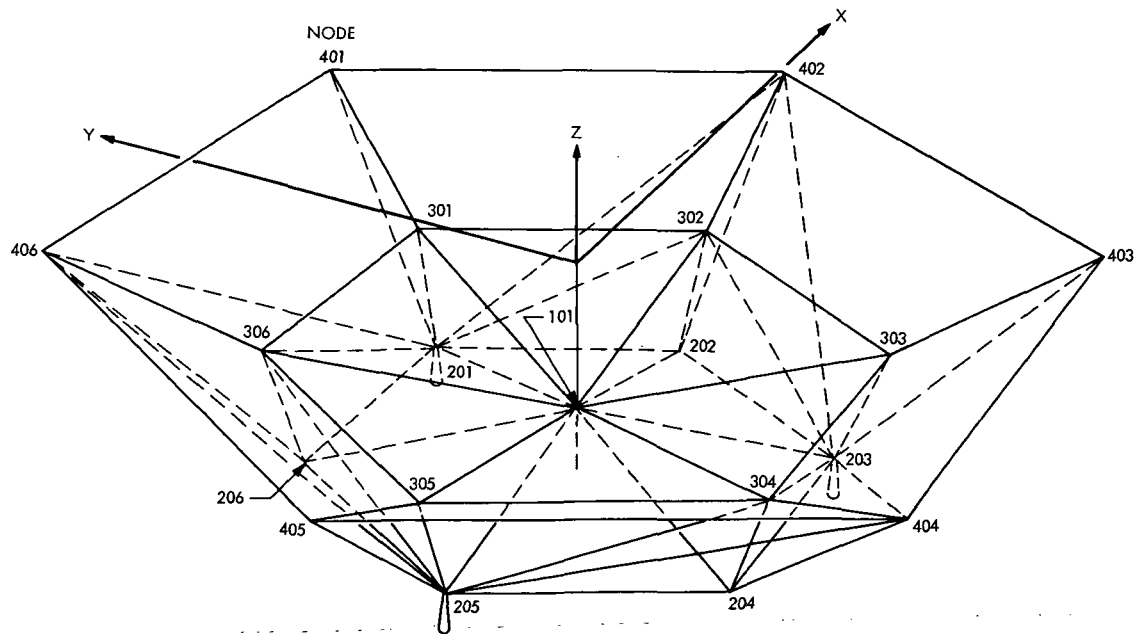


Fig. 3. Model of baseline structure

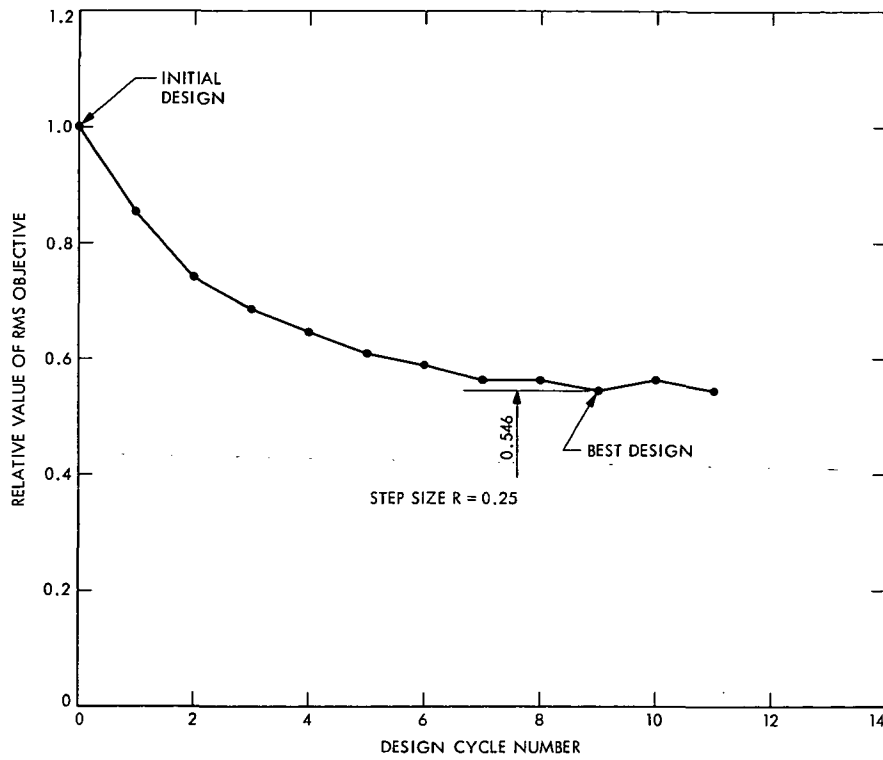


Fig. 4. Baseline structure design iterations

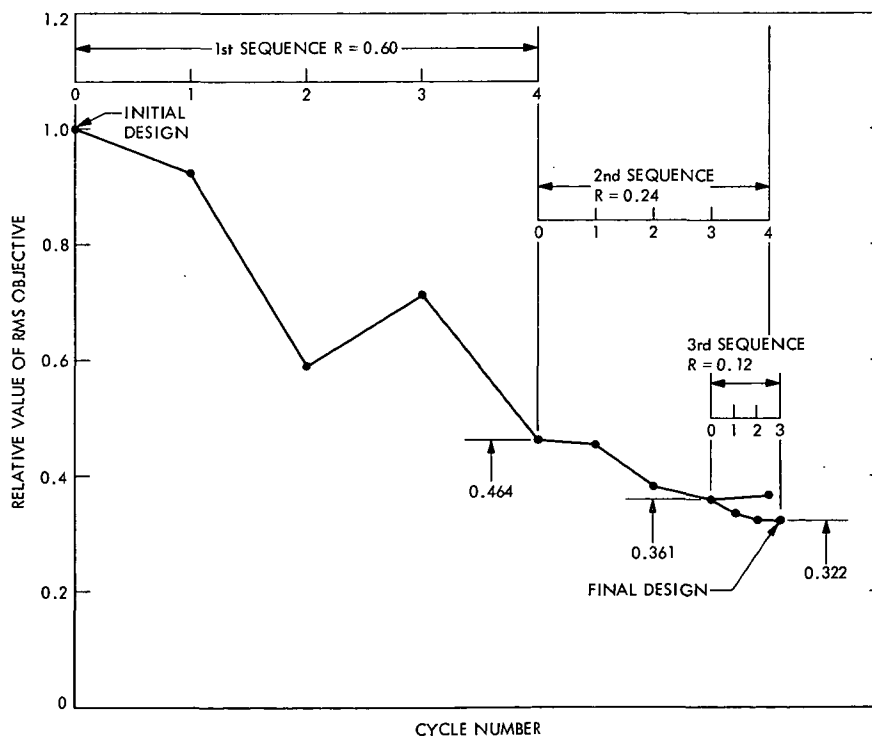


Fig. 5. Validation structure design iterations

Two-Station Interferometer Analog Input Channel

T. O. Anderson

Communications Systems Research Section

A signal sampling system, used for the Deep Space Network Venus two-station radar experiment, intended to demonstrate hydrogen maser compatibility in two-station spacecraft tracking with planetary round trip times, has been implemented. One sampling channel is described in detail. Four such channels, one for the sine and one for the cosine signal from each of two antennas, are used in the demonstration interferometer system. Each channel contains two multiplexed subchannels, and each subchannel consists of an integrating circuit, a track-and-hold circuit, and an analog-to-digital converter. All components of the subchannels are multiplexed and the output is derived from a digital multiplexing circuit which puts out digital data in parallel to line drivers for computer connection. Part of the four-channel system, a special-purpose test and calibration system, is also described.

I. Introduction

Analysis (Ref. 1) indicates that by properly processing the simultaneous two-way doppler and range data from two stations, the errors resulting from low-declination geometry of outer planet spacecraft are reduced by a factor of 2 to 4, and the errors resulting from unmodeled spacecraft accelerations are reduced by 2 orders of magnitude. To demonstrate the feasibility of maintaining phase coherence between two stations, one transmitting and both receiving, and each with its own hydrogen maser frequency standard, a Venus interferometer radar experiment was conducted during June 1972. The experiment consisted of transmitting 400 kW from DSS 14, and after a round trip delay to the planet Venus of 5-10 min, simul-

taneous reception at DSS 14 and at DSS 13. The IF signal from DSS 14 was sent over a microwave link to DSS 13, where both signals were digitally processed. The equipment used to convert the receiver output analog signals into digital form for the demodulators and subsequent range-gated spectrum analysis is described in this article.

The analog input channel has parallel integrate-and-dump, sample-and-hold, and analog-to-digital conversion circuits. The outputs of the parallel A/D converters are digitally multiplexed onto a single line to the demodulator/filter unit. Parallel channels are required to allow continuous sampling with integrate-and-dump circuits which require approximately 1 μ s to dump. The integrate-and-

dump circuits are used as a matched filter for rectangular pulses. Although this equipment was constructed primarily for radar data acquisition, the basic design is compatible with any DSN system using rectangular pulses, such as command, telemetry, and, especially, ranging.

In planning a system such as that described here, one is faced with a make-or-buy decision. Considering the large number of complete lines of digital data handling systems modules presently available in the market place, this decision becomes a selection of the optimum price/performance, yet compatible systems modules. Some additional special-purpose input/output and control circuits are also required. The only circuit for which the buy-or-make decision presented a question was the integrate-and-hold circuit. No single circuit module which would be usable for integration and subsequent holding and would also be sufficiently fast appeared to be available. Single integrate-and-reset circuits with sufficient speed and single track-and-hold circuits of sufficient speed are indeed available, however.

Other system configurations such as analog multiplexing of integrators with a single hold circuit and an A/D converter have been considered. Speed and accuracy appear to be limiting factors in analog multiplexing schemes. So-called tracking A/D converters have also been considered where the digital value of the integrator output signal may instantaneously be transferred to a hold register at any arbitrary time. No hold circuits would then be required. Tracking converters, however, are usually of lower resolution and are also high priced.

The configuration of the present system is shown in block diagram form in Fig. 1.

II. Integrate and Reset Circuit Module

Burr-Brown's sample-and-hold amplifier model 4013-2/25 is connected to operate as a switched integrator. Its block diagram is shown in Fig. 2. It includes a high-gain, wide-bandwidth field effect transistor (FET) input operational amplifier and a high-gain current output amplifier. It resets from ± 5 V to 0 ± 1 mV in less than $1 \mu\text{s}$. The 4013-2/25 model includes a $0.001 \pm 1\%$ μf polystyrene capacitor. The integrating resistor, which must not be smaller than 500Ω , is connected externally. The 4013-2/25 model also has facility for external connection of a $2\text{-k}\Omega$ potentiometer to provide a variable bias for the operational amplifier input offset voltage over a $\pm 10\text{-mV}$ range. The switched current amplifier is controlled by a transistor-transistor logic (TTL) compatible square wave derived from a high-speed flip-flop (FF).

III. Sample-and-Hold Circuit Module

The Analog Devices SHA-IIA, shown in block diagram form in Fig. 3, is used as the sample-and-hold circuit. Its accuracy and droop rate are compatible with a 12-bit resolution, $5\text{-}\mu\text{s}$ conversion time A/D converter. The accuracy is 0.01% of ± 5 V, to which it settles in 500 ns. The droop rate is $100 \mu\text{V}/\mu\text{s}$, i.e., less than 0.1 least significant bit (LSB) of a $1\text{-}\mu\text{s}$, 12-bit converter.

Confusion often exists between manufacturers' definitions of aperture time, acquisition time, and settling time. Figure 4 is a timing diagram defining these times. It also shows the specific times for the SHA-IIA. Other pertinent data on the SHA-IIA are: The input impedance is $10^{11} \Omega$. The output can supply 20 mA at ± 5 V. The settling time to 0.01% of ± 5 V or 5 mV accuracy is 500 ns maximum and for 0.1% of full scale (FS), the settling time is 300 ns. The full power frequency response in the track mode is 1.5 MHz.

The SHA-IIA has facility for connection of an external $100\text{-}\Omega$ potentiometer for zero offset adjustment. This offset adjustment controls an internal compensation voltage and should be adjusted during the hold mode. During the *track* or *sample* mode there then remains a residual offset of a few millivolts which, however, is of no concern for the final output. Figure 5 is a chart showing the zero adjusted integrator output and the zero adjusted sample-and-hold amplifier output. The integrator input is assumed to be a DC voltage.

It was discovered that the SHA-IIA offset is critically sensitive to the switching speed of the digital control signal. The logic control signal is then derived directly from a high-speed FF.

IV. Analog-to-Digital Converter Module

The DATEL ADC-N10BC3 is used as the analog-to-digital converter. It converts the output from the sample and hold circuit to a 10-bit word in less than $4 \mu\text{s}$. It is factory set for $\pm 5\text{-V}$ FS input. The output code is the 2's complement code shown in Fig. 6. The unit generates its own clock to supply a conversion rate of approximately 250 kHz. It requires a positive *start* convert pulse. It resets at the high level and starts to convert on the trailing edge. It responds with both a conversion-in-progress status signal and the bit conversion clock pulses. The unit has the facility for a $25\text{-k}\Omega$ potentiometer for offset adjustment and a $100\text{-}\Omega$ potentiometer for gain adjustment. The offset and gain adjustments are not entirely independent.

V. Output Digital Demultiplexing Circuit

Shown in Fig. 7 is the output demultiplexer implemented with wired OR line driving NAND-gates.

There are two output connections for each channel—one for the digital demodulator and one for the test system. The output to the test system is isolated from the demodulator output through a set of inverting buffers. The same digital control signal that controls the integration and sample-and-hold circuit also controls the output demultiplexer.

VI. Timing Control Unit

The input to the timing control unit shown in Fig. 8 is an auxiliary clock signal in the form of a 200-ns-wide negative pulse from +5 V to ground appearing at intervals no shorter than 5 μ s. The clock signal is received by an inverting amplifier and is used to trigger an edge-triggered high-speed FF. The output from this FF controls the integrators, the sample-and-hold circuits, and the digital demultiplexer. The input clock pulse is AND-ed with the FF outputs to form the A/D converter *begin-conversion* pulses.

VII. Test System

The test system contains a five-position 10-bit multiplexer. Each channel may be manually selected, or all channels may be scanned at high speed. The test system also contains a test channel which consists of a set of 10-bit switches. The output from the multiplexer drives a 12-bit de-glitch, D/A converter whose output may be biased ± 5 V for high-gain scope studies of \pm FS. The test system also contains a clock pulse simulator.

VIII. Clock Simulator

Figure 9 is a block diagram of the clock simulator. Cascaded programmable 4-bit binary ripple counters are used. These counters are used only as dividers and are connected to count between two vectors selected for convenient detection and set operation. This connection of the pulse simulator lends itself to easy modification.

The 5-kHz clock is intended as system clock during offset adjustment of the integrators. The 200-kHz clock is used as system clock to simulate normal operation. The test system requires a clock for driving the 5-channel multiplexer and the digital-to-analog converter (DAC) hold

register. The clock simulator output is for this purpose externally connected back into the test system.

IX. Multiplexer

Figure 10 shows the five-position 10-bit multiplexer and the bit-switches of the test channel. The multiplexer sequencer shown in Fig. 11 is a simple 3-bit binary counter equipped with a mode switch for changing its sequence from 0 through 4 to 1 through 4. During dynamic test of all channels with a known DC input signal one can then, in the 0 through 4 sequence, reference the operation of the four channels to the digital input from the test channel. During observation of channels 1 through 4 with a low-frequency dynamic input signal, a check can be made of the uniformity between the analog channels. Figure 12 shows the connection of the mode switch. In positions 1 through 4, it bypasses the sequencer and provides a 3-bit address for the multiplexer. In positions 5 and 6, the dynamic sequencer is connected to sequence between 0 and 4 and between 1 and 4 respectively.

X. Test-System Operation

With the mode switch in "CHANNEL 0" position, the bit-switches are connected through the multiplexer to the DAC which is then adjusted for zero and FS, i.e., ± 5 -V output. Zero-volt output is checked on a 4-digit digital voltmeter (DVM) and on an oscilloscope with the amplifier in a high-gain position. On the oscilloscope one can then study the switching of the LSB.

The integrators and the sample-and-hold circuits are initially zeroed with inputs grounded using clock 2 (200- μ s repetition rate) for the integrators and clock 1 (5- μ s repetition rate) for the sample-and-hold.

With the system input grounded, the analog-to-digital converter (ADC) offset is zeroed for each channel, while reading the DVM and scope with reference to channel zero. In adjusting the DAC for FS, the bit-switches of the test channel are used. In adjusting the analog channels for FS, a DC voltage is connected to all channels, which results in an integrator output voltage of 5 V after 5 μ s. The hold circuit output is observed on a high-gain oscilloscope and all integrating resistors are adjusted so that the FS hold voltage is the same for all channels. All ADCs are then zero- and gain-adjusted in the test system scanning

mode. For further details, see the adjustment procedure in Table 1.

To permit an oscilloscope to be used with high gain for FS observation during FS adjustment of a channel, an offset is made to the DAC output in the test system, resulting in an output voltage near zero. This connection is shown in Fig. 13. For further details, see Table 1.

XI. Operation Results

The analog input channels were used during June 1972 as part of the successful Venus Radar Interferometer Experiment equipment. The unit performed without failure, and recalibration of the equipment at the Goldstone Venus Site (DSS 13) proved to be easy using the built-in test system.

Reference

1. Rourke, K. H., and Ondrasik, U. J., "Improved Navigation Capability Utilizing Two-Station Tracking Techniques for a Low-Declination Distant Spacecraft," in *The Deep Space Network Progress Report*, Technical Report 32-1526, Vol. VII, pp. 51-60. Jet Propulsion Laboratory, Pasadena, Calif., February 15, 1972.

Table 1. Adjustment procedure for analog input channels

Step No.	Procedure
1.	Adjust power supplies $+5$, ± 15 to $+5.00$ and ± 15.00 using 5-digit DVM. Observe changes from no load to full load. Readjust for full load and observe long term changes.
2.	For the DAC test, set the MODE CONTROL switch to channel 0; Channel 0 refers to the manual bit switches. Set all switches to '1' and adjust DAC zero offset for reading 0.00 V on DVM and high-gain oscilloscope.
3.	Set bit switches to 1 000---00 and adjust DAC gain for $-FS$ or -5.00 V reading on DVM.
4.	Double check and readjust the zero reading.
5.	Double check and readjust the $+FS$ readings.
6.	Observe the 0 and $+FS$ readings long term.
7.	Ground inputs to all channels. Use clock simulator output 2 (200 μ s) as system clock input, and adjust zero offset of integrator (test output 1). Observe output on high-gain oscilloscope.
8.	Ground inputs to all channels. Use clock output 1 (5- μ s clock), adjust sample and hold zero offset. The internal offset during the sample period is positive. Adjust the output to read zero during the hold period. Observe on high-gain oscilloscope.
9.	Input an arbitrary DC voltage close to saturation yet observable on high-gain oscilloscope to all channels. Adjust all integrating resistor potentiometers for identical readings (clock output 2).
10.	Center set all offset and gain potentiometers for all ADCs. Input alternately ground and a DC voltage resulting in FS output. Adjust alternately all offset and gain potentiometers for all channels to converge to all zero and identical FS. Observe on high-gain oscilloscope, scanning all channels including the reference channel. The reference channel must then be changed between zero and FS adjustment. For continued observation of high-gain oscilloscope at zero volts, the DAC output must be FS offset (with offset switch) during the FS readings.
11.	Zero and FS adjustment of ADCs should, if possible, be set at points where the LSBs switch at the same point.
12.	In the 0-4 scan mode with either zero or a DC voltage input to all channels, the value of a bit-change as read on the oscilloscope may easily be identified by reference to the bit switches of the test channel.
13.	The test system affords considerable versatility, and a great many tests other than those listed above can no doubt be devised.

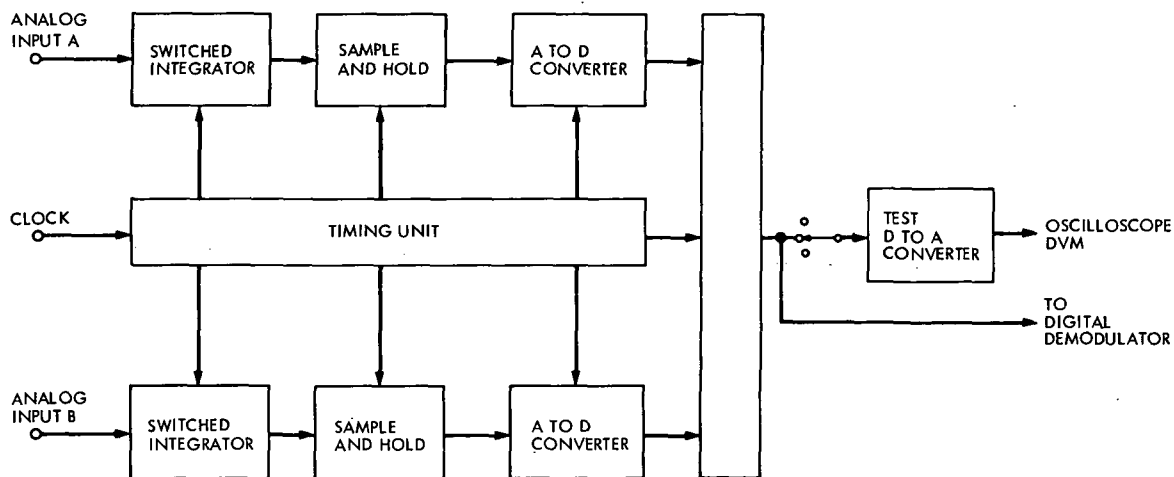


Fig. 1. Analog input integrate-and-sample system block diagram

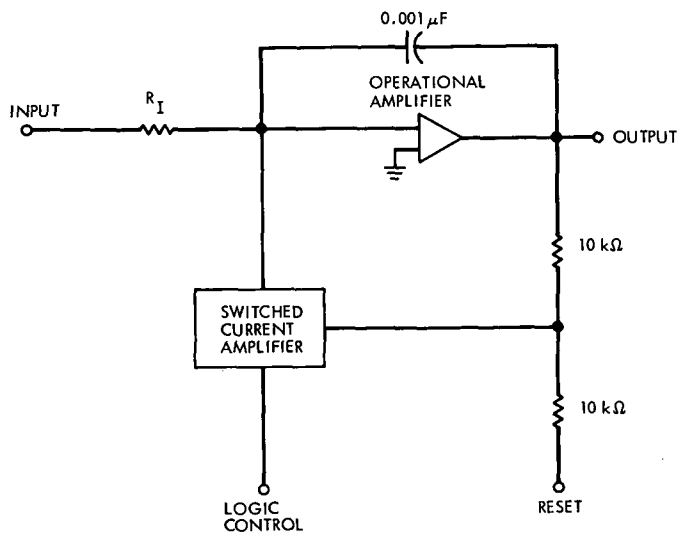


Fig. 2. Switched integrator block diagram

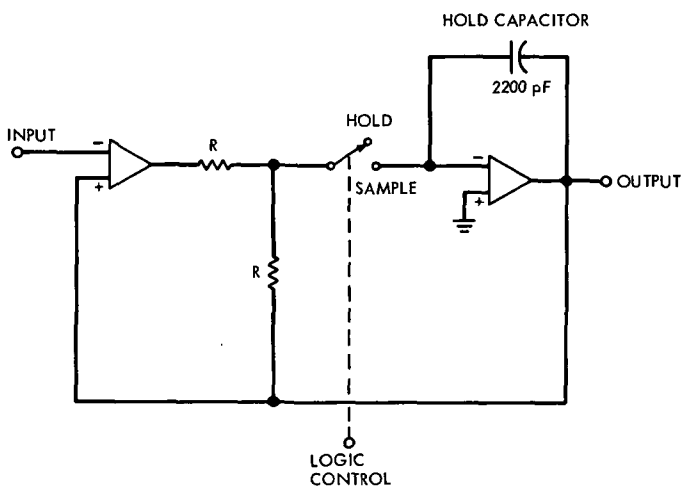


Fig. 3. Sample-and-hold amplifier block diagram

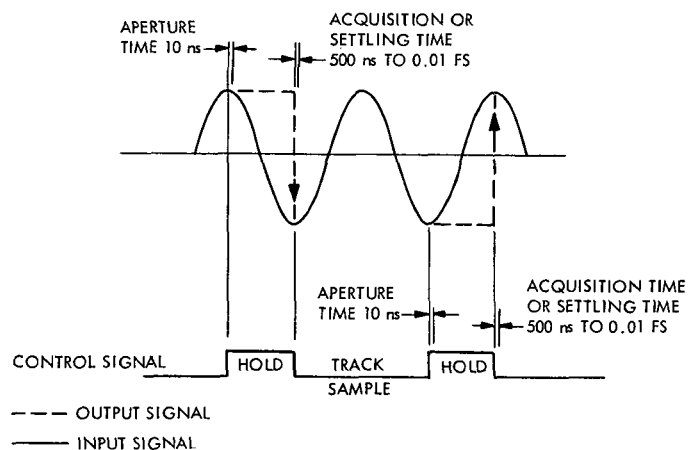


Fig. 4. Sample-and-hold timing chart and definitions

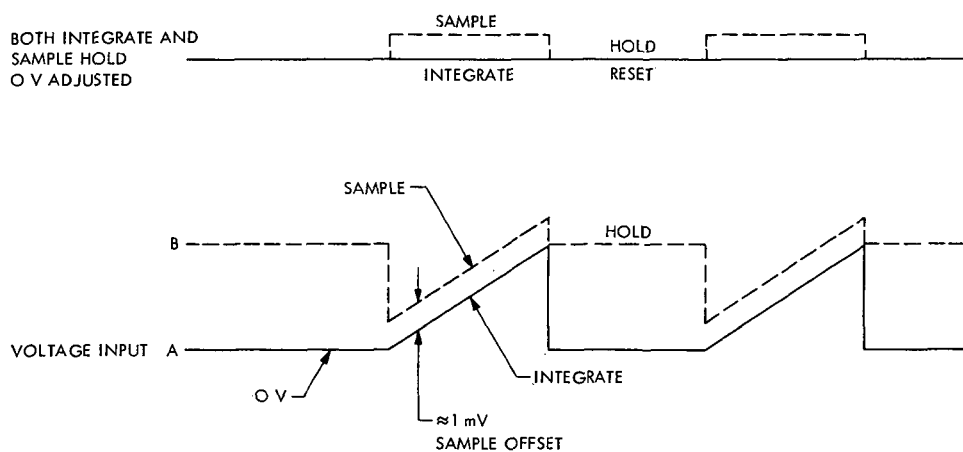


Fig. 5. Integrator output (A) and sample-and-hold output (B)

	S	2^8	2^7	2^6	2^5	2^4	2^3	2^2	2^1	2^0
+FS- LSB	0	1	1	1	1	1	1	1	1	1
+ 1/2 FS	0	1	0	0	0	0	0	0	0	0
+ LSB	0	0	0	0	0	0	0	0	0	0
ZERO REF	1	1	1	1	1	1	1	1	1	1
- LSB	1	1	1	1	1	1	1	1	1	0
- 1/2 FS	1	1	0	0	0	0	0	0	0	0
- FS	1	0	0	0	0	0	0	0	0	0

Fig. 6. 2's complement code definition

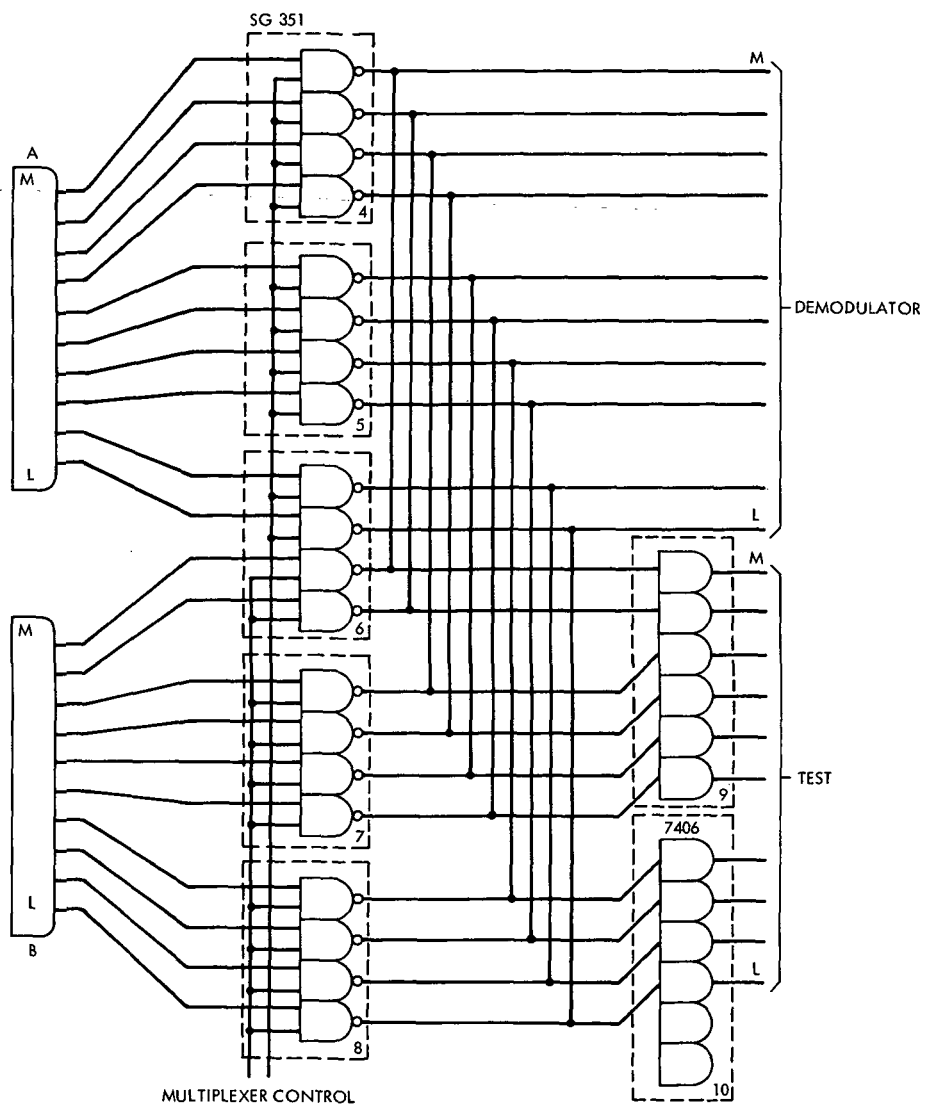
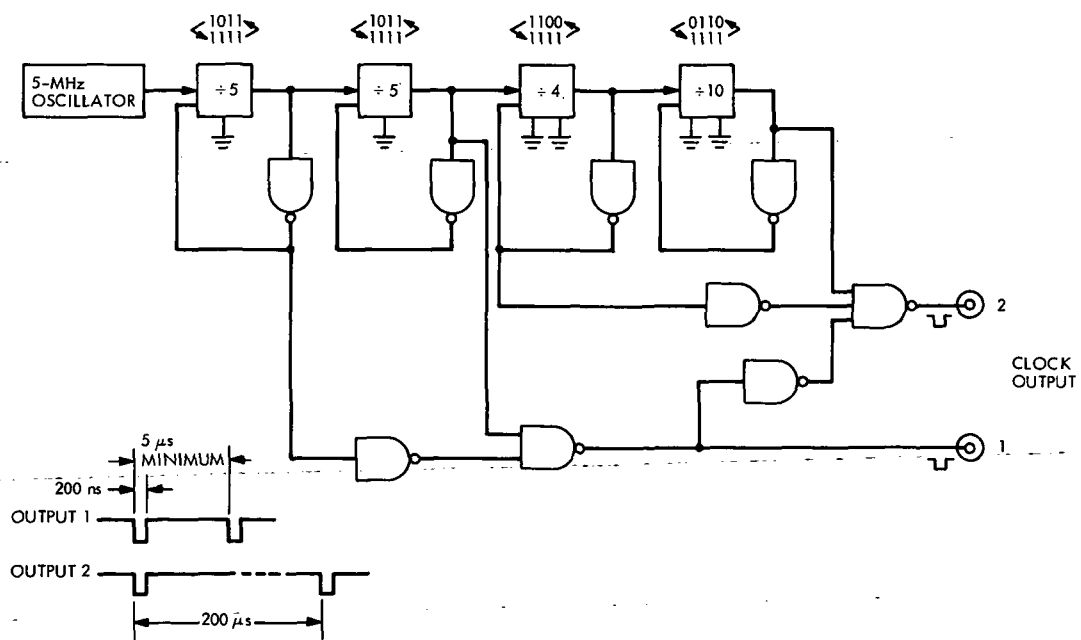
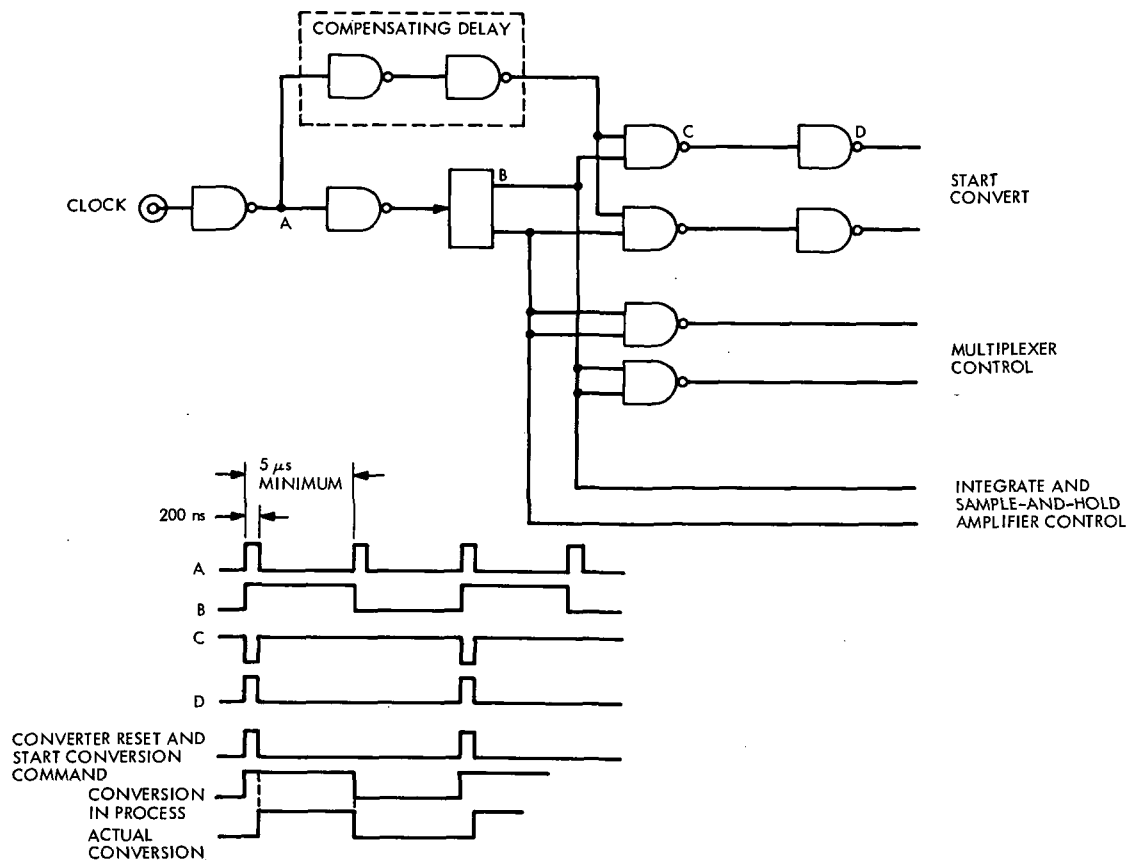


Fig. 7. Output digital demultiplexer



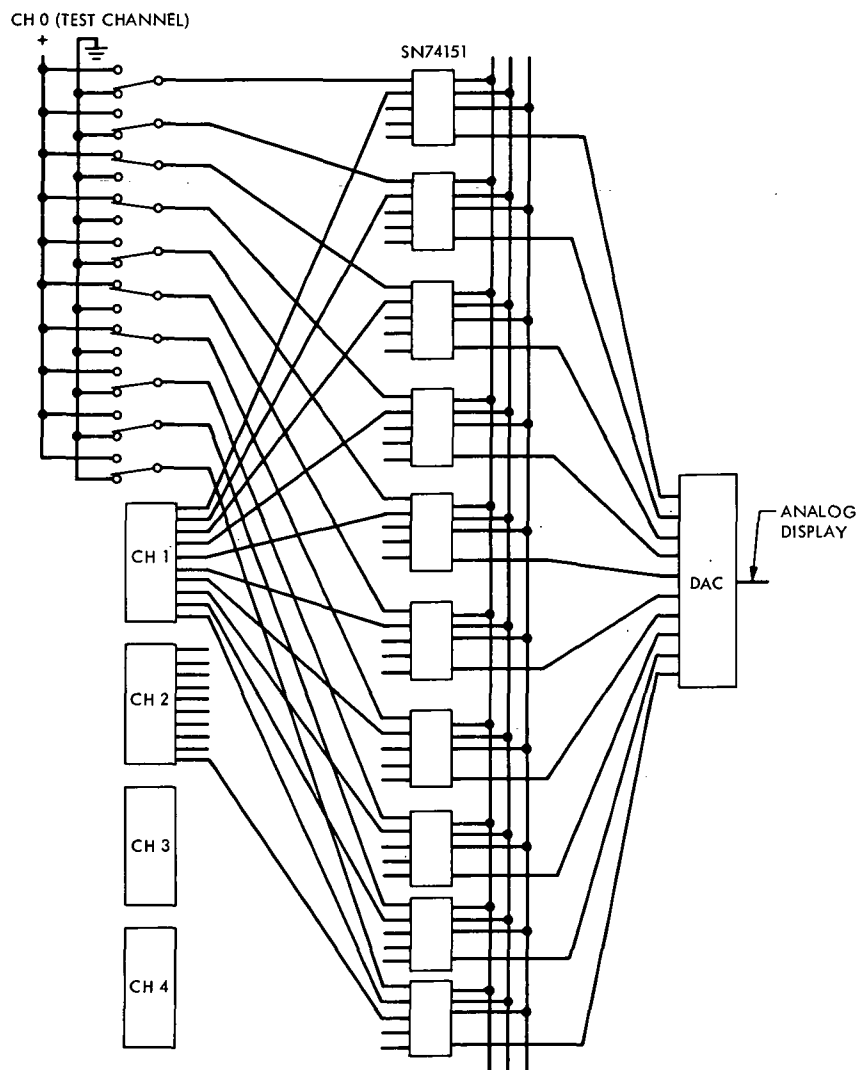


Fig. 10. 5-Channel multiplexer and test channel (bit switches)

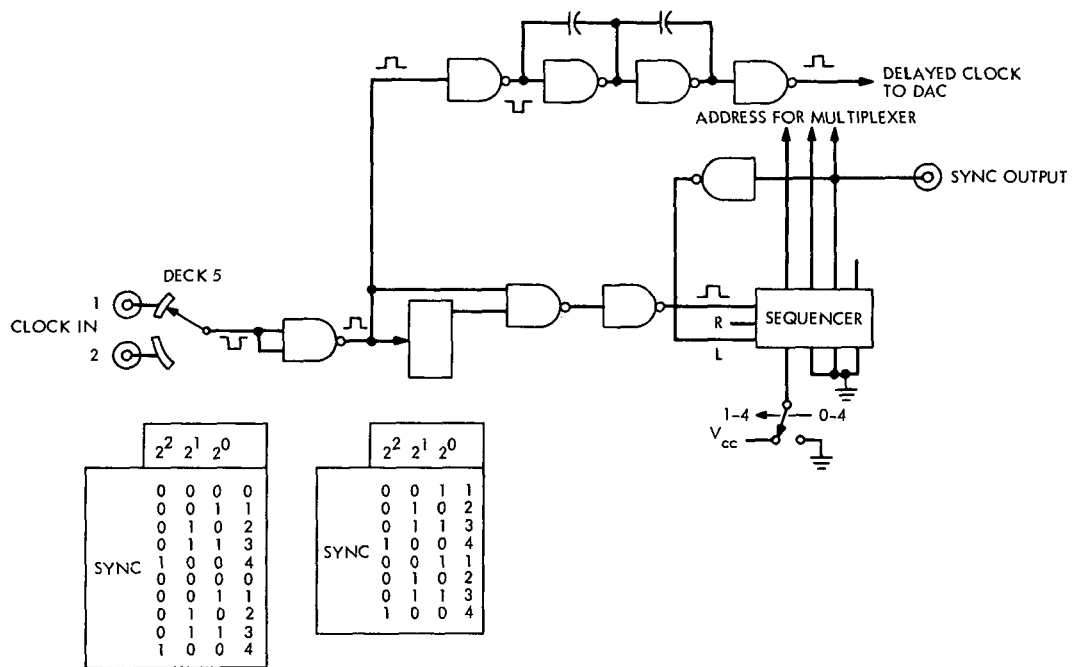


Fig. 11. Multiplexer sequencer

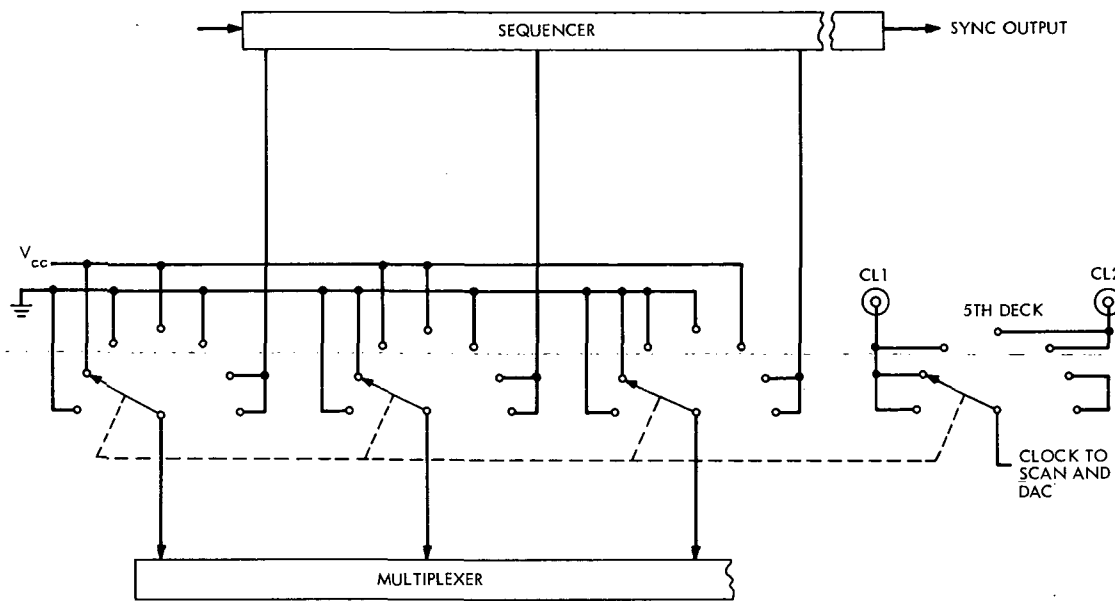


Fig. 12. Mode selector

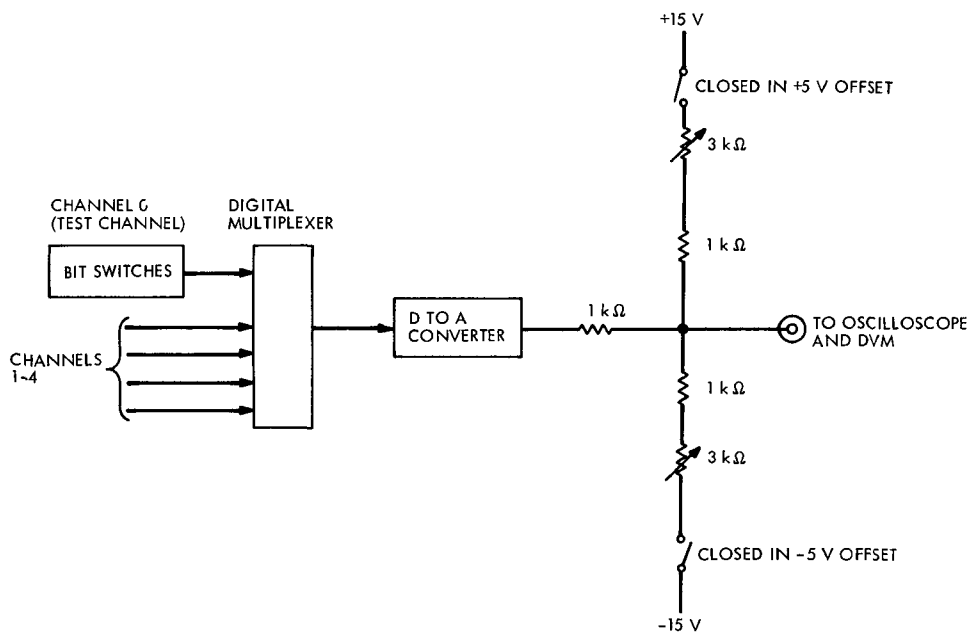


Fig. 13. DAC output offset circuit

DSN Research and Technology Support

E. B. Jackson and R. B. Kolbly
RF Systems Development Section

The activities of the Development Support Group in operating the Venus Station (DSS 13) and the Microwave Test Facility (MTF) for the period August 16–October 15, 1972, are presented, categorized by JPL section supported. Major activities include a strong planetary radar and pulsar observation program for the Communications Systems Research Section, extensive precision antenna gain measurements for the Communications Elements Research Section, and a major installation and modification effort for dual-carrier experimentation for the RF Systems Development Section. Preliminary activity in measuring the side lobe patterns of the Venus 26-m-diameter antenna is described, and the cessation of clock synchronization transmissions (due to nonavailability of polynomial predicts) is noted.

During the two months ending October 15, 1972, the Development Support Group was engaged in the following activities.

I. DSS 13 Activities

A. In Support of the Communications Systems Research Section

1. **Pulsars.** Venus Station (DSS 13) continues to devote approximately 24 hours per week (a total of 188 hours during this period) to the observation of pulsars. Information obtained includes pulse-to-pulse spacing, pulse time of arrival, and pulse shape. Pulsars regularly observed (about 22 of the 50 known pulsars) were tabulated in Ref. 1.

2. **Planetary radar.** Continuing support of the Venus/Mercury 1973 spacecraft mission, ranging measurements to the planets Mercury and Venus, have been regularly made. Ranging measurements were made with a resolu-

tion of 5 μ s (Venus) and 10 μ s (Mercury) for a total of 100 good signal runs. These measurements are made using the 400 kW transmitter and 64-m-diameter antenna at DSS 14 for transmission and reception, with pseudonoise code generation, data processing, and control being performed at DSS 13.

B. In Support of the Communications Elements Research Section

1. **Precision antenna gain measurement.** The Apollo Lunar Surface Experiments Package (ALSEP) and radio sources Cassiopeia A, Cygnus A, Hydra A, Virgo A, and 3C123 were used as calibration sources from which data were obtained to calculate the absolute gain of the 26-m-diameter DSS 13 antenna. With a known antenna gain, the absolute flux density of the "calibrator" radio sources can be ascertained and used by other stations in the DSN. A total of 269 hours was devoted to stability testing and

tracking radio sources, and 60 hours were devoted to tracking ALSEP. All measurements of the radio sources were performed using semiautomated data-taking techniques with the SDS-930 computer performing automatic boresighting. Tracking was performed using a DSS 13 computer program identified as Scan and Correct Using the Receiver (SCOUR).

2. Weak source observation. Measurements were made for a total of 185 hours on ten different radio sources (see Table 1 for sources and positions) and an additional 60 hours were spent on sky survey with the antenna fixed at various positions. Data taking is automated using the SDS-910 Computer for antenna pointing and boresighting and an HP 5360A Computing Counter with accessory plotter and printer for control and measurement.

3. Side lobe patterns (26-m-diameter antenna). Configurations of spacecraft which require tracking while pointing close to the sun (such as when the spacecraft are going through a sun occultation) result in problems with sun-generated interference entering the antenna through side lobe response. Data are being taken, using the 26-m-diameter antenna at DSS 13, of antenna patterns before and after the quadripod legs are covered with metal covers. From these data, prediction of similar response of the 64-m-diameter antenna can be made, and antenna positioning for close sun tracking can be optimized accordingly. The Communications Elements Research Section has been performing these measurements using a newly developed computer program which scans the antenna across a source with a raster scan similar to a television set raster scan. During this reporting period, a total of 58 hours of "computer-only" and 10 hours of actual antenna tracking were utilized.

C. In Support of the RF Systems Development Section

1. Acceptance testing of 400-kW klystrons. Two 400-kW, 2388-MHz klystrons (X3070), one repaired from an earlier failure, and one new, were received from Varian Associates and have successfully undergone complete testing to ascertain that performance is according to specification. These tests were performed in the High Power Test Area at Building G-53A.

2. Dual uplink carrier testing. In order to evaluate techniques of dual uplink carrier generation and methods of minimizing intermodulation resulting therefrom, an experimental facility has been established at DSS 13. This facility makes use of the 26-m-diameter antenna and the 100-kW DSN uplink frequency transmitter installed thereon. To perform testing and experimentation, the elec-

tronics room on the 26-m-diameter antenna has been equipped with a high-power harmonic filter, diplexer, maser, high-power coupler, two high-power water loads, a side-looking feedhorn, and appropriate waveguide switches, terminations, interconnecting waveguide, etc., to make a versatile test setup.

"Baseline" testing of the uplink system has been accomplished, and measurement of the intermodulation products existing in the receive band has begun. Methods of minimizing these intermodulation products will then be tested with the intent of establishing a technique by which dual carriers can be generated for support of MVM 73 with a minimum of interference to the downlink signal.

D. In Support of the DSIF Operations Section

1. Clock synchronization transmissions. Following schedules established by DSN scheduling, clock synchronization transmissions were made as indicated in Table 2. However, due to nonavailability of the necessary polynomial predictions (whose production has ceased), clock synchronization transmissions were terminated on September 27, 1972 (see Table 2).

II. Microwave Test Facility Activities

A. In Support of the RF Systems Development Section

1. Dual uplink carriers. The Microwave Test Facility has been engaged in two areas of dual carrier investigation: (1) installation of microwave components to allow diplexing in the DSIF bands on the Venus (DSS 13) 26-m-diameter antenna and (2) in cooperation with the Communications Elements Research Section, investigation of the noise properties of antenna panels and joints under RF radiation.

The installation of the microwave components for high-power diplexing was accomplished in two phases. Phase I consisted of installing a 400-kW harmonic filter and directional coupler at the output of the 100-kW DSIF transmitter in the electronics room of the Venus 26-m-diameter antenna. Phase II was the final test configuration with the addition of a diplexer, transmitting filter, maser, directional coupler, as well as load select and maser calibration waveguide switches. When Phase II was completed, the diplexer could be connected to the 26-m-diameter antenna, a water load, or a side-looking horn for isolation of noise sources. The components installed in Phase II were mounted as a subassembly on a "skid plate" for ease of removal or modification. Figure 1 is a block diagram of the Venus station electronics room as modified. System

temperature (Fig. 1 configuration) was calculated to be 35 K and measured at 33 K. This difference can be attributed to waveguide runs that were shorter than originally estimated due to a relocation of the maser.

2. Personal electromagnetic radiation monitor. The breadboard stage has been completed on a personal RF (non-ionizing) radiation monitor. This unit is a pocket-sized audible-alarm device for warning personnel when they are exposed to an RF power density in excess of a preset limit. This unit is simple in design and operates from a 9-V transistor radio battery. To minimize current drain, the output of the antenna/detector is compared with a preset voltage level using a micropower operational amplifier (RCA CA3078T), and a COS/MOS gate (RCA CD4001E) is used as a gated oscillator. This unit can be set to respond to signals below 1 mW/cm² or a higher level, and has a standby power drain of less than 1 mA. Figure 2 is a schematic of the antenna/detector/comparator/gated oscillator stage.

3. Clock synchronization buffer crowbar. When a fault is detected in the 100-kW X-band clock synchronization transmitter, the radio-frequency drive is removed by means of crystal switches. Since these switches are operating at 7149.5 MHz, their insertion loss was approximately 5 dB. A crowbar circuit which removes the drive by removing beam voltage from the driver klystron was designed by Microwave Test Facility personnel and in-

stalled with a resultant increase in available drive, as a result of the removal of the crystal switches, of approximately 5 dBmW. This decreased loss remedied a marginal drive situation and enabled reduction of the operating voltage on the driver klystron with attendant increase in life and reliability.

B. In Support of the Communications Elements Research Section

1. Noise bursts on antennas. Experiments with antenna panel joints were performed at the Microwave Test Facility (in cooperation with Communications Elements Research Section personnel) to determine the noise characteristics of different methods of joining antenna panels. Figure 3 illustrates the test configuration for testing the various panels. A Cassegrain feed cone (Model SCU) was installed horizontally and illuminated an array of four panels set at a 45-deg angle. Since this particular feed cone did not have an internal diplexer, it was necessary to mount a diplexer, transmission filter, and maser external to the feedcone.

Noise bursts were encouraged by shaking the panels with an eccentric weight on the shaft of a 250-W ($\frac{1}{2}$ hp) electric motor (Fig. 4). Various methods of joining the panels have been tested and it is planned to further test these techniques on the Venus antenna in connection with other dual-carrier tests.

Reference

1. Jackson, E. B., "DSN Research and Technology Support," in *The Deep Space Network Progress Report*, Technical Report 32-1526, Vol. VIII, pp. 68-73, Jet Propulsion Laboratory, Pasadena, Calif., Apr. 15, 1972.

Table 1. Sources and source positions used in weak source observation program

Source	Position at time of observation	
	Right ascension, deg	Declination, deg
3C33	16.850	13.179
3C45	15.564	08.050
3C147	85.132	49.839
3C248	150.977	30.598
3C273	186.929	2.202
3C348	252.449	5.044
3C353	259.772	-0.957
Beta Lyrae	282.267	33.324
Cygnus X-1	299.326	35.266
Cygnus X-3	300.391	40.870

Table 2. Clock synchronization transmission

Station	Number of transmissions
DSS 41	16
DSS 42	2
DSS 51	6
DSS 62	4

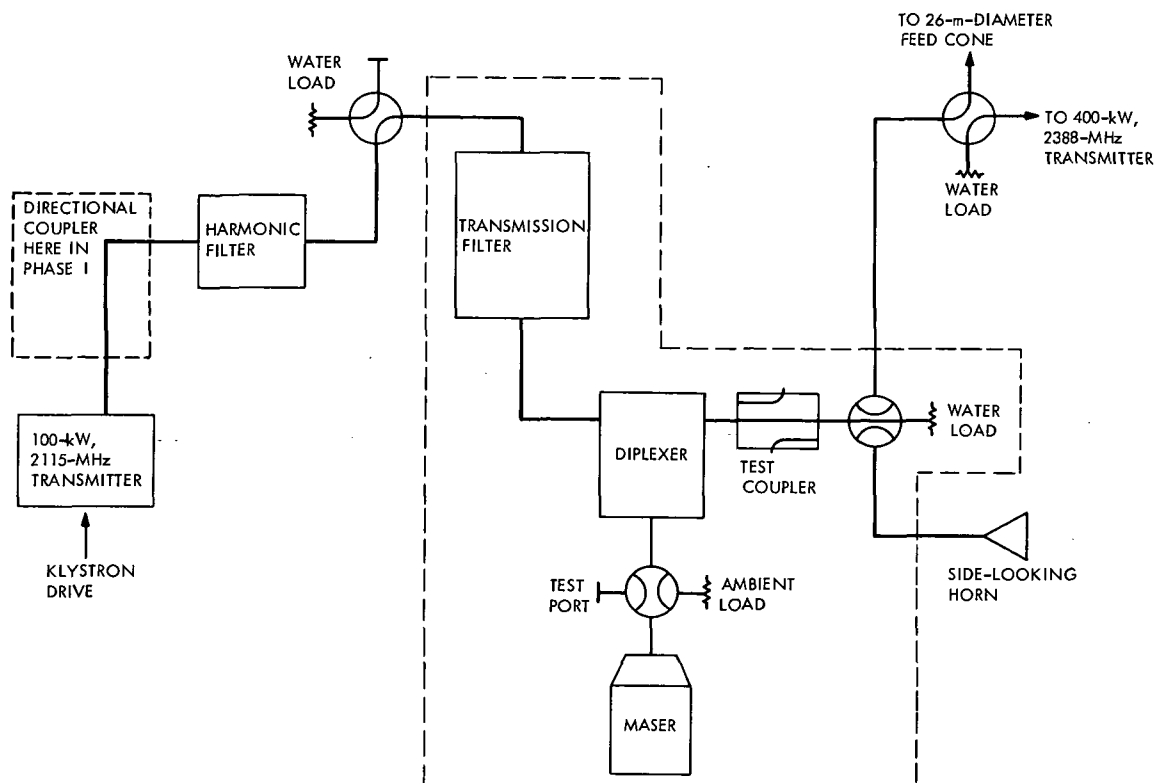


Fig. 1. Microwave configuration for dual carrier experiments at Venus 26-m-diameter antenna

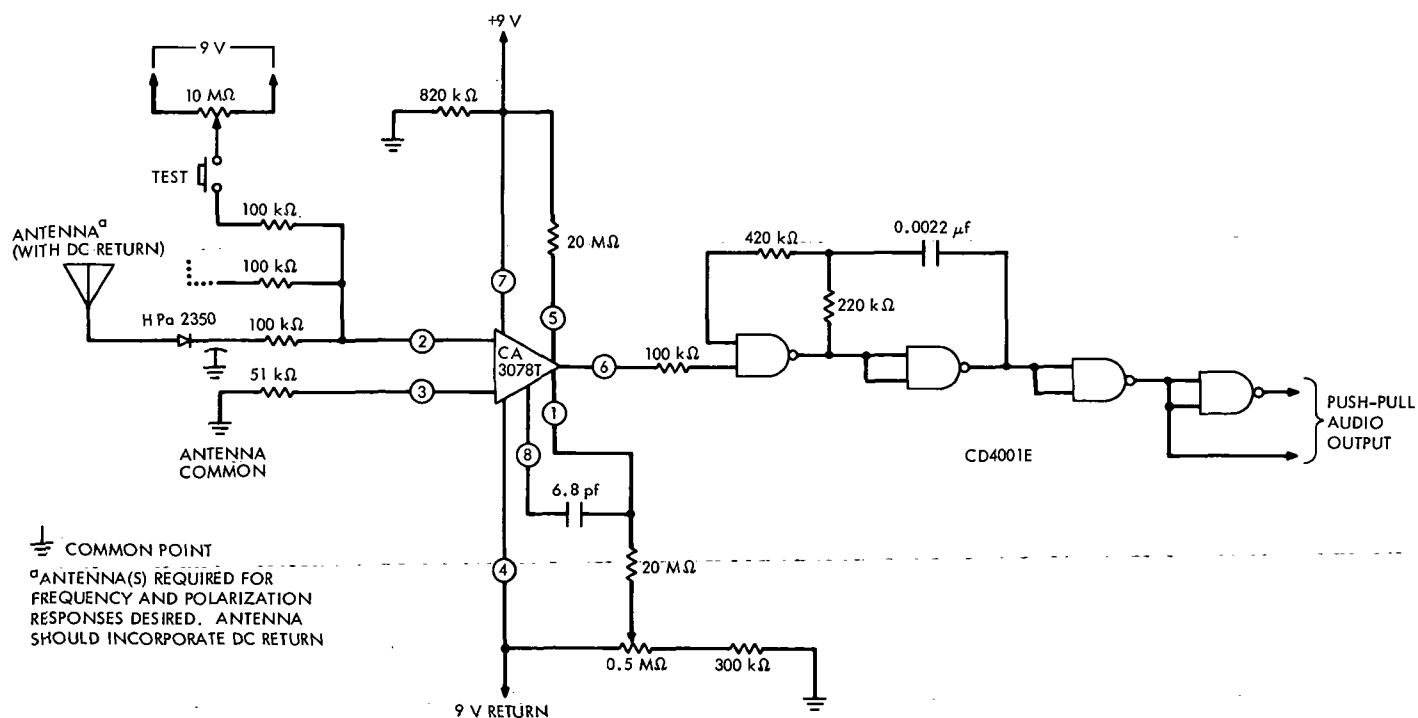


Fig. 2. Schematic diagram of personal non-ionizing radiation monitor

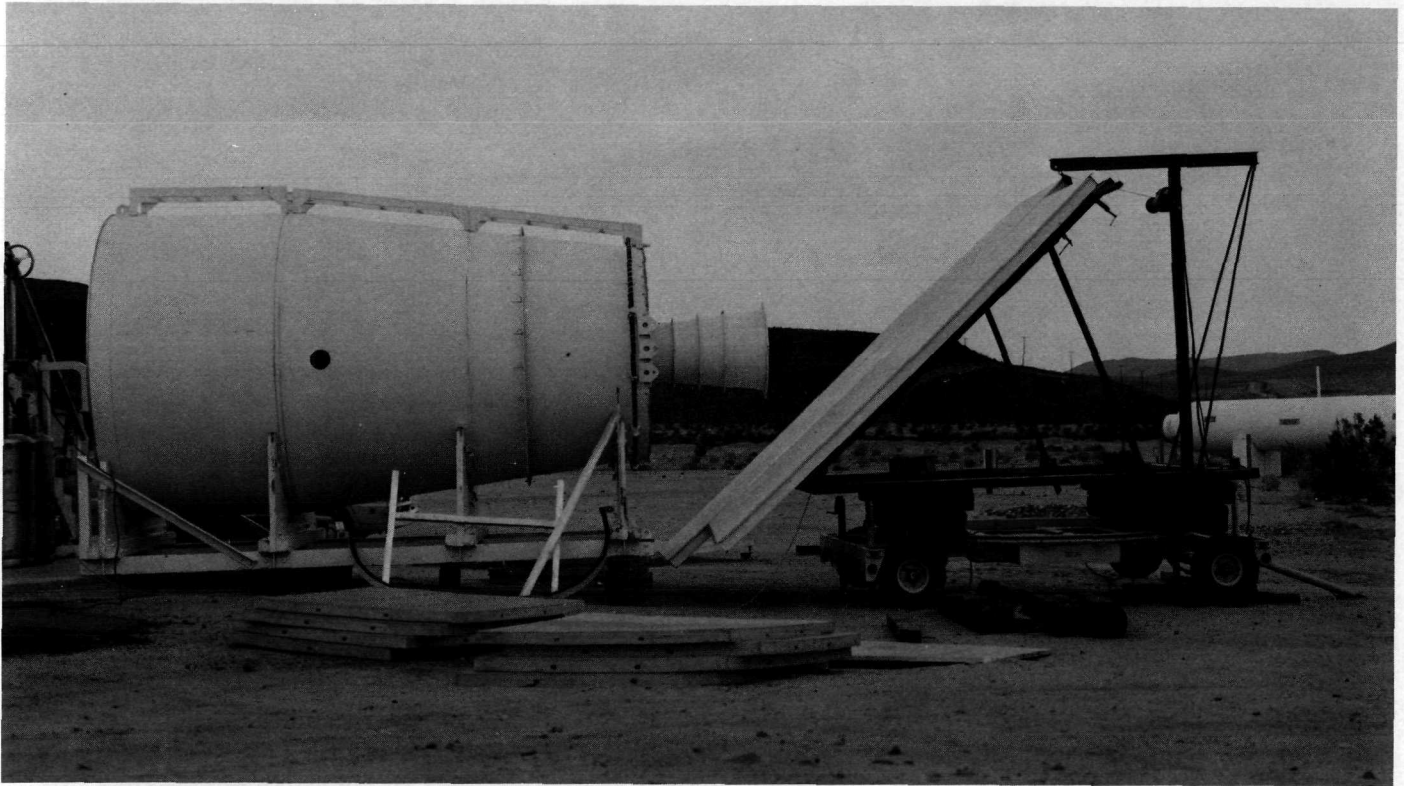


Fig. 3. Test setup for noise burst testing



Fig. 4. Details of "panel shaker" arrangement

An Inventory and Procurement Policy for the Deep Space Network

I. Eisenberger, F. R. Maiocco, and G. Lorden¹
Communications Systems Research Section

A technical description of a proposed inventory and procurement policy for ordering and allocating maintenance and operating supplies throughout the Deep Space Network is presented. This policy differs from the conventional economic lot-size procurement policy in that the reorder point for the Network Supply Depot (NSD) depends upon the stockage levels at all area station or Complex Supply Facilities (CSF), as well as on the level at the NSD. Thus, by basing reorder decisions upon the state of the inventory supplies throughout the entire DSN, an efficient cost minimizing policy is possible. Safe minimum inventory levels are established for each CSF by means of statistical decision theory techniques which require NSD to reorder whenever one or more of the CSFs reaches its prescribed minimum. Some results of a statistical study of the effect of this policy are included.

I. Introduction and Summary

The key feature of the following proposed inventory and procurement policy for the Deep Space Network is the continuous updating of data files in the Integrated Logistics System's (ILS) Supply Inventory Subsystem (SIS). These data files contain the following for each inventory item:

- (1) The stockage level on hand at each CSF and at NSD.
- (2) The (estimated) demand distribution at each CSF.
- (3) Cost parameters associated with the item.

This updating is to be accomplished by utilizing the existing Complex and Network teletype facilities which access a central computer for updating data files via a remote terminal. Another means to update data files is to automate the transaction at each CSF at the time of issuance. Such data could be stored in a cassette tape and in a specified format for later access by the central computer. The transaction information would be available for file maintenance on an as-required or near-real-time basis.

Each time a demand for a particular item occurs at one or more of the CSFs (and their computer files are updated at NSD), the sufficiency of the current stockage level at a CSF is compared to a "safe" minimum stockage level for the particular CSF. This level is a function of the probability of being out of stock during one lead period and of

¹Consultant, California Institute of Technology, Mathematics Department.

the cost parameters. If the current stock level at even one CSF falls below the minimum, a computer program determines

- (1) The numbers of units to be shipped from the NSD to certain CSFs.
- (2) If NSD is out of stock, the number of units to be ordered by the NSD from outside sources.

When a shipment is received at NSD, a program is run which prints out

- (3) The number of units to be shipped to each CSF.
- (4) The number of units (if any) to be placed in NSD inventory.

An alternative mode of operation which is slightly less effective is to make the computer run yielding (3) and (4) at the time the order is placed. The stock allocated to NSD in (4) is called the *reserve* stock. Two types of policies are considered below:

- (1) No-reserve policy (NR-policy) under which all units are allocated and shipped to CSFs as soon as they are received at NSD.
- (2) One-stage reserve policy (R-policy) under which a number of units determined in (4) are placed in NSD inventory, and all are shipped to CSFs as soon as one of the CSFs reaches its minimum level.

These policies are discussed in Section II. The choice between them depends on a tradeoff between the reduced CSF inventory levels (and, hence, costs) brought about by R-policies and the increased costs of handling and shipping from NSD to CSFs. It is anticipated that the no-reserve policy is preferable for many low-cost items.

Both policies are implemented through the use of an optimal allocation table (see Section II) which is based upon estimated mean demand rates at the CSFs. These estimates are simply the means of the demand distributions, which are continuously updated. Tables listing these optimal allocations are easily constructed for a variety of demand rates taking advantage of the fact that the allocations depend only on the ratios of CSF mean demand rates. For critical or costly items, the computational algorithm used to construct the tables can be used directly each time an allocation is necessary. Both the NR- and R-policies have another important feature in common: a minimum inventory level (greater than zero) is not maintained at NSD. Maintaining such a minimum incurs excessive inventory costs because the minimum may be reached

and NSD reorders may be placed at a time when the levels of inventory on hand at the CSFs are large. An efficient cost-minimizing policy must base reorder decisions upon the state of the entire system, i.e., the levels of inventory on hand at the CSFs as well as the NSD level. It should be noted that the lead period used to determine safe CSF minimum levels includes the time for NSD to receive the order plus the shipping time to the CSFs.

The size of the NSD reserve stock (in the R-policy) tends to be small compared to the total quantity allocated to the CSFs, typically 10–15%. This occurs because the effectiveness of the R-policy in reducing average inventory costs depends upon all CSFs reaching (or approaching) their minimum levels at approximately the same time. The most effective size for the reserve stock tends to be in the range where it serves as a small “correction” to the chance fluctuations around the mean demand rates.

The method used to determine the size of an NSD order, also discussed in Section II, is a modification of the conventional economic lot size model (Refs. 1, 2) designed to take into account the effects of ordering simultaneously for all CSFs.

The question of when to order, i.e., determining the safe minimum levels for the CSFs, is taken up in Section III. The cost parameters determine what is called (in the following discussion) a *cost-criticality quantile*. An inventory level is considered safe if it exceeds the cost criticality quantile of the (current) demand distribution. (In Section III, the current estimate of the demand distribution is called the *posterior distribution* of Y , where Y is the demand during one lead period). Thus, the heart of the method of determining CSF minimum levels is the derivation of estimated demand distributions for the CSFs. These estimates are based on:

- (1) Prior information regarding demand patterns for an item (e.g., “engineering judgment”).
- (2) The continuously updated demand experience at each CSF.

Source (1) may not be available for many items; in any case, its influence diminishes steadily as demand experience is accumulated.

A natural way of obtaining an estimate of the demand distribution is to assume that its mean is the observed mean demand and then use the standard model of a Poisson distribution with that mean. The inadequacy of this approach results not from the Poisson model (a gen-

eralized version of which is used in Section III), but rather from the unequal consequences of overestimating and underestimating the mean demand.

To illustrate, suppose the mean demand is actually 10 and the distribution of demand is given by the solid curve in Fig. 1.

The left-hand dotted curve represents the estimated demand distribution if (through chance fluctuation) one observes a mean demand of 7. The right-hand dotted curve comes from an observed mean demand of 13. For typical values of cost parameters, the cost-criticality quantile is around 0.90, so that shortages occur in only one-tenth of the lead periods. Thus if the left-hand dotted curve were assumed true, the minimum level s would be set at about 10, say, so that the shaded area is only 10% of the area under the curve. Recall, however, that the solid curve is the true demand distribution, so that the true probability of a shortage during any lead period would be about one-half. If an error of compatible magnitude were made in the opposite direction (i.e., overestimating the mean demand) one would have an estimated demand curve like the one on the right-hand side of Fig. 1 and would set s at about 16. As a consequence of this overestimation, an extra three units would be maintained in inventory, resulting in an added inventory cost. This added cost would have less impact than the very high shortage probability resulting from underestimated mean demand.

It is clear, therefore, that minimum levels should be estimated conservatively. To what degree and according to what formulas these levels should be estimated are discussed in Section III through the use of statistical decision theory. For the purpose of setting CSF minimum levels, all of the information derived from observed demand (and possibly prior information) can be summarized in the estimated (or posterior) demand distribution, which is easily updated each time a CSF demand is experienced.

Also included in Section III are some results of an extensive investigation which was carried out to evaluate the performance of the procedures developed for setting CSF minimum levels (i.e., deciding when to reorder). An additional aim of this investigation was to develop guidelines for choosing the three parameter values needed to specify such a procedure. The art of choosing these parameter values is one of the main topics of Section III. In application to the DSN, large categories of items would be subject to the same parameter choices.

II. Procurement and Allocation Policies

A. Inventory Concepts

The performance of any inventory policy is measured by the average cost it incurs per unit time and the frequency and severity of shortages. A convenient set of parameters to use in expressing the average cost is the following (all referring to a single inventory item):

M = mean demand per year for all CSFs combined

h = cost of stocking one unit for one year

K = fixed cost of preparing, handling, and shipping an order (excluding "per unit" costs)

T = mean time between reorders (in years)

W_i = average inventory at i th CSF when new shipment (not reserve shipment) is received.

Note that the last two parameters depend on the policy chosen while the first three do not. We are also concerned with the parameter

U_i = average shortage at i th CSF when reorder arrives. (When there is no shortage, "0" is averaged in.)

The average inventory cost can be expressed in terms of the specified parameters as

$$C = \frac{1}{2} MTh + \frac{K}{T} + h \sum_i W_i \quad (1)$$

and this cost is incurred along with an average shortage

$$\sum_i U_i$$

Obviously, lower average shortage can be achieved by maintaining higher stockage levels, thus resulting in greater average cost, Eq. (1). The tradeoff between the two must be made on the basis of an assessment of the importance of shortages (see Appendix A on the cost criticality quantile). To help in making this assessment, one can use the methods of Appendix A to examine the relationship between average cost and expected shortage, i.e., to see how much reduction in expected shortage is "bought" by successive increments of average cost. In this Section and Section III, we are interested in developing a range of policies, all of which are efficient in the sense that their average cost cannot be improved without incurring greater expected shortage. A mathematical device for characterizing such policies is to introduce a criticality parameter in the form of a "cost":

p = cost per unit of shortage

and consider the overall average cost per year as

$$\frac{1}{2} MTh + \frac{K}{T} + h \sum_i W_i + \frac{p}{T} \sum_i U_i \quad (2)$$

The efficient procedures, then, are those which minimize Eq. (2) for some value of $p > 0$. By partial differentiation with respect to T , it is easily seen that

$$T = \left[\frac{2(K + p \sum_i U_i)}{Mh} \right]^{1/2} \quad (3)$$

is necessary to minimize Eq. (2). The value of

$$\sum_i U_i$$

depends on the choice of minimum levels, which is considered in Section III. Since optimality in this choice depends on T , a standard iterative procedure is useful for determining both simultaneously (Ref. 2). For the ranges of parameter values typical of the DSN, the first term in the numerator in Eq. (3) dominates, so that

$$T = \left(\frac{2K}{Mh} \right)^{1/2} \quad (4)$$

is a satisfactory approximation.

Given the value of T desired, we have the problem of choosing the quantity to be ordered to achieve that value of the expected time until reorder is necessary. Assume for the time being that the following condition is imposed: shipments arriving at NSD are immediately allocated and shipped to the CSFs, with no inventory maintained at NSD. (As discussed below, this approach is a reasonable one for many low-cost items.)

B. Allocation Problem for NR-Policies

Let $t_1^i, t_2^i, t_3^i, \dots$ be the (random) waiting times between successive demands at the i th CSF. The t_j^i 's are assumed independent and exponentially distributed with mean $1/\lambda_i$ depending on the CSF (estimated from demand experience). It is assumed that each demand is for a single item. (This simplifying assumption is relaxed for the considerations of Section III, but to do so here would unnecessarily complicate the computations.) Given n_1, \dots, n_k items allocated to the CSFs (in excess of their minimum stockage levels), the expected time until one of the CSFs reaches its minimum is

$$E \min_i (t_1^i + \dots + t_{n_i}^i) = \int_0^\infty \prod_{i=1}^k F_{\lambda_i t}(n_i - 1) dt \quad (5)$$

where $F_{\lambda t}$ denotes the Poisson distribution function with mean λt . It is not necessary to compute Eq. (5) for all possible k -tuples (n_1, \dots, n_k) —only for k -tuples which are efficient in the sense that they maximize

$$E \min_i (t_1^i + \dots + t_{n_i}^i)$$

among all k -tuples with the same initial inventory total, $n_1 + \dots + n_k$. (By a Martingale systems theorem, this efficiency criterion can be shown equivalent to minimizing the expected total surplus inventory, $\sum_i W_i$.)

Let Q denote $n_1 + \dots + n_k$. A simple computer program evaluates Eq. (5) numerically and optimizes the choice of n_1, \dots, n_k recursively for $Q = k, k + 1, \dots$. Given the optimal allocation for $Q = \ell$, the optimal allocation for $Q = \ell + 1$ is obtained by computing Eq. (5) for each allocation giving one more unit to some CSF than the allocation for $Q = \ell$. There are k such allocations and the one yielding the largest value in Eq. (5) is selected. Thus one obtains an allocation table of the Table 1 type (easily stored in computer memory).

The "Expected time" column denotes the quantity in Eq. (5). The value of Q is chosen so that

Expected time \approx optimal T (mean time between orders) (6)

as closely as possible. When a reorder is necessary (i.e., at least one CSF is at its minimum) the NR-policy calls for an order size

$$\text{Order size} = Q - \sum_i (\text{residual at } i\text{th CSF}) \quad (7)$$

where the *residual* at a CSF is the inventory level at reorder time minus the minimum inventory level (e.g., zero, for the CSF that reaches minimum). The "Expected residual" column in the allocation table gives the average value of the total of these residuals, i.e., the average value of the quantity subtracted from Q in Eq. (7) to obtain the order size. Equation (7) allows for each CSF to receive as its share of the quantity ordered:

$$n_i - \text{residual at } i\text{th CSF} \quad (8)$$

where n_i is the portion of Q specified in the table. Increased efficiency of allocation can be achieved by recomputing the allocation when the new shipment arrives, thus taking into account the actual CSF inventory levels at that time. *Example:* Suppose the residuals at the CSFs at reorder time are 4,0,7,5,8,2, respectively, and $T = 1.50$ is

desired. For $Q = 117$, Table 1 gives expected time 1.50 and allocates 16,17,19,20,22,23. Thus $117 - 26 = 91$ items are ordered and are to be allocated to the CSFs by Eq. (8) as follows: 12,17,12,15,14,21.

If recomputation is made when the order arrives at NSD, then the allocation can take into account the actual inventory levels at that time. Suppose these current inventory levels (with each CSF minimum subtracted) are 2, -3, 4, 5, 6, 0, reflecting demands during lead period 2, 3, 3, 0, 2, 2, respectively. Now the actual quantity available for allocation is $91 + (2 - 3 + 4 + 5 + 6) = 105$, and Table 1 indicates the allocation of 14, 15, 17, 18, 20, 21. Subtracting the current inventory levels (in excess of minimum), we find that the 91 items are to be allocated 12, 18, 13, 13, 14, 21, which differs slightly from the results in the preceding paragraph.

C. Improved Allocation With R-Policies

We now consider some possible improvements in allocating supplies to the CSFs when the no-reserve condition is dropped and an NSD inventory can be utilized. These improvements come about by reduction of the surplus inventory term

$$h \sum_i W_i$$

in the average cost equation, Eq. (2). However, any re-supply incurs additional shipping and handling (but not ordering) costs, including the cost of placing items in NSD inventory and taking them out. These additional costs must be assessed and weighed against the expected savings in the surplus inventory term.

For low-cost items stocked in small or moderate quantities, it is clearly disadvantageous to handle an NSD supply merely to effect a small savings in CSF surplus inventory cost. For more expensive or higher-volume items, the potential savings are worth analyzing and hence a specific alternative to the no-reserve policy must be formulated.

The simplest alternative, which would incur the least increase in shipping and handling costs, is a one-stage reserve policy (R-policy) which operates as follows. A quantity R from each incoming order is placed in NSD inventory, the remainder being allocated and shipped to the CSFs. As soon as one CSF reaches its minimum stock-age level, the entire reserve stock R is allocated and shipped to the CSFs (some of them possibly receiving zero). The next time one of the CSFs reaches minimum, NSD must reorder.

The time required to ship from NSD to the CSFs is on the order of one-half the total of NSD lead period for reorder plus shipping to CSFs. Hence, the expected shortage during the waiting period for the R -supply is usually negligible. The average surplus inventory W_i is approximately equal to the average residual inventory at the i th CSF plus the minimum level, minus the mean demand during lead time. This occurs because in a typical lead period there is no shortage. Consequently, the reduction in

$$\sum_i W_i$$

resulting from an R -policy can be approximated by reduction in the total expected residual inventory (excess over minimum levels) at reorder time.

Extensive investigations of R -policies were carried out by Monte Carlo simulation on the XDS Sigma V computer and the following rules were found to be most efficient:

- (1) Choose Q and the order size as in the NR-policy (i.e., Eqs. 6 and 7).
- (2) Choose $R = 1/2$ expected residual in the allocation table, Table 1.
- (3) After subtracting R from the total quantity available for allocation, allocate the rest using Table 1 as in the NR-policy.

One more procedure needs to be specified: how to allocate the supply R among the CSFs. At the time the reserve stock is to be shipped, NSD has R units, at least one CSF has zero units in excess of its minimum level, and the other CSFs have relatively small numbers of units. In this situation the available total quantity, R plus the total excess over CSF minimum levels, often cannot be allocated according to Table 1. For example, if $R = 17$ and the CSF levels (over minimum) are 3, 7, 1, 4, 0, 8, respectively, then the total quantity available is 40, and Table 1 calls for the CSFs to have 6, 6, 6, 7, 7, 8 (over minimum), respectively.

But complex number 2 already has more than called for, and since (we are assuming) CSFs do not ship supplies to other CSFs, an alternative allocation must be made. The optimum alternative allocation subject to the constraint that every CSF is allocated no less than its current level can be calculated by an algorithm similar to the one used for the allocation table.

However, almost exactly the same results can be achieved much more simply by a modified use of the allocation table. The current quantities on hand at the CSFs

are entered in the table in place of all smaller entries. Thus none of the allocations specify fewer units for a CSF than it already has. The allocation to be used is the one in the table for which the total of the CSF allocations agrees with the number of units actually available.

In the example above, row 40 in Table 1 would be changed to 6,7,6,7,7,8, for a total of 41. Row 39 in Table 1 (not shown) would be changed from 5,6,6,7,7,8 to 5,7,6,7,7,8. The latter allocation adds up to 40 and hence would be the one used.

D. Example of Comparison Between NR-Policy and R-Policy

Suppose the row of Table 1 with $Q = 142$ is used for the NR-policy. Then, according to the table, the expected residual at reorder time is 34.8. Using the R-policy with $R = 17$, the expected residual averages 19.9. The net reduction of 14.9 is 10.5% of the initial quantity, 142, and the average inventory cost, Eq. (1), is reduced by the same percentage.

III. CSF Minimum Stockage Policies

A. General

The problem of setting minimum levels for a CSF inventory consists of minimizing the part of the average cost equation (Eq. 2) that involves the minimum levels. That part is

$$h \sum_i W_i + \frac{p}{T} \sum_i U_i = \sum_i \left(h W_i + \frac{p}{T} U_i \right) \quad (9)$$

where h , p , and T are known (see Section II) and

W_i = average inventory level at i th CSF when reorder arrives

U_i = average shortage (unfilled demands) at i th CSF when reorder arrives.

The sum over i in Eq. (9) is minimized by choosing separately for each CSF the minimum stockage level that minimizes

$$\begin{aligned} B(s+1) - B(s) &= h + \left(\frac{p}{T} + h \right) \left\{ \sum_{y=s+1}^{\infty} (y - (s+1)) P(Y=y) - \sum_{y=s}^{\infty} (y - s) P(Y=y) \right\} \\ &= h + \left(\frac{p}{T} + h \right) \left(- \sum_{y=s+1}^{\infty} P(Y=y) \right) \\ &= \left(\frac{p}{T} + h \right) P(Y \leq s) - \frac{p}{T} \end{aligned}$$

$$hW + \frac{p}{T} U \quad (10)$$

The subscripts in Eq. (10) are dropped since we will consider from now on a fixed CSF.

To find the optimum value of

s = minimum stockage level

it is necessary to express W and U in terms of the random variable

Y = total demand (in number of items) at the CSF during one lead period.

The number of units on hand at the CSF at the beginning of a lead period may be greater than s (if another CSF reached minimum first) and may be less than s (if an order for more than one unit reduces the inventory level below minimum). To obtain approximate expressions for W and U it will be assumed that the inventory level at the beginning of a lead period equals s . Then

$$W = E(s - Y)^+$$

and

$$U = E(Y - s)^+$$

where E denotes the expected value or average and “+” means “positive values of,” the negative values being averaged in as zero. (If, for example, $Y - s$ is negative, then there is no shortage and zero is averaged into the determination of U .) Therefore, the problem is to minimize

$$hE(s - Y)^+ + \frac{p}{T} E(Y - s)^+ \quad (11)$$

which equals

$$hE(s - Y) + \left(\frac{p}{T} + h \right) E(Y - s)^+ \quad (12)$$

In order to obtain a preliminary result, it will be assumed for the moment that the probability distribution of Y is known. To find the minimizing s in this case, let $B(s)$ denote the expression to be minimized (Eq. 12) and note that

Since $P(Y \leq s)$ increases with s , so does $B(s+1) - B(s)$, and the minimizing s is obviously the smallest s such that $B(s+1) - B(s)$ is positive, or, what is equivalent,

$$P(Y \leq s) > \frac{\frac{p}{T}}{\frac{p}{T} + h} \quad (13)$$

Thus the value of s minimizing $B(s)$ is the smallest s satisfying Eq. (13). Letting

$$q = \frac{\frac{p}{T}}{\frac{p}{T} + h} = \frac{1}{1 + \frac{hT}{p}} \quad (14)$$

the minimizing s is the q th quantile of the distribution of Y , the demand during lead time. This q is called the *cost-criticality quantile*.

The situation in the DSN is that the demand distribution for a CSF is unknown. However, its q th quantile can be estimated from observed demand over a time period t (measured in units of one lead period). We proceed, next, to describe a method for estimating this cost criticality quantile and thus the minimum level from observed data.

B. Estimation of the Cost Criticality Quantile q

We assume that demand is stationary over time and hence describable by a compound Poisson process. That is, orders of size k ($k = 1, 2, \dots$) arrive independently of each other with mean frequency λ_k per unit time and with probabilities

$$P(m \text{ orders of size } k \text{ during time } t) = \exp(-\lambda_k t) \frac{(\lambda_k t)^m}{m!} \quad (15)$$

$$\text{for } t > 0, m = 0, 1, \dots$$

Let X_k = the number of orders of size k observed during time $t > 0$. Then from Eq. (15) we have

$$P(X_k = x) = \exp(-\lambda_k t) \frac{(\lambda_k t)^x}{x!}, \text{ for } x = 0, 1, 2, \dots$$

Let $\mathbf{X} = (X_1, X_2, \dots)$ and $\boldsymbol{\lambda} = (\lambda_1, \lambda_2, \dots)$. Assume the minimum stockage level s is to be chosen as a function

of \mathbf{X} . Then the resulting average cost is

$$C(\boldsymbol{\lambda}) = hE_{\boldsymbol{\lambda}}(s(\mathbf{X}) - Y) + \left(\frac{p}{T} + h\right)E_{\boldsymbol{\lambda}}(Y - s(\mathbf{X}))^+$$

where the symbol $E_{\boldsymbol{\lambda}}$ is used to indicate that the expected values depend upon the true values of the λ_k 's (e.g., for large λ_k 's, both \mathbf{X} and Y will be large with high probability).

It is desired to minimize $C(\boldsymbol{\lambda})$. But it is easily seen that no rule for choosing s can minimize $C(\boldsymbol{\lambda})$ for all $\boldsymbol{\lambda}$ simultaneously. (For different $\boldsymbol{\lambda}$ s, the distribution of λ is different, and its q th quantile differs.) We can only choose $s(\mathbf{X})$ to be a good estimate of the q th quantile of the (unknown) distribution of Y , based on the observed \mathbf{X} over time t . For each $\boldsymbol{\lambda}$, define

$$R(\boldsymbol{\lambda}) =$$

$$C(\boldsymbol{\lambda}) - \min_{s \geq 0} hE \left\{ (s - Y) + \left(\frac{p}{T} + h\right)E_{\boldsymbol{\lambda}}(Y - s)^+ \right\}$$

the *regret* (in the form of extra average cost) resulting from use of the estimate $s(\mathbf{X})$ rather than the (unknown) best possible s for $\boldsymbol{\lambda}$. A reasonable goal may be roughly defined as follows: for a broad range of $\boldsymbol{\lambda}$ s, keep the regret small. This estimation problem, with the regret function (of $\boldsymbol{\lambda}$) given above, is an example of a statistical decision problem, in the sense of Wald. The general theory of such problems (Ref. 3) leads to the conclusion that essentially all worthwhile estimation rules are solutions for some probability density, $g(\boldsymbol{\lambda})$, of the following problem:

$$\text{Choose } s(\mathbf{X}) \text{ so as to minimize } \int R(\boldsymbol{\lambda}) g(\boldsymbol{\lambda}) d\boldsymbol{\lambda}$$

In other words, the worthwhile estimation rules are those which minimize some *average* of the values of the regret function (the averaging being done according to a prescribed g). Such a minimizing rule is called a *Bayes solution* with respect to the density g , which is called an *a priori density*. The Bayes solutions of the present problem can be found for a large class of g 's and the choice of an estimation rule among these solutions is easy to analyze. To do this, it is helpful to consider first the special case where all orders are of size one, so that \mathbf{X} and $\boldsymbol{\lambda}$ are one-dimensional: X and λ . We have

$$P_{\lambda}(X = x) = e^{-\lambda t} \frac{(\lambda t)^x}{x!}, \quad x = 0, 1, 2, \dots$$

and

$$P_\lambda(Y = y) = e^{-\lambda} \frac{\lambda^y}{y!}, \quad y = 0, 1, 2, \dots$$

where Y , as above, is the demand during a lead period.

Suppose g is of the form

$$g(\lambda) = \begin{cases} \alpha \cdot \frac{(\alpha\lambda)^{n-1}}{\Gamma(n)} e^{-\lambda\alpha} & \text{for } \lambda > 0 \\ 0 & \text{for } \lambda \leq 0 \end{cases} \quad (16)$$

the so-called Gamma density with $\alpha > 0$ and $n > 0$. The general theory of Bayes solutions (Ref. 3) characterizes the Bayes solution for a given *a priori* density g as follows: if $X = x$ is observed, then the optimal choice $s(x)$ is that value of s which minimizes

$$\begin{aligned} \int_0^\infty \left\{ hE_\lambda(s - Y) + \left(\frac{p}{T} + h \right) E_\lambda(Y - s)^+ \right\} g_x(\lambda) d\lambda = \\ h \int_0^\infty E_\lambda(s - Y) g_x(\lambda) d\lambda \\ + \left(\frac{p}{T} + h \right) \int_0^\infty E_\lambda(Y - s)^+ g_x(\lambda) d\lambda \end{aligned} \quad (17)$$

the so-called *a posteriori risk*, where

$$g_x(\lambda) = \frac{\left(\frac{e^{-\lambda t} (\lambda t)^x}{x!} \right) \alpha \frac{(\alpha\lambda)^{n-1}}{\Gamma(n)} e^{-\lambda\alpha}}{\int_0^\infty \left(\frac{e^{-\lambda t} (\lambda t)^x}{x!} \right) \alpha \frac{(\alpha\lambda)^{n-1}}{\Gamma(n)} e^{-\lambda\alpha} d\lambda}$$

which is called the *a posteriori* density of λ given x . A routine computation reveals that $g_x(\lambda)$ is a Gamma density with parameters $\alpha + t$ and $n + x$. Thus, the first integral in Eq. (17) can be written

$$\begin{aligned} \int_0^\infty \left(\sum_{y=0}^\infty (s - y) e^{-\lambda} \frac{\lambda^y}{y!} \right) (\alpha + t) \frac{[(\alpha + t)\lambda]^{n+x-1}}{\Gamma(n+x)} e^{-\lambda(\alpha+t)} d\lambda = \sum_{y=0}^\infty \frac{(s - y)}{y! \Gamma(n+x)} \int_0^\infty e^{-\lambda(\alpha+t+1)} (\alpha + t)^{n+x} \lambda^{n+x+y-1} d\lambda = \\ \sum_{y=0}^\infty (s - y) \cdot \binom{n+x+y-1}{y} \left(\frac{1}{1+\alpha+t} \right)^y \left(\frac{\alpha+t}{1+\alpha+t} \right)^{n+x} \end{aligned}$$

This is the expectation of $s - Y$ when Y has distribution

$$P(Y = y) = \binom{n+x+y-1}{y} \left(\frac{1}{1+\alpha+t} \right)^y \left(\frac{\alpha+t}{1+\alpha+t} \right)^{n+x}, \quad y = 0, 1, \dots \quad (18)$$

which is the negative binomial distribution with parameters $n + x, (1 + \alpha + t)^{-1}$. Similarly, the second integral in Eq. (17) is the expectation of $(Y - s)^+$ for the same distribution of Y , which we call the *a posteriori* distribution of Y . Just as in Eq. (12), therefore, the minimizing s is the q th quantile of the distribution, i.e., the Bayes solution uses for $s(x)$ the smallest s so that

$$\sum_{y=0}^s \binom{n+x+y-1}{y} \left(\frac{1}{1+\alpha+t} \right)^y \left(\frac{\alpha+t}{1+\alpha+t} \right)^{n+x} > q = \frac{\frac{p}{T}}{\frac{p}{T} + h}$$

In the general case where orders are of multiple sizes, the Bayes solutions are readily obtained for *a priori* densities on λ which are products of individual Gamma densities on $\lambda_1, \lambda_2, \dots, \lambda_m$ (assuming $\lambda_{m+1} = \lambda_{m+2} = \dots = 0$). These *a priori* densities result in an *a posteriori* distribu-

tion of Y which can be obtained as the distribution of the sum

$$Y_1 + 2Y_2 + \dots + mY_m$$

where Y_1, \dots, Y_m are independent (representing the num-

ber of orders of sizes $1, \dots, m$) and each Y_k ($k = 1, \dots, m$) has negative binomial distribution with parameters $n_k + x_k$, $(1 + \alpha + t)^{-1}$, (n_k, α being the parameters of the *a priori* Gamma density of λ_k). The distribution of Y can therefore be calculated by applying the following recursion formula for $k = 1, \dots, m - 1$ successively:

$$P(Y_1 + 2Y_2 + \dots + (k+1)Y_{k+1} = y) =$$

$$\sum_{j=0}^{[y/(k+1)]} P(Y_{k+1} = j) P(Y_1 + \dots + kY_k = y - (k+1)j)$$

where $[y/(k+1)]$ denotes the largest integer $\leq y/(k+1)$. The probabilities $P(Y_{k+1} = j)$ come from the negative binomial distribution, Eq. (18), with parameters

$$n_{k+1} + x_{k+1}, (1 + \alpha + t)^{-1}$$

As before, the Bayes solution chooses s as the q th quantile of the *a posteriori* distribution of Y .

This *a posteriori* distribution of Y can be expressed in another way which is useful for computation and for intuitive appreciation of how the choice of the parameters of the *a priori* distribution affects the determination of s . It is helpful to start with the case where all the n_k 's are positive integers. Consider three consecutive time periods of lengths $\alpha, t, 1$ (measured in units of one lead period, as above). Reasoning that any order of size k arriving during the total period of length $\alpha + t + 1$ has probability $1/(\alpha + t + 1)$ of arriving during the period of length one, we have a game of "heads and tails" where each order of size k (k fixed) is scored as "heads" if it lands in the time period of length one, and "tails" if it lands in the preceding time period of length $\alpha + t$. Our situation is this. For orders of size k , suppose we observe n_k during the time period α , then x_k during time period t . We then have a total of $n_k + x_k$ tails, but we do not know the number of heads (orders of size k during time period 1). However, since $\text{Prob. (heads)} = 1/(\alpha + t + 1)$, the probability of getting m heads before $n_k + x_k$ tails can be calculated for $m = 0, 1, 2, \dots$ and leads to the negative binomial distribution with parameters $n_k + x_k$, $(1 + \alpha + t)^{-1}$. This is precisely the distribution we found above for Y_k , the number of orders of size k in the construction of the *a posteriori* distribution of Y ! Moreover, this interpretation of the negative binomial distribution for Y_k makes clear the fact that Y_k can be constructed as the sum of $n_k + x_k$ independent and identically distributed variables: the number of heads before the first tail, the number between the first and second tails, \dots , the number between the

$(n_k + x_k - 1)$ -th and $(n_k + x_k)$ -th. Each of these has the geometric distribution

$$P(j) = \left(\frac{1}{1 + \alpha + t} \right)^j \left(\frac{\alpha + t}{1 + \alpha + t} \right), \quad j = 0, 1, 2, \dots$$

We have thus obtained a heuristic interpretation of the distribution of the Y_k 's (and, through them, an interpretation of the *a posteriori* distribution of Y). One specifies n_k orders of size k as occurring during an "*a priori* time period" of length α , one observes x_k orders of size k during a time period of length t , and from each of these $n_k + x_k$ orders of size k , one infers a geometrically distributed number of orders of size k during the lead period (on length one). (The mean of this geometric distribution is $(\alpha + t)^{-1}$, incidentally, so that the expected value of Y_k is $(n_k + x_k)/(\alpha + t)$, which is the average number of orders of size k per unit time during the combined α and t time periods).

The point of the heuristic discussion above is not to justify the Bayes solutions, whose minimization of average regret is justification enough. Apart from making the modus operandi of the Bayes solution appear plausible, the discussion is important in that it yields two important results:

- (1) The effect of α and the n_k 's is as though one observed n_k orders of size k during an "*a priori* time period" of length α . Since the n_k 's need only be positive, not necessarily integers, this interpretation applies in the general case "by interpolation."
- (2) The effect of α and the n_k 's diminishes to zero as observations are continued over a time period $t \rightarrow \infty$. (For example, the expected value of Y_k , $(n_k + x_k)/(\alpha + t)$, is asymptotic to x_k/t .)

A practical difficulty in working with the Bayes solutions obtained above is that one must specify not only α , but also the values of n_k , i.e., the number of orders of each size k during the "*a priori* time period" α . How large should k be allowed to be in this specification? If there are many possible values of k , then what recipes can be used to prescribe the n_k 's? These are difficult questions, which suggest that a considerable practical advantage can be realized by approximating the Bayes procedures for setting s by a family of procedures involving a small, fixed number of parameters. To this end, it is sufficient to find a good approximation to the *a priori* distribution of Y , which comes from convolutions of negative binomial distributions. Approximate Bayes solutions are then obtainable by "updating" the *a posteriori* distribution of Y each time an

actual order occurs during the time period t (in the manner described above). Investigation of a variety of cases indicated that satisfactory approximations were obtainable by replacing the specified *a priori* distribution of Y by a gamma distribution having the same mean and variance. (Actually, since the gamma distribution is continuous, one "discretizes" it by taking the probabilities of unit-length intervals). This was checked out by comparing the regret functions of the approximate Bayes solutions with those of the corresponding Bayes solutions.

We have now a class of (approximate Bayes) procedures for setting s for a CSF. Each member of this class has four parameters associated with it:

q = the quantile of the *a posteriori* distribution of Y that is chosen for s , the cost-criticality quantile

α = the length of the "*a priori* time period"

G = mean demand specified for *a priori* period

σ^2 = variance of demand specified for *a priori* period

It is convenient to use the parameters $G_1 = \sigma^2/G$ rather than σ^2 . The question that remains is how to choose the four parameters q , α , G , G_1 for individual items and CSFs. The relation of Eq. (14) showed that

$$q = \frac{1}{1 + \frac{hT}{p}} \quad (19)$$

is the optimal choice.

After setting the cost parameters and determining T approximately by Eq. (4), the choice of q by Eq. (19) is determined by the choice of p . The standard approach to inventory models (Ref. 2) regards p as a "penalty cost," not actually paid, but equivalent in dollars to the negative consequences of each unfilled demand. For some items it may not be difficult to estimate such a figure. For others, another approach may be easier, namely, to choose q itself directly. The latter can be accomplished by computing, for a range of specified q -values, both the expected shortage and the inventory level or, equivalently, the expected inventory cost. Thus the tradeoff between the two can be judged directly. An illustration of this approach is given in Appendix A.

With either of the methods for determining q , there is the possibility of failing to choose the truly optimal q . Both methods involve T , the mean length of the order cycle, whose determination is based in part on estimates of CSF mean demand rates. The error of these estimates

is therefore reflected in the choice of q . The effect of this error on the regret was studied and typical results are discussed in Appendix B. It was found that the increased regret from this source should be relatively small. In fact, even a mis-estimate by a factor of 2 does not cause very large additional regret. By the same token, the tradeoff between expected shortage and inventory cost does not have to be determined precisely in order to achieve near-optimum results.

C. Evaluation of Procedures for Determining s

The choices of α , G , and G_1 are potentially quite variable. The terms G and G_1 can be regarded as postulated values (perhaps "engineering estimates") of the mean demand per lead time and variance/mean ratio. (If the demand is compound Poisson, then G_1 is the average size of the order to which a randomly selected unit belongs.) The parameter α measures how much weight is placed upon these postulated values. In other words, a large value of α tends to reduce the regret in those instances where the true mean demand and variance/mean ratio are close to G and G_1 , respectively, but increases the regret if the true values are substantially different.

To investigate the consequences of various choices of the parameters α , G , and G_1 , a computer program was developed to compute to within any specified accuracy a representative set of values of the regret function for a given set of parameter values and given t . Extensive investigations were made in the cases $t = 2, 4$, and 6 because this range (in the unit of time equal to one lead period) is likely to be observed for current DSN items before their first reorder is necessary. The regret function computations (which also yielded computations of expected shortages and average inventory levels) were carried out for (true) mean demands ranging from 0.5 items per lead period (per CSF) to 30.5 items per lead period. This demand was constituted of orders of sizes 1 and 5 or 1, 3, and 10, with varying frequencies of order size to the overall demand. Thus cases like "infrequent order sizes greater than one," "frequent large order sizes," "mainly moderate order sizes" were investigated systematically, with q taking the values 0.85, 0.90, 0.95, 0.97, 0.99.

The following guidelines were developed from these investigations:

- (1) If mean demand can be estimated with high confidence of no more than a factor of 3 error (in either direction), then the range $\alpha = 0.4$ to 0.6 is most effective in minimizing regret.

- (2) The value of G should be chosen 25–50% higher than the estimated mean demand.
- (3) The value of G_1 should be chosen 40–80% higher than the estimated variance/mean ratio for demand during lead time.

These seemingly conservative choices of G and G_1 are preferable because of the nature of the regret functions for the procedures under consideration. The choice of G results from the fact that it is relatively difficult to minimize regret for higher demand rates. The choice of G_1 on the high side also helps keep the regret small for higher demand rates and, in addition, is particularly useful in protecting against sporadic demand for larger than normal order sizes. Where this sporadic demand is considered a greater possibility, still larger values of G_1 are called for.

Besides developing the guidelines for choosing specific procedures for setting CSF minimum levels, the computational investigation was aimed at evaluating the performance of this type of procedure. Specifically, it was desired to see whether the regret was fairly uniformly controlled for large ranges of demand distribution parameters. It became readily apparent that the regret tended to rise directly with the demand level. In other words, the regret tends to be a fairly constant percentage of the minimum possible overall cost (Eq. 2). (Recall that this minimum possible overall cost is attainable only if the true demand distribution is known.) In Fig. 2, the percentage regret is plotted as a function of mean demand during lead time. A separate curve is plotted for each of four cases (labeled "Frequency of Order Sizes"). It is assumed that orders are of two sizes, one unit and five units, and the cases specify the frequency of each order size.

Note that the percentage regret in all four cases is about 15% for mean demand in the range 8.5 to 30.5, and is somewhat larger, about 20–25%, for smaller demand levels. (Of

course, the regret in absolute terms is still substantially smaller for low demand than for higher demand.) This mild increase in percentage of regret at the extreme lower end of the demand range is typical, and results largely from the conservative effect of the *a priori* estimates G and G_1 , which causes the minimum levels to provide reasonable protection against shortages even if the observed demand is quite small. Figure 3 shows the results of a more elaborate investigation of the performance of the same procedure ($\alpha = 0.4$, $G = 15$, $G_1 = 7$, $q = 0.90$).

The eight cases shown in Fig. 3 represent variations of the frequency of order sizes for orders of sizes 1, 3, and 10.

Note that the regret is in the 15–20% range, approximately the same as in Fig. 2. Both figures give the results for $t = 4$ lead periods, which is on the order of one year's experience with observed demand. The range of 15–20% regret is the best that can be accomplished by any of the procedures studied uniformly over a broad range of possible mean demand levels and variations in frequency of order sizes. It is appropriate to consider this regret as the (essentially unavoidable) cost of the degree of uncertainty regarding the true demand distribution that remains after one year's observation. Of course, considerable improvement in reducing overall costs is possible in the long term if the system is implemented in a consistent fashion and the demand distributions are fairly stable. As an illustration of the improved percentage of regret typical after 1½ year's observation ($t = 6$), we have Fig. 4.

Here the pattern is similar to Fig. 2, but the regret is mainly in the 10–15% range rather than in the 15–20% range. The computations of regret become more time-consuming for large t (the time increasing with t^2), but routine mathematical arguments show that, as would be expected, the percentage regret over any fixed demand range approaches zero uniformly as t approaches infinity.

References

1. *The Economic Order Quantity Principle and Applications*, A GSA Handbook, FMPR 101-27.1, General Services Administration, Washington, D.C., May 1966.
2. Wagner, H. M., *Principles of Operations Research*, Prentice-Hall, Inc., Englewood Cliffs, N.J., 1969, Chapter 19.
3. Wald, A., *Statistical Decision Functions*, Wiley and Sons, New York, New York, 1950.

Table 1. Excerpts from a typical allocation table

Q	k = 6						CSF annual demand rates 7:8:9:10:11:12	
	n ₁	n ₂	n ₃	n ₄	n ₅	n ₆	Expected time	Expected residual
6	1	1	1	1	1	1	.018	5.00
7	1	1	1	1	1	2	.021	5.79
8	1	1	1	1	2	2	.026	6.53
9	1	1	1	2	2	2	.032	7.18
10	1	1	2	2	2	2	.040	7.71
⋮								
40	6	6	6	7	7	8	.396	17.41
⋮								
105	14	15	17	18	20	21	1.32	29.54
⋮								
117	16	17	19	20	22	23	1.50	31.35
⋮								
142	19	21	23	25	26	28	1.88	34.82

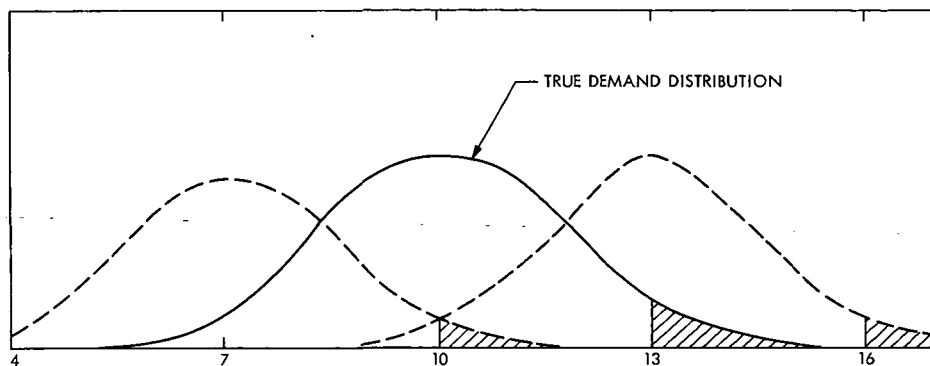


Fig. 1. Setting minimum levels at CSF

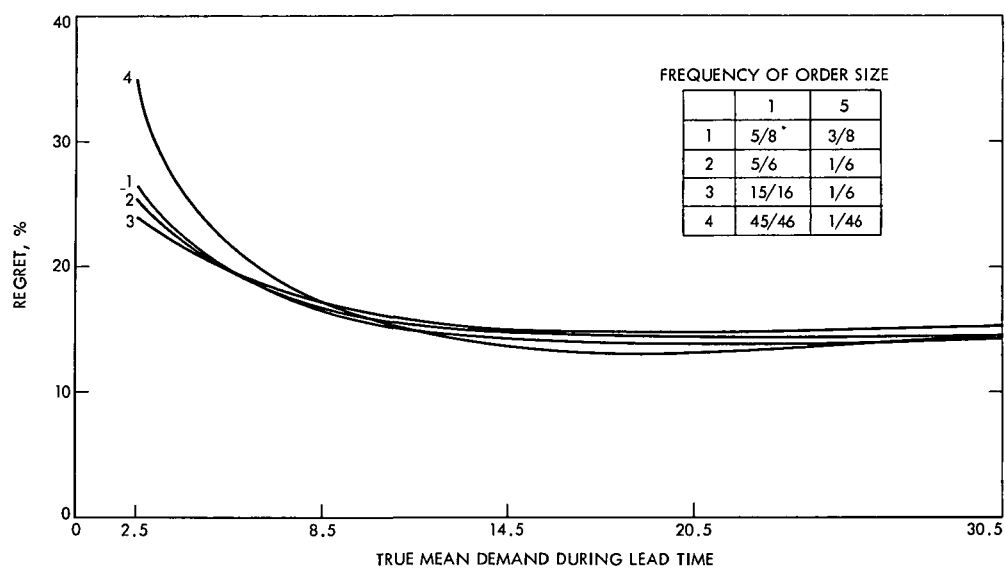


Fig. 2. Regret as a percentage of average cost for a range of demand distributions ($t = 4$, $\alpha = 0.4$, $G = 15$, $G_1 = 7$, $q = 0.90$)—order sizes 1, 5

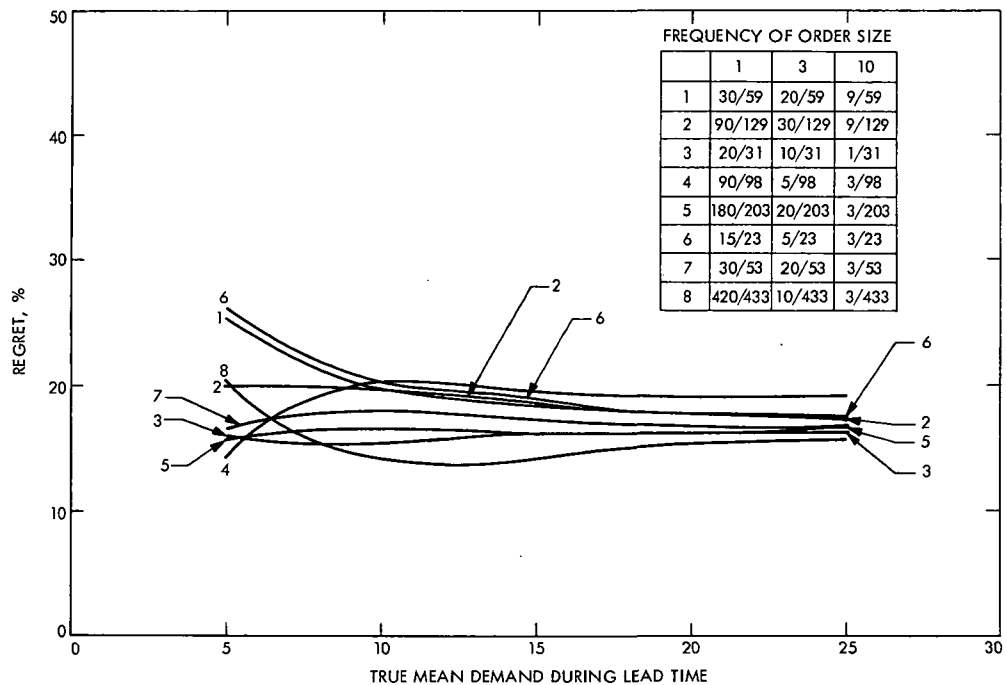


Fig. 3. Regret as a percentage of average cost for a range of demand distributions ($t = 4$, $\alpha = 0.4$, $G = 15$, $G_1 = 7$, $q = 0.90$)—order sizes 1, 3, 10

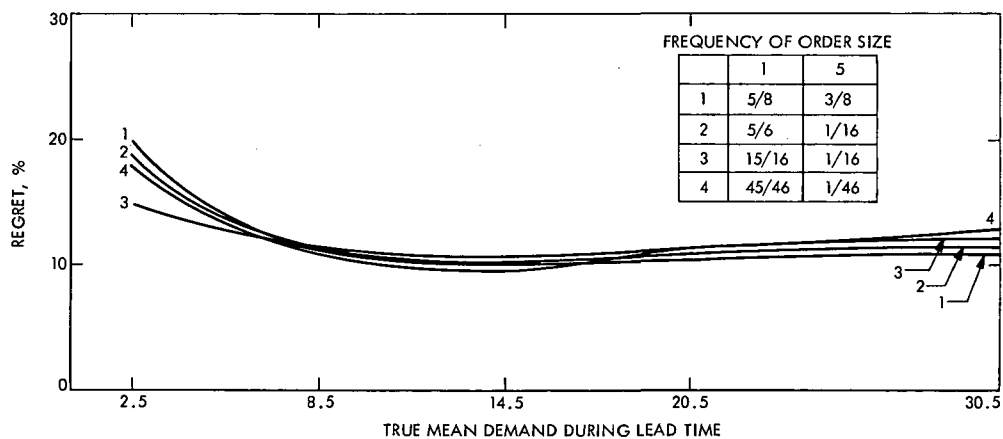


Fig. 4. Regret as a percentage of average cost for a range of demand distributions ($t = 6$, $\alpha = 0.6$, $G = 10$, $G_1 = 7$, $q = 0.90$)—order sizes 1, 5

Appendix A

Tradeoff of Expected Shortage vs Inventory Level

Each curve in Fig. A-1 corresponds to a different (true) mean demand level. The five points distinguished on each curve correspond (moving from left to right) to $q = 0.85, 0.90, 0.95, 0.97$, and 0.99 . Intermediate points can be attained by choosing intermediate values of q . Moving along a fixed curve from left to right, the expected shortage decreases (as q is increasing) while the average value of s , the minimum stockage level, increases. Increments of

small s when multiplied by h give a good approximation to increments in average inventory cost per year. Thus the curves indicate how much decrease in expected shortage is "bought" for arbitrary levels of increased inventory levels. The "flattening out" of the curves shows that in the range of 0.97 to 0.99 a relatively small rate of decrease in expected shortage is obtained by increasing the inventory level.

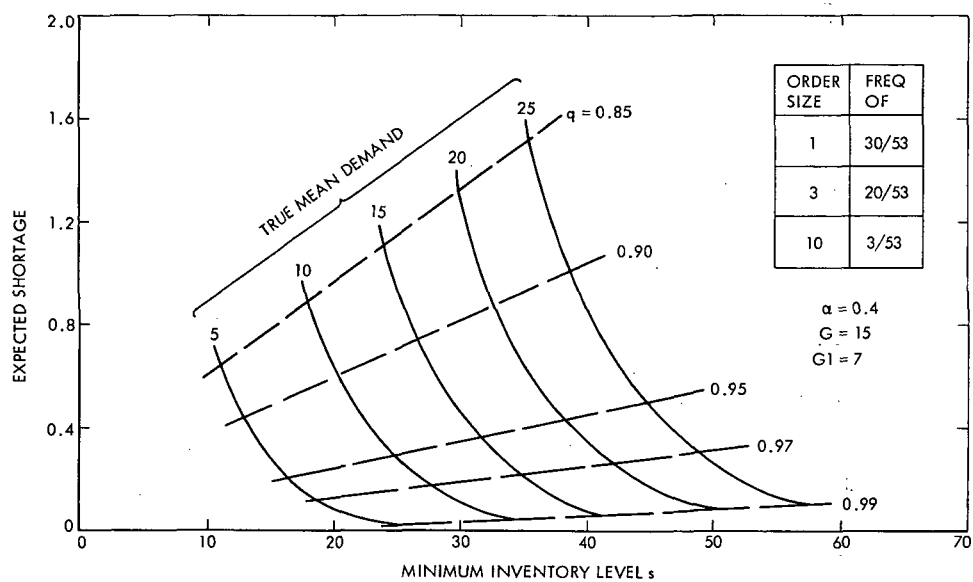


Fig. A-1. Expected shortage vs inventory level and demand

Appendix B

Effect of Mis-estimating q

Figure B-1 shows the overall average cost (Eq. 2) as a function of the mean demand per lead period. The order sizes are 1, 3, and 10, with fixed frequency of order sizes. The bottom curve plots the minimum possible cost (attainable only if the demand distribution is known). The second curve from the bottom shows the average cost incurred when the correct choice $q = 0.95$ is made. (Thus the distance between the two curves is the regret.) The two upper curves represent the average cost incurred

when an erroneous q is used (e.g., through mis-estimating T or setting p poorly).

The value $q = 0.97$ corresponds to an underestimate of T by a factor of $3/5$, while the value of $q = 0.90$ corresponds to an overestimate by a factor of 2. Even these levels of error produce an increment to average cost substantially smaller than the regret.

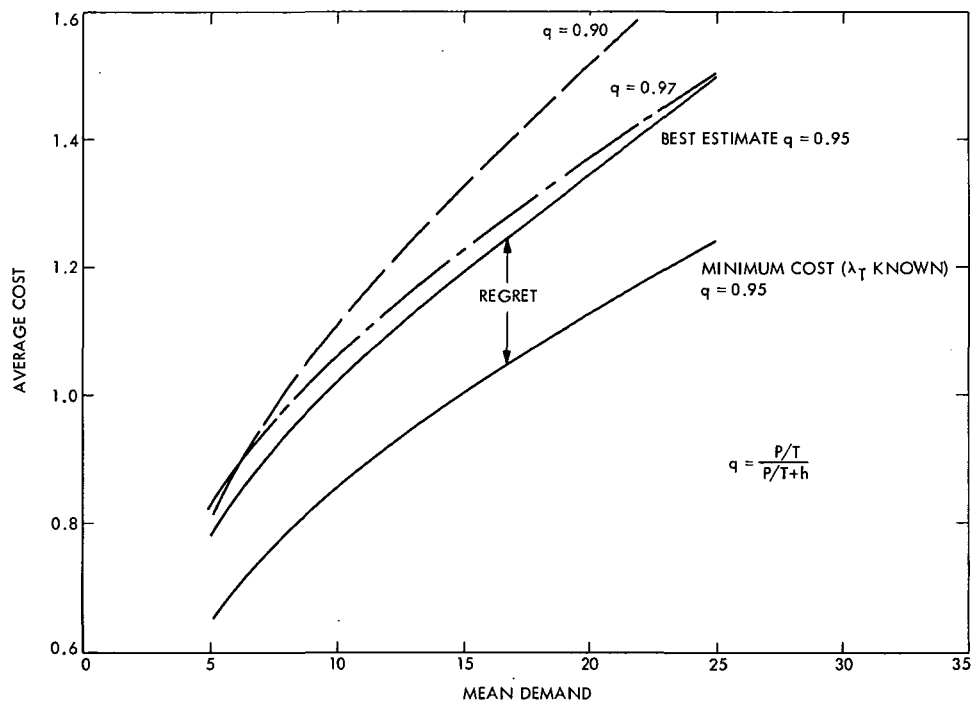


Fig. B-1. Effect of mis-estimating q

A Demonstration of DSN Clock Synchronization by VLBI

W. J. Hurd

Communications Systems Research Section

A prototype of a semi-real-time system for synchronizing the DSN station clocks by radio interferometry was successfully demonstrated on August 30, 1972. Synchronization accuracies as good as 100 ns rms were achieved between DSS 11 and DSS 12, both at Goldstone. The accuracy can be improved by increasing the system bandwidth until the fundamental limitations due to baseline and source position uncertainties and atmospheric effects are reached. These limitations are about 10 ns for transcontinental baselines.

I. Introduction

It is well known that the clocks at widely separated antenna ground stations can be synchronized by the techniques of very long baseline interferometry (VLBI). There are two reasons that an operational VLBI time synchronization system may be desirable for the DSN. First, accuracies an order of magnitude better than those currently attained by the moon-bounce system may be attainable with little initial investment and with operational costs that should be no higher than for the existing system. Second, VLBI may be the only operationally feasible method for achieving the 10–20 ns accuracies required for two-station tracking of deep space probes (Refs. 1, 2).

The time synchronization accuracy attainable by interferometry over very long baselines is fundamentally limited by the uncertainties in the differential time delay from the radio source to the antennas. These uncertainties, which increase with the baseline length, are caused by errors in the estimates of the source positions and antenna locations, and by the variable propagation delays

in the atmosphere. It is anticipated that the antenna locations will soon be known to within about 1 m, and source position errors can be reduced to this same level by interferometry. The atmospheric effects depend on frequency in a known manner, and can be calibrated by receiving on two frequencies, say S- and X-band. The fundamental limitation of accuracy can probably thus be reduced to 10 ns or less for intercontinental baselines.

Until the fundamental limit is approached, the synchronization accuracy depends primarily on the utilized bandwidth, provided that the signal-to-noise ratio (SNR) is high enough for reliable detection. The experiment reported on here confirms the two most important results of Ref. 3: first, that reliable estimates can be achieved with a small enough amount of data (about 1 million bits) so that semi-real-time processing is feasible; and second, that the rms errors are less than 0.1 times the inverse system bandwidth, so that the fundamental limitations of accuracy can be achieved with system bandwidths of only about 10 MHz.

II. Description of Experiment

As a first step in demonstrating the feasibility of an operational system for DSN clock synchronization by VLBI, an experiment was conducted on August 30, 1972, between the 26-m-diameter antennas at DSSs 11 and 12, both at Goldstone. The experiment was implemented using a minimum of special interfacing hardware in addition to standard DSN station equipment. The data were acquired and processed following the approximate maximum-likelihood method of Ref. 3.

A simplified block diagram of the experiment is shown in Fig. 1. At each station, the received signals were demodulated in two phase quadrature channels, filtered, quantized to 1 bit, and buffered into a TCP computer. Besides the receivers, the TCP computers are the major portion of the system. The special equipment for the experiment consisted of the two-channel demodulators, the filters, limiters, and samplers, and the buffers from the sampler to the TCP computers. All of this equipment was contained in one small chassis for each station, plus cables to interface to the computers.

The experiment procedure was to initiate sampling at the same time at each receiver, according to the station master clocks, and to fill the TCP computer memories with data at the highest possible sampling rate. The computer speeds limited the data rate to 500 kbps, or 250 kbps per channel, so that the system bandwidth was limited to 250 kHz. Furthermore, the maximum number of samples which could be taken at this rate was limited by the memory sizes to approximately 320,000 bits. In an operational system, the data could be transmitted directly from the computers to JPL over the high-speed data lines and processed within a few minutes in the Network Control System (NCS) or other computers. In the experiment, however, real-time operation was not required, but instead it was desired to make a number of independent estimates of time sync using each of several radio sources. Therefore, the data were written onto magnetic tape and processed later on a Sigma 5 computer at JPL. Five different radio sources were observed, with a total of 504 batches of data taken at 10-s intervals.

III. Principal Results and System Implications

The desirability of an interferometry time sync system for the DSN depends on the ability to achieve reliable results with a reasonable amount of data. This, in turn, depends on the availability of radio sources with enough correlated flux, i.e., with enough electromagnetic flux

which appears to be from an ideal point source when viewed by the long baseline interferometer. In this section, we set a standard for the required source intensity for various system configurations based on experimental and analytical results, and show that adequate sources are available to result in an operationally feasible system.

The experimental results were limited by the system parameters of two 26-m-diameter antennas with temperatures of 16.3 and 37 K, the 250-kHz bandwidth, and the 3.2×10^5 bit buffer size. For the three strongest radio sources, rms processing errors of 96, 228, and 403 ns were achieved, in close agreement with theory. The results for the weakest of these sources, with an estimated correlated flux of 4.6 fu, are most significant for two reasons: first, the estimates were reliable even though the SNR was somewhat lower than the desired minimum, and second, the results were in close agreement with theory, indicating that the theory does not break down until the SNR is reduced below this level.

Based on both the theoretical and experimental results, we conclude that a source intensity of 5.5 fu would have been adequate to reliably achieve an rms error of less than 0.4 μ s, or less than one tenth of the inverse of the system bandwidth. Whenever possible, higher accuracies should be achieved by increasing the system bandwidth and not the amount of data or the SNR, both because few sources have more than 2-3 fu of correlated flux over long baselines and because increasing the amount of data is expensive in terms of buffer storage, computer time, and ground communications facility (GCF) usage.

Table 1 presents the source intensities required to achieve the reliable performance level of one-tenth of the inverse system bandwidth for various antenna sizes and receiver noise temperatures in the DSN. Two buffer sizes are considered: the 0.32 Mbits usable in the TCP computers, and 1.0 Mbit, which is a practical size if special-purpose memories are used for wider bandwidths. In utilizing Table 1, one should keep in mind that the system temperatures increase at low elevation angles, so that the required fluxes might increase by a factor of about 1.5.

The availability of known radio sources was surveyed using Ref. 4 and a computer program for mutual visibility devised by J. G. Williams of the Tracking and Orbit Determination Section. Considering sources to be jointly visible only when the altitude from both stations is 10 deg or greater, there is always at least one source

of 1.3 fu or stronger visible by the station pairs at Goldstone and Spain, Goldstone and Australia, and Spain and South Africa. Sources of 2.0 fu are available for most of the day, and sources of 3-6 fu are normally visible for at least a few hours each day. The source 3C454.3, which is sometimes as strong as 6.38 fu (Ref. 4), is visible to each of the above pairs for at least 3 h a day, but unfortunately it has at other times been observed to be considerably weaker, and similar variations occur with some of the other strong sources. It is therefore not desirable to base a system on the few strongest sources.

Considering both the source intensities required and the availability, it is safe to say that station pairs with at least one 64-m-diameter antenna can be synchronized at will to within one-tenth of the inverse system bandwidth with 1.0 Mbit of data. That is, there would be little if any operational restriction as to time of day due to lack of mutual visibility of adequate sources. Synchronization of two 26-m-diameter antennas could be accomplished with some restrictions on time of day, or by using more data. It is important to note that the amount of data used is not restricted by the high-speed buffer size, but convenience is sacrificed if it becomes necessary to fill the buffer several times, storing the data on magnetic tape between fills, and then to transmit a larger amount of data to the central computer for processing.

We conclude that a system with 1.0-Mbit buffers would be operationally feasible. It would be less restricted than the X-band moon-bounce system, for which moon visibility restricts the time of day, and even the time of year for two northern hemisphere stations.

IV. Estimation Procedure

The estimates of time synchronization error were made using the approximate maximum-likelihood method (Ref. 3). This method is distinguished from normal cross-correlation methods in that the cross products are multiplied by appropriate weighting functions before being summed or envelope detected. This weighting accounts for changes in clock offset during the measurement time, and provides an optimum method for resolving the time estimates to greater accuracy than the time between samples.

A functional diagram of the estimation procedure is shown in Fig. 2. The i th samples in the phase quadrature channels after demodulation, filtering, and limiting are denoted by X_i and Y_i for DSS 11 and by Z_i and W_i for

DSS 12. These signals have cross correlations which depend on i and on ρ , τ , δ , ω , and ϕ , where

$$\rho^2 = \frac{T_c^2}{T_{11}T_{12}} \quad (1)$$

is the product of the input SNRs, and

T_c = increase in system temperatures due to *correlated* flux from the source

T_{11}, T_{12} = total system noise temperatures at DSSs 11 and 12, including total source flux, correlated or otherwise

δ = difference in path length from the source to the two stations, in seconds (often called τ_g)

τ = error in clocks, or actual time difference between first samples at the two stations

ω = stopped fringe frequency, or apparent doppler difference after demodulation, in radians per second

ϕ = stopped fringe phase

The cross correlations are the expected values of the cross products:

$$E\{X_i Z_j\} = \frac{2}{\pi} \rho a_{ij}(\tau, \delta) \cos(j\Delta + \phi) \quad (2)$$

$$E\{X_i W_j\} = \frac{2}{\pi} \rho b_{ij}(\tau, \delta) \sin(j\Delta + \phi) \quad (3)$$

$$E\{Y_i Z_j\} = \frac{2}{\pi} \rho c_{ij}(\tau, \delta) \sin(j\Delta + \phi) \quad (4)$$

$$E\{Y_i W_j\} = \frac{2}{\pi} \rho d_{ij}(\tau, \delta) \cos(j\Delta + \phi) \quad (5)$$

where $\Delta = \omega \cdot 4 \mu s$ and it is assumed that the timing is such that the cross products are uncorrelated except for $i \approx j$. The factor $2/\pi$ arises as a result of the hard limiting.

In general, for long baselines and measurement times, the fringe rate cannot be assumed constant, and $j\Delta$ must be replaced by a phase angle $\theta(j)$, which is known by the geometry. There is no significant difference in the estimation procedure. We assume here that the fringe rate is constant, for convenience and because this is valid for the short baseline of this experiment.

The estimation procedure is to maximize an estimator function G over assumed values for τ and ω . In calculating G , the stopped fringe rate ω is first normalized by subtracting out known quantities. Thus, the frequency variable becomes

$$f = \frac{1}{2\pi} (\omega - \omega_0) \quad (6)$$

where ω_0 is the *a priori* estimate of the stopped fringe frequency. Two factors contribute to ω_0 : the fringe rate as calculated from the geometry, and the difference in local oscillator frequencies, or effective receiver center frequencies, at the two stations. The frequency f is the sum of the errors due to geometry and to oscillator instabilities, and the estimate of f is the estimate of these errors.

The steps in the estimation procedure for τ and f are:

- (1) Assume a value of τ , say τ_k .
- (2) Form all cross products whose cross correlations are nonzero for $\tau = \tau_k$.
- (3) Multiply the cross products by the cross correlations for $\tau = \tau_k$, neglecting the sinusoidal terms, i.e., form $X_i Z_j a_{ij}(\tau_k, \delta)$, etc.
- (4) Assume a value for f , say f_j .
- (5) Evaluate $G(\tau_k, f_j)$.
- (6) Maximize $G(\tau_k, f_j)$ over the region of uncertainty in f by looping back to step 4.
- (7) Maximize $G(\tau_k, f_j)$ over the region of uncertainty in τ by looping back to step 1.
- (8) The estimates $\hat{\tau}$ and \hat{f} of τ and f are the values of τ_k and f_j which maximize G .

The distinguishing feature of this procedure is in weighting the cross products by their assumed τ -dependence before envelope detecting. This gives a natural and optimum method for resolving the estimate of τ to greater resolution than the time between samples, and for accounting for the changes in τ over the measurement time.

V. Properties and Examples of the Estimator Function

The statistics of the estimator function have been evaluated both analytically and by simulation (Ref. 3). We summarize here some of the key statistics, and then

examine graphically some typical sample functions which were observed in the experiment.

The estimation procedure is considered to be reliable when the probability is high that the estimates are in the general vicinity of the correct values of the parameters, rather than being completely extraneous. This depends on the probability distributions of G for the correct and widely erroneous values of the parameters. Once the forms of the distributions are known, the performance can be well predicted by a figure of merit which we call the signal-to-noise ratio of the estimator. It is defined as the square of the difference in the means of G for the correct and incorrect values of the parameters, to the variance of G at the correct values. When G is normalized in the natural manner, its mean is unity for widely incorrect assumed values of the parameters, and is unity also when $\rho = 0$, so that

$$R = \frac{[E\{G(\tau, f)\} - 1]^2}{\text{var}\{G(\tau, f)\}} \quad (7)$$

The estimator SNR varies approximately as ρ^2 , i.e., as the product of the input SNRs, or alternatively, as the square of the source flux density. For the particular filtering and sampling method used, it is given by

$$R = \frac{1}{2} \frac{r}{1 + \frac{1}{2r}} \approx \frac{r}{2} \quad (8)$$

where

$$r = 0.267 \rho^2 N \quad (9)$$

and N is the number of samples in each channel at each receiver. Since the system bandwidth is the inverse of the time between samples in one channel, N is also the system time-bandwidth product.

Estimation will be reliable whenever R exceeds about 10, because the maximum value of G will almost always occur in the vicinity of the correct values of τ and f unless the initial uncertainty in these parameters is large. For example, when the initial uncertainty in f is negligibly small, the number of independent values of G which must be calculated is approximately equal to the time uncertainty times twice the system bandwidth. For the 250-kHz bandwidth of this experiment, time uncertainties of ± 10 to $\pm 100 \mu\text{s}$ would require calculation of only 10 to 100 independent values of G . It can be seen from

the curves of Ref. 3 that, for these uncertainties, the results would be reliable about 98–99% of the time with $R = 10$.

The resolution of the estimates depends on the peakedness of G more than on R . An approximation to the rms error in the estimation of τ is presented in Ref. 1, and is

$$\sigma_\tau = \frac{0.79T}{\rho N^{1/2}} \quad (10)$$

where T is the time between samples in one channel, or the inverse system bandwidth. In terms of R ,

$$\sigma_\tau \approx \frac{0.289T}{R^{1/2}} \quad (11)$$

so that $R = 10$ is sufficient to reduce the rms error to less than $0.1T$ as well as to result in reliable estimation.

Insight into the capabilities of the estimator function to resolve time and frequency can be gained by studying the function at high signal-to-noise ratios. Figure 3 shows a plot of an actual sample function of $G(\tau_k, f_j)$ observed for a fairly high-intensity source, 3C279, with R estimated to be 24.8. The maximum of G is 52.844 and occurs for $f_j = -0.20$, $\tau_k = 40.97$, so that these are the estimates \hat{f} and $\hat{\tau}$ of f and τ . In the time domain, G is nominally symmetrical, and decreases to half its maximum in under $\pm 2 \mu\text{s}$ and to approximately zero in $\pm 4 \mu\text{s}$. In the frequency domain, G is also nominally symmetrical about the actual value of f , although this is not apparent from the sample function because the maximum did not occur at $f_j = 0$. The measurement time of the experiment was $NT \approx 0.64$ s, and the effective bandwidth of G is slightly less than the inverse of this time. It is observed that for different f_j , the maximum of G occurs at very close to the same value of τ_k . This implies that it may be unnecessary to maximize over f_j when only estimates of τ are required, provided that the initial uncertainty in f is small compared to $1/NT$, say less than $\pm 0.1/NT$.

The performance of the estimator when the noise is significant is illustrated in Figs. 4 and 5. Each presents three sample functions from different realizations of the experiment, with the time dependence shown only for the frequency variable fixed at the nominal value, $f_j = 0$. Figure 4 is for a weaker source, 4C39.25, with R estimated to be 3.81, which is significantly below the suggested design value of 10. In one of the three cases, the

maximum of G occurs near $\tau_k = 21 \mu\text{s}$, far removed from the true value, which is near $41 \mu\text{s}$. Extraneous results like this occur frequently at these low SNRs. Figure 5 is for source P1127-14, with R estimated to be 8.20, which is only marginally below the design point of 10. Fairly wide variations in the maximum value of G occur at this SNR, but no extraneous maxima were observed in the 72 sets of data taken for this source.

VI. Detailed Results

A total of 504 sets of data were taken using five different radio sources, and independent estimates of the time and frequency differences at the two receivers were made for each set of data. The most important results are the means and standard deviations of the estimates of τ and f as a function of the estimator SNR, R . In order to present these results, it was necessary to estimate R from the data. The method for estimating R is presented later.

A. Joint Estimation of τ and f

Table 2 presents the results of the joint estimation of τ and f for the five sources. The statistics are based on 144 independent estimates for each of the two strongest sources, 3C273 and 3C279, and on 72 cases for the other sources. Since the true values of τ and f were not known, it was not possible to compute the actual rms errors, so the standard deviations were estimated from the data using the estimates of the means. The standard deviation of the mean estimate for one source is equal to the standard deviation of one estimate for that source, divided by the square root of the number of cases. None of the mean estimates of τ differ from the value 40.97 by more than two standard deviations. All variations in the mean estimates can thus be attributed to noise. There is no evidence to suggest any effects due to errors in source or station positions, changes in the clock sync during the experiment, or errors in data processing.

The statistics of the estimates of f cannot be attributed entirely to noise, because of local oscillator instabilities. A hydrogen maser was used for the S-band reference at DSS 12, and rubidium was used at DSS 11, so the rubidium standard contribution dominated. Both the long- and short-term stabilities are on the order of one part in 10^{11} . Errors in the nominal value of f of up to 0.1 Hz were anticipated, as were short-term variations with a standard deviation on the order of 0.01 to 0.1 Hz.

Due to noise alone, the standard deviation of f should vary as $R^{-1/2}$, provided R is about 10 or greater. This relationship was nominally satisfied for the second- and third-strongest sources, with $R = 24.8$ and 8.20 , and standard deviations of 0.0946 and 0.159 Hz. For the strongest source, the frequency instability was not negligible compared to the noise. Therefore, its effect was estimated from the results for the two strongest sources, assuming the noise and instability errors to add in the mean square. The rms error due to frequency instability was estimated at 0.036 Hz, which is well within the range of uncertainty of this effect. The rms frequency estimation error due to noise is then approximately $0.468/R^{1/2}$ Hz. This relationship was also closely satisfied for the next-weakest source. An R of 10 thus results in an rms error in frequency estimate of less than 0.1 divided by the measurement time of 0.64 s, just as it results in a timing error of less than 0.1 divided by the bandwidth.

B. Estimation of τ for Fixed f

When the *a priori* uncertainty in frequency is small, τ can be estimated by maximizing G over τ only, assuming no frequency error, i.e., $f = 0$. This results in better estimates of τ than does joint estimation of τ and f when the long- and short-term frequency instabilities are very small. Before this experiment was actually performed, it was felt that the frequency stabilities would be sufficiently good to omit maximization over f , and this was confirmed in the experiment. However, the amount of long-term drift is random, and the frequency offsets in the local oscillators might have been too large on another day. It was, therefore, necessary to process the data in both manners, in order to be able to predict future performance.

The results of the estimation of τ for f fixed at zero are presented in Table 3. The theoretical rms errors in the estimation of τ are also presented, as calculated for the estimated values of R . For the three highest SNR cases, the observed and calculated rms errors were very close. For the lowest two SNRs, the observed errors were significantly higher than the calculated values. This is because the theory breaks down when R is low enough so that extraneous results occur.

The observed rms errors at low SNRs would have been still higher if the assumed region of uncertainty in τ had been greater, because there would have been more extraneous results due to noise. Throughout the experiment, the uncertainty region was assumed to be from 30 to 50 μ s.

C. Comparison of Estimation Methods

In comparing the results of estimating τ jointly with f and with f fixed at zero, it is seen that there is negligible difference in the standard deviations of the estimates for the three highest SNR cases, and that all are close to theory. For the two lower SNRs, the errors are significantly higher when f is estimated instead of assumed to be zero. There are two reasons for this. First, the estimates of f are poor enough to degrade the estimate of τ . Second, more extraneous estimates occurred, because there were effectively more independent calculations of G for noise only.

D. Estimation of R , ρ , and Flux Density

For each independent case, the approximate maximum-likelihood estimate for ρ is the square root of the maximum value of G , divided by the proper normalization factor. This is the best estimate of ρ only because the maximum value of G occurs at the best estimates of τ and f . A better estimate of ρ would be obtained from a value of G at the correct values of τ and f . Therefore, since it was desired to have the overall best estimates of ρ , and hence of R , the values of ρ were estimated using the best overall estimates of τ and f . These best estimates were taken as $\tau = 40.955$ and $f = 0.0807$ Hz, the values obtained from the strongest source. The overall estimates of ρ for each source were taken as the average of the estimates of ρ for all of the cases for that source.

The estimates of R were obtained from the estimates for ρ according to Eqs. (8) and (9). To estimate the correlated fluxes, it was assumed that the system temperatures at DSSs 11 and 12 were the cold sky temperatures of 37 and 16.3 K, respectively, raised by the source total flux at the rate of 0.11 K per flux unit. Then the correlated fluxes are given by Eq. (1).

Table 3 presents the estimated flux densities, input SNRs, and estimator SNRs for the five sources.

Acknowledgements

The author acknowledges the assistance of P. F. MacDoran, J. G. Williams, and D. S. Spitzmesser, who shared their knowledge and experience in VLBI experiments, and of S. S. Brokl and the station personnel at DSSs 11 and 12, who assisted in implementing the experiment.

References

1. Hildebrand, C. E., Ondrasik, V. J., and Ransford, G. A., "Earth-Based Navigation Capabilities for Outer Planet Missions," AIAA Paper No. 72-925, AIAA/AAS Astrodynamics Conference, Palo Alto, California, September 11-12, 1972.
2. Ondrasik, V. J., Hildebrand, C. E., and Ransford, G. A., "Preliminary Evaluation of Radio Data Orbit Determination Capabilities for the Saturn Portion of a Jupiter-Saturn-Pluto 1977 Mission," in *The Deep Space Network Progress Report*, Technical Report 32-1526, Vol. X, pp. 59-75, Aug. 15, 1972.
3. Hurd, W. J., "DSN Station Clock Synchronization by Maximum Likelihood VLBI," in *The Deep Space Network Progress Report*, Technical Report 32-1526, Vol. X, pp. 82-95, Aug. 15, 1972.
4. Kellermann, K. I., *et al.*, "High Resolution Observations of Compact Radio Sources at 13 Centimeters," *Astrophys. J.*, Vol. 151, Sept. 1970, pp. 803-809.

Table 1. Source intensity required for various system parameters

Antenna diameters, m		System temperatures, K		Amount of data or buffer size, 10 ⁶ bits	Source intensity, fu of correlated flux
26	26	17	37	0.32	5.50
26	26	17	37	1.0	3.48
26	26	17	17	0.32	3.70
26	26	17	17	1.0	2.34
64	26	17	37	0.32	2.24
64	26	17	37	1.0	1.26
64	26	17	17	0.32	1.51
64	26	17	17	1.0	0.86
64	64	17	17	0.32	0.61
64	64	17	17	1.0	0.35

Table 2. Joint estimation of τ and f

Radio source	Estimated estimator SNR	Estimation of τ		Estimation of f	
		Mean, μs	Standard deviation, μs	Mean, Hz	Standard deviation, Hz
3C273	148.	40.955	0.0956	-0.0807	0.0503
3C279	24.8	41.00	0.228	-0.0799	0.0946
P1127-14	8.20	40.95	0.403	-0.0810	0.159
DW0742+10	4.24	40.95	0.719	-0.0772	0.239
4C39.25	3.81	40.78	1.26	-0.0355	0.249

Table 3. Estimation of τ for $f = 0$

Radio source	Estimated estimator SNR	Estimation of τ		Theoretical rms error in τ , μs
		Mean, μs	Standard deviation, μs	
3C273	148.	40.955	0.0978	0.095
3C279	24.8	41.00	0.224	0.232
P1127-14	8.20	40.95	0.408	0.403
DW0742+10	4.24	40.98	0.641	0.560
4C39.25	3.81	40.92	0.952	0.591

Table 4. Estimated flux densities and estimator SNRs

Radio source	Number of cases	Total flux (Ref. 4), fu	Estimated correlated flux, fu	Estimated geo. mean input SNR	Estimated estimator SNR
3C273	144	39.	22.	0.0834	148.
3C279	144	12.2	8.1	0.0344	24.8
P1127-14	72	6.2	4.6	0.0199	8.20
DW0742+10	72	3.7	3.3	0.0145	4.24
4C39.25	72	3.8	3.1	0.0138	3.81

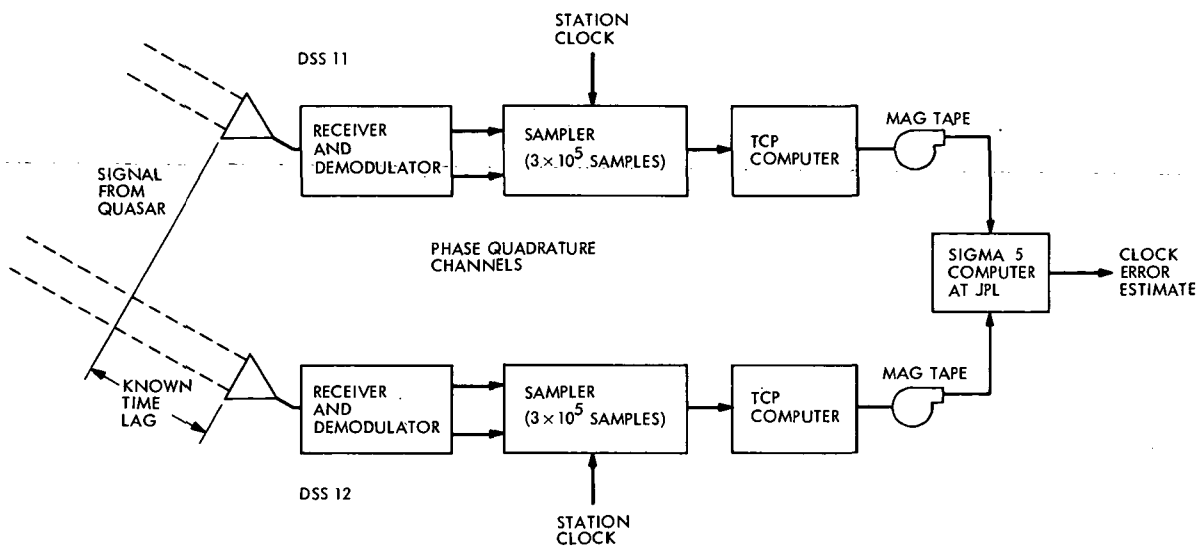


Fig. 1. VLBI time-sync demonstration block diagram

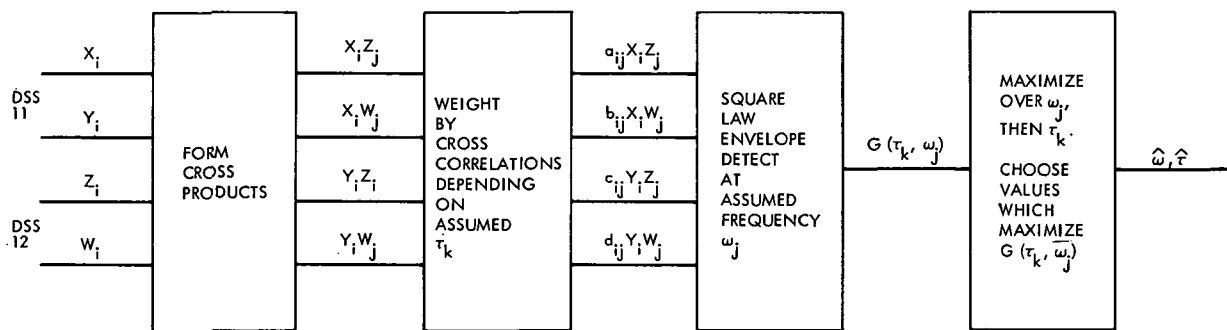


Fig. 2. Functional diagram of estimation procedure

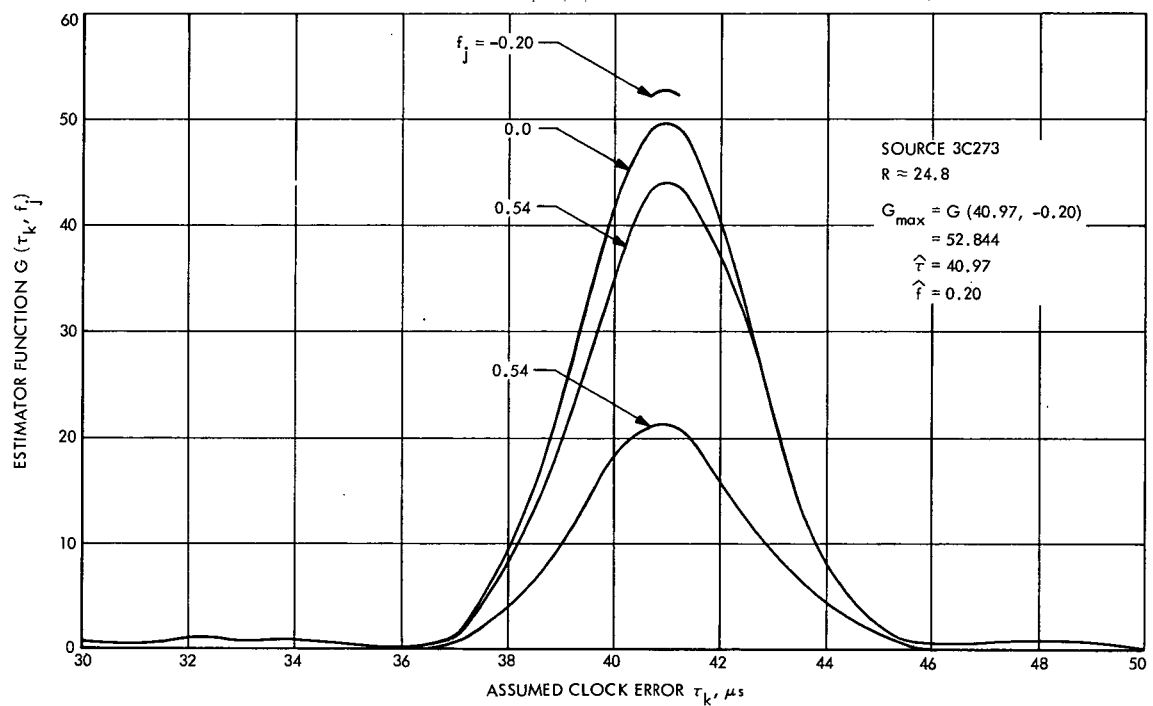


Fig. 3. An estimator sample function at a high SNR

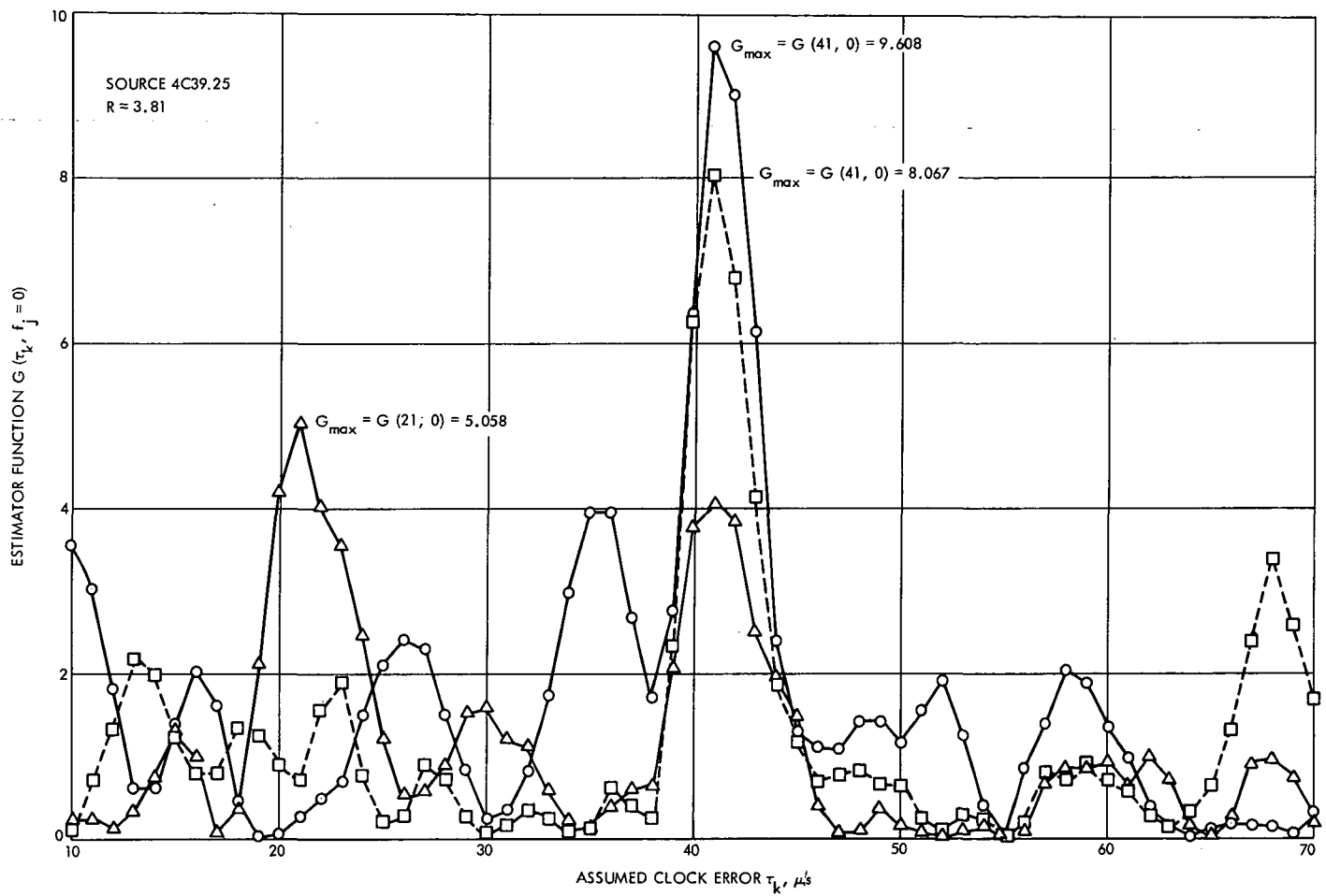


Fig. 4. Three estimator sample functions at a low SNR

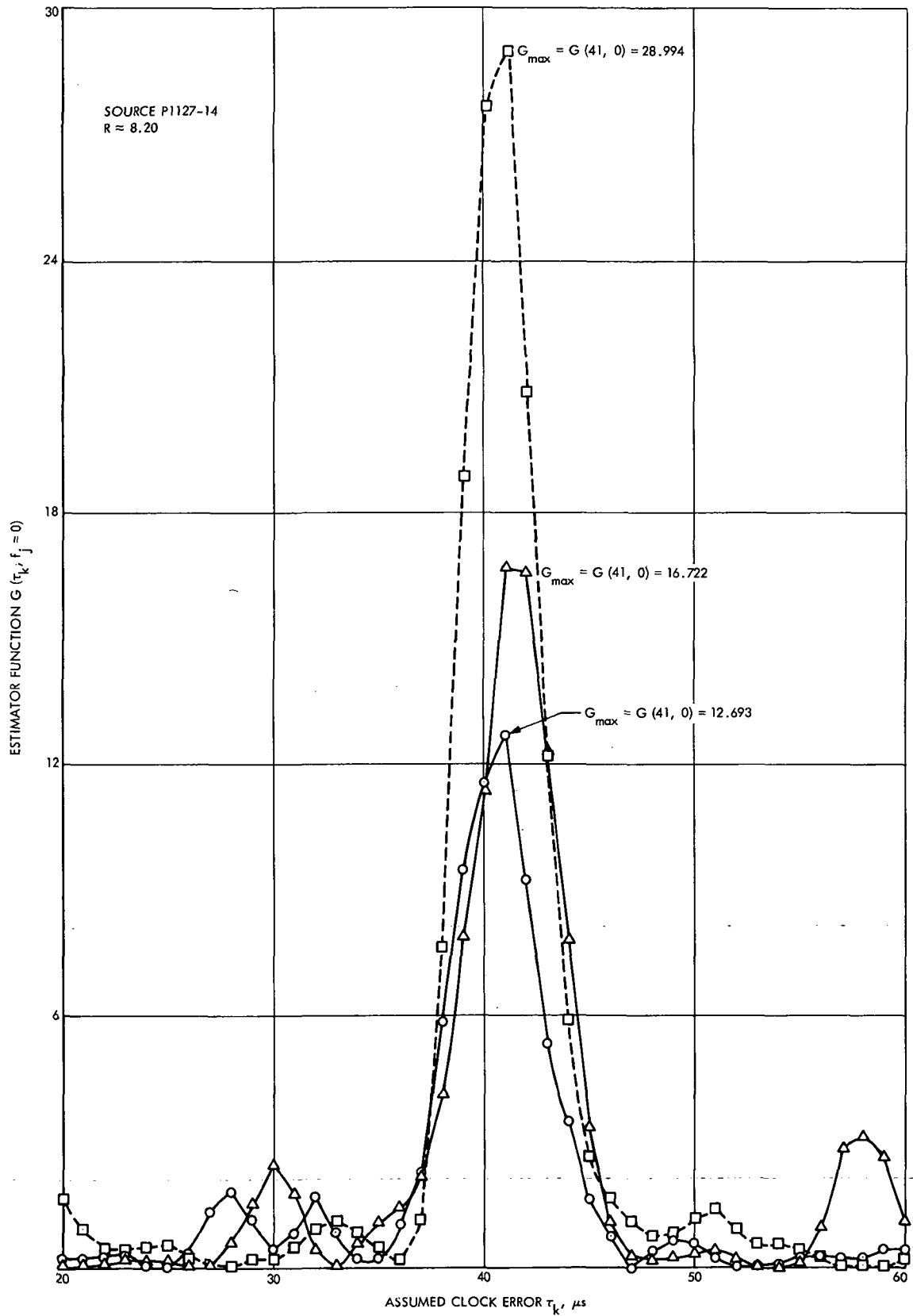


Fig. 5. Three estimator sample functions at a marginal SNR

On the Weight Enumerators of Quadratic Residue Codes

J. Mykkeltveit¹, C. Lam², and R. McEliece
Communications Systems Research Section

Binary quadratic residue codes, some of which are currently being studied for use in the Mariner Jupiter-Saturn 1977 mission, are among the most powerful known block codes. They are, however, notoriously difficult to analyze. In this paper a method is developed for obtaining information about the weights of these codes by exploiting the fact that they are left invariant by the linear fractional group.

I. Introduction

Binary quadratic residue codes are codes with rate $1/2$ and exist for all block lengths of the form $n = p + 1$, where p is a prime congruent to $\pm 1 \pmod{8}$. For example the $(8, 4)$ extended Hamming code and the $(24, 12)$ Golay code currently being studied for use in the Mariner Jupiter-Saturn 1977 mission are quadratic residue codes. These codes are very powerful, but are quite hard to decode. Practical decoding algorithms can be invented for them only after their fine structure is fully understood. In par-

ticular it is very important to have techniques for calculating the weight enumerator

$$A(Z) = \sum_{i=0}^n A_i Z^i$$

of the codes, A_i denoting the number of words of weight i in the code. The enumerator $A(Z)$ provides valuable information about the performance of the code (Ref. 1, pp. 397-400).

In this article, we develop a technique which yields valuable new information about the weight enumerators of quadratic residue codes. Our method relies heavily on the fact that every quadratic residue code is left invariant by a very large permutation group.

¹Postdoctoral Research Fellow in mathematics, California Institute of Technology.

²Graduate student in mathematics, California Institute of Technology.

II. Preliminaries

Let p be a prime congruent to $+1$ or $-1 \pmod{8}$, and let R_0 denote the set of nonzero quadratic residues \pmod{p} . Let α be a primitive p th root of unity in an extension field of $GF(2)$, and let the polynomial $h(x)$ be defined by

$$h(x) = \prod_{r \in R_0} (x - \alpha^r)$$

Then $h(x)$ is a polynomial with coefficients in $GF(2)$. The binary cyclic code of length p with check polynomial $h(x)$ is called the *expurgated quadratic residue code* (EQR code), and the code with check polynomial $(x+1)h(x)$ is called the *augmented quadratic residue code* (AQR code). The *extended quadratic residue code* (LQR code) is defined to be the set of binary n -vectors of the form $(C_0, C_1, \dots, C_{p-1}, C_\infty)$, where $(C_0, C_1, \dots, C_{p-1})$ is a codeword in the AQR code, and $C_0 + C_1 + \dots + C_{p-1} + C_\infty = 0$.

Berlekamp (Ref. 1, Theorem 15.26) proves the following theorem about LQR codes.

THEOREM: Every LQR code is invariant under the doubly transitive linear fractional group $LF(2, p)$,

$$C_u \longrightarrow C_{(au+b)/(cu+d)}$$

where $u \in GF(p) \cup \{\infty\}$; $a, b, c, d \in GF(p)$; $ad - bc = 1$. The group $G = LF(2, p)$ has order $p(p^2 - 1)/2$.

Let

$$A(Z) = \sum_{i=0}^{p-1} A_i Z^i$$

be the weight enumerator of the LQR code of length $p+1$; i.e., A_i is the number of words of weight i in the code. It is the object of this paper to show that it is possible to compute $A(Z) \pmod{p(p^2 - 1)/2}$ for many values of p which are so large that it is not possible to compute $A(Z)$ itself.

In order to compute $A(Z) \pmod{|G|}$, it is clearly sufficient to compute $A(Z) \pmod{|S_q|}$ for all primes q dividing $|G|$, S_q being a Sylow- q -subgroup of G . For $A(Z) \pmod{|G|}$ can then be computed from the $A(Z) \pmod{|S_q|}$ via the Chinese remainder theorem.

Now to find $A(Z) \pmod{|S_q|}$, we must count the number of codewords $A_i(q)$ of each weight i which are pointwise fixed by some element $q \neq 1$ of S_q . Clearly the codewords

of weight i which are fixed by no such element divide themselves into S_q -orbits of size $|S_q|$ and so

$$A_i \equiv A_i(q) \pmod{|S_q|}$$

It is known (Ref. 2, Sections 315–321) that for $q \neq 2$, the Sylow subgroups S_q of G are all cyclic. This makes it particularly easy to handle odd primes q . For example, let g_0 be an element of order q of S_q . Then if $g \neq 1$ is any other element of S_q , some power of g will equal g_0 . Thus the set of codewords fixed by some non-identity element of S_q is identical with the set of codewords fixed by g_0 . The subcode of the LQR code consisting of the codewords fixed by g_0 can then be found by solving a system of linear equations in $C_0, C_1, \dots, C_{p-1}, C_\infty$ over $GF(2)$ consisting of the parity-check equations for the LQR code together with the $p+1$ equations

$$C_u = C_{g \cdot u}, \quad u = 0, 1, \dots, p-1, \infty$$

The dimension of this subcode typically turns out to be small enough so that it is possible to calculate its weight enumerator by direct computer enumeration.

The Sylow-2 subgroup S_2 of G is dihedral of order 2^{m+1} , where 2^m is the highest power of 2 that divides $\frac{1}{2}(p-1)$ or $\frac{1}{2}(p+1)$. In order to compute the weight enumerator $\pmod{|S_2|}$, we prove a lemma which is a special case of Möbius inversion on a partially ordered set (Ref. 3, Chapter 2).

LEMMA: Let G be a finite group and let $f(H)$ be a function defined on all subgroups H of G . Let $g(\cdot)$ be a function defined on subgroups of G by

$$g(K) = \sum_{H \cong K} f(H)$$

Then if $\mu(\cdot)$ is the function on subgroups defined by the property $\mu(1) = 1$,

$$\sum_{K \leq H} \mu(K) = 0 \quad \text{if } H \neq 1$$

we have

$$f(1) = \sum_{K \cong 1} g(K) \mu(K)$$

Proof:

$$\begin{aligned} \sum_{K \cong 1} g(K) \mu(K) &= \sum_{K \cong 1} \mu(K) \sum_{H \cong K} f(H) \\ &= \sum_{H \cong 1} f(H) \sum_{K \leq H} \mu(K) \\ &= f(1) \end{aligned}$$

If C is any LQR codeword, the set of elements in $LF(2, p)$ which fix C is a subgroup, called the *stabilizer* of C . We now apply our lemma with $G =$ the S_2 - subgroup of $LF(2, p)$, $f_i(H) =$ the number of codewords of weight i with stabilizer H ,

$$g_i(K) = \sum_{H \supseteq K} f_i(H)$$

$=$ the number of codewords of weight i fixed by every element of K . Then if $A_i(G)$ denotes the number of codewords of weight i of LQR fixed by some element of G , the lemma yields

$$\begin{aligned} A_i(G) &= A_i - f_i(1) = g_i(1) - f_i(1) \\ &= - \sum_{H > 1} \mu(H) g_i(H) \end{aligned} \quad (1)$$

Furthermore, it is not difficult to calculate the function μ for a dihedral group G of order 2^{m+1} generated by $\{a, b\}$ with $a^{2^m} = 1, b^2 = 1, bab = a^{-1}$. It turns out that $\mu(1) = 1$, $\mu(H) = -1$ for all subgroups of order 2, and $\mu(H) = 2$ for all subgroups of order 4 except for the unique cyclic subgroup of order 4 for which $\mu(H) = 0$, and $\mu(H) = 0$ for all subgroups of order 8 or more.

Thus to compute the weight enumerator mod $|S_2|$ we need only compute the subcodes fixed by the various subgroups of order 2 and 4 of S_2 and apply Eq. (1). There are $2^m + 1$ subgroups of order 2 in S_2 , viz.,

$$\begin{aligned} G_2^i &= \{1, a^i b\}, & i &= 0, 1, \dots, 2^m - 1 \\ H_2 &= \{1, a^{2^{m-1}}\} \end{aligned}$$

Furthermore, these subgroups are all conjugate in $LF(2, p)$ (see Burnside, Ref. 2, Section 318), and so the weight enumerators of the LQR subcodes fixed by these groups are all identical.

Aside from the cyclic group of order 4, S_2 has 2^{m-1} subgroups of order 4, viz.,

$$G_4^i = \{1, a^{2^{m-1}}, a^i b, a^{i+2^{m-1}} b\}, \quad i = 0, 1, \dots, 2^{m-1} - 1$$

It can be shown that G_4^i and G_4^j are conjugate in S_2 if $i \equiv j \pmod{2}$ and so in order to compute the weight enumerators of the LQR subcodes corresponding to the G_4^i one needs only those of G_4^0 and G_4^1 . Thus if $A_i(S_2)$ denotes the number of codewords of weight i fixed by some element of S_2 , we have

$$A_i(S_2) = (2^m + 1) g_i(H_2) - 2^{m-1} g_i(G_4^0) - 2^{m-1} g_i(G_4^1) \quad (2)$$

In summary, let $Z_{q_1}, Z_{q_2}, \dots, Z_{q_r}$ be any set cyclic subgroups of $LF(2, p)$ of odd prime orders q_i , one for each odd prime dividing $p(p^2 - 1)/2$. Then we have shown that in order to compute the weight enumerator of LQR mod $p(p^2 - 1)/2$, it is sufficient to compute the weight enumerators of the subcodes fixed by $Z_{q_1}, Z_{q_2}, \dots, Z_{q_r}, H_2, G_4^0$ and G_4^1 . In the next section, we apply these techniques to the cases $p = 97$ and $p = 103$.

III. Applications

A. Case 1

Let $p = 97$, the smallest prime for which the weight enumerator for LQR is not known. Here $p(p^2 - 1)/2 = 456,288 = 2^5 \cdot 3 \cdot 7^2 \cdot 97$. Now according to Gleason's theorem on self-dual codes (Ref. 4) the weight enumerator $A(Z)$ of LQR (97) has the form

$$A(Z) = \sum_{k=0}^{12} K_k (1 + Z^2)^{49-4k} (Z^2 - 2Z^4 + Z^6)^k \quad (3)$$

for certain integers K_k . Now it is known (Ref. 1, p. 360), that

$$A_0 = 1, A_2 = A_4 = A_6 = \dots = A_{14} = 0$$

and this determines K_0, K_1, \dots, K_7 , leaving $K_8, K_9, K_{10}, K_{11}, K_{12}$ undetermined. However, it is possible to show that if

$$a(Z) = \sum_{i=0}^p a_i Z^i$$

is the weight enumerator for the AQR code, $p \equiv 1 \pmod{8}$, that

$$a(i) = \pm (1 + i) 2^{(p-1)/4}$$

The "+" sign holds if $k = \text{ord}_p(2)$ is even and $m = p - 1/2k$ is also even. The "-" sign holds in all other cases. On page 70 of Ref. 5 it is proved that

$$a(Z) = A(Z) + \frac{1 - Z}{p + 1} A'(Z)$$

$A(Z)$ being the weight enumerator of the LQR code. Now $A(i) = 0$ and so $A'(i) = \pm (n + 1) 2^{(n-1)/4} i$. Now if we differentiate Gleason's theorem

$$A(Z) = \sum_{k=0}^{(p-1)/8} K_k (1 + Z^2)^{(p+1)/2-4k} (Z^2 - 2Z^4 + Z^6)^k$$

and set $Z = i$, we obtain

$$A'(i) = (-1)^{(p-1)/8} 2^{(p+3)/4} i K_{(p-1)/8}$$

and so

$$\begin{aligned} K_{(p-1)/8} &= \pm (-1)^{(p-1)/8} \cdot (n+1)/2 \\ &= (n+1)/2 \text{ for } p = 41, 113, 137, 257, 281, \dots \\ &= -(n+1)/2 \text{ for } p = 17, 73, 89, 97, 193, 233, 241, \dots \end{aligned}$$

In particular, $K_{12} = -49$ for the LQR of length 98. Thus only K_8, K_9, K_{10}, K_{11} remain unknown, and so it is sufficient to know $A_{16}, A_{18}, A_{20}, A_{22}$ to find $A(Z)$.

We now compute $A_{16}, A_{18}, A_{20}, A_{22} \pmod{456288}$. It is shown in Burnside (Ref. 2) Section 317 that if q divides $p+1$, an element of order q has no fixed points. Thus no code words of weight i can be fixed by S_q unless q divides i . Thus

$$A_{16} \equiv A_{18} \equiv A_{20} \equiv A_{22} \equiv 0 \pmod{49}$$

Also, the translation $u \rightarrow u+1$ is of order 97 and fixes only $(0, 0, \dots, 0)$ and $(1, 1, \dots, 1)$. Hence

$$A_{16} \equiv A_{18} \equiv A_{20} \equiv A_{22} \equiv 0 \pmod{97}$$

To handle the prime 3, we observe that $u \rightarrow 2^{16}u$ is an element of order 3. By computer it was found that the corresponding subcode has dimension 17, with

$$\begin{aligned} A_{16} &= 0 \\ A_{18} &= 8 \\ A_{20} &= 16 \\ A_{22} &= 128 \end{aligned}$$

Thus

$$\begin{aligned} A_{16} &\equiv 0 \pmod{3} \\ A_{18} &\equiv 2 \pmod{3} \\ A_{20} &\equiv 1 \pmod{3} \\ A_{22} &\equiv 2 \pmod{3} \end{aligned}$$

This completes the work with odd prime divisions of $p(p^2-1)/2$.

For $p=2$, we must compute the weight enumerators of the three subcodes corresponding to H_2, G_4^0 , and G_4^1 . These subcodes were calculated by computer, with these results:

Subgroup	Dimension of Subcode	A_{16}	A_{18}	A_{20}	A_{22}
H_2	25	54	161	420	1740
G_4^0	13	6	3	6	0
G_4^1	14	0	15	18	38

Combining these results via the Chinese remainder theorem, we obtain:

$$\left. \begin{aligned} A_{16} &\equiv 28518 \pmod{456288} \\ A_{18} &\equiv 80801 \pmod{456288} \\ A_{20} &\equiv 19012 \pmod{456288} \\ A_{22} &\equiv 437276 \pmod{456288} \end{aligned} \right\} \quad (4)$$

Finally we used the only other known condition on the A_i 's, namely that they are non-negative, and by linear programming concluded that $A_{16} = 28518$. (If $A_{16} \geq 28518 + 456288$, some A_i would turn out to be negative). Furthermore, there are only two possibilities for A_{18} :

$$A_{18} = 80801 \text{ or } 537089$$

The latter possibility can be ruled out if we make the plausible assumption that

$$A_i < A_{i+2}, i = 16, 17, \dots, 46$$

Altogether there are 323 possible values for $A(Z)$ consistent with Eq. (4), and 162 of them satisfy the additional constraint $A_i < A_{i+1}$.

B. Case 2

Let $p=103$. In this case, all weights in LQR are divisible by 4 and Gleason's theorem takes the simpler form

$$A(Z) = \sum_{k=0}^4 K_k (1 + 14Z^4 + Z^8)^{13-3k} (Z^4(1-Z^4))^k$$

It is known (Ref. 1, p. 360) that the minimum weight in this LQR is 16 or 20, and there is compelling statistical evidence that it is in fact 20 (Ref. 6). In any event, the conditions

$$A_0 = 1, A_4 = A_8 = A_{12} = 0$$

determine all the K 's but K_4 . In order to find $A(Z)$, therefore, it is sufficient to find A_{16} .

In this case,

$$p(p^2-1)/2 = 2^3 \cdot 3 \cdot 13 \cdot 17 \cdot 103$$

As before, $A_{16} \equiv 0 \pmod{97}$ because no code word is fixed by $u \rightarrow u+1$ except 0^{98} and 1^{98} . Also, since 13 divides $p+1=104$, an element of order 13 has no fixed points, and so only words of weight divisible by 13 can be fixed by elements of order 13. Thus $A_{16} \equiv 0 \pmod{13}$.

Also, $A_{16} \equiv 0 \pmod{17}$ since no element of G has more than two fixed points and $16 \not\equiv 0, 1, 2 \pmod{17}$. Finally, the permutation $u \rightarrow 56u$ is of order 3, and its subcode turns out to be of dimension 18. However, it contains no words of weight 16. Thus $A_{16} \equiv 0 \pmod{3}$ as well. This completes the odd primes.

For $q = 2$, it turns out that the subcode corresponding to H_2 has dimension 26, but no words of weight 16. Since H_2 is a subgroup of both G_4^0 and G_4^1 , it follows that $A_{16} \equiv 0 \pmod{8}$. Thus

$$A_{16} \equiv 0 \pmod{546312}$$

Hence $A_{16} = 546312n$ for some integer n . The weight enumerator corresponding to $n = 0$ is given by Mallows and Sloane (Ref. 7). Using their calculations, we find that $n > 1$ always forces A_{20} to be negative. The possibilities turn out to be, therefore,

$$\begin{aligned} A_{20} &= 1138150 \\ &= 45526 \end{aligned}$$

LEMMA: $A_{20} > 45526$ and so $A_{20} = 1138150$.

Proof: We immediately see that no element of order 13, 17, or 103 can fix a word of weight 20. If a is a word of weight 20, let a^g denote its images under G , and S_a its stabilizer in G . Then

$$|a^g| = |G|/|S_a|$$

Since $13 \cdot 17 \cdot 103$ divides $|a^g|$, we see that

$$|S_a| = 24, 12, 8, 6, 4, 2, \text{ or } 1$$

If $|S_a| \leq 8$, then $|a^g| > 45526$, and we are through. Thus $|S_a| = 12$ or 24 . Next, our calculations in the H_2 subcode yielded 423 words of weight 20. Since the number of words of weight 20 fixed by any of the $103 \cdot 51 = 5253$ elements of order 2 is the same, and since $|S_a| \leq 24$ for any word of weight 20, the code must contain $\geq 423 \cdot 5253/24 \approx 90000$ words of weight 20. This completes the proof of the lemma.

Corollary: The minimum distance of the (104,52) LQR code is 20; and its weight enumerator is given by the following:

i	A_i
0,104	1
20,84	1138150
24,80	206232780
28,76	15909698064
32,72	567725836990
36,68	9915185041320
40,64	88355709788905
44,60	413543821457520
48,56	1036378989344140
52	1406044530294756

Proof: This calculation was performed by Mallows and Sloane (Ref. 7).

References

1. Berlekamp, E. R., *Algebraic Coding Theory*, McGraw-Hill, New York, 1968.
2. Burnside, W., *Theory of Groups of Finite Order*, 2nd ed. 1911. Reprinted by Dover, New York, 1955.
3. Hall, M., Jr., *Combinatorial Theory*, Ginn-Blaisdell, Waltham, 1967.
4. Gleason, A., "Weight Polynomials of Self-Dual Codes and the MacWilliams Identities," *Actes, Congres intern. Math.*, 1970, Vol. 3, pp. 211-215; Gauthier-Villars, Paris, 1971.
5. vanLint, J. H., *Coding Theory*, Springer Lecture Notes in Mathematics No. 201, Berlin 1970.
6. Karlin, M., "New Binary Coding Results by Circulants," *IEEE Trans. Inform. Theory IT-15*, 1969, pp. 81-92.
7. Mallows, C. L., and Sloane, N. J. A., *An Upper Bound for Self-Dual Codes*, in press.

Sequential Decoding With a Noisy Carrier Reference

J. W. Layland

Communications Systems Research Section

An approximate analysis of the effect of a noisy carrier reference on the performance of sequential decoding is presented. The limitations of the analysis are discussed and steps are described that could be taken to extend the performance region over which the model used produces accurate, rather than merely bounding, results.

I. Introduction

Convolutional encoding with sequential decoding is a very powerful technique for communicating at low error probability with deep space probes. It has been used successfully with Pioneer 9 and 10, and is planned for use on Helios. Most, if not all, of the performance data for this coding technique have been developed without regard to the effects of noisy reference signals in carrier or subcarrier tracking loops. These effects must be known with fair accuracy for the optimal design of telemetry links with sequential decoding.

II. Sequential Decoding—The Computation Problem

The convolutional codes which are sequentially decoded typically have a large enough constraint length so that the undetected error probability out of the decoder is negligible compared to the probability that a block cannot be successfully decoded in the time allowed. Thus, the limiting factor for sequential decoding is the proba-

bility that large amounts of computation are required to decode a frame of the code, rather than the probability of error. Experimental and theoretical work has shown that the distribution of the number of computations c_1 needed by the decoder to penetrate 1 bit deeper into the convolutional code tree has a Pareto distribution

$$\Pr\{c_1 > x\} \sim kx^{-a} \quad (1)$$

The exponent a is the noisy channel error exponent (Ref. 1), and k is a small constant, found by Heller (Ref. 2) to be 1.9.

The computation distribution is somewhat changed when an entire code frame is considered. The number of computations needed by the decoder to penetrate from a depth of $N - 1$ to a depth of N is certainly not independent of the number of computations needed to penetrate from depth N to depth $N + 1$. However, the number of computations needed to penetrate from depth $N - 1$ to depth N is independent of the number of computations needed to penetrate from depth $N + j - 1$ to depth $N + j$,

if $|j|$ is large enough. The magnitude $|j|$ which is large enough to establish independence is believed to be a function of the signal-to-noise ratio (SNR). The Pareto distribution has the property that for moderately large N , the probability of a single long computation of length $2N$ is much greater than the probability of two smaller computations, each of length approximately N . As a result, whenever the number of computations needed to decode a code frame is large, its distribution is dominated by single long computations, representing decoder penetration from $M - l$ to M , for some M, l . Where the number of computations is small, however, the distribution function represents the sum of many small computations. This fact is important and will be used later.

Experimental distributions of the number of computations needed to decode the Pioneer 10 frame of 192-bit length were developed at NASA Ames Research Center (Ref. 3) and are reproduced here for convenience in Fig. 1. A curve of decoder erasure probability vs. SNR can be derived from this figure by projecting the curves on the plane defined by a fixed number of computations per frame.

III. Carrier Loop Effects

The receivers of the DSN tracking stations use a narrowband phase-locked loop, tracking the carrier component of the signal received from the spacecraft, to provide a coherent reference for demodulation of the telemetry sidebands on that signal. The bandwidth of the phase-locked loop is generally wide enough to track out received doppler, yet narrow with respect to the telemetry data rate, so that the phase of the reference signal is essentially constant while several tens of bits are being received. If, for reasons of received noise or otherwise, a phase error ϕ exists between the received carrier and the local carrier reference, the amplitude of the signal entering the decoder is degraded by a factor $\cos \phi$ while that phase error ϕ persists.

The probability distribution of the phase error ϕ in a phase-locked loop has been derived elsewhere (Ref. 4) to be

$$P(\phi) = \frac{\exp(\rho_L \cos \phi)}{2\pi I_0(\rho_L)} \quad (2)$$

where $I_0(-)$ is the zeroth-order modified Bessel function and ρ_L is $2P_c/N_0W_L$.

Lindsey (Ref. 5) has used this phase error distribution to derive performance curves for the biorthogonal block

code which account for noise in the reference signal under the (reasonable) assumption that the phase error ϕ is constant while a code block is being received. The validity of this assumption depends merely upon the bandwidth of the phase-locked loop being narrow with respect to the rate at which code blocks are received. The theoretical bit-error probability curves, which are functions of bit SNR, can thus be considered functions of the phase error ϕ that existed while each block was being received, and of the bit SNR that would exist if the carrier reference were perfect. Averaging over the probability distribution of phase error ϕ results in performance curves which show the expected bit-error probability of the coded system, and account correctly for the losses due to a noisy carrier reference.

Heller and Jacobs (Ref. 6) have recently used the same technique to estimate the performance of optimally decoded, short-constraint-length convolutional codes with a noisy carrier reference. They argue that the averaging over ϕ is valid whenever the phase error is relatively constant over a period of time which is long with respect to the constraint length of the code.

For block coding, the situation in which the phase error ϕ varies during a code frame has been approximately analyzed by Tausworthe (Ref. 7), who developed a formula for interpolation between performance with constant phase (Ref. 5) and the performance expected with very rapidly varying phase error. The interpolation parameter is a function of the time-bandwidth product for the code-block integration time and the phase-locked-loop bandwidth. This same interpolation formula should be equally valid for short-constraint-length convolutional codes if we could reliably define the "integration time" of these codes.

For sequential decoding, if the phase error ϕ is essentially constant over a frame of data, then it is clear that we can average the erasure probability curves conditioned on bit SNR (and ϕ) over the distribution of phase error, and derive a valid estimate of decoding performance with a noisy reference. This condition, however, requires that the phase-locked loop be extremely narrow with respect to data rate, an unrealistic assumption which, furthermore, does not appear to be necessary.

Let us consider the characteristics of the distribution of the number of computations per frame in the region where the number of computations is large. As noted before, the computations on any block in this region are dominated by single large computations that result from

the decoder extending its penetration from depth $M - l$ to depth M , for some M and some l much less than the frame length. If the phase error ϕ is essentially constant for these l or more bits, then the distribution of computations can be considered as being conditioned on ϕ for large numbers of computations per frame.

If the total number of computations in a frame is small, then that computation must almost certainly have resulted as the sum of a (possibly large) number of independent searches, each with its own value of ϕ . The degradation in the computation distribution which results from phase jitter in this case is less than the degradation which would result if the phase error were constant over the entire frame. A lower bound on the degradation can be determined by assuming that the phase error is independent from bit to bit and computing the expected loss in signal amplitude into the decoder by averaging over the distribution of ϕ .

The pseudo-theoretical distribution of decoding computations which results from treating phase error as constant over an entire frame and averaging the perfect-reference computation distribution over the phase error distribution has thus two levels of validity: It is an accurate estimate of the low-probability, long computation events, which correspond to erasures in a typical system; and it represents an upper bound to the degradation due to phase error for the sums of several short searches, which occur with higher probability and which seldom represent erasures.

To obtain numerical results, the probability distribution family shown in Fig. 1 was approximated by functions of bit SNR (R), and average number of computations per bit (N). The chosen approximating functions are of the form

$$\Pr\{c_L > N*L\} = \exp \left\{ \sum_{\substack{n=-1.1 \\ r=0.2}} A_{n,r} R^r (\ln N)^n \right\} \quad (3)$$

The coefficients $\{A_{n,r}\}$ were determined by a two-dimensional, least-squares polynomial fit, and appear in Table 1. The frame length is L .

The solid lines of Fig. 1 show this approximation. Having thus been defined as functions of bit SNR, it is a trivial task to express these distributions as functions of total bit SNR and carrier phase error ϕ , and to numerically integrate them over the distribution of ϕ (Eq. 2) for various values of the carrier tracking loop SNR. Figure 2 shows the computed distribution of the

computation for a fixed input symbol-error probability of 6%. The loop SNRs and bit SNRs correspond to the Pioneer 10 modulation index and its range of data rates. This same family of curves has been generated experimentally by C. Grauling and J. Wilcher (Ref. 8), and is reproduced here as Fig. 3. Notice that, in general, the computed distributions predict a considerably poorer performance than observed experimentally.

To understand why the experimental and computed results disagree, we need observe that decoding performance with noisy reference depends to some significant extent upon the decoding performance at very low SNR. For large values of ϕ , the effective SNR at decoder input is very low, and is outside of the region enclosed by the data of Fig. 1. We are thus depending upon the valid extrapolation of Eq. (3) of Table 1. This extrapolation does not follow the trends observed in some recently developed experimental distributions (Ref. 9, Fig. 2): both the exponent α and the probability-axis intercept remain too high at extremely low SNR.

We can induce a better fit at low SNR by including low-SNR hypothetical data in the data set, as shown in Fig. 4. The exponent of this curve corresponds theoretically to $E_b/N_0 = -2.0$ dB (Ref. 10). At extremely low SNR and short block lengths, it has been observed (Ref. 9) that the computation distribution appears as if the code tail added to the effective signal but not so much to the noise. This would occur if the effective length of the decoding searches approached the block length. If we assume that the entire tail contributes to this effect, then there is an effective increase of over 0.5 dB for the 192-bit Pioneer 10 frame with a 24-bit tail, and about 0.1 dB for the 1152-bit Helios frame with a 32-bit tail.

The solid lines of Fig. 4 result from assuming $E_b/N_0 = -2.5$ dB for the hypothetical data, equivalent to assuming a Pioneer block with the tail fully contributing to the effective SNR. The approximation parameters appear in Table 2. Figure 5 shows the computed distribution of the computation for a fixed symbol-error probability of 6% using the approximation of Eq. (3) (Table 2). The curves of Fig. 5 are now encouragingly close to the experimental curves of Fig. 3. To improve our confidence in performance curves computed in this fashion, we must determine experimentally the computation distribution at very low SNR. This is not an easily accomplished task because the number of decoder computations needed to acquire any fixed amount of computation distribution data is large for very low SNR.

At the moment, the best estimate of sequential decoding with noisy reference performance is obtained by computing from the approximation of Eq. (3) (Table 2). The distribution of computations for fixed bit SNR using this approximation is shown in Fig. 6a-c. The hypothetical augmented data set of Fig. 4 has also been approximated assuming $E_b/N_0 = -2.0$ dB, for correspondence with long blocks, and the resultant parameters appear in Table 3. The computed distribution of the computation for this approximation is shown in Fig. 7a-c.

IV. Summary and Extensions

This article has presented a technique for analyzing the effect of a noisy carrier phase reference on sequential decoding. The technique produces a good approximation to frame erasure probability—when that probability is low—and a bound to the degradation caused by the noisy carrier reference for other regions of the distribution of computation curves. There is no previously published theory detailing the behavior of the distribution of computation in a noisy reference environment. However, the increase in SNR needed to counteract noisy reference losses and achieve a Pareto exponent $\alpha = 1$ was bounded by Heller (Ref. 11). This bound is somewhat more pessimistic than that of Fig. 2 for $\alpha \approx 1$.

One of the inputs to this analysis is the experimental distribution of decoder computations per frame, which is necessarily a function of frame length. In order to develop an analysis of the effect of phase jitter on sequential decoding which is accurate for all ranges of the computation variable and which can be adapted to all

frame lengths, an accurate model of the sequential decoding process is needed. From observation of experimental distributions of sequential decoding computation, both on a per-bit and per-frame basis, I believe that the computations needed to sequentially decode a frame of data can be represented as the sum of a number of independent searches of varying length. If within a particular frame, a search of length l ends at depth M , then the number of computations needed to penetrate from depth $M - j$ to $M - j + 1$ is strongly dependent upon the numbers of computations needed to penetrate from depth $M - 1$ to M whenever $1 < j < l$. Searches are characterized by two numbers, their length l , and the numbers of computations required to complete the search. Except for boundary effects, a frame contains some number of searches whose lengths total to the frame length. This hypothetical model can, and should, be tested by properly instrumenting a sequential decoder to determine the joint distribution of search length and number of computations. Assuming that this model is valid, the noisy reference problem could be easily attacked, since the search length l is almost certain to be short enough for the phase error ϕ to be constant throughout each search. Alternatively, the search length l is the "integration time" parameter needed to apply interpolation techniques to decoding behavior when the phase error ϕ varies during searches.

The joint distribution of search length and computations would be modified to include the effects of carrier phase jitter, employing the same numerical techniques just used, to produce a distribution family—in terms of bit SNR and carrier loop SNR—which can subsequently be used to derive all parameters of interest.

References

1. Jacobs, I. M., and Berlekamp, E. R., "A Lower Bound to the Distribution of Computation for Sequential Decoding," *IEEE Trans. Info. Theory*, IT-13, pp. 167-174.
2. Heller, J. A., "Description and Operation of a Sequential Decoder Simulation Program," in *Supporting Research and Advanced Development*, Space Programs Summary 37-58, Vol. III, p. 42, Jet Propulsion Laboratory, Pasadena, Calif., Aug. 31, 1969.
3. Lumb, D., and Hoffman, L., "Preliminary Results on Coding for Pioneer F," NASA Ames Memo, Nov. 4, 1969.
4. Viterbi, A. J., *Principles of Coherent Communication*, Chap. 4, McGraw-Hill Book Co., Inc., New York, 1966.
5. Lindsey, W. C., "Block Coding for Space Communications," *IEEE Trans. Commun. Technol.*, Vol. COM-17, No. 2, April 1969, pp. 217-225.
6. Heller, J. A., and Jacobs, I. M., "Viterbi Decoding for Satellite and Space Communications," *IEEE Trans. Commun. Technol.*, Vol. COM-19, No. 5, Oct. 1971, pp. 835-848.
7. Tausworthe, R. C., "Efficiency of Noisy Reference Detection," in *Supporting Research and Advanced Development*, Space Programs Summary 37-54, Vol. III, pp. 195-201, Jet Propulsion Laboratory, Pasadena, Calif., Dec. 31, 1968.
8. Wilcher, J. H., *DSN DDA Performance for Pioneer Telemetry*, IOM 3384-72-056, June 26, 1972. (JPL internal document)
9. Layland, J. W., "Performance of an Optimum Buffer Management Strategy for Sequential Decoding," in *The Deep Space Network Progress Report*, Vol. IX, pp. 88-96, Jet Propulsion Laboratory, Pasadena, Calif., 1972.
10. Jacobs, I. M., "Sequential Decoding for Efficient Communication from Deep Space," *IEEE Trans. Commun. Technol.*, Vol. COM-15, No. 4, Aug. 1967, pp. 492-501.
11. Heller, J. A., "Sequential Decoding with Decision Directed Phase Estimation," in *Supporting Research and Advanced Development*, Space Programs Summary 37-48, Vol. III, pp. 181-187, Jet Propulsion Laboratory, Pasadena, Calif., Dec. 31, 1967.

Table 1. $A_{n,r}$ for Pioneer data

$n \backslash r$	-1	0	1
0	-4.48	5.81	-0.329
1	4.91	-5.01	0.806
2	-1.25	0.995	-0.685

Table 2. $A_{n,r}$ for short-frame, low-SNR extrapolation

$n \backslash r$	-1	0	1
0	0.44	0.179	-0.773
1	-0.127	0.603	1.44
2	0.016	-0.401	-0.903

Table 3. $A_{n,r}$ for long-frame, low-SNR extrapolation

$n \backslash r$	-1	0	1
0	-0.88	0.374	0.617
1	1.20	0.673	-0.181
2	-0.302	-0.512	-0.431

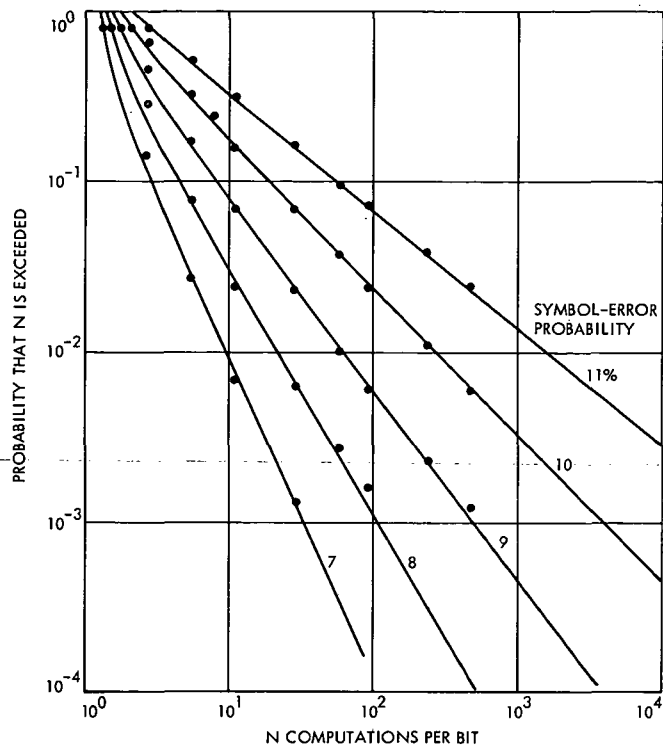


Fig. 1. Distribution of computations for sequential decoding of Pioneer 10 frame

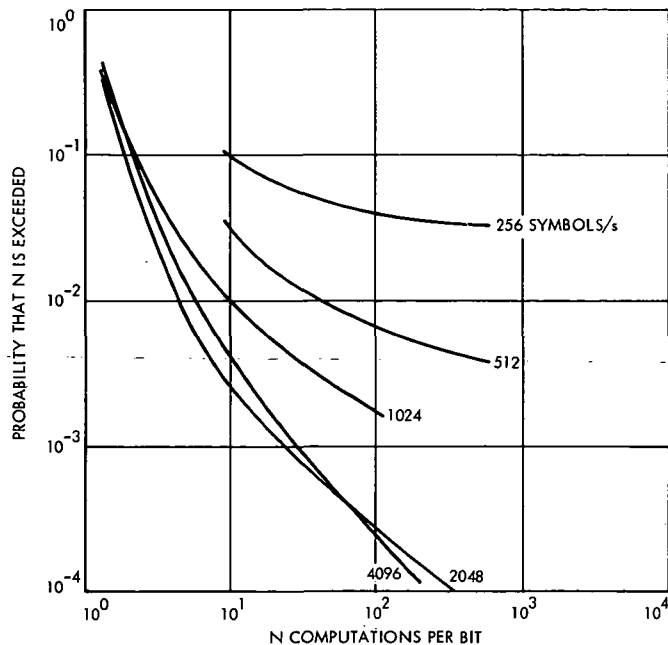


Fig. 3. Experimental computation distribution with noisy reference, at 6% symbol-error probability

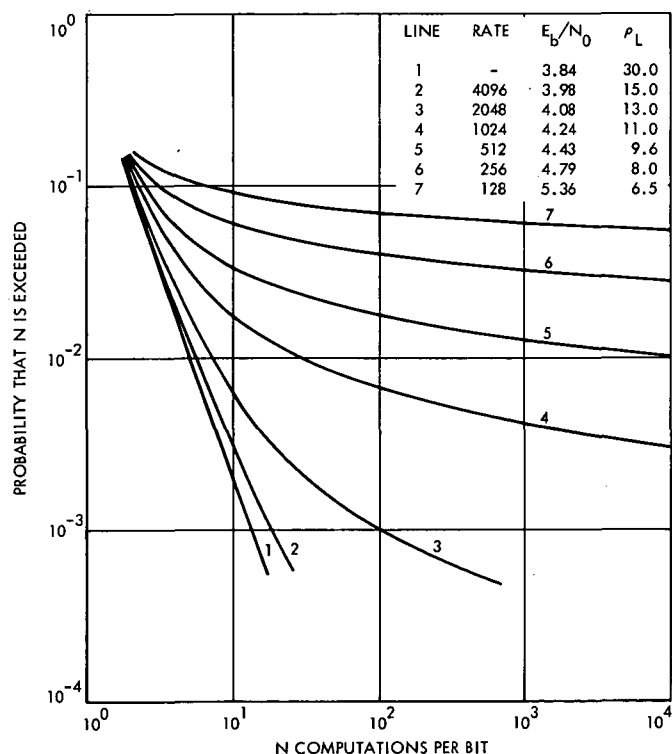


Fig. 2. Computed computation distribution with noisy reference, at 6% symbol-error probability

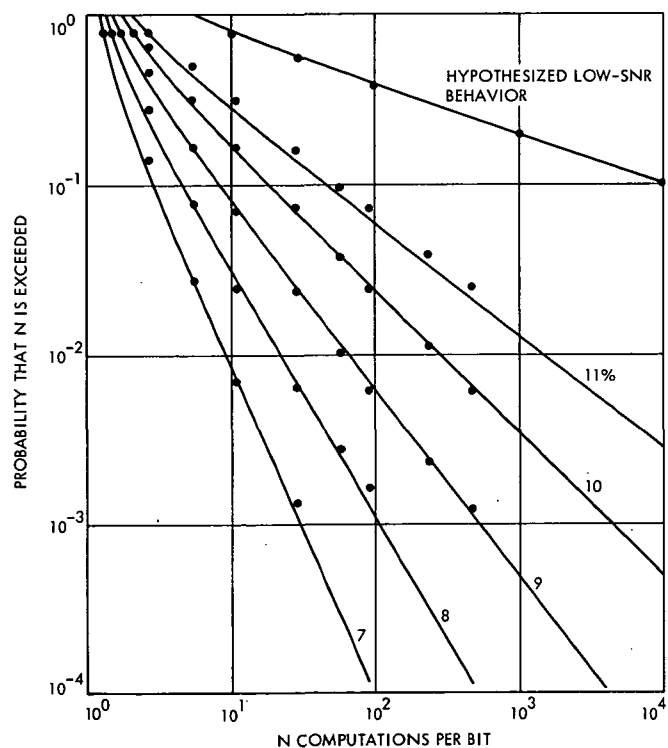


Fig. 4. Computation distribution for Pioneer 10 frame, with extrapolation to low SNR

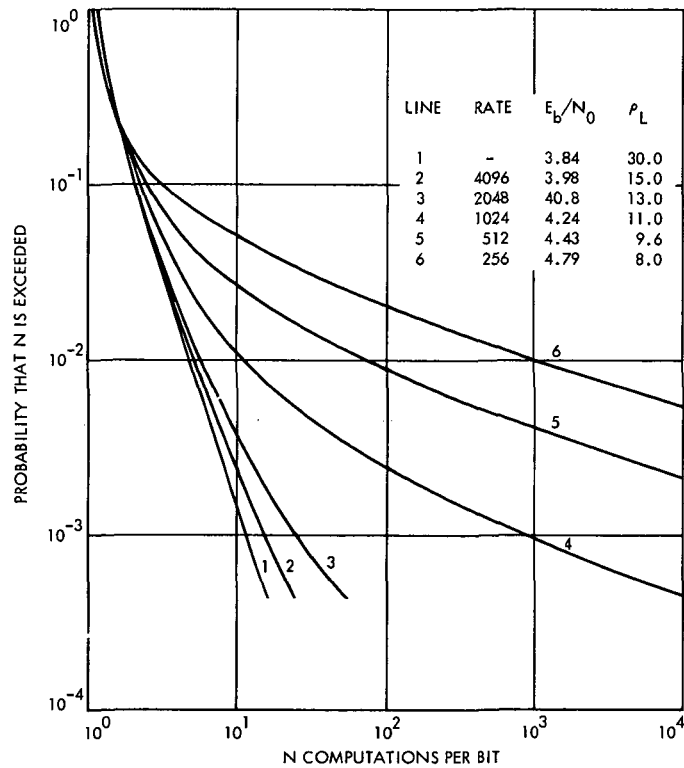


Fig. 5. Computed computation distribution with noisy reference using low-SNR extrapolation, at 6% symbol-error probability

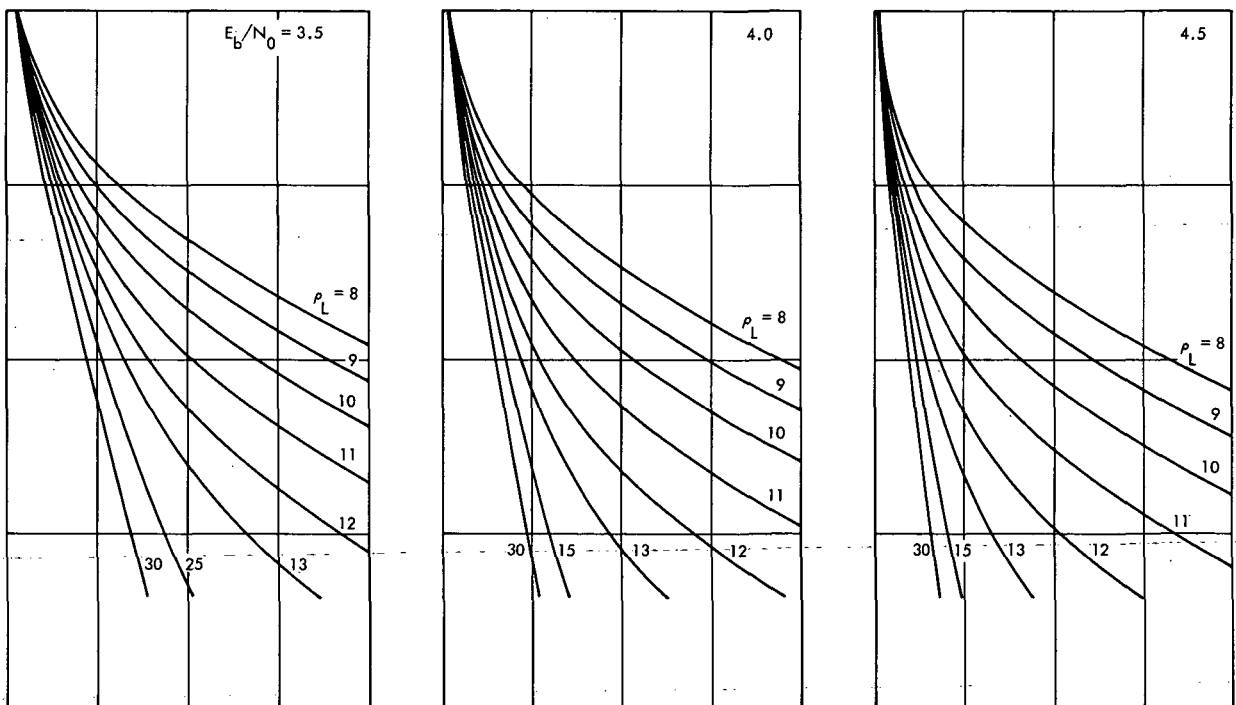


Fig. 6. Estimated computation distribution for short frames

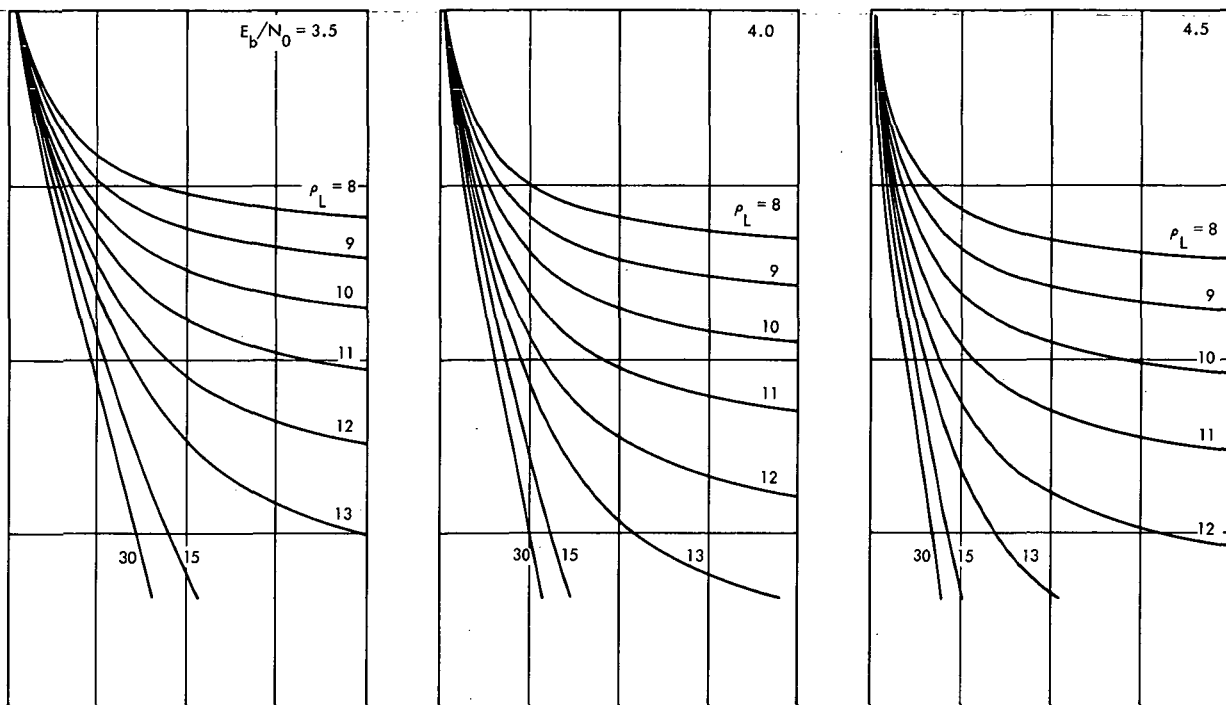


Fig. 7. Estimated computation distribution for long frames

An Execution Analyzer for the Sigma 5 Computer

C. C. Klimasauskas

Communications Systems Research Section

Since many different computers on the market today claim to perform the same class of tasks, and no uniform criterion has been established to aid the decision-making process, the problem of how to select the "best" computer for a particular job mix becomes almost a matter of personal preference and chance. One technique for evaluating the performance of a central processing unit is based on the frequency of usage of the various machine instructions. This technique is particularly applicable to machines used in a dedicated process-control activity such as those of the DSN Tracking Stations. This article describes a program which has been written for the Sigma 5 computer to gather data on the dynamic usage of computer instructions in various tasks.

I. Introduction

The technique for evaluating the performance of a central processing unit based on the frequency of usage of the various machine instructions is particularly applicable to machines used in a dedicated process-control activity such as those of the DSN Tracking Stations. This article describes a program written for the Sigma 5 computer to gather data on the dynamic usage of computer instructions in various tasks. Results of a study using this program are described in a companion article by Layland and Klimasauskas¹.

This data gathering program is named MR $\phi\phi$ 7, and its overall operation is described in Section II. Subsequent sections include instructions for MR $\phi\phi$ 7 operation, and for attaching it to various types of user programs; a description of the format in which the data gathered are written into a disk file; and a description of error conditions which may be encountered, and their associated messages. Section V describes in some detail the set of

programs which have been used to transform the data gathered by MR $\phi\phi$ 7 into a visually meaningful format, and presents an example of that output format.

II. The Interpreter

MR $\phi\phi$ 7 is an interpretive executor which dynamically tabulates instruction usage. The entire problem-solving repertoire of Sigma 5 instructions is allowed.² Results from program execution are stored in a disk file for further analysis. Instructions which communicate with the monitor (CALs) are limited to background mode only. Monitor CALs dealing with interrupts, program control transfers, and traps are excluded.

MR $\phi\phi$ 7 may be tailored to operate in either a Batch Processing Monitor (BPM) or a Batch Timesharing Monitor (BTM) environment through an assembly control parameter. This parameter (P:USER), when set equal to :BPM, produces code to interpret BPM monitor CALs.

¹Layland, J. W., and Klimasauskas, C. C., *A Myopic View of Computer-Based System Design* (to be published).

²These do not include control, and input/output instructions.

When set equal to :BTM, it produces code to interpret BTM monitor CALs.

Since this program was designed as a tool to study a wide range of problems, certain features (described in Section VI) were not considered of sufficient importance to warrant implementation. If these or other features (such as foreground CALs) must be used, their code may be bypassed through the use of a HOLD-GO pair (see Section III).

To facilitate analysis of data from MR $\phi\phi$ 7, a series of programs have been written which transform the data into informative formats. These are described in Section V.

III. Operating Instructions

A. FORTRAN Programs

MR $\phi\phi$ 7 is easily attached to any extended FORTRAN IV program. To activate it, simply use this statement:

```
CALL MR $\phi\phi$ 7
:
STOP
```

If it is desired to deactivate MR $\phi\phi$ 7 with intentions of restarting it, use the following sequence:

```
CALL MR $\phi\phi$ 7
* } Program executed under control of
* } MR $\phi\phi$ 7
* }
CALL HOLD
: } Program executed without control of
: } MR $\phi\phi$ 7
CALL GO
* } Program executed under control of
* } MR $\phi\phi$ 7
* }
STOP
```

MR $\phi\phi$ 7 also provides the option of writing its current data tables to M:EO, clearing them, and relinquishing control of the program. This effectively provides the user the capability of selectively looking at the instruction repertoire of several very different portions of the program. A word of caution: MR $\phi\phi$ 7 *must* be in control of the program when it exits to the monitor. If MR $\phi\phi$ 7 is not in control when the program is to be terminated, the data file will be lost. To close and save the output file, use "CALL WDATCLSE." This routine will exit to the

monitor on closing the file. Note that all user output files which are open will be lost. A sample sequence is:

```
CALL MR $\phi\phi$ 7
* } Program executed under MR $\phi\phi$ 7
* } control
CALL MR $\phi\phi$ 7
: } Data tables written to
: } M:EO ("DEXEC"), cleared, and
: } control relinquished
: }
: } Program executed without control
: } of MR $\phi\phi$ 7
CALL MR $\phi\phi$ 7
* } Program executed under MR $\phi\phi$ 7
* } control
CALL MR $\phi\phi$ 7
: } Data tables written to
: } M:EO ("DEXEC"), cleared, and
: } control relinquished
: }
CALL MR $\phi\phi$ 7
STOP } End sequence giving MR $\phi\phi$ 7
      } control
```

It is allowable to use any number of HOLD-GO pairs within a MR $\phi\phi$ 7 pair.

B. Assembly Programs

MR $\phi\phi$ 7 is attached to assembly programs using the assembly language equivalent of the FORTRAN calling sequences above, namely:

```
CALL MR $\phi\phi$ 7
is replaced by
REF MR $\phi\phi$ 7
LI,14 0
BAL,15 MR $\phi\phi$ 7
```

```
CALL GO
is replaced by
REF GO
LI,14 0
BAL,15 GO
```

```
CALL HOLD
is replaced by
REF HOLD
LI,14 0
BAL,15 HOLD
```

```
STOP
is replaced by
M:EXIT
```

IV. Data Record Format

MR $\phi\phi$ 7 writes the data tables to a disk file ("DEXEC") through the M:EO DCB. The DCB does not need to be assigned through an ASSIGN card, nor should it be. For each MR $\phi\phi$ 7 pair and for the MR $\phi\phi$ 7-STOP pair, a data record is written. If data already exist in file "DEXEC," they will be lost. The format of each record is as shown in Fig. 1.

V. Support Programs

To facilitate the analysis of data from MR $\phi\phi$ 7, a number of support programs have been written to transform the data to usable and meaningful terms. These programs are briefly described below.

A. PUNCH

PUNCH is a FORTRAN program which takes the file DEXEC produced by MR $\phi\phi$ 7 and generates records in the standard binary format acceptable to FORTRAN IV. It uses an assembly language subroutine RDATA to read the data blocks produced by MR $\phi\phi$ 7. Figure 2 describes the actions of PUNCH.

After each logical record is written, a !EOD is written. After the last logical record, two !EODs are written (an EOF).

B. Subroutine GETREC

GETREC is a FORTRAN subroutine which reads records produced by PUNCH into a data array. It tests sense switch 1 to determine the source device. The calling sequence is

```
CALL GETREC (IDAT(1), IDATL,999S)
```

when

IDAT(1) is the first element of the storage area. IDATL is the number of words to be read into the data storage area (currently 545). 999S is the address to which the routine will return when an end of all data (a double !EOD on the card reader, or an EOF on the DISK) is encountered.

If sense switch 1 is reset,

Data will be read from the Card Reader through F:8.

If sense switch 1 is set,

Data will be read from the DISK (DPEXEC) through F:7.

Figure 3 is a diagrammatic overview of GETREC.

C. ACCTNG

ACCTNG is a FORTRAN program which produces a graphical summary of the execution data. The summary³ consists of the following sections:

- (I) Complete execution summary—All data are displayed.

- (1) Instruction usage summary (Fig. 4)

The bar graph for the execution of an instruction shown in Fig. 4 is relative to the most used instruction. The bar graphs for indirect addressing (*), indexing (X), and indexed indirect addressing (*X) are relative to 100%. Unused instructions and addressing modes are not shown.

- (2) Register usage summary

REGISTER USAGE refers to use of a register as an operand. INDEX REGISTER USAGE refers to use of a register for indexing. Bar graphs in each section are relative to the most used register in that section, as may be seen in Fig. 5.

- (3) Execution classes

This is a one-page summary (see Fig. 6) of instruction usage. It is self-explanatory. Instructions are listed by their standard mnemonics.

- (II) Condensed summary—Selected data are displayed

- (1) Instruction usage summary

The condensed instruction usage summary is almost identical to the instruction usage summary. However, only instructions used more than 0.9% are listed, and the bar graphs for indirect, indexed, and indexed indirect addressing are relative to the individual instruction usage (see Fig. 7).

- (2) Instruction overview

The instruction overview is a bar graph on a logarithmic scale of instruction usage. Instruc-

³The example used in this section is the execution of an optimized assembly language, FFT, written by Dr. Howard Rumsey. The FFT was executed twice in succession on a 256-point complex-element array.

tion mnemonics are on the bottom of the graph, and the corresponding usage is above. If an instruction was used at all, though not enough to appear on the graph, it has a “#” on the 1% grid. The total number of instructions is displayed on the 100% grid (see Fig. 8).

An instruction overview may be very revealing. Figure 8 shows an overview for an optimized assembly language FFT. Figure 9 shows an overview for an optimized FORTRAN IV FFT. Both were used to do a double transform on a 256-point complex-data array, and both were written by a highly skilled programmer. The FORTRAN program required almost twice as many instructions to do the transform as the assembly program. However, the absolute usage of floating point instructions is about the same (9–15% for assembly, 2 X 5–7% for FORTRAN).

ACCTNG will suppress all but the instruction overview if sense switch 2 is set. ACCTNG gets data through the subroutine GETREC (described in Section VB). Additionally, ACCTNG requires an index file to give it the op codes and mnemonics of the instructions, and control information for grouping the instructions together into logical blocks. The format of records in this file is as follows:

- (1) Op code, 4-letter mnemonic (blanks are significant)
- (2) Op code | sub code, 4-letter mnemonic
- (3) O, blanks

ABORT AND WARNING FORMAT:

HHHHHHHH

R ϕ ,RBLK ϕ

```

RRRRRRRR RRRRRRRR RRRRRRRR RRRRRRRR
RRRRRRRR RRRRRRRR RRRRRRRR RRRRRRRR
RRRRRRRR RRRRRRRR RRRRRRRR RRRRRRRR
RRRRRRRR RRRRRRRR RRRRRRRR RRRRRRRR

```

R ϕ ,RBLK1

```

RRRRRRRR RRRRRRRR RRRRRRRR RRRRRRRR
RRRRRRRR RRRRRRRR RRRRRRRR RRRRRRRR
RRRRRRRR RRRRRRRR RRRRRRRR RRRRRRRR
RRRRRRRR RRRRRRRR RRRRRRRR RRRRRRRR
LLLLLLLL I I I I I I I EEEEEEEE CC $\phi\phi\phi\phi\phi\phi$ 

```

In this format,

Item (1) is the standard op code-mnemonic pair for an instruction. For example, the STORE REGISTER instruction, op code X'35', would be represented as “35,STW.”

Item (2) is for instructions which are actually a subclass of another instruction. In this case, the two-digit location of the data for the subcode is concatenated onto the two-digit op code. For example, the unconditional branch instruction (BCR,O) has data describing it stored in op code 01, and is represented as “6801,B.”

Item (3) establishes the end of a logical instruction group.

A diagrammatic summary of ACCTNG is shown in Fig. 10.

VI. Error Messages and Other Miscellany

The following is a brief description of error messages and a possible explanation as to why they may occur, followed by a discussion on some conditions which have not been implemented and may cause program failure.

MR $\phi\phi$ 7 intercepts illegal and unimplemented instructions and gives a warning accordingly. MR $\phi\phi$ 7 also aborts on CALs that are the object of an EXU instruction, and flags EXU instructions which are nested. These events are accompanied by an error dump of the format shown below.

when

RBLK ϕ — Register block zero \rightarrow the program register block.
RBLK1 — Register block one \rightarrow MR $\phi\phi$ 7 register block (or pseudo-register block).
RRRRRRRR — Hexadecimal contents of the register.
LLLLLLLL — Location of offending instruction.
IIIIIII — Offending instruction.
EEEEEEEE — SR3 from the last CAL 1 which aborted or errored.
CC $\phi\phi\phi\phi\phi\phi$ — BYTE ϕ contains the current condition code and floating control.

ERROR HEADERS (“HHHHHHHH” from above)

“ABRT CAL” — A CAL without an ERR/ABN exit has returned through the ERR/ABN exit with an abort level error code. — Abort.
“BAD CAL” — An illegal CAL or a CAL with an illegal FPT code has been encountered. — Abort.
“PRIV INS” — An attempt has been made to execute a privileged instruction. — Abort.
“DATA INS” — An illegal/unimplemented instruction has been encountered. This includes CAL2 and CAL4 in BTM and CAL2, CAL3, CAL4 in BPM. — Abort.
“EXU CAL” — An attempt to execute a CAL has been made. — Abort.
“EXU EXU” — More than one level of EXU instruction. — Warning.

Miscellaneous Information

FPTs which are longer than 40 words will be truncated to 40 words. If there are any FPTs in the user program longer than 40 words, they should be reduced to 40 words or less.

SNAP CALs inserted by the monitor have their FPTs in 01 protection type. Since MR $\phi\phi$ 7 currently modifies the FPT, the monitor will abort on a memory protection violation when the SNAP is encountered. Therefore, !SNAP cards cannot be used in a region of the program to be executed by MR $\phi\phi$ 7. (M:SNAP FPTs are in 00 protection-type memory, and may be used.)

Since MR $\phi\phi$ 7 uses the M:EO DCB for saving data, this DCB must not be used by the program. Further, to insure

that the file (DEXEC) written through the M:EO DCB is not destroyed, the user must

- (1) exit to the monitor (through an M:EXIT, M:XXX, or M:ERR) while under the control of MR $\phi\phi$ 7

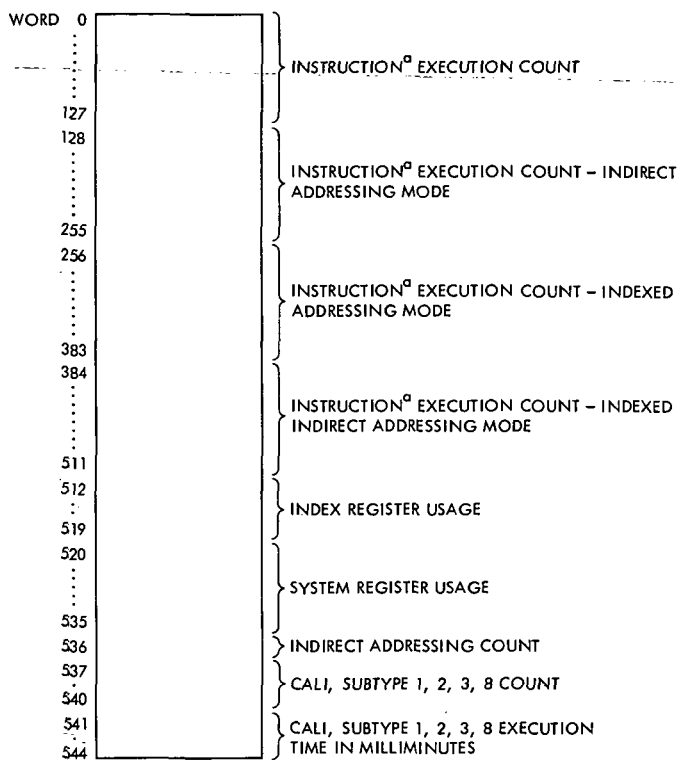
or

- (2) exit to the monitor via
CALL WDATCLSE

or

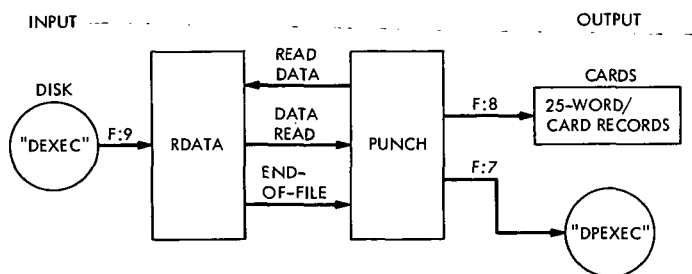
REF WDATCLSE
B WDATCLSE

This closes the M:EO DCB with SAVE. All unclosed user output files are lost.



^aAN ADDITIONAL INSTRUCTION SUBCLASS (BCR, O) HAS BEEN ASSIGNED OP CODE X'01'.

Fig. 1. Data record format for DEXEC



F:7, F:8, F:9 MUST ALL BE ASSIGNED AT LOAD AND EXECUTION TIME.

Fig. 2. Overview of PUNCH

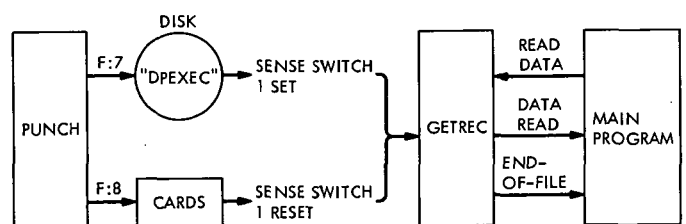


Fig. 3. Operational diagram of GETREC


```

49=BR      .004%,      21
48=EBR      .610%,     3881**
4B=AND      .007%,      41
#####

25=S       .827%,     5261***
24=SF       .406%,     2581*
#####

3D=FAS     10.556%,    67171*****
1D=FAL      .398%,     2531*
3C=FSS      9.952%,    63331*****
3F=FMS     17.489%,   111291*****
      *      4.58%,     5101***
1F=FML      .398%,     2531*
3E=FDS      .004%,      21
#####

69=BCS      5.854%,    37251*****
68=BCR      3.536%,    22501*****
      *      .71%,      161
      X     23.29%,    5241*****
      *X     .09%,      21

01 B        .846%,     5381***
      *      2.97%,     161**
      X     97.21%,    5231*****
      *X     .37%,      21

64=BDR      .002%,      11
6A=BAL      .848%,     5391***
#####

04=CAL1     .005%,      31
#####

CAL1,1:     .008MIN,    2'S *****
CAL1,2:     .000MIN,    0'S
CAL1,3:     .000MIN,    0'S
CAL1,8:     .000MIN,    0'S

```

Fig. 4. (contd)

REGISTER USAGE:

```

0 = .000%,      0!
!

1 = 1.877%,     1077!*****
!*****

2 = 8.987%,     5158!*****
!*****

3 = 1.795%,     1030!*****
!*****

4 = 7.999%,     4591!*****
!*****

5 = .004%,      2!
!

6 = .915%,      525!**
!**

7 = 1.784%,     1024!*****
!*****

8 = 25.990%,    14918!*****
!*****

9 = 9.556%,     5485!*****
!*****

A = 17.844%,    10242!*****
!*****

B = 7.152%,     4105!*****
!*****

C = 10.704%,    6144!*****
!*****

D = 3.581%,     2055!*****
!*****

E = .901%,      517!**
!**

F = .919%,      527!**
!**

```

INDEX REGISTER USAGE:

```

1 = 4.646%,     532!*****
!*****

2 = 35.816%,    4102!*****
!*****

3 = 35.851%,    4106!*****
!*****

4 = 1.197%,     137!**
!**

5 = .018%,      2!
!

6 = 4.593%,     526!*****
!*****

7 = 17.882%,    2048!*****
!*****

```

Fig. 5. Register usage summary format from ACCTNG

TOTAL INDIRECTS * 10796

TOTAL INSTRUCTIONS EXECUTED * 63636

RELATIVE USAGE OF INDIRECT ADDRESSING = 16.965 %

UNUSED INSTRUCTION SUMMARY:

LH	LCH	LAW	LCW	LCD	LAD	LS	LM
LCF1	LCF	XW	STH	STS	STM	STCF	ANL2
INT	AH	SH	SD	MI	MH	DH	AWM
MTW	MTW	CB	CU	CD	CS	CLR	FSL
FDI	PSW	PLW	PRM	PLM	MSP	EXU	BIR
CAL2	CAL3	CAL4					

INSTRUCTIONS USED LESS THAN 2.00%:

LI	LB	LAW	STB	SW	MW	DW	MTB
CI	CLM	BR	EAR	AND	S	SF	FAL
FML	FDS	R	BCR	BAL	CAL1		

INSTRUCTIONS USED MORE THAN .90%:

LI	LW	LD	STW	STD	AI	AW	AD
CW	FAS	FSS	FMS	BCS	BCR		

Fig. 6. Instruction class summary from ACCTNG

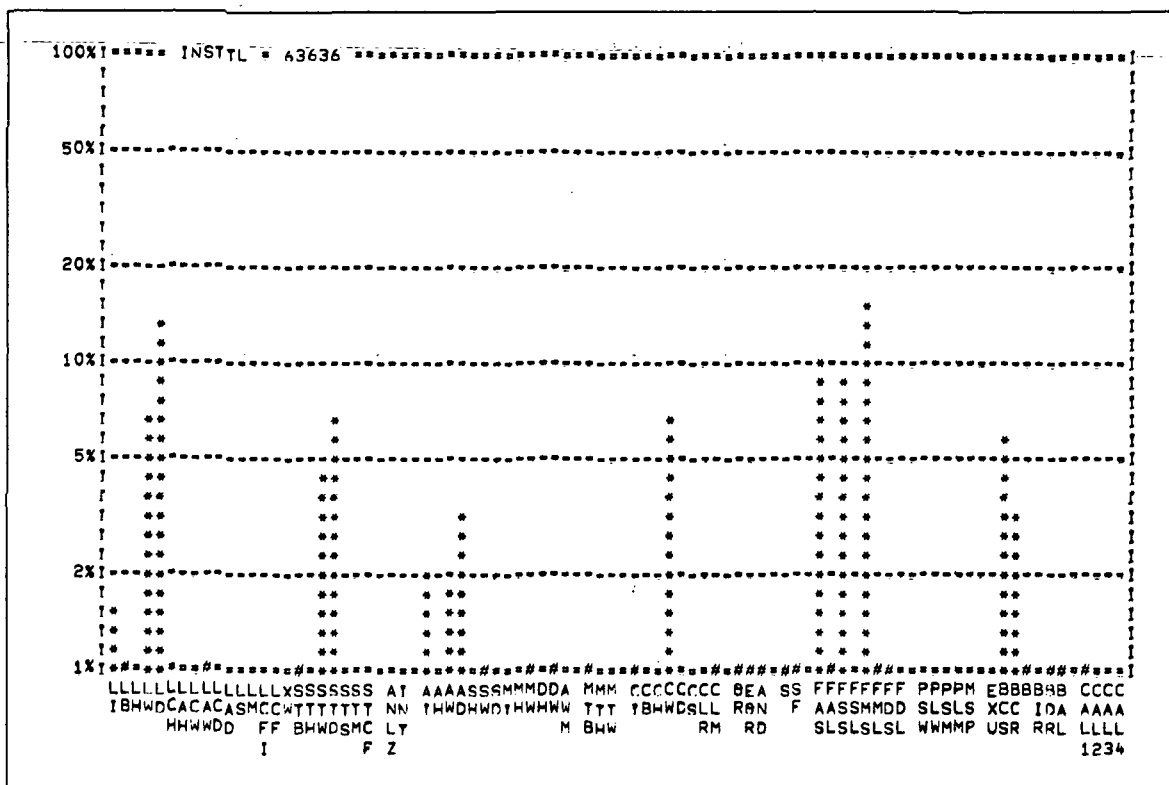


Fig. 8. Instruction overview of assembly-language FFT

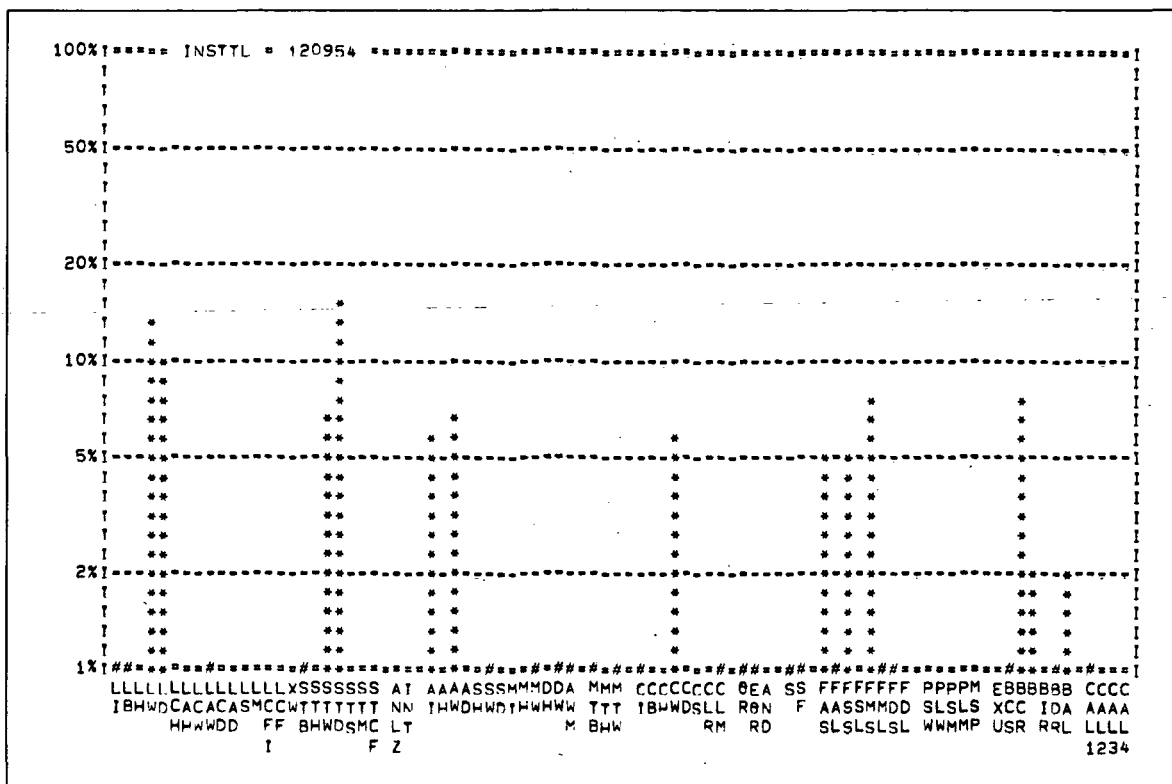
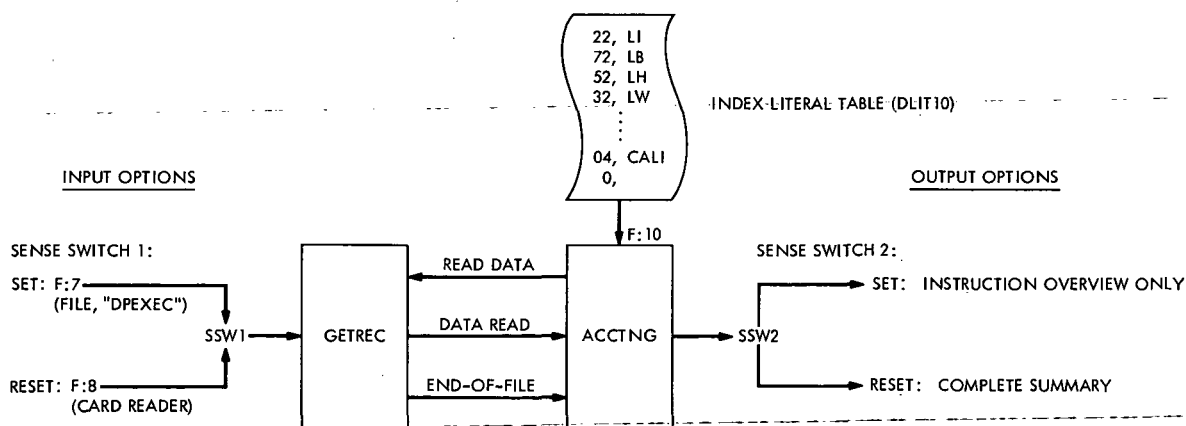


Fig. 9. Instruction overview of FORTRAN FFT



F:7, F:8, F:10 MUST BE ASSIGNED AT BOTH LOAD AND EXECUTION TIME.

Fig. 10. Diagrammatic summary of ACCTNG

Complex Mixer System

L. C. Constenla

Communications Systems Research Section

The complex mixer system is a signal preconditioner to a Fast Fourier Transform (FFT) power spectrum analyzer. It generates a complex time series output of the real-valued time series fed to its input. Two complex mixers have been constructed and installed at DSS 14. They have processed signals received from the Mariner 1971 spacecraft to investigate induced cross polarization of signals passing close to the solar corona.

I. Introduction

A new complex mixer system was installed in the pedestal control room at DSS 14. This system is an integral part of the R&D spectrum analyzer. The new system has an added 10-MHz input capability as well as a second channel. The two independent channels are able to accept either the 2.5- or the 10-MHz IF receiver outputs and have a maximum overall bandwidth of 100 kHz. This allows the spectrum analyzer to operate either with the experimental receiver/microwave link in the 2.5-MHz mode or the DSIF receiver in the 10-MHz mode.

The Mariner 1971 superior conjunction receiver experiment made use of the added capabilities of the system to simultaneously perform the S-band right- and left-circular polarization spectral measurements. Since the signal transmission path lay close to the sun, this experiment was designed to investigate the effect of solar corona turbulence on such signal characteristics as spectral broadening of the normal right-circular polarized signal component and inducement of a left-circular signal component.

II. System Description

Figure 1 shows a block diagram of the complex mixer system. In this figure, two separate channels are shown, each of them containing a relay box that selects either the experimental receiver/microwave link or one of the DSIF receivers (receivers 3 and 4). Following the relay box is a complex mixer module (CMM), which is the main topic of this report. The inputs of the CMM are the 5-MHz reference and the RF signal selected by the relay box. The outputs of the CMM are the real and imaginary components of the complex signal generated. These signals are sent through the variable filters which determine the overall bandwidth of the system. Following the filters are variable gain amplifiers needed to optimize the gain of the system.

III. Complex Mixer Module

A complex mixer module block diagram is presented in Fig. 2. This diagram shows that the RF input signal is applied to two separate channels. At the input of each channel there is a buffer amplifier needed to prevent

the modulation products generated by the mixers from contaminating the input source. These buffers also provide the 14 dB of attenuation necessary to operate the mixers linearly. The buffered RF input signal is then mixed with the locally generated $\sin \omega_0 t$ and $\cos \omega_0 t$ to shift the IF frequency ω_0 to baseband, and to produce at the same time the complex modulation products. These signals are then boosted by two 40-dB gain low-noise amplifiers whose $1/f$ noise figure is very low. Following the amplifiers there are active low-pass filters that allow the difference of the modulation products to go through, cutting off the sum products and all the harmonics. These active filters were designed to exhibit a two-pole Butterworth (maximally flat) response, with a cutoff frequency of 1 MHz. The outputs of the filters are then buffered by unity-gain power amplifiers able to drive 50- Ω coax cables terminated with 50- Ω loads. Capacitors are used to block the dc component.

The $\sin \omega_0 t$ and $\cos \omega_0 t$ are generated by a 2-flip-flop Gray code counter (sin/cos generator), driven by a 40/10-MHz clock. The outputs of this generator are the two buffered squarewave signals at 90-deg phase difference, with a frequency of one-fourth the input clock frequency.

IV. Phase-Locked Loop

The 40/10-MHz clock frequency input to the counter is generated by a phase-locked loop (PLL), whose block diagram is depicted in Fig. 3. The PLL is used instead of a much more expensive frequency synthesizer to generate the 40 or 10 MHz locked to the station standard needed to run the sin/cos generator. Figure 3 shows that preceding the PLL there is a Schmitt trigger detecting the 5-MHz station standard used as a reference. The output of the Schmitt trigger is then compared with the output of the feedback counter in a digital phase detector. Once the loop is operating in the phase mode, the output of this detector produces an analog error voltage proportional to the error in phase between the detected input reference and the countdown output frequency. The error voltage is then filtered by an active-

type filter that determines the loop bandwidth. The filtered error voltage is applied to the voltage-controlled oscillator. The loop is closed by the divide-by-four and divide-by-two counters, which allow the output frequency to be compared with the input reference, as explained above. Figure 3 also shows the switch that selects the 40- or 10-MHz clock output.

V. System Performance

Table 1 summarizes the typical characteristics of the complex mixer module. The phase relationships between the real and the imaginary outputs were measured with a Hewlett-Packard (HP) computing counter. In each complex mixer, the channels are balanced in gain to within 5% and in phase to within 6 deg over the entire operating bandwidth of 0.02 Hz to 1 MHz.

VI. Package

The complex mixer module is packaged in a newly designed RF standard DSN module, illustrated in Fig. 4. This figure shows three printed circuit sections, the phase-locked loop, the sin/cos generator, and the complex mixer itself. All the microcircuits are on sockets for easy field maintenance. Figure 5 shows the complex mixer front panel. The front panel has a receiver switch that controls the mode of operation as well as the relay box receiver selection. Two light-emitting diode (LED) indicators display the receiver mode selected by the receiver switch. The inputs and outputs to the unit are accessed through four connectors mounted on the front panel. This system, consisting of two complex mixer modules and a relay box, is housed in a DSN standard cage.

VII. Conclusion

Two complex mixer modules and a relay box were constructed to implement the system shown in Fig. 1. The system was installed in the pedestal control room at DSS 14 and successfully used to perform spectral measurements on signals from the Mariner 1971 spacecraft.

Table 1. Complex mixer module specifications

Parameters	Values	Comments
Input impedance	50 Ω	
Bandwidth	0.02 Hz-1 MHz	When loaded with 10 M Ω
Phase tracking	< 6 deg	Phase difference between channels
Amplitude tracking	< 5%	
Maximum input power	4 dBm	
Gain	20 dB	

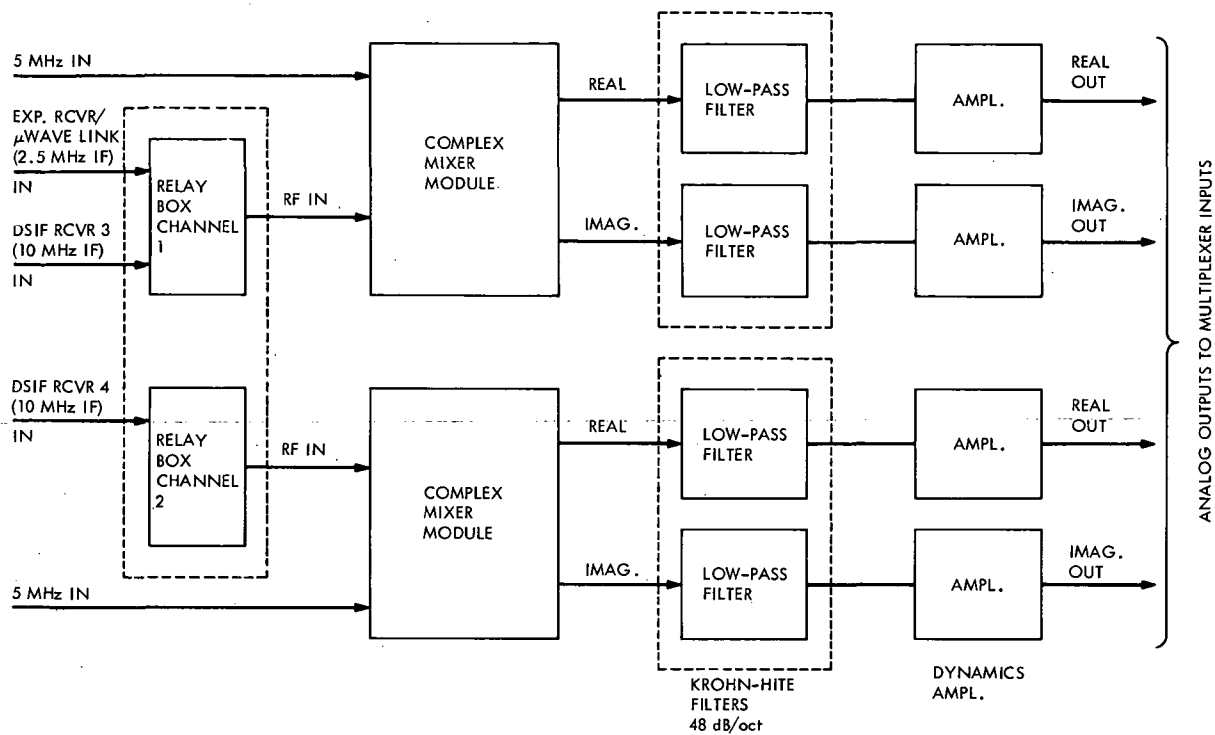


Fig. 1. Complex mixer system block diagram

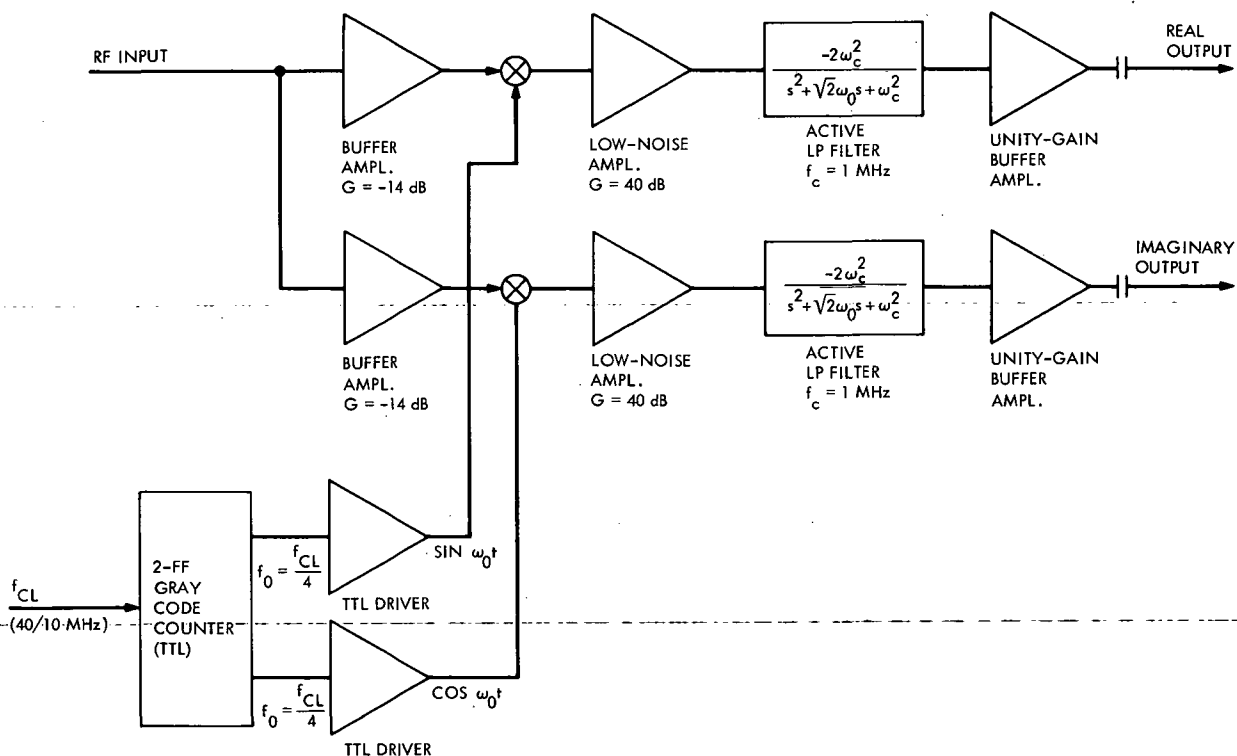


Fig. 2. Complex mixer module block diagram

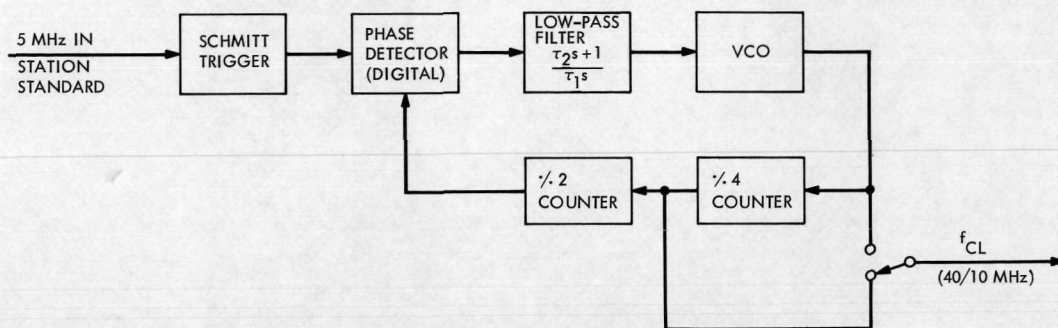


Fig. 3. Phase-locked-loop block diagram

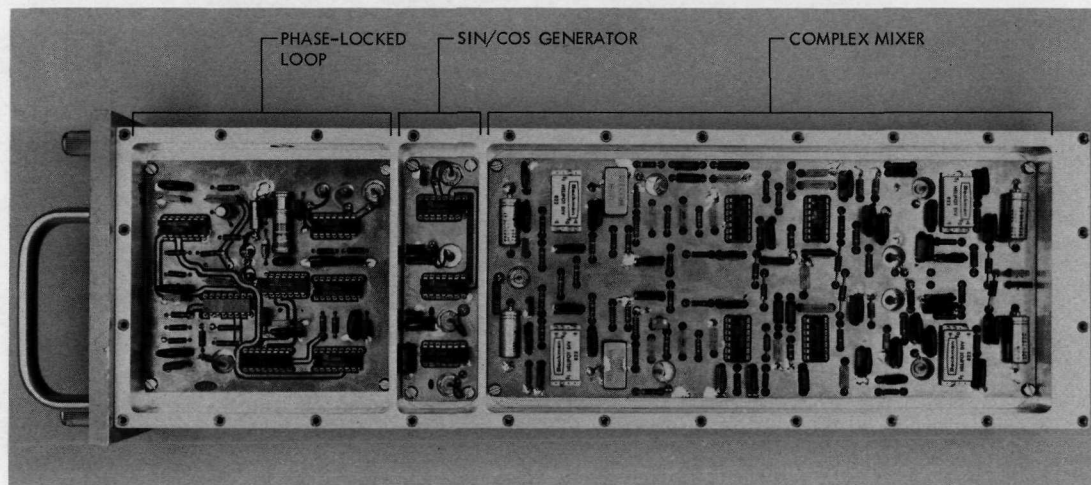


Fig. 4. Complex mixer RF standard DSN module



Fig. 5. Complex mixer front panel

A Multicomputer Communications System

J. W. Layland and W. Lushbaugh
Communications Systems Research Section

A general description is given of the requirements for, and one proposal for the provision of, the multicomputer communications facility needed in a multiple minicomputer system, such as in the anticipated future tracking station computer network of the Deep Space Network. The main features are: (1) a basically high-speed point-to-point link whose rate adapts without data loss to the capabilities of the computers with which it interfaces; and (2) a very high bandwidth transmission control unit (TCU) which provides a functional path from each computer to every other computer, while requiring only one physical link between each computer and the TCU.

I. Introduction

One of the most likely configurations for the computational complement of the tracking stations of the future is that of a number of small computers, each one performing a dedicated function, interfaced with some specific subset of the tracking station equipment; each one would, in turn, be interfaced with the other computers. A similar multiple-computer mini-network is under consideration for the DSN Control System, with each of the included small computers performing a dedicated function. Variants on this configuration have been used successfully at other facilities in a variety of process control and data acquisition systems.

In multicomputer systems such as these, the facility provided for communication between the distinct computers and the usage made of such a facility play a crucial part in their success or failure. If the communications interface between the computers is awkward or if it is too heavily used, the computers may spend significant portions of their capacity in meaninglessly manipulating intercomputer messages, much as a too-large

committee of people can spend more of its efforts in discussing who does what than in progressing toward its goal.

Intercomputer communications are expected to serve two purposes in the multicomputer systems of the DSN. The first is the transient operation of loading programs at the start of operation, or change of mode, plus the loading of diagnostic programs when failures are detected. The maximum conceivable data rate required between computers in this mode is the average data rate from the tapes or disks on which the software semipermanently resides. With current technology, this rate is on the order of 10^5 8-bit bytes/s.

The minimum acceptable data rate for this mode is the rate which will allow the system computers to be reloaded in a time-span which meets the up-time/recovery requirements on the system. For example, a system with 30 small computers with 32K of 16-bit words each could be fully loaded in slightly less than 1 min from a single data source at 5×10^4 bytes/s.

The second and primary purpose of the intercomputer communications is the relaying of the information needed by the system in the performance of its assigned real-time tasks. The sizing of this capability in the general sense is very difficult, because it depends strongly upon how the functions to be performed are partitioned between the various computers. Nevertheless, an intercomputer data rate which is significantly in excess of the feed-through data rate of the total system probably indicates that the functions were partitioned wrong. For the immediate future, the feed-through data rate will be less than 5×10^4 bits/s, the rate of the wide-band data lines (WBDLs). Consequently, a reasonable objective for the intercomputer communications capability is 5×10^4 bytes/s. This objective is readily achievable over the short distances expected within a multicomputer system.

II. The Individual Communications Link

The individual links of the system are used to connect the computers of the mini-network to a centralized switching system, or, alternatively, can be used to connect computer pairs together. This section will describe the characteristics of an individual link, with discussion of multicomputer connections deferred until later.

A typical individual link is diagrammed as Fig. 1. The link functions in a half-duplex mode; that is, it can transmit data in either direction, but only one way at a time. Signals on the two coaxial cables are balanced and transformer-isolated to minimize effects of ground level imbalances between the two computers. The two cables each carry signals in one direction only: one going from computer A to computer B, and the other in the reverse direction. The two line interface units (LIUs) in the figure are identical and contain the logic and analog circuitry needed to format the computer's data byte-by-byte for the lines, perform parity checking, etc. The computer interface units (CIUs) are similar in function but specialized in design to the type of computer to which they are attached.

Each of the four modules occupies between 45 and 60 dual in-line (DIP)-packaged integrated circuit elements. Two CIUs have been designed to date: one for the SDS-910 and one for the PDP-11. Both are interfaced in a Central Processing Unit (CPU) controlled word-by-word transfer mode. Interface to the computers via a direct memory access (DMA) channel could be done at the expense of additional circuitry and the associated design and test effort. This would decrease the load imposed upon the CPU by the communications link.

The three signals which are sent on the lines in the active state are shown in Fig. 2. When the line is inactive, there is no signal. The transmission of the carrier signal is under control of the computer to which the LIU is interfaced. From an inactive state, the switching on of the carrier by computer A is a 1-bit message to computer B that some communication is needed, and the switching on of computer B's carrier acknowledges that message. Symmetrically, the switching off of the carrier is an emphatic "I quit!" that could be used to reinitialize from quasi-catastrophic link operation. These signals used are essentially identical to those of the IBM 2790 loop system (Ref. 1), although the line protocol differs. They admit very straightforward self-synchronization and detection so that no parallel clock lines are needed.

Transmission over a link is, in fact, bit-serial, but it is conceptually on a byte-by-byte basis. The LIU transmits data in a 1-byte packet, together with a parity bit which is checked and stripped by the receiving LIU. Whenever it is able to store another byte in its CIU buffer, the receiving LIU will signal a request for the next byte with a 2-bit control packet. Computer-word buffering is provided in the CIU, and since the LIU transmits by bytes, it is implicitly assumed that the computer word-size is a multiple of 8 bits (one byte). This is valid for the SDS 900-series and Xerox Sigma-series machines, for IBM 360, and for most of the popular 16-bit minicomputers.

The "transmit-byte/receive-control packet" operation sequence provides synchronization between the communication controlling software in both computers that accommodates the link data rate to the capabilities of the computers. Unlike a link built around a self-clocked synchronous modem, no data can be lost, or erroneously inserted, if the computers do not respond within a preset time interval.

This flexibility is obtained at the expense of data rate. The basic signalling frequency of 10^6 bits/s is reduced to about 3×10^5 bits/s between LIUs over 300 m (10^3 ft) of cable. The rate is still lower when delays in transferring words in and out of the computers is added. What is gained, however, is the ability to set the priority of the intercomputer communication link to that priority which is warranted by the function it performs for the particular subsystem. Since the maintenance of the intercomputer communications link is not the prime job of the subsystem computer, but the link is one of the resources utilized by that computer in performing its prime job, this flexibility is highly desirable.

For example, in a programmed local oscillator (PLO) subsystem, the closed-loop control of the synthesizer and the voltage-controlled oscillator (VCO) can be performed on a high-priority guaranteed service basis, without interference from the intercomputer link which is periodically supplying the PLO subsystem with updated predict information. If the link had a fixed data rate, it might well have to be operated at a higher priority than the PLO equipment in order to prevent rate errors from occurring during the time intervals when the link is active. The impact of this fixed rate constraint on the PLO software could range from annoying to catastrophic, depending upon how difficult the basic PLO system is to implement without the constraint.

III. Mini-networks of Computers

A myriad of options appears when one considers the interconnection of a number of computers instead of a single pair as discussed above. One obvious answer is to provide a physical link between each pair of computers which has need to communicate. This configuration would entail $N(N-1)/2$ links for N computers. It is highly expensive in hardware, but provides the maximum flexibility. Messages directed from one computer to another are directed by addressing the physical link interface hardware attached to the source computer.

We may remove some of the links, connect each computer to only a small number of its neighbors, and yet require that functional data paths exist between computers which are not physically directly connected, provided that message-routing information is contained within the message format itself. The Advanced Research Projects Agency (ARPA) Network (Ref. 2) is of this type. If this elimination of links is carried to its maximum, the result is a star configuration with a message-switching/relaying computer at the center, with each of the subsystem computers linked to it by the points of the star. A network used at IBM manufacturing for process control/data acquisition is of this type (Ref. 3). This star configuration has the disadvantage, relative to the others mentioned, that only one message can be en route at any one time. It also happens to be a functional analog of a single-channel loop communications system where messages enter the loop on a demand basis. The important difference between the star and the analogous loop is that control is concentrated in the center of the star while it would be distributed among the (enlarged) LIUs of a loop system.

If the star network were to be implemented as described, the message switching task could almost certainly be performed by a minicomputer which could comfortably handle two to five messages simultaneously, if it had no other tasks to perform. If the number of subsystem computers were large, then the data rate through this central minicomputer would be the constraining feature of the mini-network.

The operations required at star center, however, are simple and repetitious, and, except possibly for the initial set-up of a message channel based on the message addressing information, could be easily designed indeed into a hardwired transmission control unit (TCU). If built with current transistor-transistor logic (TTL) integrated circuits, the envisioned TCU would have an effective bandwidth of well over 10^7 bits/s which would be shared on a demand basis among as many messages as could be established. At this time, the TCU has been only functionally designed, with detailed design postponed until after the LIUs have been thoroughly tested and several CIUs have been designed, built, and tested.

IV. Message Format

Since the message format utilized by a computer network such as the one described here is embedded in its software, it can be a matter of considerable evolution as experience is gained with the system. At this point there seems to be no valid reason to deviate significantly from ASCII¹ standards in current use. The suggested format skeleton is shown in Fig. 3. The control codes are all ASCII characters, as are the addresses. The addressing is by computer ID, with various tasks within that computer being isolated by a channel identifier. Many more flexible techniques have been proposed (Refs. 4 and 5) but this is sufficient for the relatively predictable real-time jobs of the DSN.

One highly desirable departure from a pure ASCII standard is not shown in Fig. 3. This is the inclusion of the provision for 8-bit binary transmission for programs, unmodified Ground Communications Facility (GCF) data blocks, or in fact almost everything not destined for human reading. The binary data are signalled by an "SO" control code appearing in the message body. The escape-to-binary is followed by the record byte count (one record is of length 1-255) and then the binary data. The binary data are error-protected by the parity bit used by the LIUs.

¹American Standard Code for Information Interchange.

V. Summary and Open Problem

The foregoing has been a general description of the requirements for, and one proposal for the provision of, the multicomputer communications facility needed in a multiple minicomputer system, such as that for the anticipated future tracking station computer network. The main features are: (1) a basically high-speed point-to-point link whose rate adapts without data loss to the capabilities of the computers to which it interfaces; and (2) a very high bandwidth transmission control unit (TCU) which provides a functional path from each com-

puter to every other computer, while requiring only one physical link between each computer and the TCU.

The primary open problems with the proposed configuration center about the capabilities of the TCU; in particular, one must consider the probability of message blocking because the desired destination is already busy. There is a possibility of deadlock if blocked messages are not properly handled. The effects on mini-network behavior of changing the TCU bandwidth, of adding message-storing capability to the TCU, etc., must be assessed.

References

1. Hippert, R. O., "IBM 2790 Digital Transmission Loop," *IBM J. Res. Develop.*, Vol. 14, No. 6, pp. 662-667, Nov. 1970.
2. Roberts, L. G., and Wessler, B. D., "Computer Network Development to Achieve Resource Sharing," *AFIPS Conference Proceedings*, Vol. 36, 1970, pp. 543-549, 1970 Spring Joint Computer Conference.
3. Stuehler, J. E., "An Integrated Manufacturing Process Control System: Implementation in IBM Manufacturing," *IBM J. Res. Develop.*, Vol. 14, No. 6, pp. 605-614, Nov. 1970.
4. Carr, S., Crocker, S. D., and Cerf, V., "HOST-HOST Communication Protocol in the ARPA Network," *AFIPS Conference Proceedings*, Vol. 36, 1970, pp. 589-597, 1970 Spring Joint Computer Conference.

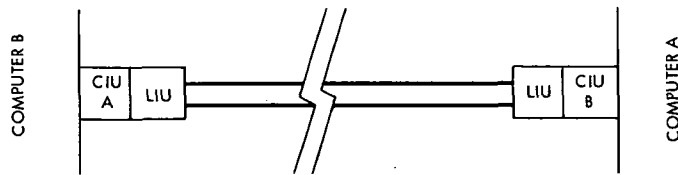


Fig. 1. Block diagram of single link

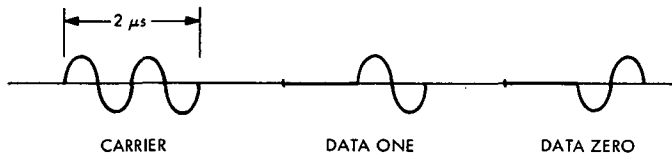


Fig. 2. Line signals

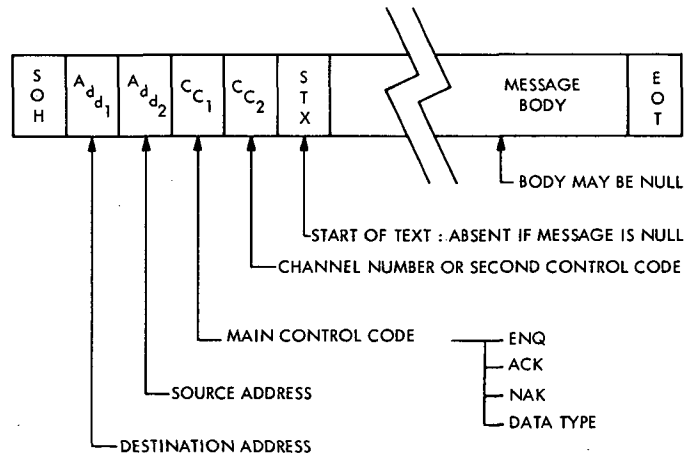


Fig. 3. Proposed message format

Dual Carrier

R. H. Smith

RF Systems Development Section

Two simultaneous (dual) uplink carriers from a single DSN 64-m-diameter antenna site are required to support the Viking 1975 project. A prototype dual-carrier exciter has been built and tested. The dual-carrier exciter amplifies and combines two standard DSN exciter signals, which are used to drive a high-power klystron operating in a linear mode (10% of normal power). The measured intermodulation products produced were at least 20 dB below the carrier's power.

I. Introduction

The Viking 1975 project requires two (dual) S-band signals to be transmitted to the orbiters and/or landers from a single DSN 64-m-diameter antenna site. The dual signals will be produced by combining two exciter signals and amplifying them with a high-power klystron. The power of each carrier in the dual mode will be limited to 10% of the maximum output of a single carrier (i.e., 400-kW transmitter limited to 40 kW per dual carrier) in order to operate the klystron amplifiers in a linear mode.

II. Test Configuration

Dual-carrier tests were conducted at DSS 14 using DSN Block IIIC exciter chains, a prototype dual exciter-combiner unit, the 400-kW transmitter, and the antenna (Fig. 1). The results were monitored at two points, one at the output of the 400-kW transmitter using the forward

ward coupler of the transmitter (A), and a second probe on the surface of the dish (B). A spectrum analyzer with a YIG preselector was used to analyze the dual output. Balanced and unbalanced carriers (40/40 kW, 40/20 kW, 40/10 kW, 10/40 kW, etc.) were investigated.

III. Test Results

The dual-carrier intermodulation products were down at least 20 dB below those of the lowest carrier. A typical output spectrum for two 40-kW carriers and the intermodulation products is shown in Fig. 2. Figures 3 and 4 show typical 40- and 20-kW, and 40- and 10-kW carriers, respectively, with their intermodulation products.

IV. Hardware

Figure 5 shows a detailed block diagram of the dual-carrier exciter. The 66-MHz filters are used to remove

any spurious signals from the $\times 3$ phase modulator. The multipliers ($\times 4$, $\times 8$) are standard DSN Block IIIC modules. The mechanical attenuator sets the drive level to the 10-W amplifier. The electronics switch is used for time multiplexing. (After the dual-carrier exciter was built, it was decided to use frequency multiplexing only.) The 10-W amplifier (Ref. 1) is used to raise the exciter power to 10 W. The single-pole double-throw (SPDT) coax switches are used in conjunction with the transfer switch to drive either the 400- or 20-kW transmitter with either of the exciters, or to drive the 400-kW transmitter with a dual carrier. The electronic attenuators balance the dual carriers, and the circulators provide added isolation between dual channels. The ring

hybrid combines the two exciter carriers to form the dual carriers. The couplers are used in conjunction with the power monitors to evaluate the subsystem performance.

V. Conclusion

The prototype dual-carrier exciter has demonstrated that two carriers can be combined and amplified by a high-power klystron. Output levels of 10% per carrier of the total output power of the klystron can be easily achieved. The intermodulation products are at least 20 dB below the carriers. Further evaluation and investigation are being carried out.

Reference

1. Smith, R. H., "10-W S-Band Amplifier," in *The Deep Space Network Progress Report*, Technical Report 32-1526, Vol. IX, pp. 196-200, Jet Propulsion Laboratory, Pasadena, Calif., June 15, 1972.

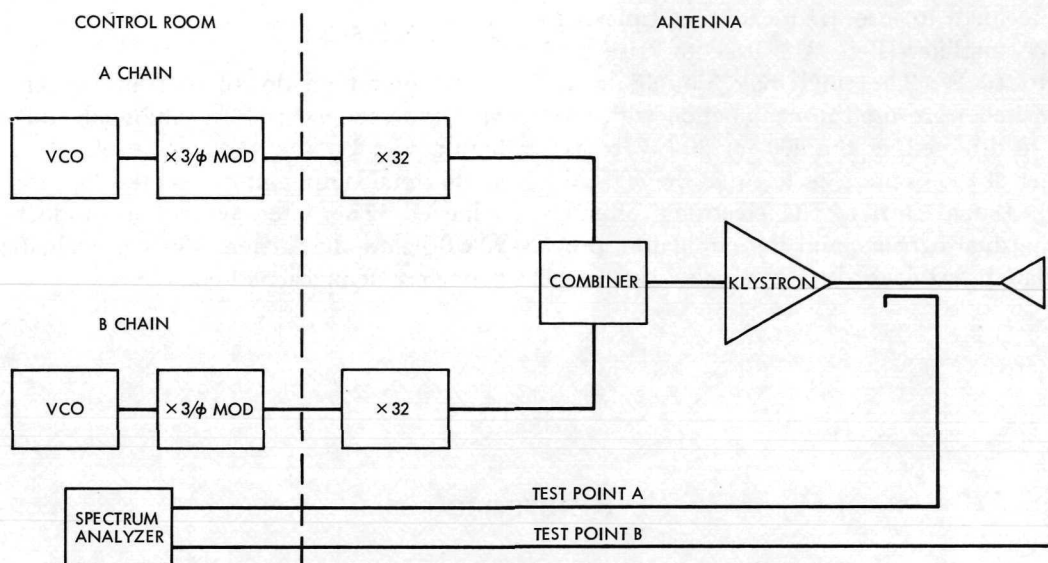


Fig. 1. Dual-carrier test at DSS 14

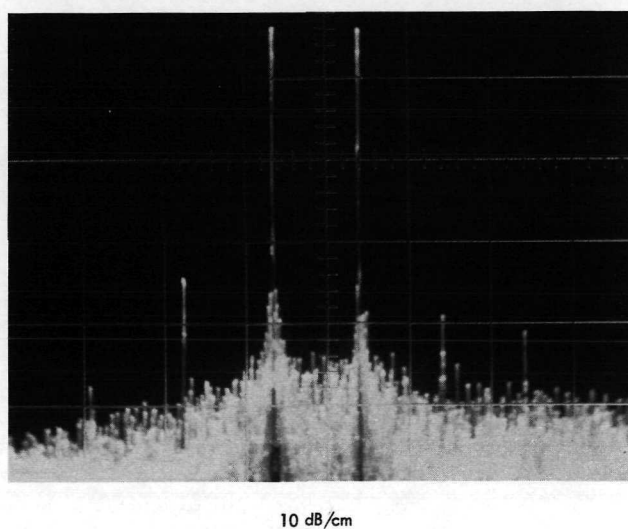


Fig. 2. Dual carrier, 40 kW each

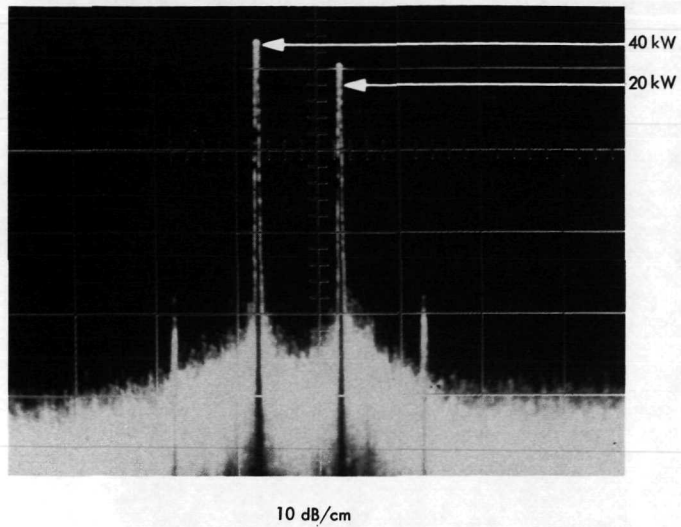


Fig. 3. Dual carrier, 40 and 20 kW

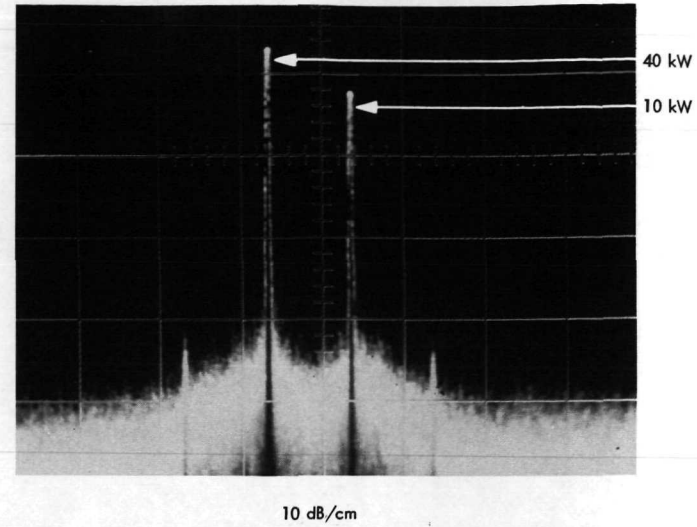


Fig. 4. Dual carrier, 40 and 10 kW

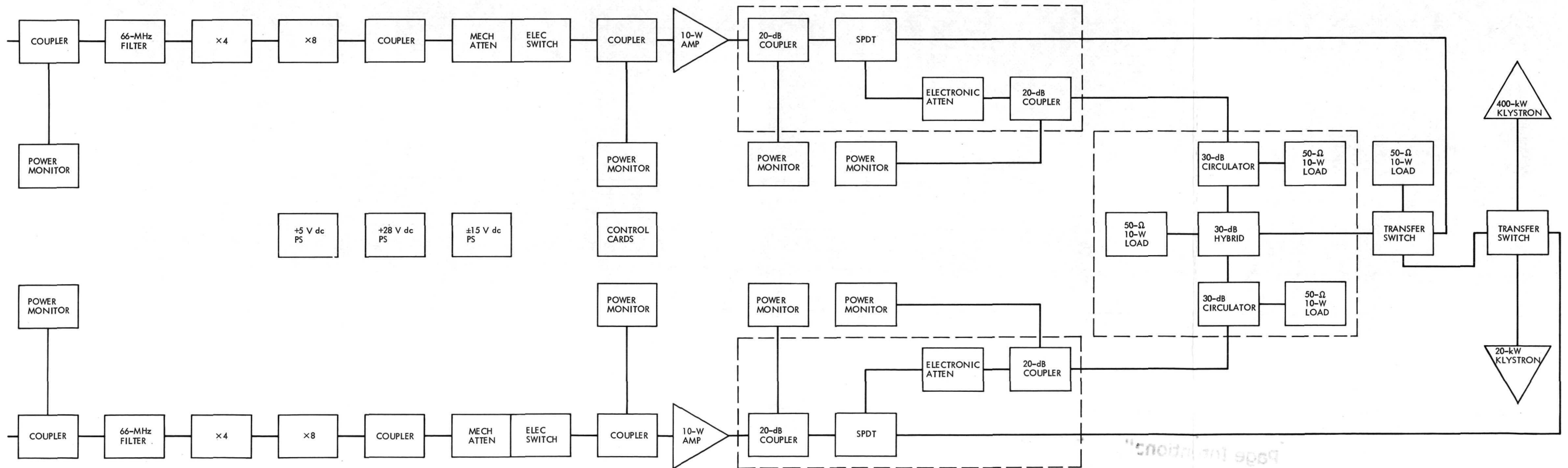


Fig. 5. DSS 14 prototype dual-carrier exciter

Page Intentionally Left Blank

A Dual-Ignitron Crowbar

E. J. Finnegan
RF Systems Development Section

A high-voltage protective device (crowbar) is described that is capable of operating at 100,000 V. This device has two ignitrons in series, with the appropriate electronics to trigger the tubes to a conducting state when desired. The crowbar is needed to increase the reliability of the transmitter, as the present tubes have difficulty operating at over 60,000 V. A new photon generator was designed and tested using light-emitting diodes and infrared-detecting pin diodes in conjunction with fiber optics for transmitting a pulse to the high-voltage deck and triggering the ignitron crowbar.

The 400-kW transmitter located at DSS 14, Goldstone, California, operates as part of the DSN, generating radio signals to control and gather data from spacecraft. The transmitter uses a klystron to generate these high-power signals. The klystron tubes operate at high voltages (70 kV) and are, therefore, subject to arcing. Arcing can easily destroy a tube, and it is mandatory to protect the tube with a crowbar. A crowbar is a protective device that senses catastrophic failure in the klystron and, in a few microseconds, short-circuits the destructive high currents until the high voltage is removed.

A prototype dual-ignitron crowbar was fabricated and tested (Ref. 1) using two small G.E. ignitron tubes. These tubes have a small capacity (10 kA) and need a holding anode power supply and interlocking circuits to disconnect the holding anode after it is energized. The prototype proved the feasibility of using two series ignitrons, and if higher voltages are needed in the future, this technique may be expanded by using the desired number

of tubes in series in order to meet the voltage requirements.

Phase II is now under way, consisting of a more rugged version of the prototype that uses two National NL1040 ignitrons. This tube is slightly larger than the prototype unit, will take higher currents (65 kA), and does not require the extra holding anode power supply. This circuit (Fig. 1) arrangement will hold off 100,000 V. The circuit works in the following manner: The klystron arc causes a surge in the high-voltage line which is sensed, and the protective circuitry develops a pulse through an infrared (IR) light-emitting diode. This IR light pulse is transmitted through fiber optics to the high-voltage deck. The fiber optics supply the necessary isolation (70 kV) from the high-voltage deck. On the high-voltage deck, the IR pulse is detected and converted to a voltage pulse to trigger the ignitrons to the conducting state. V1 then conducts, discharging C1 through R4 (Fig. 2) and ignit-

ing V2, causing both ignitrons to conduct. This short-circuits the power supply, thus protecting the klystron.

An improved method of detecting the IR pulse has been developed (Fig. 3). An IR pulse is generated on the ground level by the photon generator (an IR laser diode) and transmitted to the high-voltage deck (70 kV) through fiber optics. This light pulse then triggers a photo diode, which converts it to a voltage pulse, excites a Schmitt trigger, and gates the triggered spark gap to

place the ignitron in the conducting state. The elapsed time is less than 1 μ s.

This dual-ignitron system is the fastest tested to date by JPL and is in the configuration that will be used on the new high-powered transmitters at DSSs 63 and 43.

Table 1 shows the devices that have been tested, along with their delay times. Delay times are measured from the photon generator to the pulse at the ignitor.

Reference

1. Finnegan, E. J., "A New High-Voltage Crowbar," in *The Deep Space Network Progress Report*, Vol. III, pp. 146-148, Technical Report 32-1526, Jet Propulsion Laboratory, Pasadena, Calif., June 15, 1971.

Table 1. Dual-ignitron delay times

Photon generator	Elapsed time, μs	Detector
EG&G xenon lamp	3.5	EG&G photo diode
NE2H neon lamp	3.5	EG&G photo diode
AR9 argon lamp	2.0	EG&G photo diode
Laser diode or LED	1.0	United Detector Tech. (UJT600)
Laser diode or LED	7.0	United Detector Tech. (UJT500)
Laser diode or LED	<1.0	EG&G photo diode

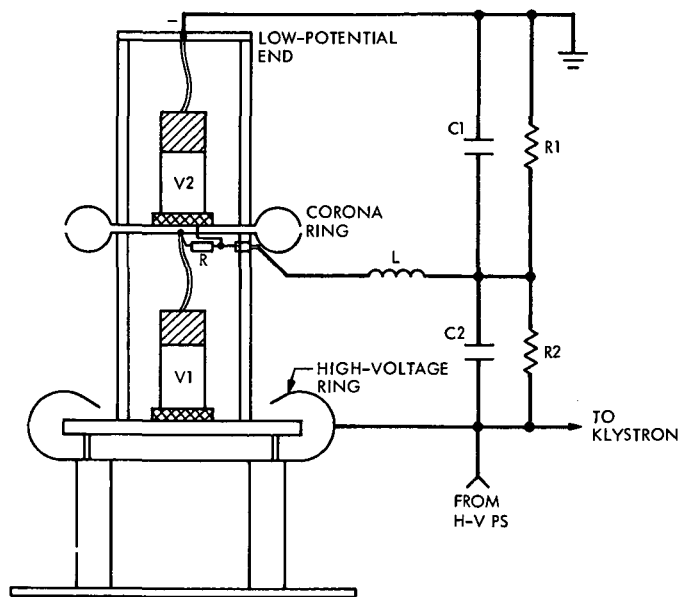


Fig. 1. Dual-ignitron crowbar

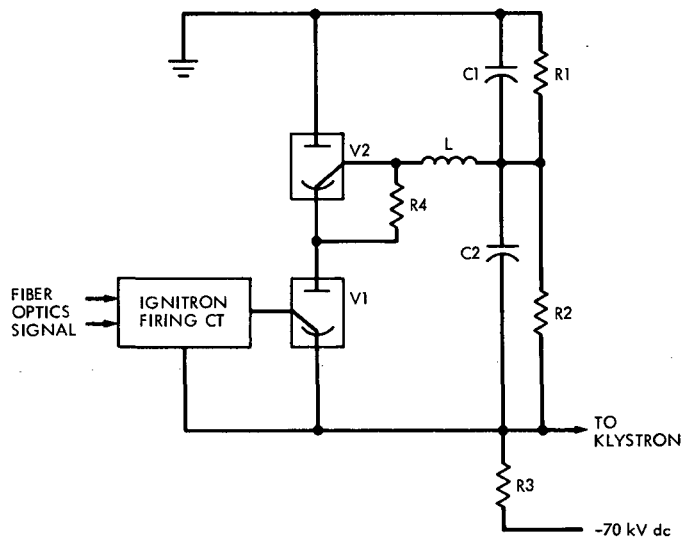


Fig. 2. Dual-ignitron schematic

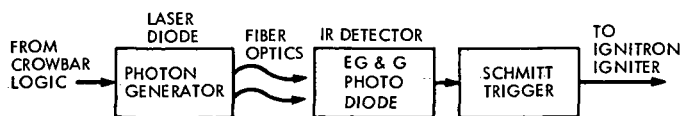


Fig. 3. Trigger and detector block diagram

Digital Frequency Shifter

R. N. MacClellan
RF Systems Development Section

Digital techniques applied to the development of frequency shifters yield a circuit that exhibits both wide bandwidth and exceptionally low phase noise while requiring no alignment.

I. Introduction

Phase-coherent frequency shifters are employed within the Block IV receiver/exciter to generate reference frequencies that are coherently related to the exciter oscillator frequency by factors of $912/221$ and $2636/221$ (Fig. 1). These reference frequencies are used both in the S- and X-band doppler extractors and coherent translators. Previously developed frequency shifters for the Block III receiver/exciter utilized parametric devices or locked oscillators to accomplish the frequency division process of the shifters (Refs. 1, 2). These methods of frequency division exhibit narrow bandwidth because of the use of tuned elements, high phase noise, and extensive alignment time because of their rigorous alignment procedure.

To eliminate the disadvantages of present frequency dividers and also provide the increased frequency range required for the Block IV receiver/exciter, high-speed synchronous digital counters are being used as the frequency division elements. This article describes the application of these counters.

II. Design

The frequency shifters utilize a family of emitter coupled logic elements (ECL) that exhibit sub-nanosecond

switching times and the ability to clock at frequencies in excess of 100 MHz. The fast switching characteristics keep the phase noise and phase drift vs. temperature ratio low.

Basic to the operation of the frequency shifters are two high-speed synchronous counters having modulus of 13 and 17. Figure 2, a block diagram of the $912/221$ frequency shifter, illustrates the relative location of these high-speed counters within the frequency shifter. The counters are used to generate signals with the prime frequency ratios of $13/221$ ($1/17$) and $17/221$ ($1/13$). These signals are then multiplied by 7 and differenced to provide an output signal related to the input by the frequency ratio of $28/221$.

Figure 3 is a functional diagram of the $28/221$ synthesizer section of the frequency shifter illustrating the logical implementation of the counters. The logical variables in the counter feedback loops were selected to provide output rectangular waveforms that are related to the 43-MHz input carrier by factors of $17/221$ and $13/221$ and yield large harmonic content in the output waveforms. The counter output waveforms are then presented to bandpass filters that select the power in the 7th harmonic and reject the power in all other spectral lines. This frequency selection effectively provides the $\times 7$ multiplication functions and generates frequencies

related to the input carrier by factors of 91/221 and 119/221. These frequencies are amplified and applied to the inputs of a balanced mixer, where a difference frequency of 28/221 relative to the input carrier is produced. The remainder of the synthesis is accomplished using a method of frequency addition and selection.

III. Performance

Phase noise and phase delay vs. temperature tests have been performed on components of the 28/221 synthesizer. Figure 4a shows a phase noise performance setup for modulo 13 and 17 counters. The counter/multiplier was compared against an identical reference assembly. The two assemblies were driven by the same signal to eliminate the noise of the source. The comparison is made in a balanced mixer configured as a phase detector. The measurement results are shown in Fig. 4b, an oscilloscope presentation of the phase detector

output. The broad baseline is setup noise, and the slight perturbations are phase noise, indicating a phase noise output of less than 0.004 deg P-P.

Phase delay vs. temperature effects were plotted using the measurement setup shown in Fig. 5. The reference channel was maintained at room ambient temperature. The assembly under test was cycled between 0 and 50°C in 5°C increments. The delay varied a total of 6 deg monotonically between the temperature extremes of 0 and 50°C for a phase shift of 0.12 deg/°C.

IV. Conclusions

Digital techniques have been successfully employed to produce RF frequency shifters that exhibit exceptional phase noise and phase delay vs. temperature characteristics, are broadband, and require no alignment except for a control to set the output power level.

References

1. Johns, C. E., "5/221 Parametric Frequency Divider," in *The Deep Space Network*, Space Programs Summary 37-22, Vol. III, pp. 7-9, Jet Propulsion Laboratory, Pasadena, Calif., July 31, 1963.
2. Johns, C. E., "57/221 Frequency Shifter—Block IIB," in *The Deep Space Network*, Space Programs Summary 37-42, Vol. III, pp. 83-86, Jet Propulsion Laboratory, Pasadena, Calif., Nov. 30, 1966.

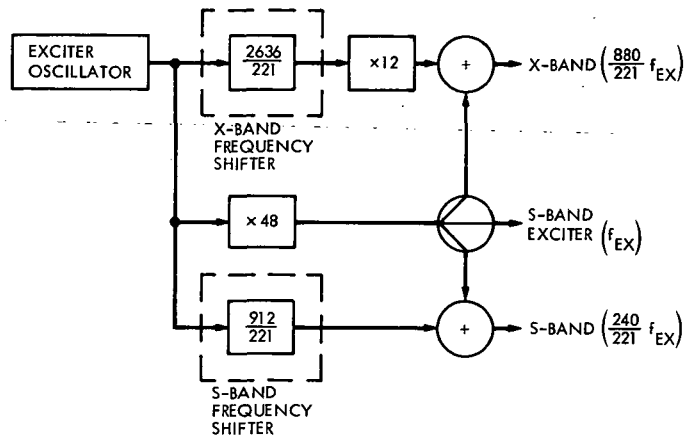


Fig. 1. Block IV frequency shifters

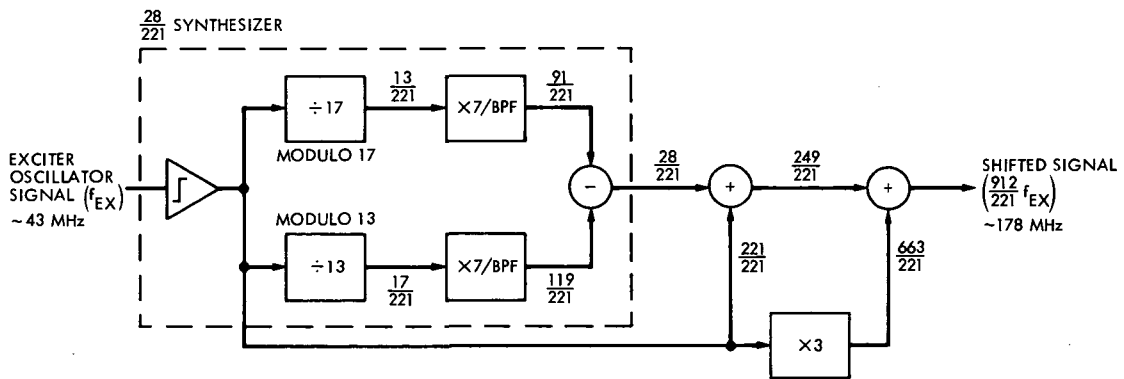


Fig. 2. 912/221 frequency shifter

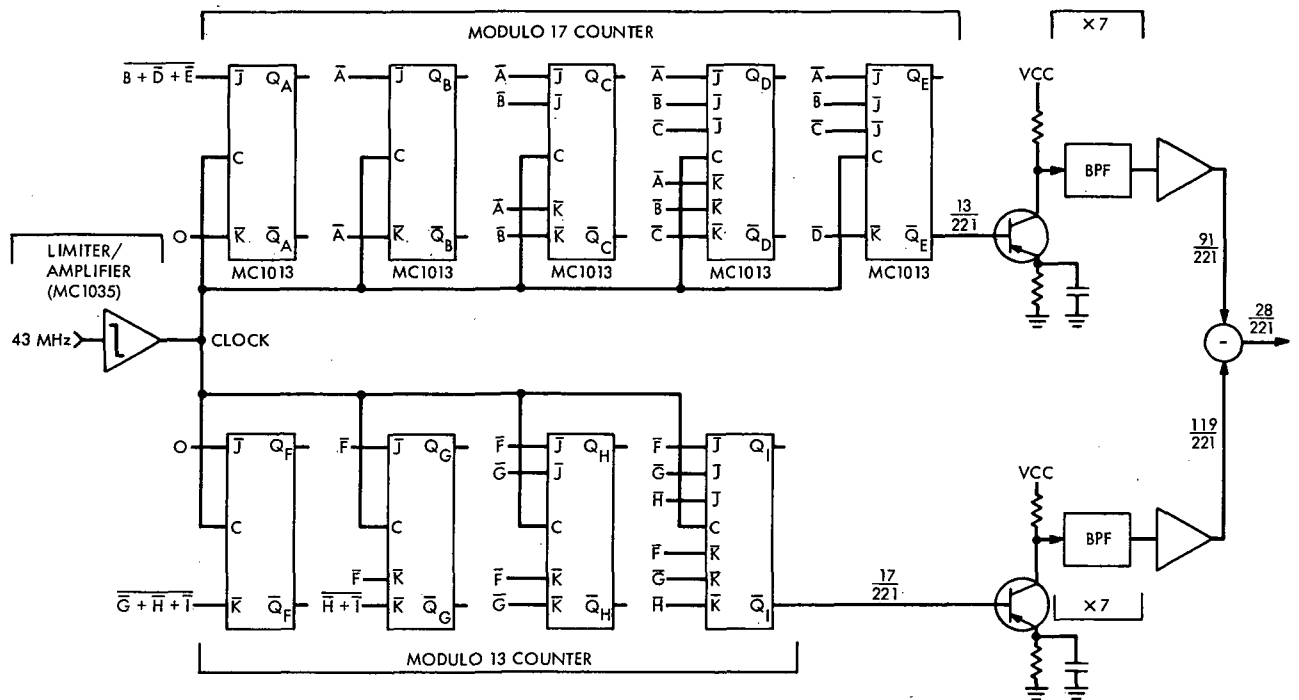


Fig. 3. 28/221 frequency synthesizer

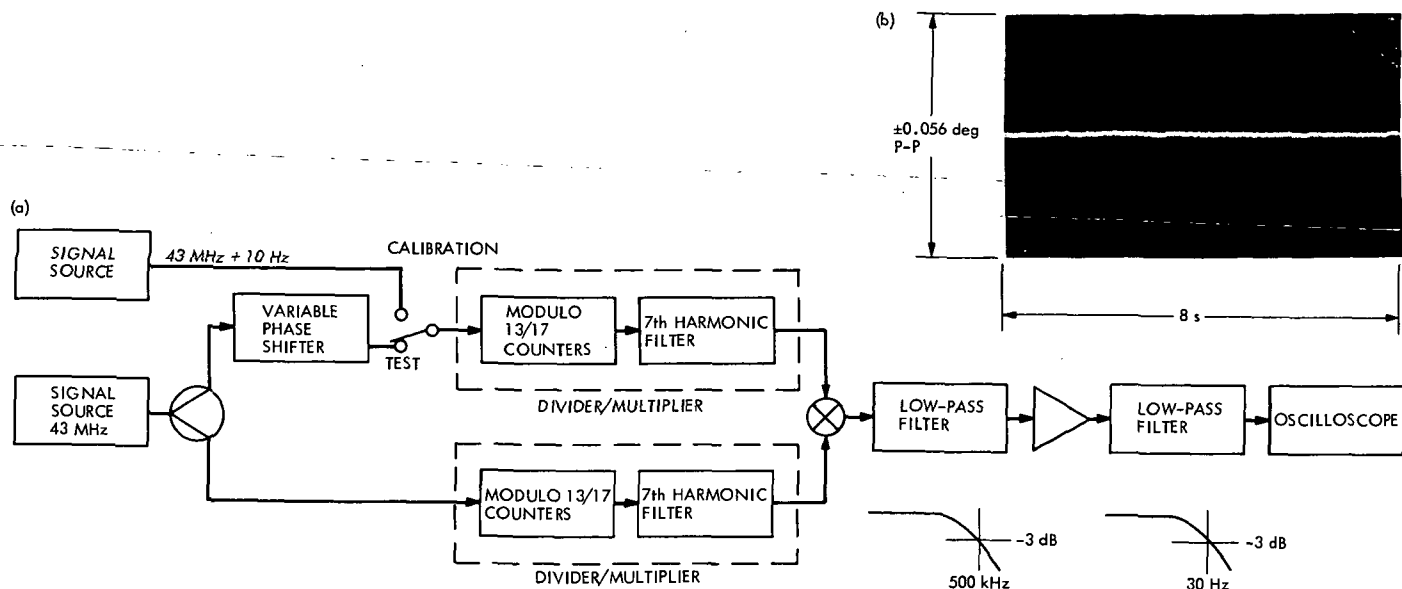


Fig. 4. Phase noise measurement

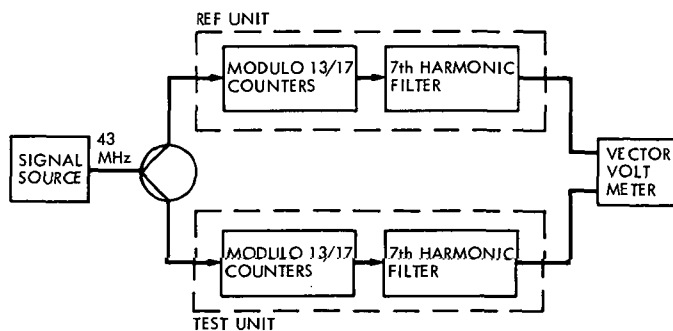


Fig. 5. Phase delay stability measurement

Hydrostatic Bearing Runner Leveling at Overseas 64-m-Diameter Antenna

H. P. Phillips
DSIF Engineering Section

The hydrostatic bearing runners on the National Aeronautics and Space Administration/Jet Propulsion Laboratory 64-m-diameter antennas must be set to flatness tolerances which represent a major field alignment problem. A method, based on the use of an electronic level, was successfully employed in setting the runners for the new 64-m-diameter antennas at Deep Space Station 43 (Australia) and Deep Space Station 63 (Spain).

I. Introduction

The alignment of the hydrostatic bearing runners on the 64-m-diameter antennas is very difficult because of the physical size of the runners and the strict flatness requirements placed on the runner by the antenna pointing and bearing operational requirements. This article describes the methods which were developed and used on the antennas at Deep Space Stations (DSS) 43 and 63.

II. Hydrostatic Bearing Runner

The hydrostatic bearing runner (Fig. 1) is a steel ring 23.4 m (920.25 in.) in diameter at the centerline, 112 cm (44 in.) wide, and 17.8 cm (7 in.) thick. It is made up of 11 segments, with connections between adjacent segments

made up tight before alignment is accomplished. Each segment has six leveling lugs each along the inside and outside edges, placed in radial pairs. The segments are supported on studs welded to steel embedded in the pedestal, which support the leveling lugs. Nuts on these studs permit local adjustment of the runner elevation.

The following requirements were established for the flatness of the hydrostatic bearing runner as installed:

- (1) The runner must be flat within 0.076 mm (0.003 in.) over any 1.52-m (60-in.) length. Each pad is 1.52 m long, and this requirement relates to the maintenance of the proper film height and pressure patterns under the pad. Compatible tolerances for the flatness of the runner as machined were established on the manufacturing drawings.

- (2) The mean plane of the runner must be within 20 arc seconds of being level with local gravity, and the entire runner must be within ± 0.25 mm (0.010 in.) of the mean plane. These requirements establish the verticality of the azimuth axis of the antenna and limit the wobbling of the antenna as it rotates in azimuth. A value of 20 arc seconds is equivalent to an elevation difference across a diameter of the runner, at the runner cross section centerline, of 2.3 mm (0.090 in.).
- (3) Any radial line on the top surface of the runner must be within 10 arc seconds of an arbitrary datum, which in turn must be within ± 48 arc seconds of local gravity. This requirement is to limit the twist in the runner seen by the pads as the antenna moves in azimuth. The 48-arc-second requirement permits an elevation difference of 2.5 mm (0.100 in.) between the inside and the outside edges of the runner, and the 10-arc-second tolerance represents an elevation difference of 0.050 mm (0.002 in.).

III. Leveling the Runner

The initial intent on the overseas antennas was to survey points on the top surface of the azimuth bull gear on a radial line with each pair of leveling lugs on the runner, using an N3 level mounted at the center of the antenna. The runner was then to be set with reference to these points using the pintle radial tooling assembly, measuring from the bull gear to the runner. In practice it was found that this was not a satisfactory arrangement because of errors inherent in surveying the bull gear surface at a range of 11 m (35 ft.) and because temperature changes in the aluminum members of the pintle radial tool necessitated frequent recalibration at a reference point to maintain satisfactory accuracy.

To avoid these problems, special alignment tools, based on the Talyvel electronic level, were constructed (Fig. 2). These consist of a T-shaped structure with a Talyvel level and a bubble cross level mounted near the center. Adjusting screws are located at each end of the leg of the T and of the cross bar. When the level was set on the runner, one arm of the cross bar hung away from the runner and the level was supported on the three remaining screws (Fig. 3). A small movable counterweight assured that the level was stable when so set and would not fall off the runner.

One level (Fig. 4) was made 1.17 m (46 in.) long, about midway between the chordal distance between the leveling lugs on the inside and between those on the outside.

The other was 0.55 m (21 $\frac{1}{4}$ in.) long, which related to the chordal distances between the lugs across the joints. The longer level had an additional adjusting screw, placed in the leg about 1 m (40 in.) from the cross arm. This permitted the use of the level to measure across the runner, from inside to outside. When the level was used in this way, 0.32-cm (0.125-in.) ground shims were placed under supporting screws to assure that the reading was not affected by the unintentional contact of one of the other screws.

The level was adjusted by setting it along the edge of the runner and adjusting the supporting screw at the end of the cross arm to set the cross level within about 30 arc seconds of level (Fig. 3). Tests had indicated that cross level errors up to about one arc minute did not affect the accuracy of the Talyvel level. By reversing the position of the level on the runner, the two screws on the cross arm could be set independently. The screw at the foot of the T was then adjusted so that the level gave the same reading, with opposite signs, when reversed (plunged) on the same two points. This adjustment, which assured that zero on the level represented a true level, was primarily used to assure that the Talyvel readout stayed on scale in subsequent readings. The Talyvel readout was in arc seconds directly, with one arc second being equivalent to an elevation difference of 0.0056 mm (0.00022 in.) on the long level and 0.0024 mm (0.0001 in.) on the short.

All runner adjustments were made at night, to avoid the thermal distortions of the runner due to heat from the sun. In using the levels, leveling points approximately 5 cm (2 in.) in from the edge at each lug were established, and all surveys were with respect to these points. The long level span was a little greater than the distance between these points on the inside, and a little less on the outside. Because of the flatness requirement held in machining the runner surfaces, the error in being slightly off the survey points was considered negligible. Data were recorded in terms of arc seconds for each level, with closures and correction being made in arc seconds. The transition to centimeters or inches was then necessary only in the last step after a survey was complete.

At DSS 43, the outside leveling points were set using the T levels, and the inside points were set using the cross level portion of the pintle radial tool, which was not affected by the problems previously described. In the use of the T levels, the elevation difference between adjacent leveling points was determined by taking readings with the level in a forward and reverse position, with the elevation

difference determined from the mean of the two readings. This procedure eliminated the need for frequent zero checks of the level and provided a quick check for gross inaccuracies, which were indicated if the absolute value of the forward and reverse readings had a large difference. After the runner was set it was surveyed by running a traverse completely around the outside of the runner and measuring inner elevations from the related outside point. Closure on the traverse was 0.11 mm (0.0044 in.).

The final survey data showed a total elevation range, inside and outside, of 0.24 mm (0.0095 in.). Elevation difference across the runner ranged from 0.06 to 0.15 mm (0.0025 to 0.006 in.), with the inside always low and a maximum out of flatness, determined by the runner twist from one pair of survey points to the next, of 0.075 mm (0.003 in.). Thus the runner, as leveled, and before grout placement or loading, met each of the requirements previously listed.

At DSS 63, the pintle radial tool was used only for preliminary leveling. In final leveling, adjustments were made

to the T levels directly. After the first stage of leveling was complete on a segment, a traverse was made around the segment and appropriate adjustment made. A final survey, consisting of two passes around each segment, was made, together with a similar traverse around the four lugs adjacent to each joint. Again the traverses, closing within 0.051 mm (0.002 in.), were corrected for closure and the two traverses averaged to determine the final elevation.

The T levels were built by JPL and used jointly by JPL and the contractor. The Talyvel levels were little affected by the frequent movement and maintained excellent repeatability. The original levels made on site in Australia (shown in Fig. 2), were somewhat heavy to use, and the counter weight tended to jar the Talyvel level if not moved with care. The improved levels made at JPL (shown in Figs. 4 and 5) were about half the weight of the original levels, and the counterweight was arranged to eliminate the jarring stop. With these instruments, a full traverse of the runner could be accomplished in about 3 hours. The overall adjustment of the runner took approximately one week.

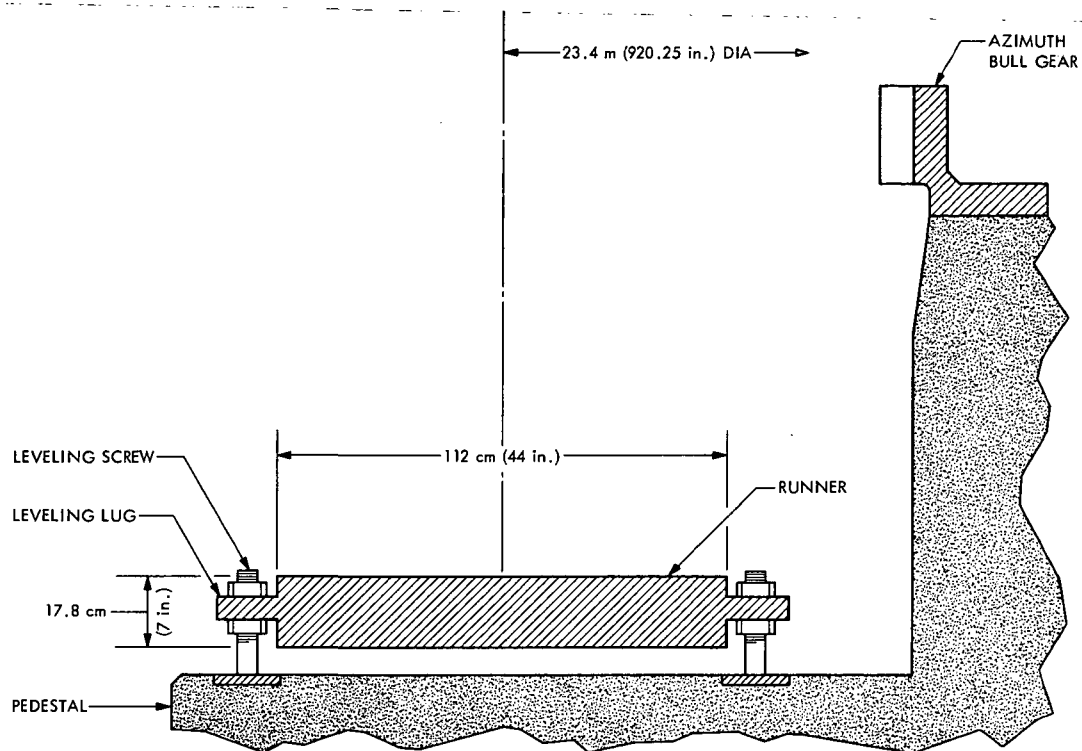


Fig. 1. 64-m-diameter antenna hydrostatic bearing runner

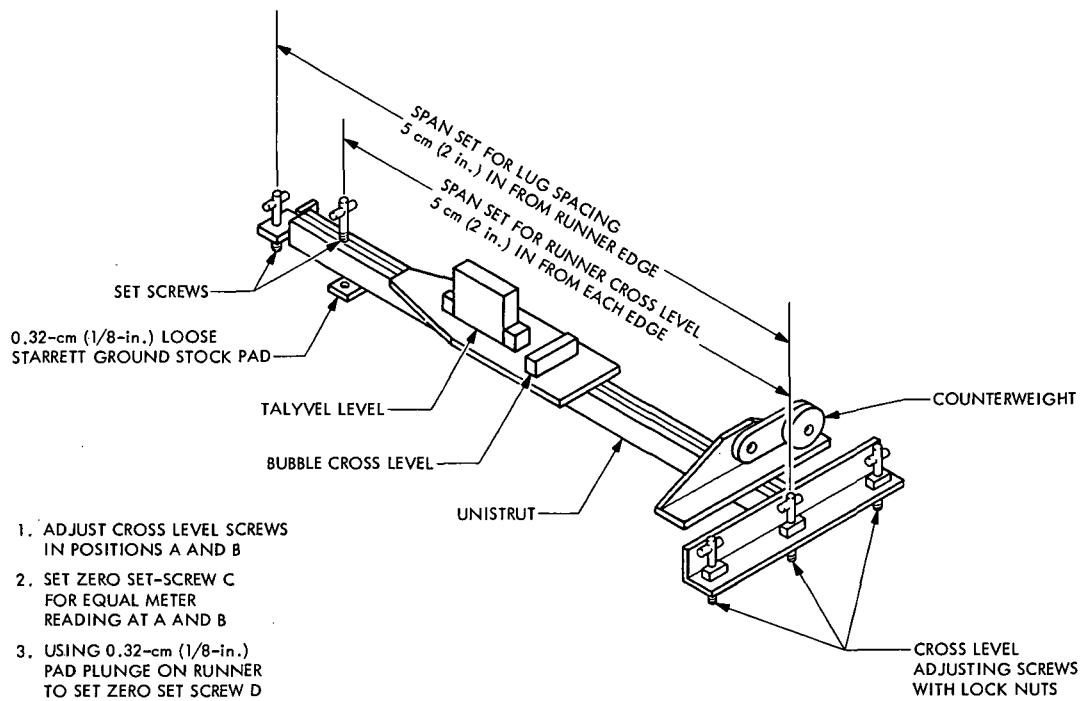


Fig. 2. Runner level check tool

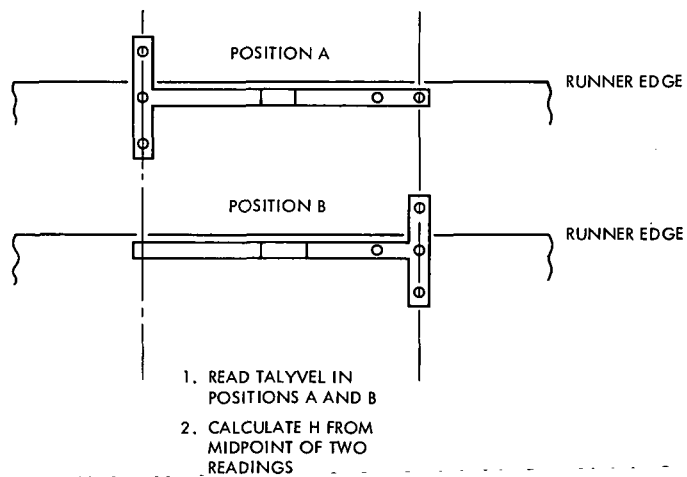


Fig. 3. Level positioning on runner

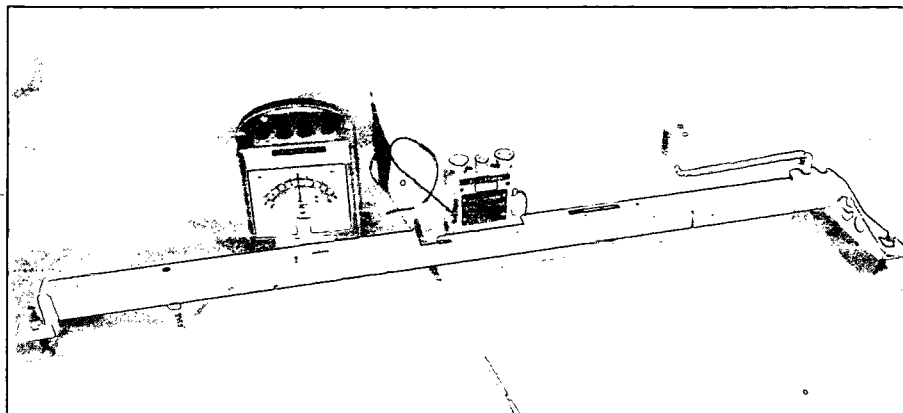


Fig. 4. Long runner alignment tool

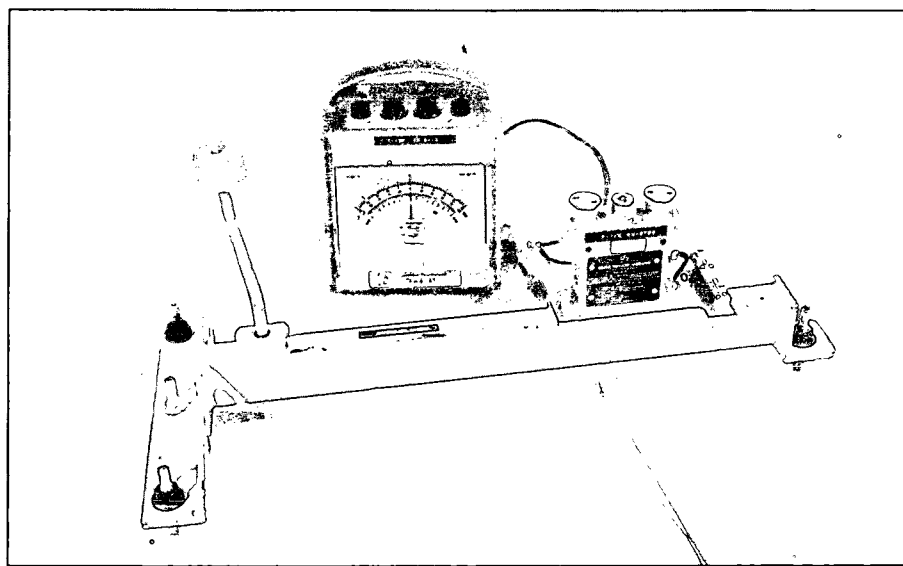


Fig. 5. Short runner alignment tool

DSS Receiving System Saturation at High Signal Levels

H. C. Younger
DSN Operations Organization

A loss of telemetry data from the Lunar Module occurred at DSS 14 during the Apollo 16 mission. This was caused by saturation of the first mixer in the DSS 14 receiving system by a very strong Command Module signal. Tests have been conducted to determine the saturation characteristics of the major components of the DSS receiving system. The problem will be avoided during the Apollo 17 mission by using a lower-gain maser as prime, and by adding a pad following the high-gain backup maser.

I. Introduction

During the Apollo 16 mission, DSS 14 (the Goldstone Mars station, which is equipped with a 64-m-diameter antenna) experienced a loss of data from the Lunar Module (LM). This occurred while the LM was being tracked at 2282.5 MHz, with a signal level of approximately -118 dBm. The time of data loss coincided with the Command and Service Module (CSM) switching to its high-gain antenna, resulting in a CSM signal level of approximately -88 dBm at 2287.5 MHz at DSS 14.

The very high signal level from the CSM was believed to have caused saturation of some component in the DSS 14 receiving system. After the mission, tests were conducted to determine the precise location of the saturation phenomenon, and to develop means of preventing a similar problem during the Apollo 17 mission.

II. DSS 14 Receiving System Tests

There are several possible areas in the DSS 14 receiving system which could have saturated. Referring to Fig. 1, these are the maser, the post-amplifier, and the receiver first and second mixers. Tests were conducted to determine the saturation characteristics of each of these components. The testing was performed over a period of several weeks during the summer of 1972, as station time became available.

Various configurations were established for the tests to isolate the saturation contributions of the various system components. All tests were essentially identical, and consisted of measurement of receiving system noise temperature, followed by measurement of receiver automatic gain control (AGC) characteristics. AGC data measurements covered the range from -80 to -120 dBm, which included the suspected saturation region.

III. Test Results and Analysis

The results of the test series, given in Figs. 2-6, clearly show that the maser, the post-amplifier, and the first mixer all contribute to the saturation effect, with the first mixer being most significant. All of these tests used the Mod 3 maser, which has normally been used for Apollo support.

Figure 2 shows AGC curves in the normal (Apollo 16) configuration. These curves begin to deviate from perfect linearity near -105 dBm, and show nearly complete saturation at -90 dBm. It is a safe assumption that this nonlinearity is the explanation for the telemetry loss experienced during the Apollo 16 mission.

Figure 3 shows the same curves, with 20 dB additional attenuation introduced at attenuator A406. If the second mixer were saturating, a substantial improvement in performance could be expected in this configuration. Figure 3 shows no change, demonstrating that second mixer saturation is insignificant.

Figure 4 shows AGC curves with 20-dB attenuation added in front of the first mixer of receiver 1 (point 4 in Fig. 1). To compensate for this, 20 dB of attenuation was removed from A406, allowing the remainder of the receiver to operate at normal levels. No changes were made to receiver 2. The effect of the 20-dB pad is simply to operate the first mixer of receiver 1 at 20 dB below normal levels, while all other elements of the receiving system operate normally. It is clear that a substantial improvement has been made in the strong signal performance of receiver 1. There is still a departure from perfect linearity, but it is not nearly as severe as that evident in receiver 2. Figure 4 thus demonstrates that, while other elements of the system are also beginning to saturate, the first mixer is by far the most significant contributor.

Figure 5 was obtained with the 20-dB pad moved to point 5 in Fig. 1. This allows both the post-amplifier and first mixer to operate 20 dB below normal levels. The curve for receiver 1 is almost identical to that of Fig. 4, demonstrating that saturation of the post-amplifier is insignificant. The curve for receiver 2 has also straightened out and follows the same shape as that for receiver 1, as expected. (The receiver 2 curve of Fig. 5 is dis-

placed from that in the preceding figures. This is believed to be due to an error in setting up attenuator A406, which was not noticed until the test was completed.)

Figure 6 shows the receiver 1 curves of Figs. 2, 4, and 5 replotted on the same graph, along with a dashed line representing a completely linear system. This clearly shows the improvement to be obtained by introducing the 20-dB pad at the maser output. Curve 1, the normal (Apollo 16) configuration, has a pronounced knee near -95 dBm. Curves 2 and 3 show a much more gradual degradation. The difference between curves 2 and 3 is attributable to gain compression in the transistor post-amplifier. The offset between curve 1 and the other curves at low signal level is attributable to a calibration error between the added 20-dB pad and the compensating 20 dB subtracted from attenuator A406. The gradual curvature of curve 3 is typical of the saturation characteristics of a maser, and is doubtless due to gain compression in the maser itself.

System temperature measurements were also made. A zenith temperature of 24.1 K was measured in the normal configuration. Introducing the 20-dB pad before the first mixer raised this temperature to 24.7 K. Introducing the pad before the post-amplifier raised it to 27.5 K. Inasmuch as the Apollo configuration will normally be used with the antenna pointed at the 300 K lunar background, this increase in system temperature is insignificant and can safely be ignored.

IV. Conclusions and Preparation for Apollo 17

As shown in Figs. 5 and 6, there is still some gain compression evident above about -105 dBm with a 20-dB pad installed behind the Mod 3 maser. Whether this will be sufficient to cause problems for Apollo 17 cannot be determined from RF tests. Telemetry system tests, using simulated Apollo telemetry, will be conducted prior to Apollo 17 support to determine the precise levels at which trouble can be anticipated.

Gain compression in a maser is normally found when the maser output level approaches -40 dBm. Since the Mod 3 maser operates at about 50-dB gain, this can be expected in the area of -90 dBm received signal power, which is confirmed by Figs. 5 and 6. It would seem that the problem could be eliminated by simply reducing the gain of the maser. However, the design of the Mod 3

maser is such that its gain cannot be reduced in the field below about 48 dB. Insertion of attenuation ahead of the maser, while it would eliminate the saturation problem, is not an acceptable alternative since it would eliminate the gain advantage of the 64-m-diameter antenna.

There is another maser available at DSS 14, known as the Polarization Diversity S-Band (PDS) maser. This is R&D equipment which has not been used as the prime maser on previous Apollo missions. The PDS maser is capable of covering the full Apollo bandwidth, and it can be operated at a much lower gain than the Mod 3 maser. Characteristics of the PDS maser are given in

Ref. 1, which shows that it is capable of a 1-dB bandwidth of 32 MHz while operating at 27-dB gain.

Since the PDS maser operates with approximately 20 dB less gain than the Mod 3 maser, system performance with it should be about the same as that shown in Figs. 5 and 6, with the ordinates of these figures shifted by about 20 dB. This would indicate that linear operation can be extended to at least -80 to -85 dBm by use of the PDS maser.

Current planning calls for the PDS maser to be used as prime for Apollo 17, with the Mod 3 maser followed by a 20-dB attenuator available for backup.

Reference

1. Clauss, R., and Quinn R., "Low-Noise Receivers: Microwave Maser Development," *The Deep Space Network*, Space Programs Summary 37-58, Vol. II, pp. 50-52, Jet Propulsion Laboratory, Pasadena, Calif., July 31, 1969.

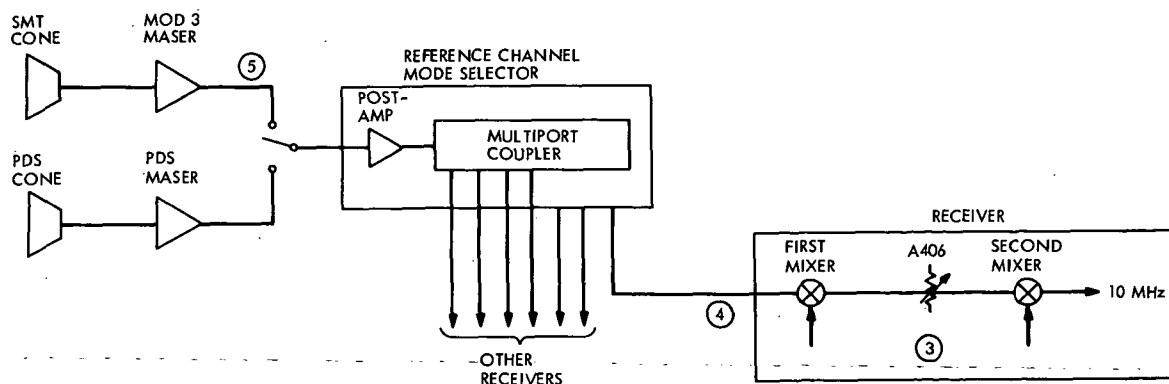


Fig. 1. DSS 14 receiving system, simplified block diagram

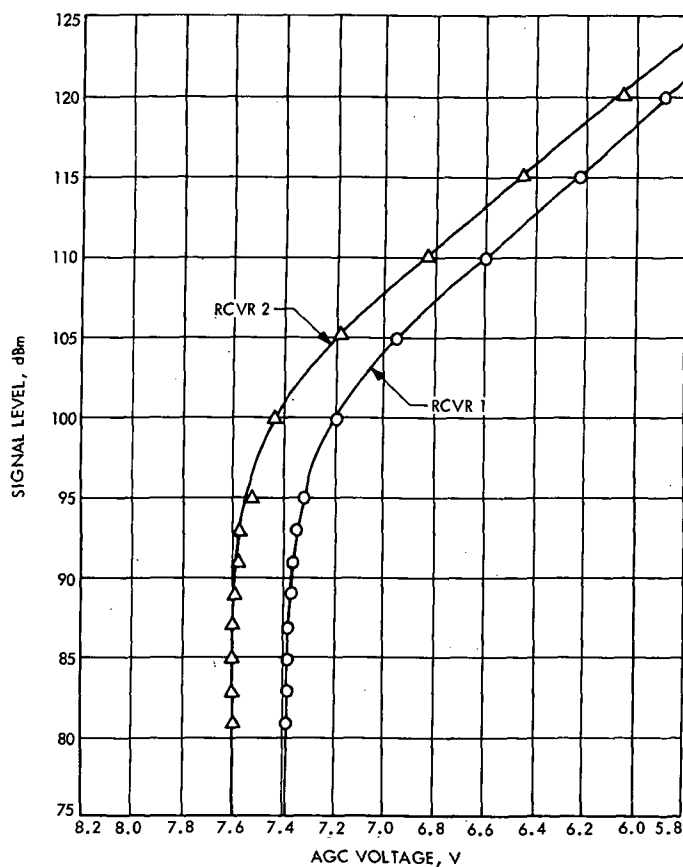


Fig. 2. AGC voltage vs. signal level—normal Apollo configuration (Mod 3 maser)

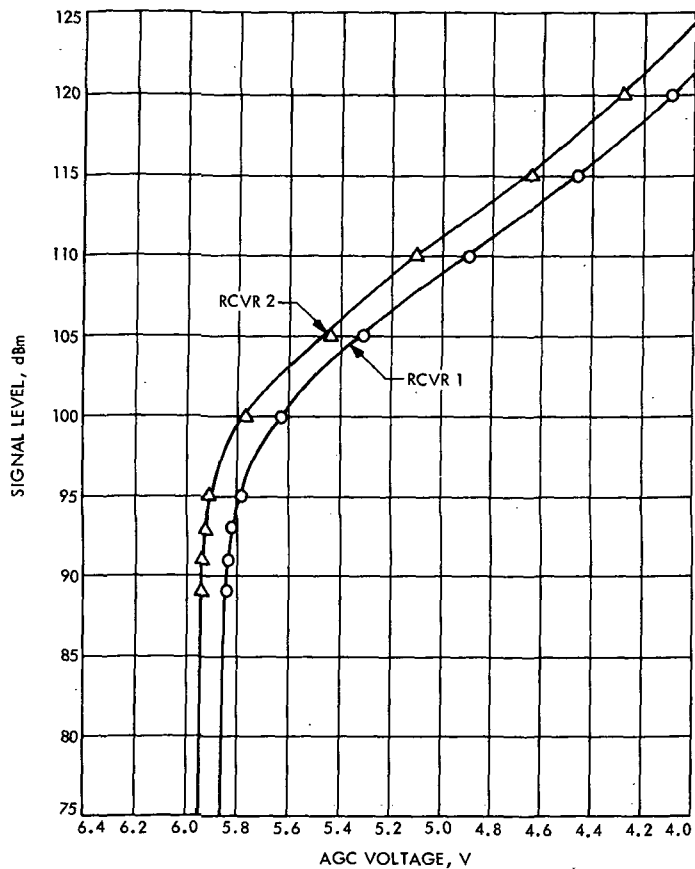


Fig. 3. AGC voltage vs. signal level—20-dB attenuation added to A406 (both receivers)

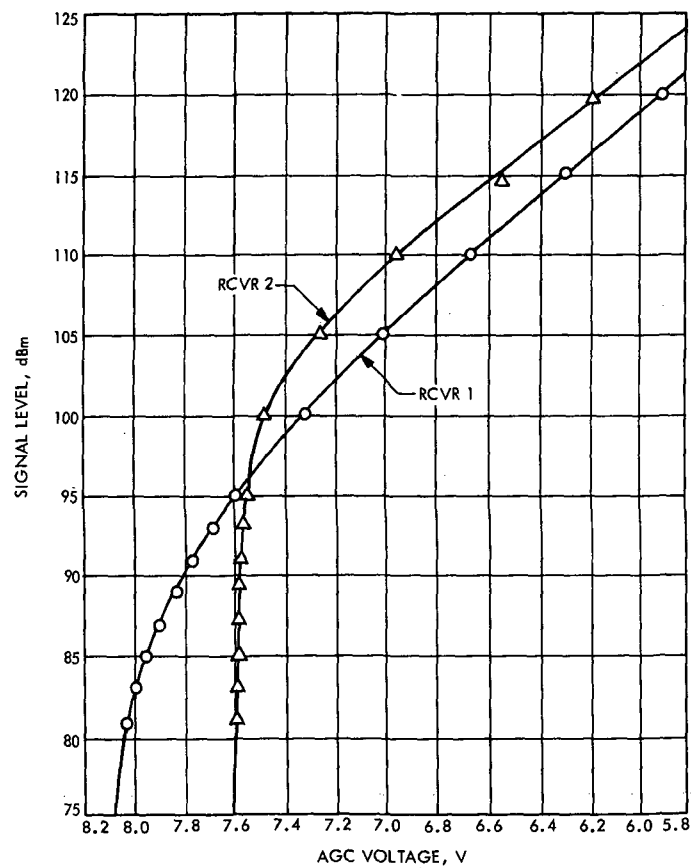


Fig. 4. AGC voltage vs. signal level—20-dB attenuation added before receiver 1 (receiver 2 normal)

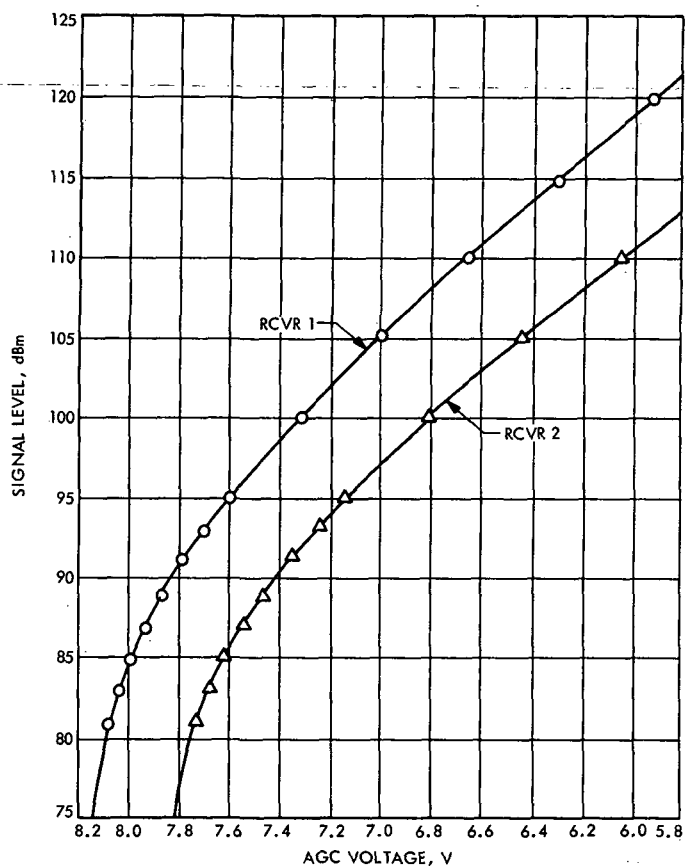


Fig. 5. AGC voltage vs. signal level—20-dB attenuation added after Mod 3 maser

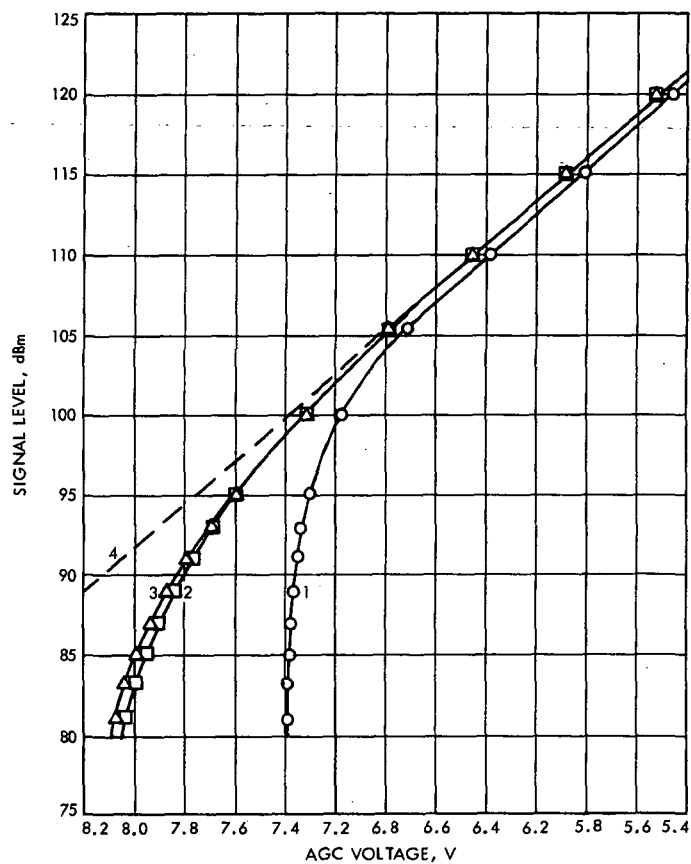


Fig. 6. AGC voltage vs. signal level—receiver 1 AGC (1) normal configuration, (2) 20-dB attenuation added before receiver first mixer, (3) 20-dB attenuation added before post-amplifier, (4) ideal configuration

Spectrum of an Asynchronously Biphase Modulated Square Wave

J. R. Lesh
Network Operations Office

An exact closed-form expression for the power spectrum of a square-wave carrier (or subcarrier) which is biphase modulated by a random binary data stream is presented. The resulting expression is valid for any carrier frequency and data bit rate, provided that the two sources are not phase-coherently related. Also presented is an approximate expression which can be used to alleviate some computational difficulties of the exact expression at low spectral frequencies.

I. Introduction

Equations for the spectrum of a phase-modulated sinusoidal carrier can be found in almost any elementary textbook on communications. Yet there appears to be little in the literature on spectra resulting from square-wave carriers. Some work has been done by Titsworth and Welch (Ref. 1) and later by Levitt (Ref. 2). These studies, however, were concerned with the case where the data bit stream and carrier are phase coherently related, with the ratio of the data bit to carrier periods an integer, or at most an elementary rational number.

In this article we shall determine an exact, closed-form expression for a square-wave carrier biphase modulated by a random binary data stream of any fixed bit rate. We shall require only that the data stream and carrier be generated in a noncoherent manner.

II. Spectrum Derivation

Let $s(t)$ denote a square-wave carrier taking on the values of $+1$ and -1 with period T_s . The spectrum $S_s(\omega)$ of this signal is given by

$$S_s(\omega) = \sum_{k=1}^{\infty} \frac{4}{\pi^2 (2k-1)^2} \times \{ \delta[\omega - (2k-1)\omega_s] + \delta[\omega + (2k-1)\omega_s] \} \quad (1)$$

where $\omega_s = 2\pi/T_s$ and $\delta(\cdot)$ is the Dirac delta function. Also consider a random binary data stream $b(t)$ which assumes the values of $+1$ or -1 with equal probability

and with bit period T_b . It is well known that the spectrum of b is given by

$$S_b(\omega) = \frac{4 \sin^2\left(\frac{\omega T_b}{2}\right)}{T_b \omega^2} \quad (2)$$

Now, if s and b are not coherently related, then (Ref. 1) the spectrum $S(\omega)$ of $s(t)$, biphase modulated by $b(t)$, could be found by the convolution of $S_s(\omega)$ with $S_b(\omega)$; that is,

$$S(\omega) = \frac{16}{\pi^2} \sum_{k=1}^{\infty} \frac{1}{(2k-1)^2} \left\{ \frac{\sin^2\left[\frac{(\omega - (2k-1)\omega_s)T_b}{2}\right]}{T_b [\omega - (2k-1)\omega_s]^2} + \frac{\sin^2\left[\frac{(\omega + (2k-1)\omega_s)T_b}{2}\right]}{T_b [\omega + (2k-1)\omega_s]^2} \right\} \quad (3)$$

However, a closed form for Eq. (3) does not appear to be readily available. Therefore, let us proceed temporarily in the time domain. From transform theory we know that

$$S(\omega) = F\{R(\tau)\} \quad (4)$$

where $F\{\cdot\}$ is the Fourier transform,

$$R(\tau) = R_s(\tau) R_b(\tau) \quad (5)$$

and $R_s(\tau)$ and $R_b(\tau)$ are the autocorrelation functions of $s(t)$ and $b(t)$ respectively. It is clear that

$$R_s(\tau) = 1 - \frac{4|\tau|}{T_s}; \quad -\frac{T_s}{2} \leq \tau \leq \frac{T_s}{2} \quad (6)$$

$$R_b(\tau) = 1 - \frac{|\tau|}{T_b}; \quad -T_b \leq \tau \leq T_b \quad (7)$$

and that $R_s(\tau + kT_s) = R_s(\tau)$, $k = \dots, -1, 0, 1, 2, \dots$. The functions $R_s(\tau)$ and $R_b(\tau)$ are shown in Figs. 1 and 2 respectively.

Now, let us define n as the greatest integer in the quantity

$$\frac{2T_b}{T_s}$$

that is, n is the number of carrier half-periods which can be totally contained in one data bit time. Then, with the aid of Figs. 1 and 2, one can easily show that the spectrum of the modulated carrier is given by

$$S(\omega) = 2 \sum_{k=1}^n \int_{[(k-1)T_s/2]^{kT_s/2}} (-1)^{k-1} \left(1 - \frac{\tau}{T_b}\right) \left[(2k-1) - \frac{4\tau}{T_s}\right] \cos \omega \tau d\tau + 2 \int_{nT_s/2}^{T_b} (-1)^n \left(1 - \frac{\tau}{T_b}\right) \left[(2n+1) - \frac{4\tau}{T_s}\right] \cos \omega \tau d\tau \quad (8)$$

After integrating we have, for $\omega \neq 0$,

$$S(\omega) = \frac{32}{T_s T_b \omega^3} \sum_{k=1}^n (-1)^k \sin \frac{k\omega T_s}{2} + \frac{8}{T_b \omega^2} \sum_{k=1}^n (-1)^{k-1} k \cos \frac{k\omega T_s}{2} + \frac{16}{T_s \omega^2} \sum_{k=1}^n (-1)^k \cos \frac{k\omega T_s}{2} + \frac{2}{T_b \omega^2} + \frac{8}{T_s \omega^2} + \frac{2(-1)^n}{\omega^2} \left[\frac{4}{T_s} - \frac{(2n+1)}{T_b} \right] \cos \omega T_b + \frac{16(-1)^{n-1}}{T_s T_b \omega^3} \sin \omega T_b, \quad \omega \neq 0 \quad (9)$$

Equation (9), even though in closed form, is unattractive computationally since the number of computations depends on the size of n . Fortunately, we can further sim-

plify this expression. First we note that

$$\sum_{k=1}^n (-1)^{k-1} k \cos \frac{k\omega T_s}{2} = -\frac{2}{T_s} \frac{d}{d\omega} \left\{ \sum_{k=1}^n (-1)^k \sin \frac{k\omega T_s}{2} \right\} \quad (10)$$

Then by using the identities (Ref. 3)

$$\sum_{k=1}^n (-1)^k \sin kx = \frac{\sin \left[\frac{n(x+\pi)}{2} \right] \sin \left[\frac{(n+1)(x+\pi)}{2} \right]}{\cos \frac{x}{2}} \quad (11)$$

and

$$\sum_{k=1}^n (-1)^k \cos kx = \frac{1}{2} \left[\frac{(-1)^n \cos \left(\frac{2n+1}{2} x \right)}{\cos \frac{x}{2}} - 1 \right] \quad (12)$$

we have the power spectrum given by

$$\begin{aligned}
 S(\omega) = & \frac{2(-1)^n}{\omega^2} \left[\frac{4}{T_s} - \frac{(2n+1)}{T_b} \right] \left[\cos \omega T_b + \frac{\cos \frac{(2n+1)\omega T_s}{4}}{\cos \frac{\omega T_s}{4}} \right] \\
 & - \frac{2}{T_b \omega^2} \left[\frac{(-1)^n \sin \frac{(2n+1)\omega T_s}{4} \sin \frac{\omega T_s}{4}}{\cos^2 \left(\frac{\omega T_s}{4} \right)} - \frac{1}{\cos^2 \left(\frac{\omega T_s}{4} \right)} - 1 \right] \\
 & + \frac{16}{T_s T_b \omega^3} \left\{ (-1)^n \left[\frac{\sin \frac{(2n+1)\omega T_s}{4}}{\cos \frac{\omega T_s}{4}} - \sin \omega T_b \right] - \frac{\sin \frac{\omega T_s}{4}}{\cos \frac{\omega T_s}{4}} \right\}
 \end{aligned} \quad (13)$$

where

$$\omega \neq 0, \quad \omega \neq \frac{2m\pi}{T_s}, \quad m \text{ is an odd integer.}$$

Equation (13) is the desired expression for the modulated square-wave spectrum. Note, however, that it need not yield the correct result at direct current ($\omega = 0$) and at the carrier frequency harmonics

$$\omega = \frac{2m\pi}{T_s}, \quad m = \text{odd integer}$$

Consequently, we must determine the expressions for the spectrum at these points. For $\omega = 0$, we can use Eq. (8) without the cosine functions to obtain

$$\begin{aligned}
 S(0) = & \frac{T_s^2}{24T_b} [1 - (-1)^n] \\
 & + (-1)^n \left[(2n+1)T_b - n(n+1)T_s + \frac{n^2 T_s^2}{12T_b} (2n+3) - \frac{4T_s^2}{3T_b} \right]
 \end{aligned} \quad (14)$$

When ω corresponds to the carrier harmonics, we can return to Eq. (9) and evaluate the summations directly. The resulting expression is

$$\begin{aligned}
 S\left(\frac{2m\pi}{T_s}\right) = & \frac{(-1)^n T_s^2}{2\pi^2 m^2} \left[\frac{4}{T_s} - \frac{2n+1}{T_b} \right] \cos\left(\frac{2m\pi T_b}{T_s}\right) \\
 & + \frac{(2n+1)T_s}{\pi^2 m^2} - \frac{2(-1)^n T_s^2 \sin\left(\frac{2m\pi T_b}{T_s}\right)}{\pi^3 m^3 T_b} \\
 & - \frac{(2n^2 + 2n - 1)T_s^2}{2\pi^2 m^2 T_b}, \quad m = \text{odd integer}
 \end{aligned} \quad (15)$$

(Actually, by using limit arguments, one can show that Eq. (13) goes to Eqs. (14) and (15) at the appropriate points and hence is valid for all ω .)

By using Eqs. (13–15), one should be able (at least in theory) to compute the desired spectrum for any value of ω . Practically, however, one finds that a significant error results when Eq. (13) is used at relatively low values of ω . This error results from the computational accuracy needed to compute Eq. (13) at these frequencies. For example, the terms of Eq. (13) may be of the order of 10^{+5} while their

sum is of the order of 10^{-5} . To circumvent this problem, we can expand the trigonometric functions of Eq. (13) in their appropriate Taylor series. If we retain only the first two terms of each expansion, Eq. (13) becomes

$$S(\omega) = \frac{2T_s^2}{3T_b(32 - \omega^2 T_s^2)^2} \{64[1 - (-1)^n] - (-1)^n(6n^4 - 6n^2 - 11)\omega^2 T_s^2 + \omega^2 T_s^2\} \\ + 4(-1)^n \left[\frac{2(2n+3)n^2 T_s^2}{3T_b(32 - \omega^2 T_s^2)} - \frac{T_s}{3T_b} - \frac{8n(n+1)T_s}{32 - \omega^2 T_s^2} \right] \\ + (-1)^n(2n+1)T_b, \quad |\omega| \text{ small} \quad (16)$$

Note that Eq. (16) reduces to Eq. (14) when $\omega = 0$.

The frequency below which Eq. (16) should be used rather than Eq. (13) will naturally depend on the problem to be solved. One limit which appears to work quite well is for

$$|\omega| < \frac{0.02}{T_s}$$

However, one may wish to use other limits depending on the carrier frequency, data bit rate, and computational accuracy available.

To see the results of these equations, refer to Figs. 3 and 4. Figure 3 shows the computed spectrum of a 100-Hz square-wave carrier modulated by a 10-bit/s data stream. The data signal spectrum is clearly located around each of

the carrier harmonics. Figure 4 shows the spectrum of the same carrier when the data bit rate is increased to 81.3 bits/s. One can easily see the interference resulting from neighboring harmonics.

III. Conclusion

The spectrum of a square-wave carrier asynchronously biphase modulated by binary random data is derived and presented in the form of Eqs. (13-15). These equations are useful in that they are exact expressions and are given in closed form. It was pointed out, however, that Eq. (13) requires extremely high computational accuracies when evaluated at low spectral frequencies. For this reason, an approximate expression (Eq. 16), which is valid at low frequencies, was determined and can be used in place of Eq. (14).

References

1. Titsworth, R. C., and Welch, L. R., *Power Spectra of Signals Modulated by Random and Pseudorandom Sequences*, Technical Report 32-140, Jet Propulsion Laboratory, Pasadena, Calif., Oct. 1961.
2. Levitt, B. K., "MVM 73 S-Band Telemetry Power Spectra," JPL Internal Document 3396-71-223, Jet Propulsion Laboratory, Pasadena, California, Aug. 1971.
3. Gradshteyn, I. S., and Ryzhik, I. M., *Table of Integrals, Series, and Products*, 4th ed., translated by A. Jeffrey, Academic Press, New York, 1965, p. 30.

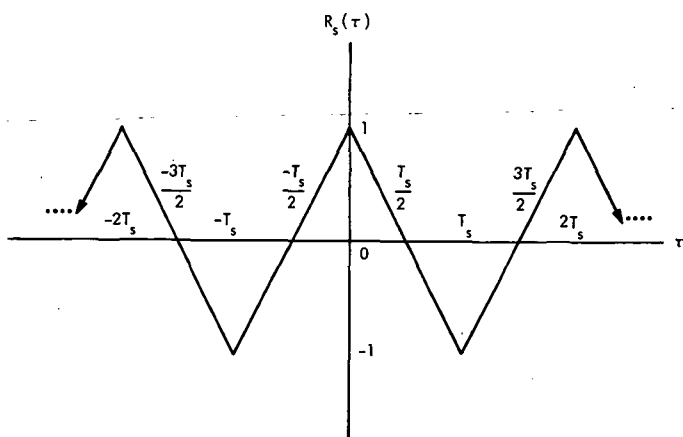


Fig. 1. Autocorrelation function of $s(t)$

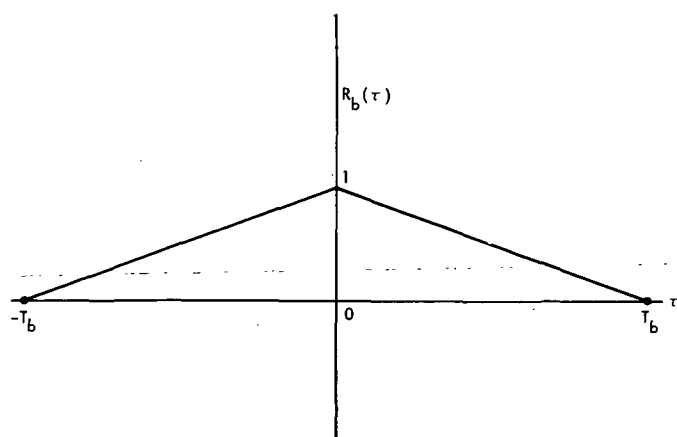


Fig. 2. Autocorrelation function of $b(t)$

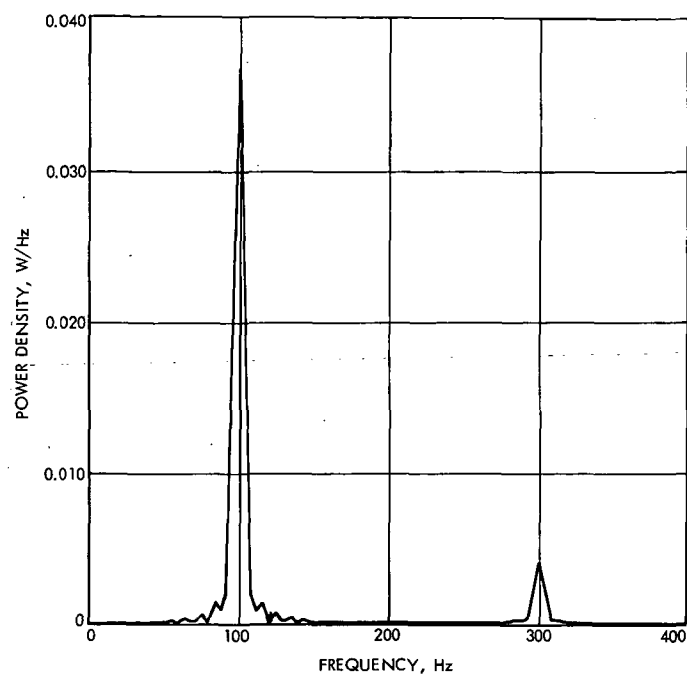


Fig. 3. Computed power spectrum of a 100-Hz carrier modulated by a 10-bit/s data stream

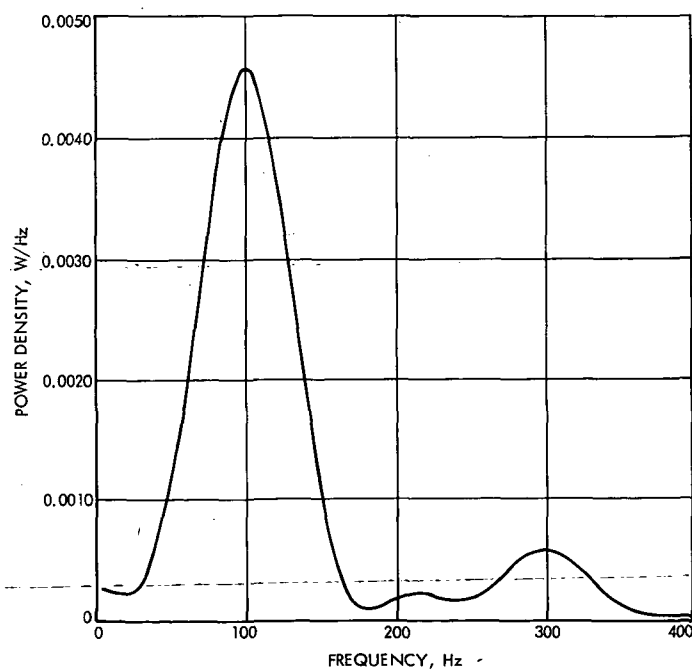


Fig. 4. Computed power spectrum of a 100-Hz carrier modulated by a 81.3-bit/s data stream

Bibliography

- Anderson, J. D., *Determination of the Masses of the Moon and Venus and the Astronomical Unit from Radio Tracking Data of the Mariner II Spacecraft*. Technical Report 32-816. Jet Propulsion Laboratory, Pasadena, Calif., July 1, 1967.
- Anderson, J. D., et al., "The Radius of Venus as Determined by Planetary Radar and Mariner V Radio Tracking Data," *J. Atmos. Sci.*, pp. 1171-1174, Sept. 25, 1968.
- Berman, A. L., *Tracking System Data Analysis Report, Ranger VII Final Report*, Technical Report 32-719, Jet Propulsion Laboratory, Pasadena, Calif., June 1, 1965.
- Berman, A. L., *ABTRAJ—On-Site Tracking Prediction Program for Planetary Spacecraft*, Technical Memorandum 33-391. Jet Propulsion Laboratory, Pasadena, Calif., Aug. 15, 1968.
- Cain, D. L., and Hamilton, T. W., *Determination of Tracking Station Locations by Doppler and Range Measurements to an Earth Satellite*, Technical Report 32-534. Jet Propulsion Laboratory, Pasadena, Calif., Feb. 1, 1964.
- Carey, C. N., and Sjogren, W. L., "Gravitational Inconsistency, in the Lunar Theory: Confirmation by Radio Tracking," *Science*, Vol. 160, pp. 875, 876, Apr.-June 1968.
- Curkendall, D. W., and Stephenson, R. R., "Earthbased Tracking and Orbit Determination—Backbone of the Planetary Navigation System," *Astronaut. Aeronaut.*, Vol. 7, May 1970.
- Curkendall, D. W., "Planetary Navigation: The New Challenges," *Astronaut. Aeronaut.*, Vol. 7, May 1970.
- Efron, L., and Solloway, C. B., *Proceedings of the Conference on Scientific Applications of Radio and Radar Tracking in the Space Program*, Technical Report 32-1475. Jet Propulsion Laboratory, Pasadena, Calif., July 1970.
- Flanagan, F. M., et al., *Deep Space Network Support of the Manned Space Flight Network for Apollo: 1962-1968*, Technical Memorandum 33-452, Vol. I. Jet Propulsion Laboratory, Pasadena, Calif., July 1970.
- Flanagan, F. M., et al., *Deep Space Network Support of the Manned Space Flight Network for Apollo: 1969-1970*, Technical Memorandum 33-452, Vol. II. Jet Propulsion Laboratory, Pasadena, Calif., May 1, 1971.
- Fjeldbo, G., and Eshleman, V. R., "Radio Occultation Measurements and Interpretations," in *The Atmospheres of Venus and Mars*, p. 225. Gordon and Breach, Science Publishers, Inc., New York, N.Y.
- Georgevick, R. M., "Mathematical Model of the Solar Radiation Force and Torques Acting on the Components of a Spacecraft," Technical Memorandum 33-494. Jet Propulsion Laboratory, Pasadena, Calif., Oct. 1, 1971.
- Goldstein, R. M., "Radar Time-of-Flight Measurements to Venus," *Astron. J.*, Vol. 73, No. 9, Aug. 1968.
- Goldstein, R. M., and Rumsey, H., Jr., "A Radar Snapshot of Venus," *Science*, Vol. 169, Sept. 1970.

Bibliography (contd)

- Gordon, H. J., et al., *The Mariner 6 and 7 Flight Paths and Their Determination From Tracking Data*, Technical Memorandum 33-469. Jet Propulsion Laboratory, Pasadena, Calif., Dec. 1, 1970.
- Hamilton, T. W., et al., *The Ranger IV Flight Path and Its Determination From Tracking Data*, Technical Report 32-345. Jet Propulsion Laboratory, Pasadena, Calif., Sept. 15, 1962.
- Kellermann, K. I., et al., "High Resolution Observations of Compact Radio Sources at 13 Centimeters," *Astrophys. J.*, Vol. 161, pp. 803-809, Sept. 1970.
- Kliore, A., "Radio Occultation Measurements of the Atmospheres of Mars and Venus," in *The Atmospheres of Venus and Mars*, p. 205. Gordon and Breach Science Publishers, Inc., New York, N. Y.
- Labrum, R. G., Wong, S. K., and Reynolds, G. W., *The Surveyor V, VI, and VII Flight Paths and Their Determination from Tracking Data*, Technical Report 32-1302. Jet Propulsion Laboratory, Pasadena, Calif., Dec. 1, 1968.
- Lieske, J. H., and Null, G. W., "Icarus and the Determination of Astronomical Constants," *Astron. J.*, Vol. 74, No. 2, Mar. 1969.
- Lorell, J., and Sjogren, W. L., *Lunar Orbiter Data Analysis*, Technical Report 32-1220. Jet Propulsion Laboratory, Pasadena, Calif., Nov. 15, 1967.
- Lorell, J., *Lunar Orbiter Gravity Analysis*, Technical Report 32-1387. Jet Propulsion Laboratory, Pasadena, Calif., June 15, 1969.
- Lorell, J., et al., "Celestial Mechanics Experiment for *Mariner*," *Icarus*, Vol. 12, Jan. 1970.
- McNeal, C. E., *Ranger V Tracking Systems Data Analysis Final Report*, Technical Report 32-702. Jet Propulsion Laboratory, Pasadena, Calif., Apr. 15, 1965.
- Melbourne, W. G., et al., *Constants and Related Information for Astrodynamical Calculations*, Technical Report 32-1306. Jet Propulsion Laboratory, Pasadena, Calif., July 15, 1968.
- Melbourne, W. G., "Planetary Ephemerides," *Astronaut. Aeronaut.*, Vol. 7, May 1970.
- Miller, L., et al., *The Atlas-Centaur VI Flight Path and Its Determination from Tracking Data*, Technical Report 32-911. Jet Propulsion Laboratory, Pasadena, Calif., Apr. 15, 1966.
- Moyer, T. D., "Mathematical Formulation of the Double-Precision Orbit Determination Program (DPODP)," Technical Report 32-1527, Jet Propulsion Laboratory, Pasadena, Calif., May 17, 1971.
- Mulhall, B. D., et al., *Tracking System Analytic Calibration Activities for the Mariner Mars 1969 Mission*, Technical Report 32-1499. Jet Propulsion Laboratory, Pasadena, Calif., Nov. 15, 1970.
- Mulholland, J. D., and Sjogren, W. L., *Lunar Orbiter Ranging Data*, Technical Report 32-1087. Jet Propulsion Laboratory, Pasadena, Calif., Jan. 6, 1967.

Bibliography (contd)

- Mulholland, J. D., *Proceedings of the Symposium on Observation, Analysis, and Space Research Applications of the Lunar Motion*, Technical Report 32-1386. Jet Propulsion Laboratory, Pasadena, Calif., Apr. 1969.
- Muller, P. M., and Sjogren, W. L., *Consistency of Lunar Orbiter Residuals With Trajectory and Local Gravity Effects*, Technical Report 32-1307. Jet Propulsion Laboratory, Pasadena, Calif., Sept. 1, 1968.
- Muller, P. M., and Sjogren, W. L., *Lunar Mass Concentrations*, Technical Report 32-1339. Jet Propulsion Laboratory, Pasadena, Calif., Aug. 16, 1968.
- Null, G. W., Gordon, H. J., and Tito, D. A., *Mariner IV Flight Path and Its Determination From Tracking Data*, Technical Report 32-1108. Jet Propulsion Laboratory, Pasadena, Calif., Aug. 1, 1967.
- O'Neil, W. J., et al., *The Surveyor III and Surveyor IV Flight Paths and Their Determination From Tracking Data*, Technical Report 32-1292. Jet Propulsion Laboratory, Pasadena, Calif., Aug. 15, 1968.
- Pease, G. E., et al., *The Mariner V Flight Path and Its Determination From Tracking Data*, Technical Report 32-1363. Jet Propulsion Laboratory, Pasadena, Calif., July 1, 1969.
- Renzetti, N. A., *Tracking and Data Acquisition for Ranger Missions I-V*, Technical Memorandum 33-174. Jet Propulsion Laboratory, Pasadena, Calif., July 1, 1964.
- Renzetti, N. A., *Tracking and Data Acquisition for Ranger Missions VI-IX*, Technical Memorandum 33-275. Jet Propulsion Laboratory, Pasadena, Calif., Sept. 15, 1966.
- Renzetti, N. A., *Tracking and Data Acquisition Support for the Mariner Venus 1962 Mission*, Technical Memorandum 33-212. Jet Propulsion Laboratory, Pasadena, Calif., July 1, 1965.
- Renzetti, N. A., *Tracking and Data Acquisition Report, Mariner Mars 1964 Mission: Near-Earth Trajectory Phase*, Technical Memorandum 33-239, Vol. I. Jet Propulsion Laboratory, Pasadena, Calif., Jan. 1, 1965.
- Renzetti, N. A., *Tracking and Data Acquisition Report, Mariner Mars 1964 Mission: Cruise to Post-Encounter Phase*, Technical Memorandum 33-239, Vol. II. Jet Propulsion Laboratory, Pasadena, Calif., Oct. 1, 1967.
- Renzetti, N. A., *Tracking and Data Acquisition Report, Mariner Mars 1964 Mission: Extended Mission*, Technical Memorandum 33-239, Vol. III. Jet Propulsion Laboratory, Pasadena, Calif., Dec. 1, 1968.
- Renzetti, N. A., *Tracking and Data System Support for Surveyor: Missions I and II*, Technical Memorandum 33-301, Vol. I. Jet Propulsion Laboratory, Pasadena, Calif., July 15, 1969.
- Renzetti, N. A., *Tracking and Data System Support for Surveyor: Missions III and IV*, Technical Memorandum 33-301, Vol. II. Jet Propulsion Laboratory, Pasadena, Calif., Sept. 1, 1969.
- Renzetti, N. A., *Tracking and Data System Support for Surveyor: Mission V*, Technical Memorandum 33-301, Vol. III. Jet Propulsion Laboratory, Pasadena, Calif., Dec. 1, 1969.

Bibliography (contd)

- Renzetti, N. A., *Tracking and Data System Support for Surveyor: Mission VI*, Technical Memorandum 33-301, Vol. IV. Jet Propulsion Laboratory, Pasadena, Calif., Dec. 1, 1969.
- Renzetti, N. A., *Tracking and Data System Support for Surveyor: Mission VII*, Technical Memorandum 33-301, Vol. V. Jet Propulsion Laboratory, Pasadena, Calif., Dec. 1, 1969.
- Renzetti, N. A., *Tracking and Data System Support for the Mariner Venus 67 Mission: Planning Phase Through Midcourse Maneuver*, Technical Memorandum 33-385, Vol. I. Jet Propulsion Laboratory, Pasadena, Calif., Sept. 1, 1969.
- Renzetti, N. A., *Tracking and Data System Support for the Mariner Venus 67 Mission: Midcourse Maneuver Through End of Mission*, Technical Memorandum 33-385, Vol. II. Jet Propulsion Laboratory, Pasadena, Calif., Sept. 1, 1969.
- Renzetti, N. A., *Tracking and Data System Support for the Pioneer Project. Pioneer VI. Prelaunch to End of Nominal Mission*, Technical Memorandum 33-426, Vol. I. Jet Propulsion Laboratory, Pasadena, Calif., Feb. 1, 1970.
- Renzetti, N. A., *Tracking and Data System Support for the Pioneer Project. Pioneer VII. Prelaunch to End of Nominal Mission*, Technical Memorandum 33-426, Vol. II. Jet Propulsion Laboratory, Pasadena, Calif., Apr. 15, 1970.
- Renzetti, N. A., *Tracking and Data System Support for the Pioneer Project. Pioneer VIII. Prelaunch Through May 1968*, Technical Memorandum 33-426, Vol. III. Jet Propulsion Laboratory, Pasadena, Calif., July 15, 1970.
- Renzetti, N. A., *Tracking and Data System Support for the Pioneer Project. Pioneer IX. Prelaunch Through June 1969*, Technical Memorandum 33-426, Vol. IV. Jet Propulsion Laboratory, Pasadena, Calif., Nov. 15, 1970.
- Renzetti, N. A., *Tracking and Data System Support for the Pioneer Project. Pioneer VI. Extended Mission: July 1, 1966-July 1, 1969*, Technical Memorandum 33-426, Vol. V. Jet Propulsion Laboratory, Pasadena, Calif., Feb. 1, 1971.
- Renzetti, N. A., *Tracking and Data System Support for the Pioneer Project. Pioneer VII. Extended Mission: February 24, 1967-July 1, 1968*, Technical Memorandum 33-426, Vol. VI. Jet Propulsion Laboratory, Pasadena, Calif., Apr. 15, 1971.
- Renzetti, N. A., *Tracking and Data System Support for the Pioneer Project. Pioneer VII. Extended Mission: July 1, 1968-July 1, 1969*, Technical Memorandum 33-426, Vol. VII. Jet Propulsion Laboratory, Pasadena, Calif., Apr. 15, 1971.
- Renzetti, N. A., *Tracking and Data System Support for the Pioneer Project. Pioneer VIII. Extended Mission: June 1, 1968-July 1, 1969*, Technical Memorandum 33-426, Vol. VIII. Jet Propulsion Laboratory, Pasadena, Calif., May 1, 1971.
- Renzetti, N. A., *Tracking and Data System Support for the Pioneer Project. Pioneers VI-IX. Extended Missions: July 1, 1969-July 1, 1970*. Technical Memorandum 33-426, Vol. IX. Jet Propulsion Laboratory, Pasadena, Calif., Aug. 15, 1971.
- Sjogren, W. L., *The Ranger III Flight Path and Its Determination From Tracking Data*, Technical Report 32-563. Jet Propulsion Laboratory, Pasadena, Calif., Sept. 15, 1965.

Bibliography (contd)

- Sjogren, W. L., et al., *The Ranger V Flight Path and Its Determination From Tracking Data*, Technical Report 32-562. Jet Propulsion Laboratory, Pasadena, Calif., Dec. 6, 1963.
- Sjogren, W. L., et al., *The Ranger VI Flight Path and Its Determination From Tracking Data*, Technical Report 32-605. Jet Propulsion Laboratory, Pasadena, Calif., Dec. 15, 1964.
- Sjogren, W. L., et al., *Physical Constants as Determined From Radio Tracking of the Ranger Lunar Probes*, Technical Report 32-1057. Jet Propulsion Laboratory, Pasadena, Calif., Dec. 30, 1966.
- Sjogren, W. L., *Proceedings of the JPL Seminar on Uncertainties in the Lunar Ephemeris*, Technical Report 32-1247. Jet Propulsion Laboratory, Pasadena, Calif., May 1, 1968.
- Sjogren, W. L., "Lunar Gravity Estimate: Independent Confirmation," *J. Geophys. Res.*, Vol. 76, No. 29, Oct. 10, 1971.
- Spier, G. W., "Design and Implementation of Models for the Double Precision Trajectory Program (DPTRAJ)," Technical Memorandum 33-451, Jet Propulsion Laboratory, Pasadena, Calif., Apr. 15, 1971.
- Stelzried, C. T., *A Faraday Rotation Measurement of a 13-cm Signal in the Solar Corona*, Technical Report 32-1401. Jet Propulsion Laboratory, Pasadena, Calif., July 15, 1970.
- Stelzried, C. T., et al., "The Quasi-Stationary Coronal Magnetic Field and Electron Density as Determined From a Faraday Rotation Experiment," *Sol. Phys.*, Vol. 14, No. 2, pp. 440-456, Oct. 1970.
- Thornton, J. H., Jr., *The Surveyor I and Surveyor II Flight Paths and Their Determination From Tracking Data*, Technical Report 32-1285. Jet Propulsion Laboratory, Pasadena, Calif., Aug. 1, 1968.
- Vegos, C. J., et al., *The Ranger IX Flight Path and Its Determination From Tracking Data*, Technical Report 32-767. Jet Propulsion Laboratory, Pasadena, Calif., Nov. 1, 1968.
- Winn, F. B., *Selenographic Location of Surveyor VI, Surveyor VI Mission Report: Part II. Science Results*, Technical Report 32-1262. Jet Propulsion Laboratory, Pasadena, Calif., Jan. 10, 1968.
- Winn, F. B., "Post Landing Tracking Data Analysis," in *Surveyor VII Mission Report: Part II. Science Results*, Technical Report 32-1264. Jet Propulsion Laboratory, Pasadena, Calif., Mar. 15, 1968.
- Winn, F. B., "Post Lunar Touchdown Tracking Data Analysis," in *Surveyor Project Final Report: Part II. Science Results*, Technical Report 32-1265. Jet Propulsion Laboratory, Pasadena, Calif., June 15, 1968.
- Winn, F. B., *Surveyor Posttouchdown Analyses of Tracking Data*, NASA SP-184. National Aeronautics and Space Administration, Washington, D.C., p. 369.
- Wollenhaupt, W. R., et al., *The Ranger VII Flight Path and Its Determination From Tracking Data*, Technical Report 32-694. Jet Propulsion Laboratory, Pasadena, Calif., Dec. 15, 1964.

N73-14258

TECHNICAL REPORT STANDARD TITLE PAGE

1. Report No. 32-1526, Vol. XII	2. Government Accession No.	3. Recipient's Catalog No.	
4. Title and Subtitle THE DEEP SPACE NETWORK PROGRESS REPORT FOR SEPTEMBER AND OCTOBER 1972		5. Report Date December 15, 1972	
		6. Performing Organization Code	
7. Author(s) JPL Staff		8. Performing Organization Report No.	
9. Performing Organization Name and Address JET PROPULSION LABORATORY California Institute of Technology 4800 Oak Grove Drive Pasadena, California 91103		10. Work Unit No.	
		11. Contract or Grant No. NAS 7-100	
		13. Type of Report and Period Covered Technical Report	
12. Sponsoring Agency Name and Address NATIONAL AERONAUTICS AND SPACE ADMINISTRATION Washington, D.C. 20546		14. Sponsoring Agency Code	
15. Supplementary Notes			
16. Abstract This report describes work performed for the JPL/NASA Deep Space Network (DSN). Progress is presented on DSN supporting research and technology, advanced development and engineering, and implementation, and DSN operations which pertain to mission-independent or multiple-mission development as well as to support of flight projects. Each issue contains a description of the functions and facilities of the DSN.			
17. Key Words (Selected by Author(s)) Antennas and Transmission Lines Information Theory Telemetry and Command Tracking		18. Distribution Statement Unclassified -- Unlimited	
19. Security Classif. (of this report) Unclassified	20. Security Classif. (of this page) Unclassified	21. No. of Pages 235	22. Price

HOW TO FILL OUT THE TECHNICAL REPORT STANDARD TITLE PAGE

Make items 1, 4, 5, 9, 12, and 13 agree with the corresponding information on the report cover. Use all capital letters for title (item 4). Leave items 2, 6, and 14 blank. Complete the remaining items as follows:

3. Recipient's Catalog No. Reserved for use by report recipients.
7. Author(s). Include corresponding information from the report cover. In addition, list the affiliation of an author if it differs from that of the performing organization.
8. Performing Organization Report No. Insert if performing organization wishes to assign this number.
10. Work Unit No. Use the agency-wide code (for example, 923-50-10-06-72), which uniquely identifies the work unit under which the work was authorized. Non-NASA performing organizations will leave this blank.
11. Insert the number of the contract or grant under which the report was prepared.
15. Supplementary Notes. Enter information not included elsewhere but useful, such as: Prepared in cooperation with... Translation of (or by)... Presented at conference of... To be published in...
16. Abstract. Include a brief (not to exceed 200 words) factual summary of the most significant information contained in the report. If possible, the abstract of a classified report should be unclassified. If the report contains a significant bibliography or literature survey, mention it here.
17. Key Words. Insert terms or short phrases selected by the author that identify the principal subjects covered in the report, and that are sufficiently specific and precise to be used for cataloging.
18. Distribution Statement. Enter one of the authorized statements used to denote releasability to the public or a limitation on dissemination for reasons other than security of defense information. Authorized statements are "Unclassified-Unlimited," "U. S. Government and Contractors only," "U. S. Government Agencies only," and "NASA and NASA Contractors only."
19. Security Classification (of report). NOTE: Reports carrying a security classification will require additional markings giving security and downgrading information as specified by the Security Requirements Checklist and the DoD Industrial Security Manual (DoD 5220.22-M).
20. Security Classification (of this page). NOTE: Because this page may be used in preparing announcements, bibliographies, and data banks, it should be unclassified if possible. If a classification is required, indicate separately the classification of the title and the abstract by following these items with either "(U)" for unclassified, or "(C)" or "(S)" as applicable for classified items.
21. No. of Pages. Insert the number of pages.
22. Price. Insert the price set by the Clearinghouse for Federal Scientific and Technical Information or the Government Printing Office, if known.